Effects and benefits of nanoparticle assisted microwave imaging for the detection of breast cancer

Lahri, Rachita

Awarding institution:
King's College London

Effects and benefits of nanoparticle assisted microwave imaging for the detection of breast cancer

by

Rachita Lahri

A thesis submitted to King's College London in partial fulfilment for the degree of

Doctor of Philosophy

Supervisors:

Dr. Maya Thanou

Dr. Panagiotis Kosmas

Abstract

Microwave imaging/sensing is an emerging technology that shows potential for healthcare diagnostic applications, particularly in breast cancer detection. This technique is found to assess the anatomically variant dielectric properties of the breast and use this information for image configuration. The contrast between malignant and fatty breast tissues may be as large as 10:1, however, the distinction between malignant and healthy fibro-glandular tissues can be as low as 10%. Nevertheless, it is suggested that contrast agents would enhance this difference. Like other imaging modalities, nanoparticles (NPs) could potentially be utilized as contrast agents to increase the contrast between healthy and malignant tissues. In this project, aqueous suspensions of NPs such as zinc oxide, silicon dioxide, different types (different length & functionalization) of carbon nanotubes, commercial iron oxides and effective conductivity Aldrich, Sienna^{+} and ferrofluid from Liquid Research (FF) and zinc ferrites were tested. Two zinc ferrites with different compositions of zinc and iron have been synthesized via thermal decomposition method to investigate the effect of Zn doping on the dielectric properties. These synthesized ferrites were functionalized with PMAO (poly-maleic anhydride-alt-1-octadecene)) polymer. Dielectric studies of the NPs are carried out to assess their potential effective contrast in different mediums such as RO water, 60% glycerol and TM (tissue mimicking) phantom for microwave imaging. Characterization of the NPs has been achieved using atomic force microscopy (AFM) and scanning electron microscopy (SEM). The size and stability of colloidal dispersions have been characterized by dynamic light scattering technique (DLS) and Ultraviolet-visible spectrophotometry (UV-Vis). Raman Spectroscopy is carried out for carbon nanotubes to characterize their different structures. The dielectric characterization of the aqueous-based colloidal suspensions in different media is recorded over the microwave frequency range between 1 and 4 GHz. Zinc oxide NP dispersion has shown an increase in the dielectric constant compared to the background medium. Addition of Polyethylene glycol on ZnO NPs can achieve a valid increase in the dielectric constant compared to water, which was shown to be concentration

dependent. MWNT-OH (hydroxylated multi-walled carbon nanotube) shows an increase in the dielectric constant compared with other carbon nanotubes in RO water and the change is higher in 60% glycerol and in TM phantom. Sienna^{+} and FF showed an increase in the dielectric properties compared with SA, because of the surface modifications. Dielectric properties of Sienna^{+} and FF are higher in 60% glycerol compared with RO water. From the two synthesized zinc ferrites, [$(Zn_{0.18}Fe_{0.82})$ Fe_2O_4]-PMAO showed higher dielectric properties compared with [$(Zn_{0.39}Fe_{0.61})Fe_2O_4$]- PMAO in RO water, 60% glycerol and TM phantom. These results suggest that ZnO nanomaterials, MWNTs, and zinc ferrites have the potential to be used in biomedical applications such as breast imaging to improve diagnostic capabilities.

Table of Contents

1 GENERAL INTRODUCTION 1

1.1 Current breast imaging modalities 3

1.2 Introducing microwave imaging as a sensing and imaging modality 7

1.2.1 Dielectric theory 8

1.2.2 The frequency response of dielectric mechanisms 10

1.3 Dielectric polarisation mechanisms 10

1.3.1 Electronic polarisation 11

1.3.2 Orientational (dipolar) polarisation 11

1.3.3 Atomic polarization 12

1.3.4 Dielectric polarization in a single & multi-component system 12

1.4 Dielectric characterization studies of biological tissues 14

1.5 Microwave techniques for measuring dielectric properties 17

1.5.1 Coaxial probe technique 18

1.5.2 Resonant cavity method 19

1.5.3 Transmission line system method 20

1.5.4 Free space method 20

1.6 Overview of Microwave Imaging 21

1.6.1 Microwave Tomography 22

1.6.2 Radar based approach 24

1.7 Use of NPs as contrast agents 26

1.7.1 Enhanced permeation & retention effect (EPR) 27

1.7.2 Nanoparticles in medicine 28

1.7.3 Dielectric studies of nanoparticles 28

1.8 Conclusions 38

2 MATERIALS & METHODS 40

2.1 Materials 41

2.1.1 Materials used for chapter 3; 41
2.1.2 Materials used for chapter 4; 41
2.1.3 Materials used for chapter 5; 41
2.1.4 Material used for TM (tissue mimicking) phantom 42

2.2 Methods 43
2.2.1 Morphological characterisation of nanoparticles 43
2.2.2 Turbidity measurement using Ultraviolet-Visible Spectrophotometry (UV-Vis) 44
2.2.3 Nanoparticle size measurement using Dynamic Light Scattering (DLS) 45
2.2.4 ZnO nanoparticle surface modification using PEG (polyethylene glycol) 46
2.2.5 Synthesis of ferrites by thermal decomposition 46
2.2.6 Functionalisation of ferrites with PMAO 47
2.2.7 Tissue-mimicking (TM) phantom preparation 47
2.2.8 Sample preparation for dielectric characterisation 49
2.2.9 Characterisation of dielectric Properties 49
2.2.10 Raman Spectroscopy 50
2.2.11 Total reflection X-ray fluorescence spectroscopy (TXRF) 50

3 CARBON NANOTUBES AS CONTRAST ENHANCING AGENTS FOR MWI 51

3.1 Introduction 52
3.1.1 Short history of CNT 53
3.1.2 Method of CNT synthesis 55
3.1.3 Electrical and conductive properties of CNTs 57
3.1.4 Functionalisation of CNTs 60
3.1.5 Bio fate of CNTs and biomedical applications 61

3.2 Study objectives 62
3.2.1 Aims of the study 62

3.3 Results 64
3.3.1 CNTs morphology and analysis 64

3.4 Dielectric properties of CNT suspension at MW frequencies 66
3.4.1 Dielectric properties of CNT suspensions in RO water 66

3.5 Discussion 70

3.5.1 CNT morphology analysis 71

3.5.2 Dielectric analysis 71

3.5.3 Effect of length on CNTs on the dielectric properties of mediums 72

3.5.4 Effect of functionalisation of CNTs on the dielectric properties of a medium 74

3.6 Conclusion & Summary 77

4 ZINC OXIDE NPS AS CONTRAST ENHANCING AGENTS FOR MICROWAVE IMAGING AND SENSING 78

4.1 Introduction 79

4.1.1 Polyethylene glycol (PEG) as enhancer of colloidal stability 81

4.2 Study objectives 83

4.2.1 Aims of the study 83

4.3 Results 84

4.3.1 Morphology and Stability Analysis 84

4.4 Dielectric properties of nanoparticle suspensions in water 87

4.5 Dielectric properties of ZnO and ZnO PEG colloidal dispersions at different concentrations in 60% glycerol and in TM phantom 91

4.5.1 Dielectric properties of ZnO colloidal dispersion at different concentrations in 60% glycerol 91

4.5.2 Dielectric properties of ZnO-PEG colloidal dispersion at different concentrations in 60% glycerol 93

4.5.3 Dielectric properties of ZnO and ZnO-PEG colloidal dispersions in TM phantom 94

4.6 Dielectric properties of nanomaterials in water at a higher frequency range 95

4.7 Dielectric properties of ZnO and ZnO-PEG colloidal suspensions at different probe positions at different time intervals 96

4.8 Discussion 98

4.8.1 Morphology and stability analysis 98

4.8.2 Dielectric analysis 99

4.8.3 Evaluation of NP colloidal dispersions (I) 100

4.8.4 Impact of PEGylation on dielectric constant 102
4.8.5 Evaluation of NP colloidal dispersion (II) 104

4.9 Conclusion & Summary 105

5 IRON OXIDE AND FERRITE NPS AS POTENTIAL CONTRAST AGENTS FOR MWI 106

5.1 Introduction 107
5.1.1 Structure of iron oxide NPs used in biomedicine 108
5.1.2 Superparamagnetic iron oxide (SPION) and ferrite NPs biomedical applications 110

5.2 Study objectives 111
5.2.1 Aims of the study 112

5.3 Description of commercial iron oxide NPs studied 112
5.3.1 Commercially available or clinically tested Sienna$^+$ from Endomagnetics 112
5.3.2 FF obtained from Liquid Research UK 113
5.3.3 Iron oxide – SA 113

5.4 Results (I) – Commercial iron oxides 114
5.4.1 Morphology and colloidal stability analysis using DLS, UV-Vis and SEM 114

5.5 Dielectric properties of commercial iron oxide nanoparticle suspension at different concentrations in water 117
5.5.1 Dielectric properties of SA at different concentrations in water 118
5.5.2 Dielectric properties of Sienna$^+$ at different concentrations in water 120
5.5.3 Dielectric properties of FF at different concentrations in water 121

5.6 Dielectric properties of commercial iron oxide nanoparticle suspension in 60% Glycerol 124
5.6.1 Dielectric properties of iron oxide (sigma), iron oxide (Sienna$^+$) and Ferrofluid at different concentrations in 60% glycerol 125

5.7 Result (II)- Zinc ferrites with PMAO polymer 130
5.7.1 Morphology and colloidal stability analysis of zinc ferrites via DLS, UV-Vis and SEM 131
5.7.2 Dielectric properties of zinc ferrites in water, 60% glycerol and tissue-mimicking phantom 134

5.8 Discussion 137

5.8.1 Stability and dielectric properties of commercial iron oxides 138

5.8.2 Stability and dielectric properties of PMAO coated zinc ferrites 141

5.9 Conclusion & Summary 144

6 SUMMARY & FUTURE PERSPECTIVE 145

7 REFERENCES 150

List of Figures

Figure 1-1: From left to right: almost entirely fatty, scattered areas of fibro-glandular density, heterogeneously dense and extremely dense breasts are shown [20]. 3

Figure 1-2: Schematic representation of breast screening by microwave imaging. Multiple antennas are placed around the breast. An antenna will be selected, and signals received by other antennas are collected. The transmitting antennas are selected to obtain data [25]. 7

Figure 1-3: Lewis structure of a water molecule. It follows a bent structure due to the 2 pairs of electrons on the oxygen atom forcing repulsion to the more positive hydrogen atoms. Oxygen is more electronegative than hydrogen. The hydrogen atoms have a net charge that consists of a vertical and horizontal component. The horizontal component cancels each other out, as they are the same magnitude but have opposite direction. While the vertical components of each atom are in the same direction and are thus constructive [89] 8

Figure 1-4: Different polarization mechanisms occurring over different frequency ranges [26].. 10

Figure 1-5: Maxwell-Wagner-Sillars effect in heterogeneous media. The simplest case with a single liquid crystal (LC) droplet surrounded by a host polymer matrix [31]..... 13

Figure 1-6: Variation of dielectric constant and effective conductivity with frequency for skin and muscle (high water content tissues) and fat (low water content). Data are from and plotted over the range from 100 MHz to 100 GHz [21]. 15

Figure 1-7: Schematic representation of a vector network analyser [51]. 17

Figure 1-8: A typical coaxial probe system consists of a vector network analyzer, a coaxial probe, an external computer [51]. 18

Figure 1-9: Schematic representation of two types of probe design (a) High temperature probe (b) Slim form probe [51] 18

Figure 1-10: Schematic representation of a resonant Cavity System [51]..... 19

Figure 1-11: Schematic representation of a free space system [51] 20

Figure 1-12: Microwave tomographic system at Dartmouth College [88]. 22

Figure 1-13: MARIA M4/M5 array and bed system. (a) MARIA M4/M5 array and bed system. (a) Rotable 60 antenna array and switch assembly which moves as a unit around the breast cup. (b) MARIA M4 position in clinic [68]..... 25

Figure 1-14: Enhanced permeability and retention (EPR) effect and passive targeting. Nanocarriers can extravasate into the tumours through the gaps between endothelial cells and accumulate there due to poor lymphatic drainage [76] 27

Figure 1-15: (a) relative permittivity and (b) effective conductivity of tissue mimicking materials with varying concentrations of single walled carbon nanotubes, measured over the frequency range from 0.6 to 20 GHz. Each curve represents the average properties of three different samples of the same concentration [79]. 30

Figure 1-16: (a) Dielectric constant and (b) loss tangent of the nanocomposites measured at 1 kHz as a function of aspect ratio and volume fraction of $BaTiO_3$ NWs [84]. 35

Figure 3-1: (a) Single-walled CNT, (b) double-walled carbon nanotubes (DWNT). These nanotubes are made of two concentric carbon nanotubes in which the outer tube encloses the inner tube, and (c) multi- walled CNT. Figure adapted from [109] 53

Figure 3-2: Schematic representation of a hybridized carbon atom forming a graphene layer followed by CNTs..... 57

Figure 3-3: Schematic representation of reconstructed monovacancy 5-membered pentagonal ring [107]. 58

Figure 3-4: Schematic representation of Stones-wales defect. Figure adapted from [107] 59

Figure 3-5: The morphology is observed from SEM. SEM images of SWNT (top left with a scale of 600nm), MWNT (top middle) and sSWNT (top right), SWNT-OH (bottom left with a scale of 375nm), MWNT-OH (bottom middle), and sSWNT-OH. Images were taken at room temperature. SEM images were taken in a vacuum by Hitachi scanning electron microscope (S4000 FEG SEM with Oxford Instruments INCA EDX). 64

Figure 3-6: Raman spectra of SWNT-OH (top left), MWNT-OH (top middle), sSWNT-OH (top right), SWNT (bottom left), MWNT (bottom middle) and sSWNT-OH (bottom right). 65

Figure 3-7: (a) dielectric constant, (b) effective conductivity (c) average change in epsilon, and (d) average change in sigma of different CNTs in water characterised between 1-4 GHz at a concentration of 2mg/mL in RO water. Each curve represents the average of three different samples (n=3+/-SD)..... 66

Figure 3-8: (a) dielectric constant, (b) effective conductivity (c) average change in epsilon, and (d) average change in sigma of different CNTs at a concentration of 2 mg/mL in 60% glycerol and RO water characterised between 1-4 GHz. Each curve represents the average of three different samples (n=3+/-SD)..... 68

Figure 3-9: (a) dielectric constant, (b) effective conductivity (c) average change in epsilon, and (d) average change in sigma of different CNTs at a concentration of 2 mg/mL in TM phantom characterised between 1-4 GHz. Each curve represents the average of three different samples (n=3+/-SD)..... 69

Figure 3-10: Schematic representation of coaxial probe inserted inside our in-house made TM phantom for dielectric measurements..... 71

Figure 3-11: Reaction scheme for the modification of MWNTs with hydroxyl groups. Figure adapted from [76]..... 75

Figure 3-12: The mechanism scheme of the reaction between MWNTs and $NaAlO_2$. Figure adapted from [77]..... 76

Figure 4-1: The surface morphology is observed from AFM and SEM. AFM images of SiO_2, ZnO and ZnO-PEG. SEM images of SiO_2, ZnO and ZnO-PEG. Images were taken at room temperature. SEM images were taken in a vacuum environment by Hitachi scanning electron microscope (S4000 FEG SEM with Oxford Instruments INCA EDX), while the AFM images were taken in open air conditions via Bruker icon dimension atomic force microscope. 84

Figure 4-2: (a) Effect of PEG on colloidal stability of ZnO NP. Light transmission through ZnO NP and ZnO-PEG (MW=8000) in ddH_2O, where λ=415nm. n=6 +/-SD, (b) Polydispersity index (PDI) and (c) Hydrodynamic size (nm) of ZnO and ZnO-PEG NPs in ddH_2O over a time of 240 minutes. n=6 +/-SD 85

Figure 4-3: Averaged dielectric constant of colloidal dispersions of (a) CNT-OH in RO water, (b) SiO2 with 1 % Pluronic, ZnO with 1 % Pluronic, and (d) ZnO-PEG in RO water characterised between 1-4 GHz. The control is the dispersant used for each NP. Each curve represents the average of three different samples (n=3+/-SD). 87

Figure 4-4: Averaged effective conductivity of colloidal dispersions of (a) CNT-OH in RO water, (b) SiO2 with 1 % Pluronic, (c) ZnO with 1 % Pluronic, and (d) ZnO-PEG in RO water characterised between 1–GHz. The control is the dispersant used for each NP. Each curve represents the average of three different samples (n=3+/-SD). 89

Figure 4-5: Average change of the dielectric constant of colloidal dispersions of (a) CNT-OH and b) ZnO-PEG in aqueous solution from 1–4 GHz. Each curve represents the average of three different samples (n=3+/-SD). 89

Figure 4-6: Average change of the effective conductivity of colloidal dispersions of (a) CNT-OH and b) ZnO-PEG in aqueous solution from 1–4 GHz. Each curve represents the average of three different samples (n=3+/-SD). 90

Figure 4-8: (a) dielectric constant, (b) effective conductivity, (c) average percent change of dielectric constant and d) average percent change of effective conductivity of ZnO colloidal dispersion at different concentrations in 60% glycerol characterised between 1-4 GHz. Each curve represents the average of three different samples (n=3+/-SD).**(d)** 91

Figure 4-7: (a) dielectric constant, (b) effective conductivity, (c) average percent change in epsilon and d) average percent change in sigma of ZnO NP colloidal dispersion at different concentrations in 60% glycerol characterised between 1-4 GHz. Each curve represents the average of three different samples (n=3+/-SD). 91

Figure 4-9: (a) dielectric constant, (b) effective conductivity, (c) average change in dielectric constant and d) average change in sigma of ZnO and ZnO-PEG colloidal dispersion at 2mg/mL in TM phantom characterised between 1-4 GHz. Each curve represents the average of three different samples (n=3+/-SD). 94

Figure 4-10: Dielectric properties of ZnO NPs at a concentration of 2 mg/mL in RO water with 1% Pluronic at three different probe positions from frequency range of 1-4 GHz at t = 0. Each curve represents the average of three different samples (n=3+/- SD). 96
Figure 4-11: Dielectric properties of ZnO NPs at a concentration of 2 mg/mL in RO water with 1% Pluronic at three different probe positions from frequency range of 1-4GHz at t = 25mins. Each curve represents the average of three different samples (n=3+/-SD). 96
Figure 4-12: Dielectric properties of ZnO-PEG NPs at a concentration of 2 mg/mL in RO water at three different probe positions from frequency range of 1-4GHz at t = 0. Each curve represents the average of three different samples (n=3+/- SD). 97
Figure 4-13: Dielectric properties of ZnO-PEG NPs at a concentration of 2 mg/mL in RO water at three different probe positions from frequency range of 1-4GHz at t = 25mins. Each curve represents the average of three different samples (n=3+/-SD). 97
Figure 5-1: Crystal structure of magnetite [16]. The black spheres represent $Fe^{2+,}$ the green spheres represents Fe^{3+} and, the red spheres represent O^{2-} [16]. 108
Figure 5-2: UV-Vis analysis of iron oxide Sienna+, FF and SA, at a wavelength (λ) of 415nm. The measurements were taken over a 4-hour period n=6 +/-SD. 114
Figure 5-3: Z- average size and PDI of Sienna^{+} and FF over a period of 4 hours n=6+/-SD .. 115
Figure 5-4: Z- average size and PDI of SA over a time of 4 hours with a sample n=6+/-SD .. 115
Figure 5-5: The surface morphology is observed from SEM. SEM images of Sienna^{+} (left), FF (middle) and SA (right). Images were taken at room temperature and in a vacuum environment with a Hitachi scanning electron microscope (S4000 FEG SEM with Oxford Instruments INCA EDX). 116
Figure 5-6: (a) dielectric constant, (b) effective conductivity, (c) average change in epsilon and (d) average change in sigma of colloidal dispersion of SA at different concentrations in RO water characterised between 1- 4 GHz. Each curve represents the average of three different samples (n=3+/- SD)..... 118
Figure 5-7 118

Figure 5-8: (a) dielectric constant, (b) effective conductivity, (c) average change in epsilon and (d) average change in sigma of colloidal dispersion of Sienna$^+$ at different concentrations in RO water characterised between 1- 4 GHz. Each curve represents the average of three different samples (n=3+/-SD)..... 120

Figure 5-9: (a) dielectric constant, (b) effective conductivity, (c) average change in epsilon and (d) average change in sigma of colloidal dispersion of FF at different concentrations in RO water characterised between 1- 4 GHz. Each curve represents the average of three different samples (n=3+/-SD)..... 122

Figure 5-10: : (a) dielectric constant, (b) effective conductivity, (c) average change in epsilon and (d) average change in sigma of colloidal dispersion of SA at different concentrations in 60% glycerol characterised between 1- 4 GHz. Each curve represents the average of three different samples 125

Figure 5-11: (a) dielectric constant, (b) effective conductivity, (c) average change in epsilon and (d) average change in sigma of colloidal dispersion of Sienna$^+$ at different concentrations in 60% glycerol characterised between 1- 4 GHz. Each curve represents the average of three different samples (n=3+/-SD)..... 127

Figure 5-11: (a) dielectric constant, (b) effective conductivity, (c) average change in epsilon and (d) average change in sigma of colloidal dispersion of Sienna$^+$ at different concentrations in 60% glycerol characterised between 1- 4 GHz. Each curve represents the average of three different samples (n=3+/-SD)..... 127

Figure 5-12: (a) dielectric constant, (b) effective conductivity, (c) average change in epsilon and (d) average change in sigma of colloidal dispersion of FF at different concentrations in 60% glycerol characterised between 1- 4 GHz. Each curve represents the average of three different samples (n=3+/-SD)..... 128

Figure 5-13: UV-Vis analysis of Fe_3O_4 – PMAO, [$(Zn_{0.18}Fe_{0.82})$ Fe_2O_4]- PMAO and, [$(Zn_{0.39}Fe_{0.61})$ Fe_2O_4] - PMAO at a wavelength (λ) of 415nm. The measurements were taken over a 4-hour period n=6 +/-SD.Figure 5-12: (a) dielectric constant, (b) effective conductivity, (c) average change in epsilon and (d) average change in sigma of colloidal dispersion of FF at different concentrations

in 60% glycerol characterised between 1- 4 GHz. Each curve represents the average of three different samples (n=3+/-SD). 128

Figure 5-13: UV-Vis analysis of Fe_3O_4 – PMAO, [($Zn_{0.18}Fe_{0.82}$) Fe_2O_4]- PMAO and, [($Zn_{0.39}Fe_{0.61}$) Fe_2O_4] - PMAO at a wavelength (λ) of 415nm. The measurements were taken over a 4-hour period n=6 +/-SD. 131

Figure 5-14: Z- average size and PDI of [Fe_3O_4]-PMAO, [($Zn_{0.18}Fe_{0.82}$)Fe_2O_4]-PMAO and [($Zn_{0.39}Fe_{0.61}$)Fe_2O_4]-PMAO over a period of 4 hours n=6+/-SDFigure 5-13: UV-Vis analysis of Fe_3O_4 – PMAO, [($Zn_{0.18}Fe_{0.82}$) Fe_2O_4]- PMAO and, [($Zn_{0.39}Fe_{0.61}$) Fe_2O_4] - PMAO at a wavelength (λ) of 415nm. The measurements were taken over a 4-hour period n=6 +/-SD. 131

Figure 5-14: Z- average size and PDI of [Fe_3O_4]-PMAO, [($Zn_{0.18}Fe_{0.82}$)Fe_2O_4]-PMAO and [($Zn_{0.39}Fe_{0.61}$)Fe_2O_4]-PMAO over a period of 4 hours n=6+/-SD 132

Figure 5-15: The surface morphology is measured via SEM. Fe_3O_4-PMAO (left), [$Zn_{0.18}Fe_{0.82}$]Fe_2O_4-PMAO (middle) and [$Zn_{0.39}$ $Fe_{0.61}$]Fe_2O_4-PMAO (right). Images were taken at room temperature and in a vacuum environment 133

Figure 5-16: (a) dielectric constant, (b) effective conductivity, (c) average change in epsilon and (d) average change in sigma of Fe_3O_4-PMAO, [$Zn_{0.18}Fe_{0.82}$] Fe_2O_4-PMAO and [$Zn_{0.39}Fe_{0.61}$]Fe_2O_4-PMAO in water characterised at a concentration of 2mg/mL between 1-4 GHz. Each curve represents the average of three different samples, n=3+/-SDFigure 5-15: The surface morphology is measured via SEM. Fe_3O_4-PMAO (left), [$Zn_{0.18}Fe_{0.82}$]Fe_2O_4-PMAO (middle) and [$Zn_{0.39}$ $Fe_{0.61}$]Fe_2O_4-PMAO (right). Images were taken at room temperature and in a vacuum environment 133

Figure 5-16: (a) dielectric constant, (b) effective conductivity, (c) average change in epsilon and (d) average change in sigma of Fe_3O_4-PMAO, [$Zn_{0.18}Fe_{0.82}$] Fe_2O_4-PMAO and [$Zn_{0.39}Fe_{0.61}$]Fe_2O_4-PMAO in water characterised at a concentration of 2mg/mL between 1-4 GHz. Each curve represents the average of three different samples, n=3+/-SD 134

Figure 5-17: (a) dielectric constant, (b) effective conductivity, (c) average change in epsilon and (d) average change in sigma of [Fe_3O_4]-PMAO, [($Zn_{0.18}$ $Fe_{0.82}$) Fe_2O_4]-PMAO and [($Zn_{0.39}Fe_{0.61}$)Fe_2O_4]-PMAO in 60% glycerol at a concentration of 2mg/mL characterised between 1-4

GHz. Each curve represents the average of three different samples, n=3+/-SD.Figure 5-16: (a) dielectric constant, (b) effective conductivity, (c) average change in epsilon and (d) average change in sigma of Fe_3O_4-PMAO, [$Zn_{0.18}Fe_{0.82}$] Fe_2O_4-PMAO and [$Zn_{0.39}Fe_{0.61}$]Fe_2O_4-PMAO in water characterised at a concentration of 2mg/mL between 1-4 GHz. Each curve represents the average of three different samples, n=3+/-SD 134

Figure 5-17: (a) dielectric constant, (b) effective conductivity, (c) average change in epsilon and (d) average change in sigma of [Fe_3O_4]-PMAO, [($Zn_{0.18}Fe_{0.82}$) Fe_2O_4]-PMAO and [($Zn_{0.39}Fe_{0.61}$)Fe_2O_4]-PMAO in 60% glycerol at a concentration of 2mg/mL characterised between 1-4 GHz. Each curve represents the average of three different samples, n=3+/-SD. 136

Figure 5-18: (a) dielectric constant, (b) effective conductivity, (c) average change in epsilon and (d) average change in sigma of Fe_3O_4-PMAO, [($Zn_{0.18}Fe_{0.82}$)Fe_2O_4]-PMAO and [($Zn_{0.39}Fe_{0.61}$)Fe_2O_4]PMAO in TM phantom characterised between 1-4 GHz at a concentration of 2 mg/mL. Each curve represents the average of three different samples, n=3+/-SDFigure 5-17: (a) dielectric constant, (b) effective conductivity, (c) average change in epsilon and (d) average change in sigma of [Fe_3O_4]-PMAO, [($Zn_{0.18}Fe_{0.82}$) Fe_2O_4]-PMAO and [($Zn_{0.39}Fe_{0.61}$)Fe_2O_4]-PMAO in 60% glycerol at a concentration of 2mg/mL characterised between 1-4 GHz. Each curve represents the average of three different samples, n=3+/-SD. 136

Figure 5-18: (a) dielectric constant, (b) effective conductivity, (c) average change in epsilon and (d) average change in sigma of Fe_3O_4-PMAO, [($Zn_{0.18}Fe_{0.82}$)Fe_2O_4]-PMAO and [($Zn_{0.39}Fe_{0.61}$)Fe_2O_4]PMAO in TM phantom characterised between 1-4 GHz at a concentration of 2 mg/mL. Each curve represents the average of three different samples, n=3+/-SD 137

Figure 5-19Figure 5-18: (a) dielectric constant, (b) effective conductivity, (c) average change in epsilon and (d) average change in sigma of Fe_3O_4-PMAO, [($Zn_{0.18}Fe_{0.82}$)Fe_2O_4]-PMAO and [($Zn_{0.39}Fe_{0.61}$)Fe_2O_4]PMAO in TM phantom characterised between 1-4 GHz at a concentration of 2 mg/mL. Each curve represents the average of three different samples, n=3+/-SD 137

Figure 5-19 140

List of Tables

Table 1-1: Summary of data for microbubbles assessed at 3 GHz. NA: Not available [78]. 29

Table 1-2: Electrical properties of SWCNT dispersions at 3 GHz [79]. 31

Table 1-3: Electrical properties of SWCNT dispersions at 3 GHz[79]. 31

Table 1-4: Dielectric properties of clinically used Gadolinium agents and ferroelectric nanoparticles at 1 and 2.45 GHz [83]. 34

Table 1-5: Dielectric properties of clinically used Gadolinium agents and ferroelectric nanoparticles at 1 and 2.45 GHz[83]. 34

Table 1-6: Dielectric properties of ferroelectric nanoparticles at 1 and 2.45 GHz [24] 35

Table 1-7: Dielectric properties of ferroelectric nanoparticles at 1 and 2.45 GHz[24] 35

Table 2-1: Length, diameter and purity of different CNTs received from Cheap tubes Inc. (USA) 41

Table 2-2: Different amount of $Fecl_2$, $Fe(acac)_3$, and $ZnCl_2$ required to prepare different zinc ferrite compositions 47

Table 2-3: Different materials and their amounts required to prepare TM phantoms 48

Table 3-1: Table showing the dielectric properties of SWNT in water at different concentrations between at 1, 2, 3 and, 4 GHz. 67

Table 4-1: Nanoparticle sizes of SiO_2, ZnO, ZnO-PEG obtained by AFM and SEM 84

Table 4-2: Dielectric properties of ZnO (1% Pluronic), ZnO-PEG (RO H2O), SiO_2 (1% Pluronic), and CNT- OH (RO H_2O) between the frequency range of 5–10 GHz. 95

Table 5-1: Size (nm) and PDI obtained at t_0 and t_{60} for commercial magnetite's via DLS 116

Table 5-2: Average percent change in epsilon of SA at concentrations of 2, 1, 0.5,0.25 mg/mL at frequency range between 1-4GHz 119

Table 5-3: Table 5-3: average change in epsilon of Sienna+ at concentrations of 2, 1, 0.5, 0.25mg/mL at frequency range between 1-4 GHz 121

Table 5-4: average change in epsilon of FF at concentrations of 2, 1, 0.5, 0.25mg/mL at frequency range between 1-4 GHz 123

Table 5-5: Average change in epsilon of SA at concentrations of 2, 1, 0.5, 0.25mg/mL at frequency range between 1-4 GHz in 60% glycerol..... 126

Table 5-6: Average change in epsilon of sienna+ at concentrations of 2, 1, 0.5, 0.25mg/mL at frequency range between 1-4 GHz in 60% glycerol..... 128

Table 5-7: Average change in epsilon of FF at concentrations of 2, 1, 0.5, 0.25mg/mL at frequency range between 1-4GHz in 60% glycerol..... 129

Table 5-8: Different zinc ferrites prepared for this study. (AcAc stands for Acetal Acetate and PMAO stands for Poly (maleic anhydride-alt-1-octadecene)..... 130

Acknowledgement

First and foremost, I would like to thank the BBSRC research council and mediwise, for providing the funding towards my project and making it possible to complete my doctoral studies. My very special thanks to my supervisor, Dr. Maya Thanou who has been a great motivator and a brilliant mentor throughout my studies. Without her encouragement and continued support, achieving publications and completing my studies would have not been possible. My sincere thanks to my second supervisor, Dr. Panagiotis Kosmas, who has directed me throughout my studies.

I would like to express my special gratitude to my all my lab group members; Dr. Michael Wright, Dr. Miguel Centelles, Paul Cressy, ZiHong Mok, Shahd Abu Hilal, Mohammed Wahid Rahman, Jana Javorovic and Maral Emarahli. I would like to express my deepest gratitude to Mohammed Wahid Rahman, who has always helped me with everything during my studies, be it planning experiments, or discussing ideas or generating publications. He has been the biggest moral and emotional support throughout my doctoral studies.

Finally, I acknowledge the people who mean a lot to me, my grandparents, my parents, my husband, and my sister. My grandparents: baba and dadi, who always believed that I could reach heights in life, and it's all because of their belief and blessings that I have been able to achieve this milestone in life. Wish they were around to see me complete my doctoral studies. My parents: papa and maa, two people I look up to the most in this world. Thank you for always having faith in me and for encouraging me to achieve wonderful things in life. I salute you for all the sacrifices you both have made to shape my life. I would never be able to pay back the love and affection showered by my parents. My younger sister, for her selfless love and care, which contributed a lot for the completion of my thesis.

My husband: Got married to this wonderful person, on 22.01.2017. Would like to express my special thanks to him for his continued and unfailing love, support, patience and understanding during the pursuit of my doctoral studies. Without his support the completion of my studies would

have not been possible. You have always helped me to keep things in perspective and I thank you deeply for believing in me always.

Would like to thank my other friends in London. Dipa Gurung, Amrut Varsha, Mayra luz vera avilés and Tugba Kose. They have always been there for me during my tough times, especially Mayra luz vera avilés, she has been such a positive energy for me during my studies and I am going to miss her the most when I leave.

Research aim & objectives

Chapter 1 gives an overview of current imaging techniques for the detection of breast cancer. Flaws within these techniques have been highlighted and how there is a need of designing a new imaging modality for breast cancer detection has been discussed. Previous work carried out by researchers in identifying a suitable contrast agent for Microwave Imaging purpose has been extensively discussed.

Chapter 2 highlights the materials and the methodology used in this study.

Chapter 3 describes the structural and dielectric properties of diverse types of carbon nanotubes (SWNTs) in RO water, 60% glycerol and TM phantom. SWNTs have been extensively studied before as reported previously for MWI purposes. However, the effect of different lengths of SWNTs and functionalization of SWNTs has on the dielectric properties of a medium, has never been explored before. In this chapter, the effect of different lengths/diameter and functionalization of SWNTs has on the dielectric properties of three different mediums- water, 60% glycerol and tissue-mimicking phantoms. The phantoms have been selected to mimic healthy and tumour tissues.

Chapter 4 describes the effect of materials such as zinc oxide NPs (ZnO), silicon dioxide NPs (SiO_2) and single-walled carbon nanotube (CNT-OH) functionalized with -OH in water have on the dielectric properties of a high, low dielectric constant medium and on TM (tissue-mimicking) phantom. ZnO NPs will be further PEGylated with poly-ethylene-glycol (Mw= 8000), to improve the dispersion properties of ZnO NPs further in RO water, 60% glycerol and TM phantom.

Chapter 5 describes the stability and dielectric properties of commercial iron oxides, such as iron oxide (Effective conductivity Aldrich Ltd.), carboxy dextran coated Sienna$^+$ (Endomagnetics Ltd.) and ferrofluid with anionic surfactant (Liquid Research Ltd.). Dielectric properties of each will be measured in RO water and 60% glycerol. Zinc ferrites coated with PMAO (poly-maleic anhydride-alt-1-octadecene) with different ratio of zinc will be synthesized. Dielectric results obtained will be correlated with commercial iron oxides.

1 General Introduction

Biomedical imaging is one of the main pillars of comprehensive cancer care. It has many advantages including real-time monitoring, accessibility without tissue destruction, and minimal to non-invasive methods. Imaging is playing a key role in all phases of cancer management, which includes screening, biopsy, guidance for detection, staging, therapy, planning, therapy guidance, therapy response, and recurrence. Currently, clinical imaging techniques used are, radiography fluoroscopy, angiography, mammography, computed tomography, ultrasound and ultrasound/Doppler, magnetic resonance imaging and nuclear medicine [1]. Non-ionizing electromagnetic radiation imaging techniques such as near-infrared spectroscopy, electrical impedance spectroscopy, and microwave imaging have been investigated mainly from breast imaging [2].

Breast cancer remains to be the most common cancer and the leading cause of cancer mortality in women worldwide. It is most common in older women and had the highest mortality in women in the European Union towards the end of the 1990s until the early beginning of 2000s [3][4]. According to the World Health Organisation (WHO), prompt detection remains the keystone for breast cancer control and a challenge to scientists and engineers. According to the study carried out by Malvezzi *et al.*, breast cancer still has the second highest predicted mortality rate in women with about 92,700 deaths within the European Union in 2018. Data collected concerning detection of breast tumors in initial stages indicate that screening has the potential of increasing the 5-year survival rate to 95% [5]. While early detection does not necessarily initiate an early intervention or treatment, it keeps the disease under control [6]. These numbers indicate that there is a requirement for the development of novel improved and accessible methods for breast cancer screening. This thesis' topic is investigating the potential of MW imaging/sensing (MWI/S) and novel contrast agents to be used for imaging and sensing of pathologies and especially breast cancer. In this introduction, the current imaging modalities will be described. Then the topic of microwave

sensing will be introduced. Finally, the first nanomaterials that have been studied as contrast agents have been discussed.

1.1 Current breast imaging modalities

Current imaging techniques for breast imaging and screening are X-ray mammography, ultrasound, MRI, and positron emission tomography (PET) [7][8]. X-Ray mammography is the gold-standard for detecting breast cancer. It has been effective in reducing mortalities in numerous ways and is the most fundamental and frequently employed imaging modality in clinical standards [9]. It uses low-energy X-rays to illuminates the breast, and the image generated shows the different densities between different types of tissues.

Tumors without a distinct mass or calcification are difficult to identify mammographically. The overall sensitivity of mammography decreases to 42-68% in women with dense breasts [10]. It has been shown that the percentage of water content in breasts within young females, who generally have dense breasts, is much higher than that of elderly women (Fig. 1-1).

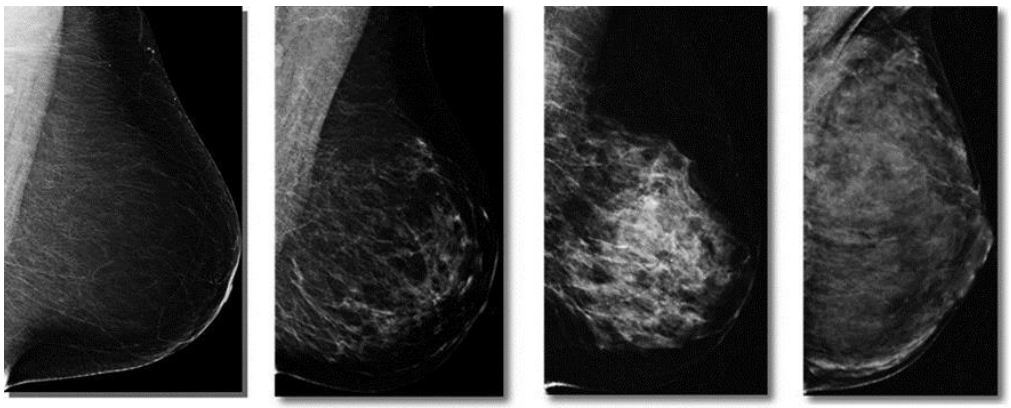

Figure 1-1: From left to right: almost entirely fatty, scattered areas of fibro-glandular density, heterogeneously dense and extremely dense breasts are shown [20].

This implies that high water content breast tissues reduce mammography sensitivity. X-ray attenuation properties of water, lipid, and proteins are indistinguishable in the diagnostic energy range [10]. The probability of tumour detection in dense breasts is much lower than of breasts mainly comprised of fatty breasts [11]. Other effects of mammography include overtreatment, the

false-positive rate is 15-30%, which leads to many benign findings and follow-up testing. Furthermore, X-ray mammography needs compression of the breast as the person has to lie as flat as possible during the examination, which induces discomfort.

Ultrasound sonography uses high frequency (1-10 MHz) sound waves to image internal body structures. A transducer is placed on the skin, which sends ultrasound pulses into the body and detects the echoes from inside the body, which is then used to produce images. This technique is in conjunction with mammography. Many studies have shown an increase in the detection of small, invasive node-negative cancers compared to mammography alone [12][13].

Abnormalities identified on ultrasound images are assessed for signs that favour malignancy. Further, guided needle biopsies are needed to diagnose solid lesions regardless of ultrasound findings. However, two critical issues need to be considered, firstly, ultrasound has low resolution and does not have the ability to distinguish between a malignant and benign tissue and secondly a thorough screening ultrasound examination of both breasts is time-consuming.

Magnetic resonance imaging (MRI) is the most sensitive imaging modality for the detection of breast cancer, in elevated risk patients. Sensitivities for invasive cancers using gadolinium-based contrast agents are greater than 90% [14]. It has the potential to provide accurate diagnostic information. MRI involves the use of contrast agents, which is taken up differently by benign and malignant tissue [15]. Tracking the uptake of the contrast agent results in a complex image reconstruction. In general principle, radiofrequency pulses re-align hydrogen atoms that naturally exist within the body. As the hydrogen atoms return to their natural alignment, they emit different amounts of energy, which vary according to the types of body tissues. MRI scanner captures this energy and creates a picture of the tissues scanned. Three different patterns of contrast enhancement have been characterized, type I shows slow progressive contrast uptake over time and is suggestive of benignity. Type II contrast pattern (plateau) shows a rapid uptake in contrast

and then levelling off uptake, suggestive of malignancy, and type III curve shows rapid uptake of contrast and then a sudden wash-out of contrast, indicating malignancy.

Advantages of MRI of the breast are that it can be used in women with denser breasts and can detect if cancer has spread to the chest wall. Also, it can check for the recurrence of cancer in women. However, the disadvantages are that it is highly sensitive to small abnormalities, cannot image calcifications, can trigger claustrophobia and requires long scan times with comparison to x-ray and mammograms [16]. MRI screening costs are high and therefore are not suitable for an early detection screening method.

A Positron emission tomography (PET) have proven useful in the evaluation of many cancers. Many types of PET radiotracers have been developed to noninvasively interrogate *in vivo* tumor metabolism, the most widely used is the FDA approved PET radiotracer, 2-deoxy-2-(18F) fluoro-D-glucose (FDG) [17]. FDG is based on glucose metabolism. FDG is transported into the cells by glucose transporters, but unlike glucose, FDG is not metabolized but is irreversibly phosphorylated by hexokinase and is trapped within the cell. Glucose transport is upregulated in cancer cells, FDG PET exploits greater uptake of FDG within most cancer cells compared with normal healthy cells. To visualize tumors, for e.g. FDG uptake is greater with triple negative breast cancer and lower with luminal A subtypes [17]. Many groups have evaluated suspicious breast lesions, with sensitivity values ranging between 80-90% and specificity between 71-95% [18]. PET can be useful in identifying involved axillary nodes and distant metastases, as axillary lymph node status is an important indicator of the spread of breast cancer in patients [19]. PET is also more sensitive in the detection of bone metastasis compared to other techniques.

Digital Breast Tomosynthesis (DBT), known as 3D mammography, got approved by FDA in 2011 as a supplement for routine digital mammography. DBT is being developed to improve detection and characterization of breast lesions especially in women with fatty breasts. Images obtained from conventional two-dimensional mammography represents a superimposition of all features of the

breast, which results in difficulties such as, composite densities and the masking of pathology by overlying normal glandular tissue, hence DBT has been developed to overcome these problems. A principle of DBT is that they acquire multiple images at different angles of a compressed breast and images are reconstructed to create a stack of slices. This allows the radiologist to 'unpick' composite densities and to further assess the mammographic morphologies. A potential disadvantage of this technique is increased patient radiation dose. Early studies have suggested that DBT plus conventional mammography can reduce recall rate and improve cancer detection rate [20]. There is an increased cost and increased physician interpretation time associated with DBT. This technique is becoming more widely available and is well-tolerated by patients while the breast positioning and compression level stay like mammography.

Molecular breast imaging (MBI) uses dual gamma detectors to identify metabolically active cells and is not affected by higher density in breast tissue. The breast is lightly compressed between two detectors with a mild compression force, which is approximately 1/3 of mammography. MBI has a similar sensitivity and specificity for detection of breast cancer as MRI, but the patient will experience radiation exposure and is not widely available to the general population. Therefore, MBI is usually reserved for elevated risk in women who cannot undergo MRI.

Such limitations of existing breast diagnostic imaging methods have motivated researchers to explore the potential of alternative imaging methods. One class of innovative approach, microwave imaging (MWI), is based on the complex electrical property differences of breast tissues and has been researched as an alternative to X-ray mammography. Microwave images present a map related to the electromagnetic (EM) properties of tissues and liquids in a region with different types of tissue properties. Breast imaging is particularly attractive from MWI point of view, because it is easy to access. MWI uses scattered waves and reflected waves which arise from the contrast in the dielectric properties between the normal and malignant breast tissues to generate a 2-D or 3-D map[21].

1.2 Introducing microwave imaging as a sensing and imaging modality

MWI has emerged as a new imaging modality and is based on identifying the dielectric profile of the breast, to detect cancers [22]. The use of non-ionizing EM radiation at microwave frequencies for medical diagnosis shows several advantages, such as low cost and low health risk, compared to other radiation-based imaging techniques [23]. MWI offers a non-invasive way for the diagnosis of pathological conditions [24].

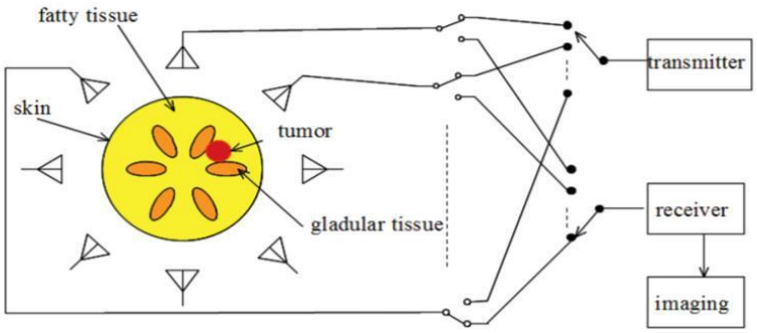

Figure 1-2: Schematic representation of breast screening by microwave imaging. Multiple antennas are placed around the breast. An antenna will be selected, and signals received by other antennas are collected. The transmitting antennas are selected to obtain data [25].

The general principle is depicted in Figure 1-2. Microwave signals that are transmitted from an antenna is received by the antennas after signal reflection and scattering. Microwave mammography consists of multiple antennas placed around the breast as shown in fig 1-2. An antenna is selected, and a microwave signal is transmitted. At the same time, signals received by other antennas are also collected. The transmitting antennas are sequentially selected to obtain received data. Dielectric property map is created to by using the received data. Different tissues cause a different amount of scattering [25].

In the next section, the dielectric theory and studies on dielectric from the past have been highlighted in detail.

1.2.1 Dielectric theory

When a permanent dipole, presented in Figure 1-3, has an electric field applied to it, the medium becomes polarised with polarisation vector $\overline{\boldsymbol{P}}$ (Equation 1).

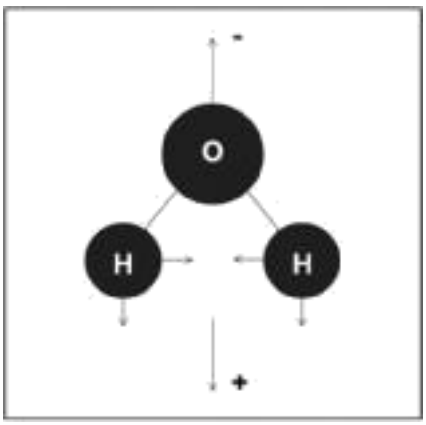

Figure 1-3: Lewis structure of a water molecule. It follows a bent structure due to the 2 pairs of electrons on the oxygen atom forcing repulsion to the more positive hydrogen atoms. Oxygen is more electronegative than hydrogen. The hydrogen atoms have a net charge that consists of a vertical and horizontal component. The horizontal component cancels each other out, as they are the same magnitude but have opposite direction. While the vertical components of each atom are in the same direction and are thus constructive [89]

The electric field exercises a torque on the molecule which will cause the dipole to rotate and align with the direction of the electric field. The total electric field in a dielectric material is the sum of the applied electric field and of an induced electric field resulting from the polarization of the material.

As an example, an electric conductor is defined as an equipotential material. If the points in the material are at the same electric potential, then the electric field must be zero and there can be no electric charges within the material. When the electric conductor is subjected to an applied electric field, the applied field exists in all points of the material. To have a total electric field, the material must develop an induced electric field such that the sum of the applied field and the induced field vanishes in all points of the material. A new vector $\overline{\boldsymbol{D}}$ is then defined as the displacement flux density or the electric flux density, $\boldsymbol{E}$ is the electric field, $\overline{\boldsymbol{P}}$ is the polarisation vector and the permittivity of free space is represented by $\boldsymbol{\varepsilon_0}$ [Fm^{-1}].

$$\overline{D} = \varepsilon_0 E + \overline{P} \quad [Cm^{-2}] \text{ (coulomb/metre)} \qquad \textbf{(Equation 1)}$$

Dielectric properties can be represented as a function of frequency. Equation 2 refers to the frequency dependent complex dielectric constant. The real part, which is called the dielectric constant, $\varepsilon'(\omega)$, represents how much energy the material stores, and the imaginary part $\varepsilon''(\omega)$ refers to the energy loss in a dielectric medium and is also related to the conductivity of the material. The imaginary number is represented by j, and ε_0 represents the permittivity of vacuum.

$$\varepsilon_r^*(\omega) = \varepsilon'_r - j\varepsilon''_r = \varepsilon'_r - j\frac{\sigma}{\omega\varepsilon_0} \qquad \textbf{(Equation 2)}$$

The polarization can be delayed with respect to the variation of the electric field. The dielectric constant and the imaginary part can also be expressed as the tangent of the loss angle (Equation 3). The tan δ is defined as the ratio of the energy lost with respect to the energy stored and is characteristic of a material. In equation 3, Q represents the quality factor, which is the reciprocal of the loss tangent. For low loss materials, the angle δ is very small, so the magnitude is close to the real component, however, at microwave frequencies, biological tissues with high water content such as breast tissues, have a larger imaginary component leading to a higher loss tangent.

$$\tan\delta = \frac{\varepsilon''}{\varepsilon'} = \frac{1}{Q} \qquad \textbf{(Equation 3)}$$

1.2.2 The frequency response of dielectric mechanisms

When submitted to an electric field, an actual material will exhibit a variety of polarisation mechanisms. Figure 1-4 represents the general features of the frequency dependence on the real and imaginary parts of the dielectric constant. A material may have several dielectric polarisation mechanisms that contribute to its overall permittivity. Dipolar and ionic polarisation mechanisms interact strongly at microwave frequencies. Atomic and electronic mechanisms are relatively weak, but usually constant over the microwave region. As the frequency increases, low frequency mechanisms tend to drop leaving the high-frequency mechanisms to contribute to the dielectric constant [26].

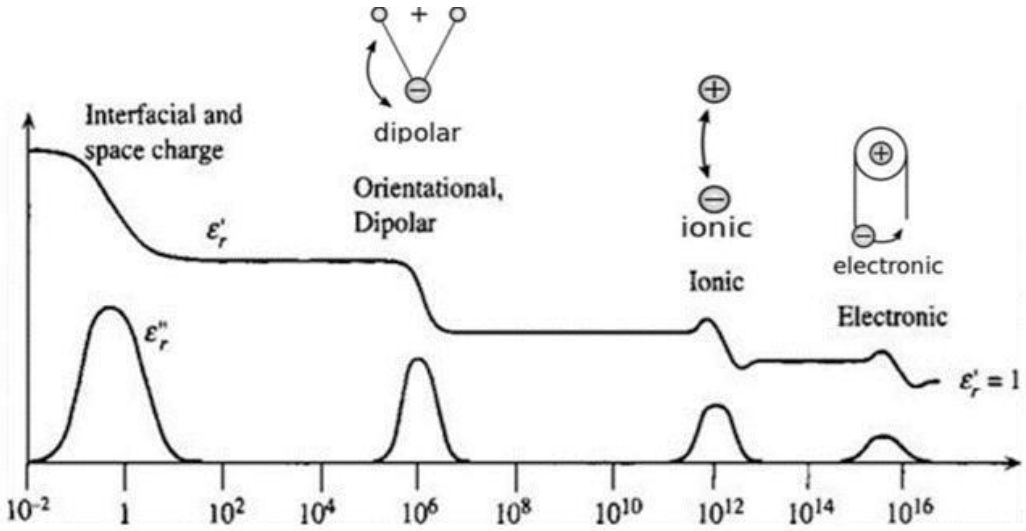

Figure 1-4: Different polarization mechanisms occurring over different frequency ranges [26].

1.3 Dielectric polarisation mechanisms

A material may have several dielectric mechanisms or polarization effects that contribute to its overall dielectric constant. The polarization of a material may be classified according to;

1. *Electronic polarization*
2. *Orientational polarization*
3. *Atomic polarization*

1.3.1 Electronic polarisation

At the centre of the atom, consists of positively charged protons and electrically neutral neutrons. The electrons move about in the closed orbits. At any instant, the electron and the nucleus form a dipole with a moment directed from the negative charge to the positive charge. When the atom is situated in an electric field, the charged particles experience an electric force because of which the centre of the negative charge cloud is displaced with respect to the nucleus. A dipole moment is induced in the atom, and the atom is said to be electronically polarized.

$$\alpha_e = (4\pi\varepsilon_0 R^3)E \qquad \textbf{(Equation 4)}$$

The electronic polarizability **αe** can be calculated by making an approximation that the charge is spread uniformly in a spherical volume of radius $\boldsymbol{R}$ (Equation 4), where ε_0 is the permittivity of free space. For any given atom, the quantity inside the brackets is constant and therefore the dipole moment is proportional to the applied electric field $\boldsymbol{E}$. Dielectric moment will be zero once the electric field is removed since the charges will be restored to the undistributed positions [27].

1.3.2 Orientational (dipolar) polarisation

This type of polarization is typical for polar liquids and polar gases. It also happens in the solid if there are permanent dipoles within the structure. In general, molecules are randomly oriented because of thermal agitation when an electric field is absent. Once an electric field E is applied, dipoles will try to align parallel to the direction of the E field and consequently, the material will exhibit net polarization. Hence, compared with the electronic and ionic polarization, orientational polarization is strongly temperature dependent and decreases as the temperature increases [28]. Orientational polarization is dominant in materials with structural dipoles, such as water.

1.3.3 Atomic polarization

Atomic polarizability α_a arises due to the displacement of the nuclei atoms forming the molecule, relative to each other. This is in contrast with the electronic polarizability, which arises due to electronic displacement, in an electric field. Whether a molecule possesses a permanent dipole or not, if it has polar bonds, the applied field will induce a displacement. Atomic polarization exists in all molecules, it is more pronounced in molecules that have relatively weak bonds. Atomic polarizability can be determined by the difference between the total polarization and the sum of electronic and orientational polarization [26]. For example, when an electric field is applied in a molecule of sodium chloride, the chlorine atom becomes a negative ion and the sodium atom becomes a positive ion. As a result, there will be a relative displacement of the charge centres, and the molecule will possess a permanent dipole moment. When there is no electric field, the molecules are oriented at random and there is no dipole moment. Equation 5 explains the total polarizability α_T, where is orientational polarisation, is atomic polarisation and, is electronic polarization.

1.3.4 Dielectric polarization in a single & multi-component system

Polarization processes, such as dielectric polarization, Maxwell-Wagner-Sillars (MWS) polarization and lattice polarization have a very close relationship with the dielectric constant. When the applied field frequency is low, the dipoles have enough time to respond to the EM field. Upon increasing the frequency of the external field, polarizability cannot be maintained, which results in a decrease in the dielectric constant.

Dielectric polarisation within a single-component system mainly arises from dipolar polarization, space-charge polarization, and electronic polarization, which have been described in the above section. Molecules (polar or non-polar molecules) have intrinsic dipole moments which would

rearrange along with the electric field direction. Factors such as defects can influence the dielectric polarisation.

For example, a study was carried out by Yangfang *et al.*, where hybrids of MoS_2/rGO (molybdenum disulfide/ reduced graphene oxide) were prepared. Results showed that they can be promising microwave absorbing materials [29]. Defect polarisation caused by MoS_2 nanocrystal as well as the defect polarisation of imperfect carbon structures played a significant role in EM wave attenuation.

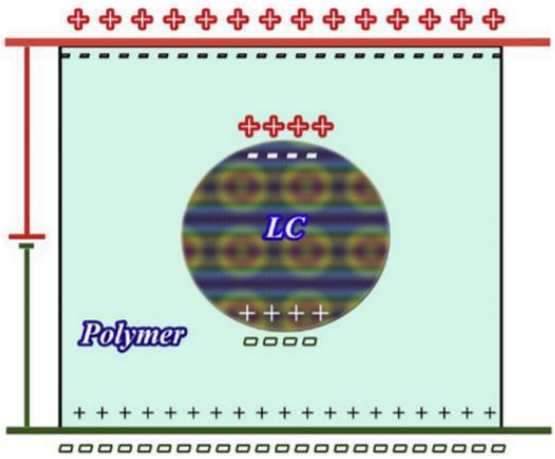

Figure 1-5: Maxwell-Wagner-Sillars effect in heterogeneous media. The simplest case with a single liquid crystal (LC) droplet surrounded by a host polymer matrix [31].

Generally, incorporation of an element within any crystal lattice leads to inhomogeneity within the crystal structure, due to which the obtained defect and dipole produced induces additional polarisation. Electrons are trapped within the defects and polarization charges are created.

A study was carried out where frequency dependent permittivity of Ni/carbon-based composites and nitrogen-doped Ni/carbon-based composites were evaluated. After nitrogen doping, more free charges were trapped by the N-doping-induced defects under EM fields, thus inducing more asymmetric charges around the defects. This leads to additional dipolar polarisation. The dielectric constant values were higher for nitrogen-doped Ni/C composite compared with just Ni/ carbon-based composite [30]. In a multi-component heterogenous media, there is a significant interfacial polarization mechanism, interfacial polarization. Interfacial polarization effect is often called the

Maxwell-Wagner-Sillars (MWS) effect [31]. The MWS effect often occurs in heterojunction structures. A heterojunction is an interface that occurs between two layers i.e. layers of two different materials. MWS effect in heterogeneous structures is due to the accumulation of charges at the interface as well as the dipoles on the individual particles. Figure 1-5 shows the schematic representation of the MWS effect in a heterogeneous mixture of liquid crystal (LC) and a polymer. In these kinds of structures, additional charge accumulation occurs at the LC-polymer boundaries under an external field because of the differences in dielectric characteristics and electrical conductivity.

Leistriez *et al.*, performed dielectric measurements on a neat acrylic core-shell particle as well as core-shell modified epoxy networks. It was demonstrated that properties of interphases strongly affect the interfacial polarization processes and dielectric properties of a polymer blend. Interfacial dipoles amplify the response to the incoming EM field and thus enhanced microwave properties is observed [32][33]. Chen *et al.*, proposed collective-movement-of-interfacial dipole (CMID) based on hydrogenated TiO_2. The enhanced microwave absorption is due to CMID in the a natase/rutile and crystalline disordered interfaces which induces collective interfacial polarisation amplified microwave contrast enhancement properties [34].

1.4 Dielectric characterization studies of biological tissues

In the microwave spectrum, the dielectric contrast is impacted strongly by the resonance of water molecules. Living tissues are characterized as high-water content (muscle, blood, brain) and low water content (bone, fat) tissues (Fig. 1-6) [35].

Due to the large permittivity of water, high-water content and low-water-content tissues exhibit a large dielectric contrast, which can be exploited for imaging applications. Understanding the dielectric behaviour of different tissues helps identify if different tissues can be recognized by their

unique electrical properties. The increased volume of water within the cancerous tissue is responsible for the strong electromagnetic scattering which can be differentiated from other tissues using MWI. The increased amount of water, within the tumour cells, leads to greater conductivity and dielectric constant of tumour tissues compared with healthy tissues. The data presented in Figure 1.6 was collected by Gabriel *et al.*, and plotted over the range 100 MHz to 100 GHz[35][36].

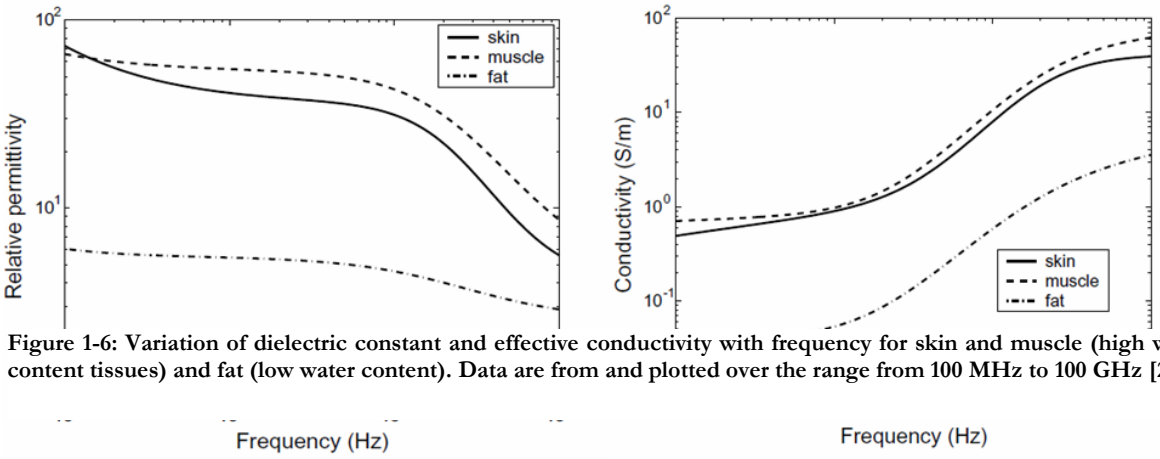

Figure 1-6: Variation of dielectric constant and effective conductivity with frequency for skin and muscle (high water content tissues) and fat (low water content). Data are from and plotted over the range from 100 MHz to 100 GHz [21].

The dielectric properties of normal and cancerous tissues of various human organs have been explored in many studies previously [37][38][39][40]. However, focussing on just the breast tissues, in 1984, Chaudhary *et al.*, measured the dielectric properties of *ex vivo* normal and malignant breast tissues between 3 MHz and 3 GHz[41]. The average set of measurements showed an increase in the electrical properties of malignant tissues when compared with normal tissue. In 1988, Surowiec *et al.*, measured the dielectric properties of *ex vivo* infiltrating breast carcinoma and its surrounding tissue at frequencies between, 20 KHz and 100 MHz[42]. They observed significantly higher permittivity values for the central part of a tumour and the infiltrating margins compared from the periphery of a tumour. They suggested that the increase in the permittivity within the infiltrating margins was because of tumour cell proliferation. In 1992, Campbell and Land, measured the dielectric properties of human breast tissue at 3.2 GHz. Campbell opposed that dielectric

measurements made by Surowiec *et al.*, may have been inaccurate, since, samples were kept in saline, and results at microwave frequencies may have been altered by the salinity of the sample. Campbell and Land examined four types of tissues: fatty tissue, fibro-glandular tissue, benign breast tumour tissue, and malignant breast tissue. They were able to see a significant dielectric contrast between normal (fat tissue and all the other breast tissue) and tumour tissue [43].

In 1994, Joines *et al.*, measured the properties of normal and malignant tissues between 50 and 900 MHz[44]. Results indicated that breast tissue had the largest contrast between normal and malignant tissue compared to other tissues such as colon, kidney, liver, lung, and muscle. The permittivity of malignant tissue was 3.4 times higher, and conductivity was 6.8 times higher over the frequency range between 50-900 MHz. In 2000, Meaney *et al.*, used a clinical prototype of a microwave tomographic system to estimate the dielectric properties of normal breast tissue *in vivo*[45]. They measured the average dielectric constant and conductivity of cancer-free breast tissue. They noted that the average dielectric constant values of normal tissue at 900 MHz were significantly higher than those previously published by Joines *et al.,* Meaney also suggested that a correlation existed between the average dielectric constant and density of the breast tissues with high-fat content. Tissues with high-fat content had an average dielectric constant value of 31, while patients' dense breasts had an average dielectric constant value between 35 and 36 [45].

More recently, Choi *et al.*, measured the dielectric properties of breast cancer tissue with the properties of metastasized lymph nodes and normal lymph nodes, within the frequency range between 0.5 and 30 GHz. Results suggested a contrast between malignant and normal tissue[46].

One of the most recent studies was carried out by Lazebnik *et al.*, (2007), [47][48]. In her first study, she examined the breast tissues obtained from breast reduction surgeries. More recently, a series of *ex vivo* studies carried out by Lazebnik *et al.*, characterized the broadband electrical properties (0.5–20 GHz) of diverse breast tissue types, taken from breast reduction surgeries on a large sample population. The results showed that dielectric properties were determined by the

percentage content of adipose (fat) in each sample and that other factors such as age, and tissue temperature variability were negligible. The second segment of the large-scale study from cancer surgeries by Lazebnik *et al.*, reports the dielectric characterization of normal, benign and malignant tissue samples. The contrast between malignant and fatty breast tissues may be as large as 10:1, however the distinction between malignant and healthy fibro-glandular tissues can be as low as 10%.

1.5 Microwave techniques for measuring dielectric properties

A vector network analyser (VNA) consists of a signal source, a receiver and a display (Fig. 1-7). The receiver is set to a frequency range to detect the reflected and transmitted signals from the material under test (MUT). The receiver is tuned to that frequency to detect the reflected and transmitted signals from the material. The measured response of the MUT produces the magnitude and the phase data at that frequency. The source is then stepped to the next frequency and measurement are repeated to display the reflection and transmission measurement response as a function of different frequencies.

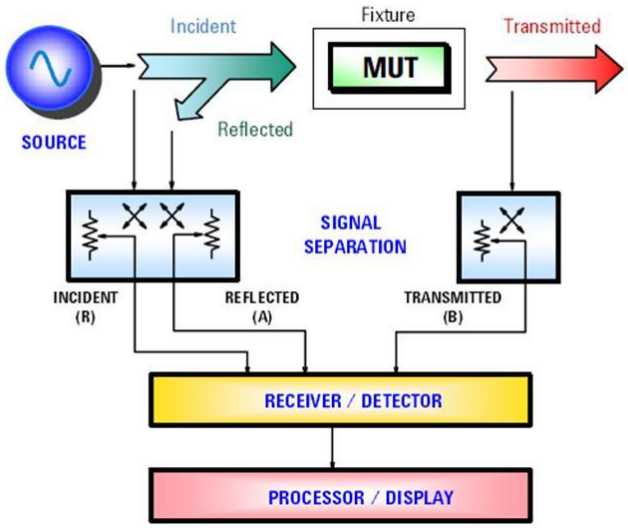

Figure 1-7: Schematic representation of a vector network analyser [51].

A measurement calibration is used to eliminate the systematic measurement errors due to the imperfection of the system. Random errors can be caused due to noise, drift, or the environment (temperature, humidity, pressure) cannot be removed with a measurement calibration. Because of this, microwave measurements are susceptible to errors from very small changes in the measurements system. Errors can be eliminated by adopting a good measurement practice and minimizing any physical movements of the VNA and by making sure that at the connector and the cables remain intact [49]. A typical coaxial probe system (Fig. 1-8) consists of a vector network analyser, a coaxial probe, an external computer with the software.

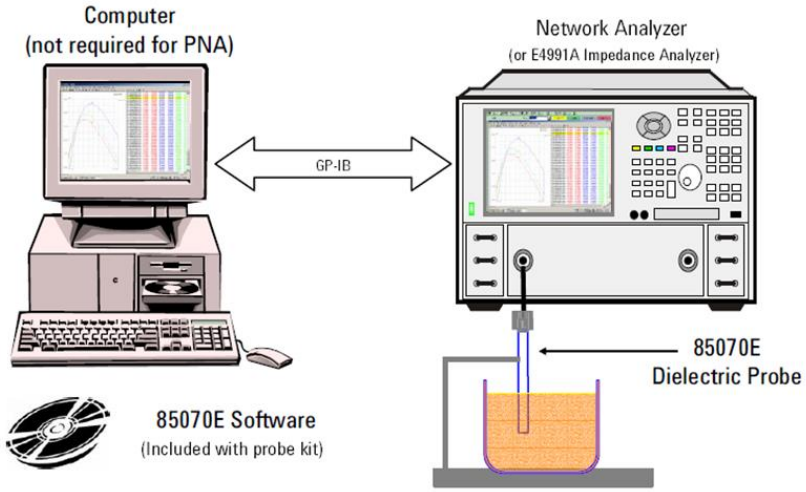

Figure 1-8: A typical coaxial probe system consists of a vector network analyzer, a coaxial probe, an external computer [51].

1.5.1 Coaxial probe technique

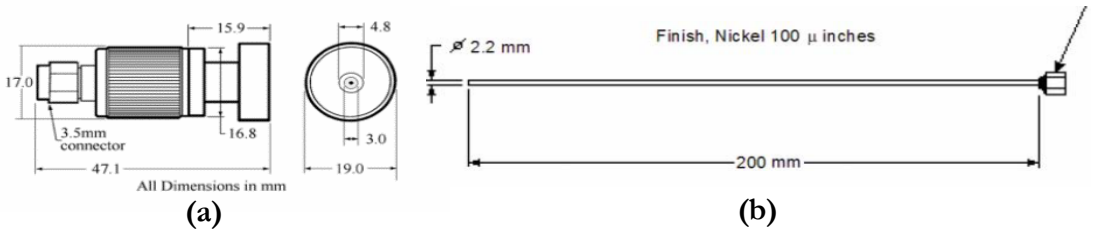

Figure 1-9: Schematic representation of two types of probe design (a) High temperature probe (b) Slim form probe [51]

1.5.1.1 High temperature probe

A high temperature probe (Fig. 1.9 a) operates between 0.2 – 20 GHz and is capable of withstanding temperatures form -40 to 200°. Due to the design of this probe, it allows the measurements of flats surfaced solids in addition to liquids and semi-solids [49].

1.5.1.2 Slim form probe

A slim form probe (Fig. 1.9 b) operates between 0.5-50 GHz and can fit in very tight smaller spaces. Due to the design of the probe, it allows measurements for liquids and semi-solids only.

A coaxial probe technique in general is best for liquids and semi-solid materials. Special precautions like, avoiding air gaps between the sample and the probe is necessary. Material under test should be non-magnetic, needs to have thickness >1cm. Sample needs to be homogenous and isotropic . This measurement method is very convenient, simple, non-destructive and with one measurement, user can sweep up to 50GHz [50].

1.5.2 Resonant cavity method

A resonant cavity system consists of a resonant cavity connected between two ports of a network analyser with coaxial cables (Fig. 1.10)[50].

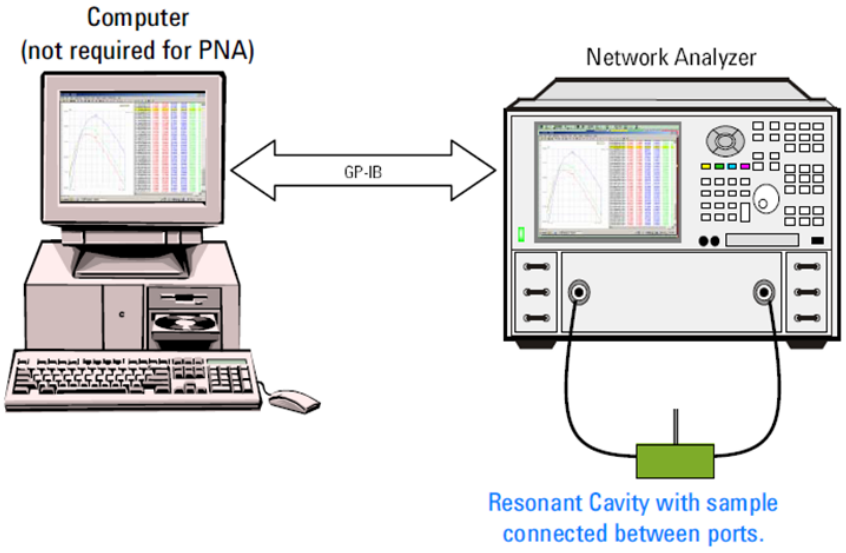

Figure 1-10: Schematic representation of a resonant Cavity System [51].

The dielectric properties are calculated form the transmission response of the cavity, which is first measured empty and then with the sample which are either semi-solids or in powder form.

1.5.3 Transmission line system method

A transmission line system consists of a vector network analyser and a sample holder which is connected between the two network analyser ports. Agilent provides a software which can convert the reflection and transmission coefficients to dielectric properties. Transmission line system and resonant cavity have similarities in there set ups. Both systems have a broad frequency range from 0.1 to 110 GHz. They can measure magnetic materials and hard solid materials. However, a large sample size is required for low frequencies and small sample size for high frequencies. Both techniques have better accuracy for extremely low loss measurements[50].

1.5.4 Free space method

A typical free space system (Fig. 1.11) consists of a vector network, two antennas facing each other with a sample holder in between them. Agilent provides a software which can convert the transmission coefficients to dielectric properties. This kind of system makes permittivity measurements without contacting the material sample. This system is ideal for remote sensing and for high temperature applications.

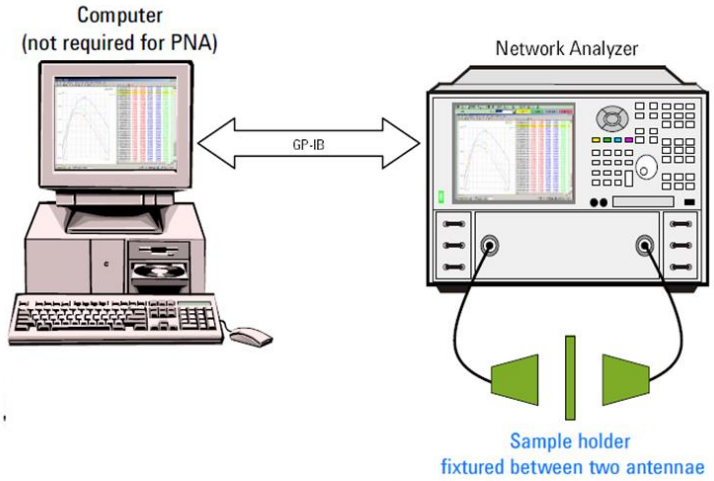

Figure 1-11: Schematic representation of a free space system [51]

However, sample needs to have a flat surface and need to be facing parallelly. A large sample will be required for low frequencies and resonant cavity technique are considered to have better accuracy compared with free space technique.

The open-ended coaxial probe has become the most commonly used method to measure the dielectric properties of tissues. This methodology has been used in this study as well. This method is commonly used for following reasons: it is easy to use; sample handling is minimal and is non-destructive. It can also measure liquids, semi-solids and malleable solids. However, the open-ended coaxial method assumes a homogenous solution which needs to be in good contact with the probe. To avoid errors, air bubbles and uneven surfaces can lead to challenges [51]. Probe is sensitive to any movement, which can lead to systematic errors.

In this study for our dielectric measurements, open ended-coaxial probe measurement technique was used. Before dielectric measurements were performed, a three-step standard calibration procedure is carried out i.e. open circuit, short circuit and water. Open circuit is air, short circuit is a conductive elastomer which mimics the properties of a metal and RO (reverse osmosis) water at 20º C. Calibration is performed to reduce any systematic errors.

1.6 Overview of Microwave Imaging

The pioneering research that was carried out during 1970-1980, identified most of the challenges in the near-field microwave tissue imaging. These images can be quantitative, by estimating the different tissue electrical properties (microwave tomography), or qualitative, for which the location and shape of an object that is a strong "scatterer", usually a tumour lesion, are identified by radar-based MWI [52].

Microwave tomography generates an image that maps the electrical properties and their distribution in tissues, based on signals acquired from the antennas that surround the organ to be

imaged. These dielectric properties are translated by the received parameters from the multiport imaging system that surrounds the organ to be imaged. Experimental electromagnetic (EM) measurements are susceptible to noise and errors from various sources, such as errors caused from the source (VNA), mechanical error, model discrepancies, background noise and lossy materials in the measurement region. To control the amount of loss, various liquids (coupling mediums) can be used in between the antennas and the organ, to improve impedance matching between the boundaries and thus decrease loss in a manner like ultrasound gel for ultrasound imaging techniques. The use of coupling medium and the extent of loss in tissues is has been described in a review by Nikolova.

1.6.1 Microwave Tomography

The tomography imaging approach employs an array of antennas, where a transmitter antenna illuminates the region being imaged, and the remaining antennas receive the transmitted waves [53]. The process is repeated sequentially for each of the antennas in the array [54]. The received signals are used to produce a quantitative image using an inverse scattering technique, which estimates the spatial distribution of the dielectric properties of tissues [55]. Inverse scattering uses scattering signals including diffraction from objects. This creates a map of permittivity and conductivity through inversion of those signals.

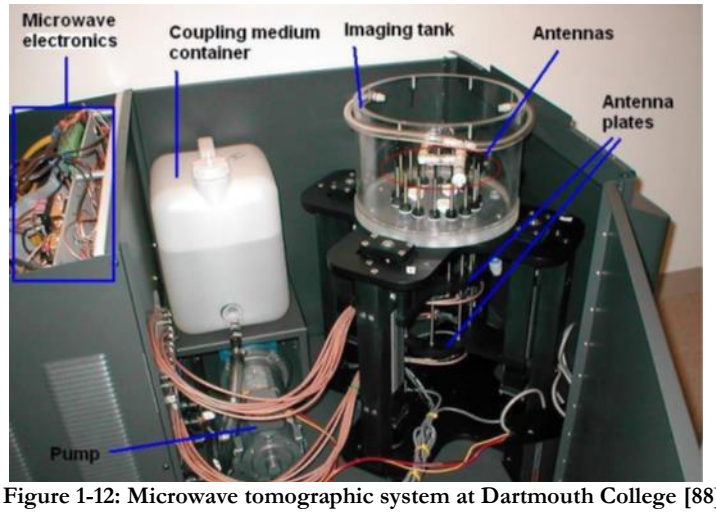

Figure 1-12: Microwave tomographic system at Dartmouth College [88].

Microwave tomography has been studied by several research groups [56][57][58]. The first MWI system, which was tested in the clinic, was the tomographic system developed by Dartmouth College [59][60][61]. The Dartmouth MWI system composes of an examination table with an insertion hole in the top, for the breast (Fig. 1.12).

The woman to be examined lies on her stomach with her breast extending through a hole in the examination table. A tank containing the coupling medium (glycerol and water mixture) is located beneath the table. Using a coupling medium with lower permittivity will reduce imaging artefacts and can provide improved object detection. The tank contains array of antennas (monopoles) used to illuminate the breast and receive scattered signals. 16 antennas form a circle with 15 cm diameter, which result in an imaging region with 13cm diameter. For a three-dimensional scan of the breast, the antenna array is scanned vertically from the nipple towards the chest wall. A model-based image reconstruction approach is used to create images from the measured data. 7 vertical array positions with 1 cm separation are used to complete a scan of the breast. The scan at each vertical position consists of an antenna which is then recorded by 9 opposite transmitter antennas. The signals measured at the received antennas will vary based on the imaging object, and the location of the antenna (antennas closer to the transmitter may receive stronger signals). The results have demonstrated variation within the permittivity. Lower permittivity region corresponded to lumpectomy location and higher permittivity corresponded to ex vivo measurements of tissues, and the average permittivity values appeared to correlate with breast density.

Another imaging system had been developed by Klemm *et al.* [52]. They used a mechanical array rotation to extract the tumour response from raw measured data. Using a physical 3D curved breast phantom, the authors demonstrated the ability to detect small tumours (4mm and 6mm). The team had concluded that such a system could be used for breast cancer detection clinical trials.

Lo Vetri *et al.* presented a pilot study using a microwave tomography system in which they imaged the forearms of 5 adult male and female volunteers between the ages of 30 and 48. Microwave scattering data were collected between 0.8 to 1.2 GHz with 24 transmitting and receiving antennas located in a fluid of deionized water and salt. Inversion of the microwave data was performed with a balanced version of the multiplicative-regularized contrast source inversion (CSI) algorithm formulate using the finite-element method (FEM-CSI). Initial imaging results showed that the image quality is dependent on the thickness of the arms peripheral adipose tissue layer; thicker the layers of adipose tissue lead to poorer overall image quality. They also showed that introducing prior information into the FEM-CSI algorithm, the internal anatomical features of all the arms are resolved and images are improved significantly[62].

1.6.2 Radar based approach

Radar-based breast tumour detection indicates the location of strongly scattered objects, rather than producing a distribution map of dielectric properties. The first pulsed radar system for breast cancer detection was introduced in 1998 by Susan Hagness [63].

To acquire the data, the imaging domain is illuminated with an ultra-wideband pulse (UWB), and the same antenna is responsible for collecting the back scattered signal. The sensor is scanned to many locations surrounding the breast, and this process is repeated. To identify the presence and location of a tumour, the reflections observed at the collection of the sensor locations are focused. The scattered signals are recorded, and an algorithm operates on the received signal, which exploits the time delay for a round-trip from the transmitter antenna to the focused point. This is carried out by computing the travel time between each sensor location and a selected focal point, then time shifting and summing the reflections. The process is repeated as the focal point is scanned through a region of interest to create an image. When the focal point is located at a reflecting object (e.g. tumour), the reflections from the object add together, resulting in a significant response

in the image. Tumour detection is based on the idea that reflections from the tumour add coherently, while clutter tends to add incoherently.

Radar-based MWI can be done through two approaches: frequency domain analysis and time-domain analysis. Several microwave systems reported in literature are based on frequency domain analysis. Figure 1.13 shows a system based around 31 UWB (ultra-wideband) antennas called 'MARIA M4' at the University of Bristol, UK. This MWI system operates in the 3-8 GHz region using multistatic data collection [64]. It uses a 2 port VNA and takes 90 seconds to scan a patient. Subsequently, the team developed a 60-element antenna array with 8 port VNA.

There were 86 patients recruited, who were scanned with a prototype design. The resultant three-dimensional images were compared with available ultrasound and mammogram images to determine the efficiency of this prototype.

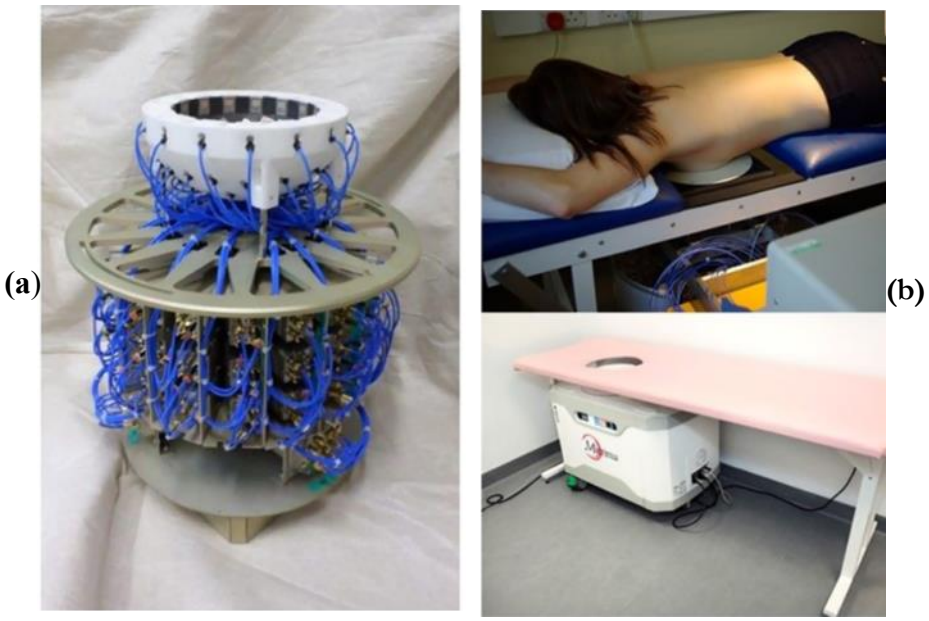

Figure 1-13: MARIA M4/M5 array and bed system. (a) MARIA M4/M5 array and bed system. (a) Rotable 60 antenna array and switch assembly which moves as a unit around the breast cup. (b) MARIA M4 position in clinic [68].

The 86 studies reviewed, 66 had mammograms available for comparison. Images showed the location of the strongest signal, and this corresponded in both older and younger women, with sensitivity of >74%, found in dense breasts. The results of this pivotal clinical trial indicated that

these imaging systems can find rapid application and give promise for an easy and safe detection of breast tissue abnormalities.

Patients undergoing MARIA M4 reported that the procedure was acceptable and appreciated the lack of breast compression. The MARIA system produces a high contrast 3D image of the breast and offers the provision of a safer, more comfortable and inexpensive breast screening compared to other imaging modalities. In 2006, MICRIMA was founded to develop and commercialize the technology of microwave radar breast imaging at the University of Bristol, UK. The MICRIMA's MARIA system has undergone clinical trials at several breast cancer imaging centres in the UK and got European regulatory approval in 2015 [65]. University of Calgary have developed a tissue sensing adaptive radar (TSAR) prototype of radar-based breast imaging system (Fig. 1.13 (b). The patient lies face down on the table to be scanned and the breast is immersed in a tank filled with immersion liquid. For a TSAR scan, the antenna is physically scanned to synthesize an array tat encircles the breast. A small group of people were scanned, and the several images restored were like clinical results[66].

1.7 Use of NPs as contrast agents

All medical imaging modalities have limitations to resolution and imaging depth to certain stages. The notion of contrast was introduced to make clear and decisive diagnosis. Contrast enhancing agents that are based on nanomaterials are used in medical imaging due to their accumulation in tumours [67]. Medical imaging modalities exploit certain tissue natural properties, which alter the transmitted signal from one part of the body differently from other parts. For MWI, this will the dielectric properties of the tissues. The region of interest which requires more contrast is the tumour, because the dielectric difference between low water content tissue, such as adipose and tumour tissue is 10:1, however, the dielectric difference between the fibro-glandular tissue and

tumour tissue is as low as 10%. Since most of the breast tumours arise within the fibro-glandular, contrast agents are required to improve the difference.

1.7.1 Enhanced permeation & retention effect (EPR)

Nanoparticles are appropriate for contrast enhancement as well as being nanocarriers of therapeutic drugs, due to the enhanced permeability retention (EPR) of small molecules[68][69][70]. Maeda *et al.*, showed that macromolecules such as polymers and proteins with molecular weight larger than 40-50KDa show selective accumulation in tumour tissues compared with normal tissues. This phenomenon is known as the enhanced permeation and retention effect (Fig. 1.15). Due to this, an EPR based tumour targeting strategy was developed by using polymer modification, nanoparticles, micelles, liposome, all of which exhibited more than 10-200 times higher concentrations in tumour than that in normal tissues, such as skin, muscle, heart, and kidney, after systemic administration due to the EPR effect. Due to this design, EPR has now become a gold standard for anticancer drug design [71].

To grow, tumour cells develops a neovasculature to ensure adequate supply of nutrients and oxygen. As the tumour starts to grow, they form new blood vessels for their survival. Tumour vasculature unlike normal cells, has incomplete endothelial lining causing relatively large pores (0.1-3 μm in diameter), leading to higher vascular permeability.

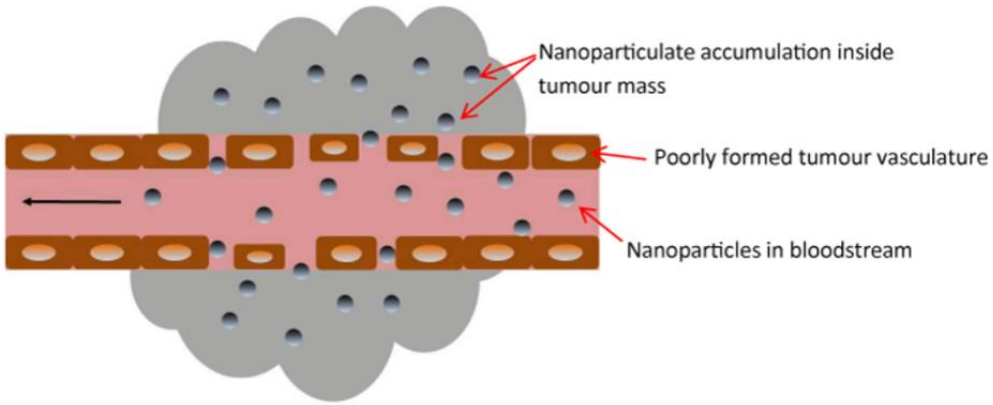

Figure 1-14: Enhanced permeability and retention (EPR) effect and passive targeting. Nanocarriers can extravasate into the tumours through the gaps between endothelial cells and accumulate there due to poor lymphatic drainage [76]

Nanoparticles can extravasate through leaky vasculature to reach the tumour and stay there due to poor lymphatic drainage of tumours. However, NPs used for the drug delivery system should be large enough to prevent filtration by the kidney and small enough to be captured by the liver and spleen [72].

Intravenously administered long-circulating nanosized constructs have been known to exhibit passive tumour targeting due to the EPR effect. Several products like Doxil®, Abraxane® are already in clinical use [71].

1.7.2 Nanoparticles in medicine

Most commonly studied NPs include quantum dots, carbon nanotubes, paramagnetic NPs, liposomes, gold NPs, polymeric lipid and silver NPs. Magnetic NPs have been used for cell sorting, MRI, drug-delivery and magnetic hyperthermia therapy. Lipid and polymeric NPs have been used to encapsulate therapeutic molecules to increase drug solubility and drug efficiency through EPR effect. Carbon-based NPs have the potential of being used for drug-delivery and biomedical applications [72].

In the next section different nanoparticles which have been used as potential to improve the contrast agents for MWI have been highlighted in detail.

1.7.3 Dielectric studies of nanoparticles

Microbubbles as a dielectric contrast agent for enhancing the sensitivity of breast cancer detection was suggested. Mashal *et al.*, used microbubbles that were air-filled glass spheres (iM30K, 3M) with an average diameter of 18 μm and density of 0.6 g mL^{-1}. Ethylene glycol was used as a dispersant as it has dielectric properties that are in the range of the biological tissues at microwave frequency (3 GHz). Mixtures of ethylene glycol with 0%, 5%, 10%, 20% and 30% by weight concentration of microbubbles were prepared and characterised from a frequency range of 0.5–6 GHz by open ended coaxial probe technique[73]. Results suggested that microbubbles significantly lowered the

dielectric properties. Also, the stability of the dispersion had large effects on the dielectric characterisation. Since microbubbles are less dense that the background medium, they float to the top of the surface, therefore measurements were taken with respect to time. Measurements at t_0 & $t_{2.5}$ min was compared. Table 1.1 shows that a heavy weight percentage of microbubbles produces the same/similar electrical properties at t_0 at a lower weight percentage at $t_{2.5}$ min. Therefore, dielectric measurements with the coaxial probe are highly dependent on the colloidal stability of the material under test in question, as the measurement depth is very small [44]. Hence measurements with the dielectric probe must be dispersed completely to produce comparable results.

Later studies by the same authors were performed on single walled carbon nanotubes (SWNTs) and they have shown to increase the dielectric contrast of a background medium, and hence can act as a contrast agent for MWI. However, biocompatibility and toxicity of SWNTs is an issue. This has been discussed in detail in chapter 3. They have also shown to increase the temperature while being illuminated by a high intensity microwave signal. This is a new field that may shows promise.

Table 1-1: Summary of data for microbubbles assessed at 3 GHz. NA: Not available [78].

Solution	Initial microbubble concentration (% by weight) at 0 min	Estimated actual concentration (% by weight) at 2.5 min	Average ε_r (3 GHz)	Average σ (3 GHz) (S m^{-1})
1	0	0	14.03	2.32
2	5	20	9.66	1.33
3	10	30	8.34	1.11
4	20	35	7.38	0.95
5	30	40	6.86	0.84
6	100	100	NA[a]	NA[a]

Mashal *et al.*, reported that SWCNTs manufactured by Cheap Tubes Inc. using a chemical vapour deposition technique and purified using an acid treatment, have the potential to enhance dielectric contrast between malignant and normal tissue for microwave detection of breast cancer. Pristine carbon nanotubes may have high conductivity and therefore could be used as nanomaterials that

could affect the dielectric properties of tumours. Mashal *et al.* used tissue mimicking materials in their study to replicate the dielectric properties of tumour tissue over a broadband frequency range, were mixed with varying concentrations of SWCNTs. Their dielectric properties were characterized over a frequency range of 0.6–20 GHz (Fig. 1.15 a and 1.15 b) [74].

At SWCNT concentrations of less than 0.5% by weight, significant increase in the relative dielectric constant and effective conductivity was observed. Table 1-1 shows the dielectric constant and the effective conductivity of a basic oil in gel phantom and same consistency phantoms with varying concentrations of SWCNTs. Probe measurements showed that the SWCNTs increase the dielectric constant of the medium.

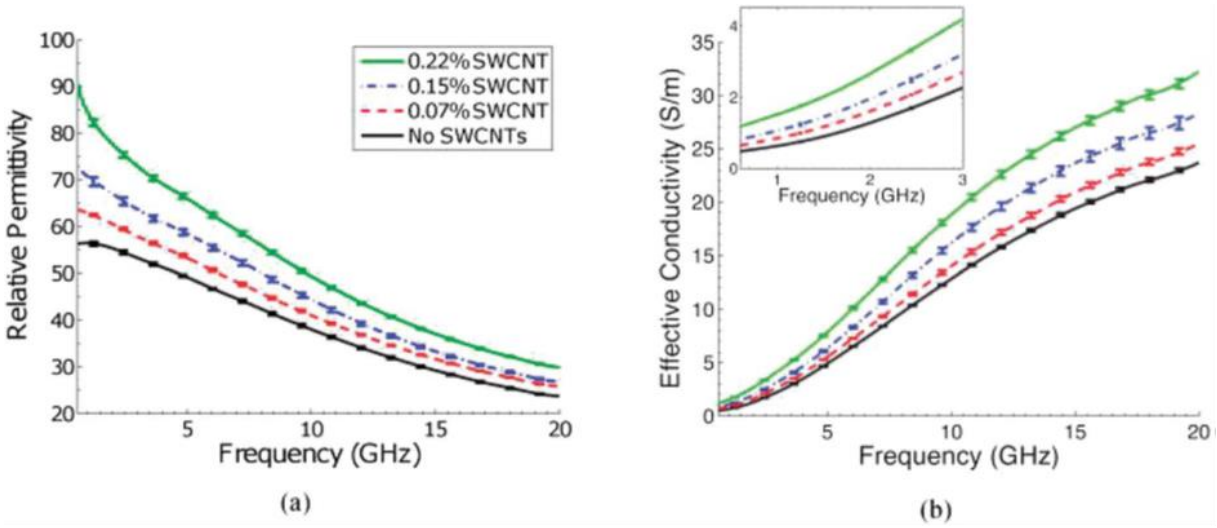

Figure 1-15: (a) relative permittivity and (b) effective conductivity of tissue mimicking materials with varying concentrations of single walled carbon nanotubes, measured over the frequency range from 0.6 to 20 GHz. Each curve represents the average properties of three different samples of the same concentration [79].

The average dielectric constant of a pure phantom with no SWCNTs, 1 mg mL^{-1} (0.07%), 2 mg mL^{-1} (0.15%) and 3 mg mL^{-1} (0.22%) mg mL^{-1} of SWNTs was 53.3, 57.9, 63.7 and 77.3 respectively at 3 GHz (Table 1-2). Therefore, not only showing increase in dielectric contrast from the background medium but also increase dependency with increase in nanoparticle concentration.

Results suggest that even at very low concentrations, SWCNTs have the potential to significantly increase the dielectric properties. Therefore, SWCNTs could be utilized to be used as a contrast agent to enhance the contrast for MWI for breast cancer detection.

Table 1-2: Electrical properties of SWCNT dispersions at 3 GHz [79].

% Weight concentration of SWCNTs	Average ε_r (3 GHz)	Average σ_C (3 GHz)
None	53.3	2.3 S m^{-1}
0.07%	57.9	2.7 S m^{-1}
0.15%	63.7	3.2 S m^{-1}
0.22%	73.0	4.2 S m^{-1}

Heating response of tumour mimicking gels were also measured by Mashal *et al.* in the same study. Tumour mimicking gels prepared with and without the dispersion of SWCNTs at the same concentration from dielectric characterisation was set into a tube connected to a fibre optic thermometer. This tube was placed inside an S-band (WR-284) rectangular waveguide with cross-sectional dimensions of 72 mm × 34 mm that was connected to an Agilent 83623B signal generator, and an amplifier (Mini-Circuits, ZHL-42W) produced 1 W of continuous microwave power at 3 GHz to the waveguide to heat the gel for 3 minutes with a 5-minute cool down time. Results show that the temperature of the gel is increased by 2–8 °C depending on the SWNT concentration to the basic gel phantom. It was also shown that the temperature increases in each phantom scaled relatively linear with the effective conductivity and those from previous experiments with SWCNTs in colloidal dispersion showed similar heating trends, as well as similar proportionality with temperature increase and the effective conductivity [73].

Xie *et al.*, could achieve exceptionally high microwave frequency dielectric properties with stable high concentration (~20 mg mL^{-1}) of 1:1 mixture of single- and double-walled carbon nanotubes (CNTs)[75]. The method involved functionalising CNTs (Cheap tubes, Inc.) via sonication in nitric and sulphuric acid (H_2SO_4:HNO_3, 3:1). Samples for dielectric measurements were prepared by

dispersing treated CNTs in deionised water with mannitol (50 mg mL^{-1}) and the dielectric properties were characterised by dielectric probe at frequency range of 0.5–6 GHz. Properties of CNTs were also measured before and after passing them through a 25-gauge needle. The study indicated the effect of functionalisation on either the dielectric properties or the dispersion, and subsequently on their assessed permittivity. The dielectric properties of CNT dispersions were shown to be significantly higher than those of the control. The dielectric constant of CNT dispersion before passing through the needle was increased by 14% at 10 mgmL^{-1} and 68% at 20 mg mL^{-1} and effective conductivity was increased by 66% and 404% for 10 and 20 mg mL^{-1} samples. The authors suggested that such high increase in dielectric properties was due to the successful functionalization of CNTs with carboxylic and sulfonic groups after the acid treatment on the outer CNT walls. This was responsible for their stabilisation and their increased dispersion and colloidal stability was attributed to the stronger length-shortening effect.

Xie *et al.*, also carried out acid purification methods (hydrochloric acid/hydrogen peroxide method and nitric acid reflux method) for synthesis of single walled carbon nanotubes, Co-CNTs (CNTs synthesized by catalytic chemical vapor deposition) and Fe-CNTs (CNTs synthesized by high pressure CO method) and their dielectric properties were studied using a slim form probe between 0.5–6 GHz [76]. For microwave frequency dielectric measurements, 3 mg mL^{-1} of SWCNTs were dispersed in 0.1% aqueous PL-PEG_{5400}-NH_2 (Phospholipid-polyethylene glycol-amine) or DSPE-PEG (1,2-Distearoyl-sn-glycero-3-phosphoethanolamine-Polyethyleneglycol) and sonicated for 12 hours. These lipids and amphiphiles are widely used to improve the colloidal stability and biocompatibility of nanomaterials.

The authors observed a significant increase in the dielectric properties for pristine (non-purified) Co-SWCNT compared to the control. For example, at 3 GHz, the average dielectric constant increased by 10% and the average effective conductivity increases by 45%. The dielectric properties of the (HCl +H_2O_2)-purified Co-SWCNT dispersion were slightly lower than those of

the pristine dispersion, indicating an effect of possible oxidation affecting the SWCNT dielectric properties. At 3 GHz, the average dielectric constant decreases by 1.6% and the average effective conductivity decreases by 8.7%. The dielectric properties of the HNO_3-purified Co-SWCNT dispersion were closer to those of the control sample than the pristine SWCNT dispersion. These results show that the HNO_3 purification method more severely reduces the microwave-frequency dielectric properties enhancement effect of Co-SWCNTs in dispersion than the HCl + H_2O_2 purification method. Their study demonstrated the following: (1) Aqueous dispersions of pristine Co-SWCNTs and Fe-SWCNTs synthesized by two distinct methods, with significant differences in morphology, show similarly elevated microwave dielectric properties compared to a control: (2) acid-purification-based changes in SWCNT structure and composition decreases the length and fraction of metallic nanotubes, as well as increases in amorphous carbon and covalent functionalization of SWCNTs depending on the purification method and dramatically reduces the microwave dielectric properties of SWCNT aqueous dispersions. These findings have important implications in the development of SWCNT-based formulations of microwave-frequency theranostics agents for biomedical applications.

Li *et al.*, measured the effective dielectric properties of PL-PEG functionalised SWCNTs at a concentration of 2 mg mL^{-1}. Dielectric properties were measured from 0.5–10 GHz by using a precision open-ended coaxial probe technique. They were shown to have a 90% increase in effective conductivity and 10% in dielectric constant compared to the properties of PL-PEG in water at 1 GHz. SWCNT (0.5 μm length) colloidal dispersions (0.5 and 1 $mgmL^{-1}$) produced by Stony Brook University were also stated to increase the dielectric constant compared to aqueous back-ground and that other forms of carbon such as Bucky balls show no effective contrast. The significant difference of aspect ratio between the SWCNTs and the Bucky balls was stated as the reason why SWCNTs increase the dielectric constant[77].

Metallic nanoparticles have also been characterised previously; dielectric properties of colloidal dispersions consisting of 30% volume fraction of copper nanoparticles (384 nm) in ethylene glycol, by using both wideband open-ended coaxial probe technique and narrowband cavity perturbation technique were performed. There was no meaningful change in the effective conductivity, however, a 20% increase in the dielectric constant compared to background medium at 2 GHz was observed.

This percentage increase is only related and that a sizable percentage of NP was dispersed in solution, compared to the characterisation of CNT colloids. This characterisation experiment shows that different measurement techniques have good agreement with each other, with respect to a stable and fully dispersed medium that is isotropic.

Ogunlade *et al.*, used a resonant cavity perturbation technique to characterise the dielectric properties of superparamagnetic carboxydextran coated iron oxide (EM1301 which contains 0.5 M of iron as iron oxide NPs) and paramagnetic gadolinium-based contrast agents; Magnevist®, Dotarem® and Prohance® at concentration of 0.5 M at 3 GHz (Table 1-3).The authors stated that the contrast originating from gadolinium compounds was not because of gadolinium itself but it was due to the dis-association of gadolinium salt which increased the ionic conductivity [78].

Table 1-4: Dielectric properties of clinically used Gadolinium agents and ferroelectric nanoparticles at 1 and 2.45 GHz [83].

Contrast agent	ε_r	σ_c
Magnevist®	49.75	0.568
Dotarem®	56.65	0.435
Prohance®	60.54	0.0504
EM1301	74.70	0.0097
Water	77.76	0.0002

Iron oxide particles were also found to produce low but measurable dielectric contrast due to dielectric polarisation loss.

This was due to the carboxylated dextran coating on the NPs and not because of iron oxide itself. They concluded that gadolinium-based contrast agents and iron oxide have little merit as contrast agents[78].

Table 1-6: Dielectric properties of ferroelectric nanoparticles at 1 and 2.45 GHz [24]

	1 GHz		2.45 GHz	
	ε'	ε''	ε'	ε''
$CaTiO_3$	135	52	97	45
$BaTiO_3$	128	122	67	72

Semenov *et al.*, measured the dielectric properties of certain ferroelectrics as potential contrast agents for microwave tomography. Barium titanate ($BaTiO_3$) and calcium titanate ($CaTiO_3$) with a particle size of 50 nm were suspended in glycerol.

Measurements were conducted using a well-established coaxial probe technique. Results suggested that with the presence of ferroelectric NPs (Table1- 4), the dielectric contrast observed is much higher compared to biological tissue such as muscle which has a dielectric constant of 56 at 1 GHz. This contrast with ferroelectrics is even more evident if compared with lower water content tissues such as fat [24].

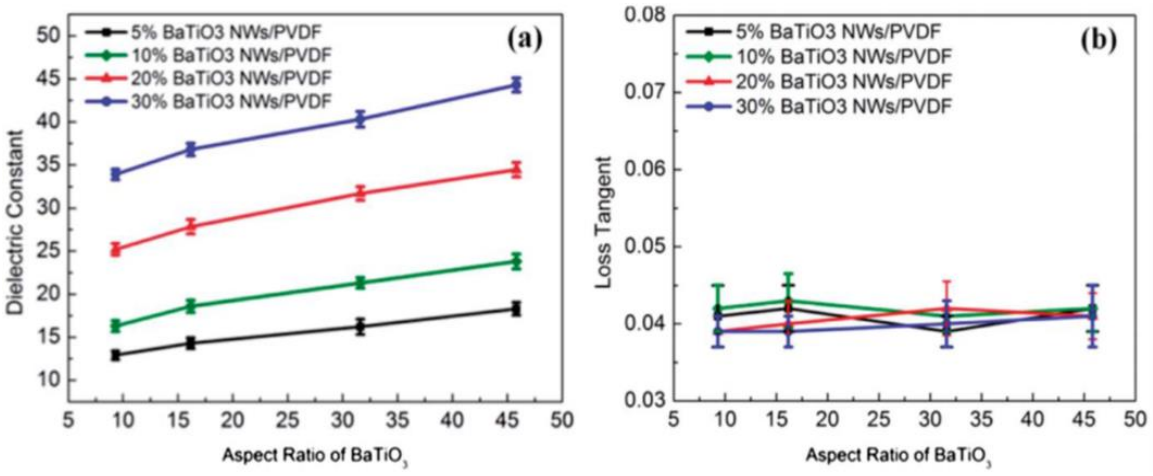

Figure 1-16: (a) Dielectric constant and (b) loss tangent of the nanocomposites measured at 1 kHz as a function of aspect ratio and volume fraction of $BaTiO_3$ NWs [84].

It is demonstrated that the dielectric constant of the nanocomposite can be significantly improved by increasing the aspect ratio of $BaTiO_3$ Nanowires (NW), while the loss tangent shows slight variation with value around 0.04 at 1 kHz under different of aspect ratio and volume fraction of $BaTiO_3$ NWs. The loss tangent of PVDF matrix is around 0.06 at 1 kHz, which indicates that integration of $BaTiO_3$ NWs decreases the loss tangent of the film. This study was able to determine the relation between the aspect ratio of fillers and dielectric constant of the nanocomposites. It shows that the dielectric constant of the nanocomposites can be improved by higher aspect ratio fillers [79].

Tang *et al.*, demonstrated that the dielectric constant of the nanocomposite increases with the aspect ratio of barium titanate ($BaTiO_3$) nanowires. The aspect ratio of $BaTiO_3$ nanowires can be successfully controlled by adjusting the temperature of the hydrothermal growth from 150 to 240 °C, corresponding to aspect ratios from 9.3 to 45.8, respectively. Figure 1-16 clearly shows that the aspect ratio of $BaTiO_3$ nanowires highly depend on the hydrothermal temperature[79].

The dielectric constant of the nanocomposites was measured with an Agilent 4980A LCR meter at a frequency of 1 kHz. The dependency of the nanocomposite dielectric constant on the concentration and aspect ratio of the fillers is shown in Figure 1-16. The dielectric constant of the increases with increasing volume fraction of the fillers due to the higher dielectric permittivity of $BaTiO_3$ as compared with the PVDF polymer (9.8 at 1 kHz).

Magnetic nanoparticles (MNPs) have gained an immense interest in biomedicine because of their biocompatibility, easy functionalisation and magnetic properties [80][81][82]. In principle, MNP-enhanced MWI has the potential of significantly reducing the occurrence of false positives and false negatives due to low dielectric contrast between healthy and fibro-glandular tissues. Bucci *et al.*, carried out a study in which MNPs were dispersed in a biocompatible environment, such as water or phosphate buffer saline (PBS), known as water-based ferrofluids (WFF)[83][84]. The concentration of MNPs used are achievable in practice (few tens of mg mL^{-1} of magnetic material).

WFF is a colloidal suspension of magnetite nanoparticles dispersed in water and coated with anionic surfactant. The colloidal suspension was diluted in PBS to an MNP concentration of about 25 mg mL^{-1}. The investigated frequency range was 0.1–8 GHz and S11 and S21 were measured at 601 equispaced points with a vector network analyser (Planar 804/1 from copper mountain technologies) connected to the measurement coaxial cell. This consists of N-male and N-female connectors together to obtain a sealed cell of fixed length. The cell is made of non-magnetic metal. The WFF is injected into the cell through two small holes on the lateral ferrofluids with a low concentration of magnetite MNPs in PBS have been reported and discussed. Characterization of a diluted WFF sample has never been presented in the literature before and represents an essential prerequisite for the implementation and the subsequent optimization of all the applications exploiting the response of MNPs to microwave and electromagnetic fields.

The MNP contrast imaging technique consists of microwave antennas surrounding a region of interest connected to a vector network analyser. In contrast to common MWI systems, a polarising magnetic field (PMF) is used to induce magnetic contrast, which is attributed to the amplitude modulation of the PMF. This is advantageous because it can detect extremely low magnetic contrast.

Also, it was shown that it is possible to detect amounts of commercially available MNPs as low as 2-7 mg, depending on the breast type for a reliable imaging[85].

To this end, an ad hoc measurement strategy and setup have been exploited. To investigate in detail, the nature of the measured response, as well as to obtain an analytical description of the magnetic properties of the investigated sample in the considered ranges of frequency and polarising magnetic field intensity, the measurement results have been fitted with the simplest dispersion model reflecting the basic physical requirements, namely, a superposition of resonant and relaxation responses.

The above-mentioned studies indicate that nanomaterials can be used as contrast enhancing agents for MWI. It is likely that these nanomaterials can have therapeutic properties. For instance, some of the nanoparticles could provide ablative hyperthermia in tumours when combined with EM techniques. Alternatively, these contrasts enhancing nanomaterials could be combined with therapeutics and promote their targeted drug delivery effect in lesions. The development of such systems is yet to be seen. Nevertheless, MW imaging and hyperthermia systems are a promising new tool that when combined with nanomaterials could offer a safe and accessible method of diagnosis and treatment.

1.8 Conclusions

Microwave systems can provide sensing and imaging therapeutics. Research efforts on the effects of EM radiation at MW frequencies and the development of MW sensing equipment indicate an emerging research area that aims to provide systems for diagnosis and therapy that are safe (non-ionising) and accessible (low cost). Nanomaterials such as carbon nanotubes and iron oxide nanoparticles could function as contrast enhancing agents for microwave imaging due to their advantage of affecting the dielectric properties of the medium that they are dispersed within. These nanomaterials show a preference in localising in cancer lesions due to their extravasation from the leaky angiogenic blood vessels into the tumour. Nevertheless, their properties in vivo imaging experiments is yet to be seen. More screening work is required for the identification of nanomaterials that can affect the dielectric properties of tissues.

This thesis discusses the aim of identifying and developing potential biocompatible contrast agents which can be used to enhance the dielectric properties between a malignant and a healthy tissue for MWI purposes for breast cancer detection. Some of the nanomaterials explored in this study have never been explored previously as contrast agents for therapeutic purposes. This thesis highlights the fact that to observe true dielectric behaviour of a nanomaterial, they need to be

dispersed well in their respective mediums. Also, having a molecular structure which makes a nanomaterial polar is crucial for attaining high dielectric property results. Therefore, this work provides an improved understanding of selecting appropriate materials which would show high dielectric property behaviour and become useful for MWI applications. My thesis ends with an overview of the data collected and critical analysis of the requirements of contrast enhancers for microwave imaging and a future perspective of how these nanomaterials should be designed to be used as contrast enhancers.

2 Materials & Methods

2.1 Materials

2.1.1 Materials used for chapter 3;

Table 2-1: Length, diameter and purity of different CNTs received from Cheap tubes Inc. (USA)

Carbon nanotubes (CNTs)	Length Reported (μm)	Diameter (nm)	Purity	Nomenclature
Single wall/ Double Wall carbon nanotube	5-30	1-4	>90%	SWNT
Multi – walled carbon nanotube	10-30	20-30		MWNT
Short single wall/ Double Wall carbon nanotube	0.5-2.0	1-2	>90%	sSWNT
Single wall/ Double wall carbon nanotube - OH	5-30	1-4	>90%	SWNT-OH
Multi – walled carbon nanotube – OH	10-30	20-30	>95%	MWNT-OH
Short Single Wall/ Double wall carbon nanotube - OH	0.5-2.0	1-2	>90%	sSWNT-OH

2.1.2 Materials used for chapter 4;

Zinc oxide (effective conductivity-Aldrich Company Ltd; Stated manufacturer size of <100 nm), silicon dioxide - quartz, (effective conductivity-Aldrich Company Ltd; Stated manufacturer size of 10-20 nm), polyethylene glycol (effective conductivity-Sigma Aldrich Company Ltd; average molecular weight (MW) of 8000 Da), pluronic – F127 (effective conductivity-aldrich Company Ltd) and CNT-OH (Cheap tubes, Inc.; Stated manufacturer size of 1-4 nm in diameter and 5-30 μm in length; > 90 % purity; 3.9 % OH groups used, as they have better dispersion properties).

2.1.3 Materials used for chapter 5;

Iron oxide (effective conductivity-Sigma Aldrich Company Ltd, United Kingdom, 50-100 nm) iron oxide (Liquids Research Company Ltd, United Kingdom, size - 10 nm), iron oxide

(Endomagnetics Ltd, United Kingdom, size – 60 nm) (III) acetylacetonate (Acros Organics, United Kingdom; average molecular weight: 353.17 g/mol), 1,2 – hexadecanediol (Sigma-Aldrich Company Ltd, United Kingdom; MW:258.44g/mol), oleylamine (Sigma-Aldrich Company Ltd, United Kingdom; MW:267.49g/mol,), oleic acid (Sigma -Aldrich Company Ltd, United Kingdom; MW: 282.46), hexane fraction from petroleum, (Sigma -Aldrich Company Ltd, United Kingdom; MW: 86.18), benzyl ether, (Acros Organics, United Kingdom; MW: 198.26 g/mol), ethanol (absolute) analytical reagent grade (Fisher Scientific Ltd, United Kingdom), poly (maleic anhydride-alt-1-octadecene), powder (Free-flowing), (Sigma -Aldrich Company Ltd, United Kingdom; MW: 30,000-50,000 g/mol), chloroform, (Sigma -Aldrich Company Ltd, United Kingdom; MW: 119.38 g/mol,), sodium hydroxide ≥ 97.0% (T) pellets, (Fluka Analytical Ltd, United Kingdom; MW: 40 g/mol), silicone solution for siliconizing glass and metal in isopropanol, (SERVA Electrophoresis GmbH, Germany).

2.1.4 Material used for TM (tissue mimicking) phantom

2-propanol (anhydrous, 99.5%, Sigma -Aldrich Company Ltd, United Kingdom), gelatin (from porcine skin, gel strength 300, type A, Sigma Aldrich company Ltd, United Kingdom), T(triton)X-100 (effective conductivity- Sigma Aldrich Company Ltd, United Kingdom), formalin (for molecular biology, 36.5-38% in H_2O, Sigma Aldrich Company Ltd, United Kingdom), safflower oil (Carthamus tinctorius, Fischer Scientific Ltd, United Kingdom), kerosene (Fischer Scientific Ltd, United Kingdom).

2.2 Methods

2.2.1 Morphological characterisation of nanoparticles

Morphological studies provide detailed surface data of nanoparticles. Topographical, morphological and compositional information regarding the surface of a sample is obtained from SEM and AFM. The information obtained from these microscopies may indicate the particle diameter and its shape in its normal physical state.

2.2.1.1 Atomic force microscopy (AFM)

Sample preparation;

Chapter 4 - For AFM analysis 1 mg/mL of SiO_2, ZnO and ZnO-PEG was prepared in water and 100 µl was pipetted on the glass microscopic slide which was dried using nitrogen gas.

Images were taken using the Bruker icon dimension atomic force microscope, with the standard tapping mode applied. The scanning area started at a large region of 10 x 10 µm and is decreased to a smaller region of interest (ROI) of 1.66 x 1.66 µm. The scan rate decreased from 0.99 to 0.70 Hz as the scan size decreased, to improve image quality. The software uses a PID feedback system to improve the trace and retrace signals. To improve the reliability of image acquisition, the scan angle of the probe is altered from 0° to 90° and the raster scan for the images is repeated. This is a confidence check to observe any artefacts produced because of particles/dust stuck onto the cantilever.

2.2.1.2 Scanning electron microscopy (SEM)

Sample preparation;

Chapter 3 - Prior to imaging, 2 mg/mL solution of the different CNT NP suspensions were prepared in water and 100 µl of each was pipetted on the glass microscopic slide.

Chapter 4 - Prior to imaging 2 mg/mL of SiO_2, ZnO and ZnO-PEG in water was prepared and 100 µl of each was pipetted on the glass microscopic slide.

Chapter 5 - Prior to imaging, 1 mg/mL solution of sienna$^+$, FF and SA were prepared and 100 µl of each was pipetted on the glass microscopic slide. For zinc ferrites; from 2 mg/mL of $[Fe_3O_4]$-PMAO, $[(Zn_{0.18}Fe_{0.82})Fe_2O_4]$-PMAO and, $[(Zn_{0.39}Fe_{0.61})Fe_2O_4]$-PMAO 100 µl of each was pipetted on the glass microscopic slide.

After the desired amount was pipetted onto a glass microscopic slide it was dried using nitrogen gas. The glass slide was coated with an electrically conducting layer of gold. Coating is crucial as it prevents charging of the specimen, which would otherwise occur due to accumulation of static electric field. SEM images were taken using a Hitachi scanning electron microscope with EDX elemental analysis (Oxford instruments) (model - S4000 FEG SEM with Oxford Instruments INCA EDX) which has a resolution of ~10 nm at 25 kV and 80 kX magnification.

2.2.2 Turbidity measurement using Ultraviolet-Visible Spectrophotometry (UV-Vis)

Sample preparation;

Chapter 4 - ZnO and ZnO-PEG NPs were suspended in aqueous solution at a concentration of 1mg/mL and serially diluted to 20 µg/mL.

Chapter 5 - Prior to imaging, 1 mg/mL solution of sienna$^+$, FF and SA were prepared which was serially diluted to 10 µg/mL. For zinc ferrites; 2 mg/mL of $[Fe_3O_4]$-PMAO, $[(Zn_{0.18}Fe_{0.82})Fe_2O_4]$-PMAO and, $[(Zn_{0.39}Fe_{0.61})Fe_2O_4]$-PMAO was serially diluted to 20 µg/mL.

After the desired concentration had been prepared for respective samples, the suspensions were sonicated for 60 min and vortex shaken at 10 min intervals and measurements of light transmission were taken at a wavelength (λ) of 415 nm. Samples were then transferred to a UV cuvette which was then placed vertically in the spectrophotometer.

Transmission measurements were taken by the S2000 UV/Vis Spectrophotometer. A spectrophotometer was used to measure the turbidity of our samples. A spectrophotometer measures the amount of light that can pass through a solution. It is apparent that less light would pass through a solution which is more turbid or is a coloured solution. This technique was used to measure the stability of the dispersion of NPs in water over a time of 4 hours, with a sample population of 6 elements.

2.2.3 Nanoparticle size measurement using Dynamic Light Scattering (DLS)

Dynamic light scattering is a technique which records the averaged intensity weighted particle diameter of the NPs in a suspension. As the dielectric measurements are performed in suspensions, it was crucial to understand the macroscopic and microscopic particle interactions when in solution compared to their physical state.

Sample preparation;

Chapter 4- ZnO and ZnO-PEG NPs were suspended in aqueous solution at a concentration of 1mg/mL and serially diluted to 20 μg/mL

Chapter 5 - Prior to imaging, 1 mg/mL solution of Sienna^{+}, FF and SA were prepared which was serially diluted to 10 μg/mL. For zinc ferrites; 2 mg/mL of $[Fe_3O_4]$-PMAO, $[(Zn_{0.18}Fe_{0.82})Fe_2O_4]$-PMAO and, $[(Zn_{0.39}Fe_{0.61})Fe_2O_4]$-PMAO was serially diluted to 20 μg/mL.

Measurements were carried out on six set of samples for each NP with a 2 min equilibration time, taken at 25 °C over a period of 4 h, with a sample population of 6 elements. DLS was carried out using the Malvern Zetasizer Nano S, which provides the Cumulants analysis; Z-average size (nm) and polydispersity index (dimensionless).

2.2.4 ZnO nanoparticle surface modification using PEG (polyethylene glycol)

750 mg of PEG (MW = 8000 Da) stirred into 100 mL of reverse osmosis (RO) purified water until it was completely dissolved. 606.9 mg (15 mg/mL) of zinc oxide powder was suspended into 40 mL of RO water and sonicated (f = 37 kHz, P = 160 W) vigorously for 1 h, and vortex shaken at 20 min intervals. The pH of the solution was adjusted to be 8.5 by adding 0.05 M sodium hydroxide (NaOH) followed by 30 min of stirring and a following 30 min of sonication. 10 mL of the PEG solution was added to the ZnO NPs suspension followed by a final 1h of sonication. The reaction mixture was stirred for 48 h at room temperature. The NPs were collected in a centrifuge and washed in water, followed by further washing procedure, to remove unabsorbed polymer. The powder was dried overnight [86].

2.2.5 Synthesis of ferrites by thermal decomposition

0.706 g of $Fe(acac)_3$ and 2.58 g of hexadecandiol were added to a 50mL three neck round bottom flask along with (2.11 mL) oleic acid, (2.82 mL) oleylamine and (20 mL) benzyl ether. The mixture was then stirred and heated to 200 °C for one hour and 300 °C for two hours under nitrogen. After the reaction was cooled to room temperature, the mixture was added to two 50 mL falcon tubes with 40 mL of ethanol. Falcon tubes were centrifuged for 30 min at 4000 g. Ethanol, i.e. the supernatant was discarded. The pellet left in the falcon tube was resuspended in 20 mL of hexane, and 50 μL of oleic acid and oleylamine were added. The solutions were combined into only one falcon tube. Tube was centrifuged for 10 min at 4000 g. Supernatant was kept and pellet was discarded. Then 20 ml of ethanol was added to the falcon tube and was centrifuged for 30 min at 4000 RPM. Supernatant was discarded, and the pellet was left to dry under vacuum overnight. Fe_3O_4 were synthesised as above, however the first step was modified for each composition, and instead of hexadecandiol, $FeCl_2$, $Fe(acac)_3$ and $ZnCl_2$ were added as seen in table 2-2.

Table 2-2: Different amount of $Fecl_2$, $Fe(acac)_3$, and $ZnCl_2$ required to prepare different zinc ferrite compositions

Zinc ferrite composition	Amount of materials		
	$FeCl_2$ (g)	$Fe(acac)_3$ (g)	$ZnCl_2$ (g)
Fe_3O_4 - PMAO	-	0.353	-
$[(Zn_{0.18}Fe_{0.82})\ Fe_2O_4]$- PMAO	0.06	0.353	0.01
$[(Zn_{0.39}Fe_{0.61})\ Fe_2O_4]$ - PMAO	0.04	0.353	0.03

2.2.6 Functionalisation of ferrites with PMAO

PMAO (45mg) was dissolved in 20mL of chloroform in a round bottom flask and left to stir vigorously for 1 minute. After a clear solution was obtained, 2 mg of SPIONs were added to the flask. The solution was then left to stir with a magnetic stirrer for 1 hr at room temperature in the sealed flask, until a translucent solution with a red-brown tint was produced. The flask was then placed in a rotary evaporator for 20 min (set to room temperature) to separate the chloroform. Chloroform (1mL) was then added to the flask to re-dissolve the SPIONs followed by 15 mL of 0.05 M NaOH in water. The flask was continually agitated whilst left on a hot plate set to 60 °C. After ten min, a further 10 mL of NaOH was added whilst still heating and agitating the flask. This was done until a clear black solution showing no evidence of a biphasic system was produced. The solution was poured into two centrifugal filter units and centrifuged for 15 min. The nanoparticles were removed from the filter with distilled water and pipetted in new glass vials.

2.2.7 Tissue-mimicking (TM) phantom preparation

Different materials and the amounts used have been highlighted in table 2-3. In a cylindrical glass beaker, mix in 2-propanol and double distilled water in the beaker while being stirred with a magnetic bead. Slowly pour in the gelatine powder; otherwise the gelatine will congeal in the beaker. Cover the beaker with foil and place on a heat block, increasing the temperature slowly to 100 °C, so the mixture doesn't burn. Heating the mixture to 95 °C is a minimum. In a separate beaker, pour in the oil at 1:1 ratio of kerosene and safflower oil. Heat this beaker on a heat block

to 65 °C. When the temperature of the gelatine solution has reached a minimum of 95 °C, remove the beaker from the block and let it cool to 60 °C. Keep stirring the beaker using the magnetic stirrer, while the viscosity of the mixture is low. Once the temperature of the gelatine solution has dropped to 60 °C, remove the oil mixture from the heat block (oil temp = 65 °C) and pour it into the gelatine solution, and set the stirrer to its highest value. The emulsion of the oil and water should start to form.

Once the temperature of this solution has dropped to 50 °C the viscosity will increase. Pour in the surfactant and the emulsion of oil and water should turn white (opaque). If the colour of the mixture isn't pure then add 1/10 of the required surfactant again, until the solution is completely white, and the oil droplets are less than 3 mm in size. Pour in the desired concentration of nanoparticles (2, 1, 0.5, 0.25 mg/ml) and stir vigorously until the aggregates aren't visible to the naked eye. During this phase, the nanoparticles don't aggregate. If aggregates occur, add a 1/10 of the required surfactant until dispersion is visible. When the temperature of the solution is at 40 °C, pour the mixture into moulds, and then pour in formaldehyde. Leave the phantoms in the fume hood to degas for a minimum of 24 hours. Fill the moulds with oil to stop the water inside the phantoms from evaporating. Cover the moulds with foil and place in a fridge to set.

Table 2-3: Different materials and their amounts required to prepare TM phantoms

Final volume of phantom prepared 200 ml	**Amount of materials**						
	2-Propanol (ml)	**Distilled water (ml)**	**Gelatine (g)**	**Kerosene (ml)**	**Safflower oil (ml)**	**TX-100 (ml)**	**Formalin**
	0.6	147.58	26.54	8.52	8.52	1.62	0.62

2.2.8 Sample preparation for dielectric characterisation

Colloidal dispersions were made in a final volume of 20 mL with 1 % (v/v %) pluronic-F127. Pluronic-F127 is a non-ionic triblock copolymer composed of a central hydrophobic chain of polyoxypropylene with two hydrophilic chains of polyoxyethylene. Pluronic is known to have high solubility in water. The surfactant was used to improve the dispersion of NPs in water. Samples were vortex shaken for 2 min and sonicated for 30 min at room temperature (20°C) to ensure a complete dispersion and a homogenous solution.

2.2.9 Characterisation of dielectric Properties

Dielectric characterisation was recorded using a commercial open-ended coaxial cable method [87]. The slim-form probe was calibrated using three known dielectric materials; air, short block (conductive elastomer that mimics electrical properties of metal), and RO water (20 °C). The minimum and maximum frequencies for the dielectric measurements was set to 1 and 4 GHz, respectively. This range was chosen as it is the relevant frequency range for microwave tomography studies [88]. Three different samples for each NP were prepared and ten set of measurements for each were taken at room temperature. The probe operates between 0.5–50 GHz and needs a minimum of 5 mm sample thickness for measurement. The ideal measurement requires the immersion of the probe into an isotropic medium.

The network analyser measures the reflection coefficient of the material under test (MUT), not its dielectric constant. The software, through a model, translates the reflection coefficient to complex dielectric constant values, which captures the permittivity and conductivity of the material via the frequency dependent equation;

$$\varepsilon_r^*(\omega) = \varepsilon'_r - j\varepsilon''_r = \varepsilon'_r - j\frac{\sigma}{\omega\varepsilon_0} \qquad \text{(Equation 1)}$$

Equation (1) refers to the frequency dependent complex dielectric constant $\varepsilon_r^*(\omega)$, which is equal to the real part (dielectric constant) ε', the imaginary part ε" (j=√-1), which in turn is related to the effective conductivity (σ) of the material at specific frequencies.

The plotted average change in chapters 3,4 and 5 is the difference between the mean of the respective data and the averaged control divided by the averaged control (Equation 2) where $\bar{x}$ is the mean.

$$\text{Average change} = \frac{\bar{x}_{Np} - \bar{x}_{control}}{\bar{x}_{control}} \times 100 \ (\%) \qquad \text{(Equation 2)}$$

2.2.10 Raman Spectroscopy

Small amount of the dry sample i.e. carbon nanotubes were added to the sample holder. Dry state Raman spectroscopy was carried out via an InVia Raman Spectrometer (Renishaw Plc, Wotton ender Edge, UK), using a x20 / 0.45 NA objective lens and a 1200 line per millimetre defraction grating. The illumination source was a 633 nm ion laser, which was used at 50% power and had a power at the sample of 2.4 mW.

2.2.11 Total reflection X-ray fluorescence spectroscopy (TXRF)

TXRF measurements were carried out with a Bruker S2 Picofox. This technique works as follows; a monochromatic X-ray beam impinges samples at a small angle and is totally reflected. An energy dispersive X-ray detector then measures the emitted characteristic fluorescence of the samples. Samples were prepared as follows: 1-2 mL of silicone solution was pipetted onto four numbered glass plates in petri dishes. These were then left to dry in a 60 °C oven for 80 min. Two dilutions were then prepared for three ferrites using a gallium standard (20mg/mL). For all SPIONs, a 50:50 and a 1:10 dilution was prepared, and the final volume prepared was between 1-2 mls.

3 Carbon nanotubes as contrast enhancing agents for MWI

3.1 Introduction

Carbon nanotubes (CNTs) are the members of the fullerene family, which were discovered by Kroto *et al.*, [89]. CNTs have attracted considerable attention in the field of nanoscience due to their unique structural, high conductivity, outstanding chemical stability and mechanical properties [90]. Carbon materials, such as carbon fibres, CNTs and silicon carbide fibres have been found to be good candidates for electromagnetic (EM) wave absorption due to their low density[91][92][93] [94] [95]. CNTs have become very important due to their excellent dielectric polarization properties and low density, which allows excellent EM wave absorption with a reduction in thickness and weight [96][97]. For example, carbon nanocoils exhibit superior microwave absorbing properties compared with larger carbon nanocoils. Carbon nanotubes are known to be electronic conductive materials and have been used to vary the dielectric properties of compositions [98]. The size and unique physiochemical properties of CNTs make them an ideal candidate for tumour targeting applications [99]. CNT based contrast agents have shown promise for molecular imaging by magnetic resonance, positron- emission tomography, nuclear, and photoacoustic imaging modalities [100]. Involvement of CNTs in the treatment of cancer has shown to improve the speed and efficacy of both detection and in therapy schemes.

Other, studies where CNTs have been used as potential contrast agents have been discussed in chapter 1. However, studies carried out previously have only explored one kind of CNT, which is the single-walled CNT (SWNT) in tissue-mimicking (TM) phantom, SWNTs functionalized with PL-PEG (phospholipid – poly ethylene glycol), and in the presence of 1% Pluronic. In this study, the aim is to explore the effect of several types of CNTs with different lengths and functionalization without the aid of surfactants. To explore their dielectric properties in water (high dielectric constant medium), 60% glycerol (low dielectric constant medium) and in TM phantoms. The effects of different concentrations of SWNTs has on the dielectric properties of water is also

discussed. We believe that dispersion properties and concentrations of a material will influence the dielectric properties of a medium.

3.1.1 Short history of CNT

Iijma first synthesized multi-walled carbon nanotubes (MWNTs) in 1991 using simple arc-evaporation method [101]. But, CNTs were discovered long before that, in 1952[102]. Radushkevich and Lukyanovich, discovered 'worm-like' carbon formations. These were discovered during their study of the soot formation by the decomposition of carbon monoxide on iron particles at 600ºC [103]. Based on characterization techniques, it was concluded that the formed product consisted of needle-like carbon crystal with diameters of about 50 nm. In 1976, Oberlin, Endo, and Koyama showed hollow carbon fibres with a nanometre-scale diameter using a vapor growth method[104]. In 1979, John Abrahmson described carbon nanotubes as carbon fibers which were produced as carbon anodes during arc-discharge [105]. In 2006, an editorial was written by Marc Monthioux and Vladimir Kuznestov where they described the origin of the carbon nanotube [106].

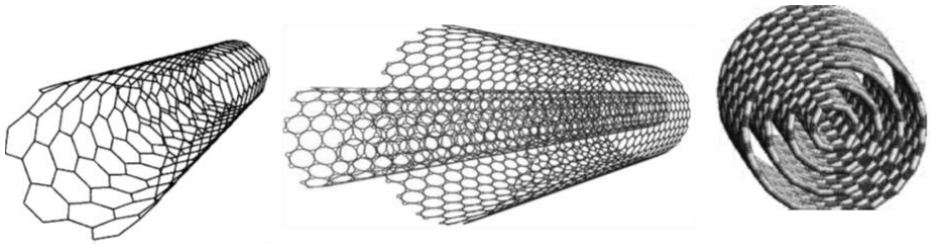

Figure 3-1: (a) Single-walled CNT, (b) double-walled carbon nanotubes (DWNT). These nanotubes are made of two concentric carbon nanotubes in which the outer tube encloses the inner tube, and (c) multi- walled CNT. Figure adapted from [109]

Carbon is the chemical element with the atomic number six and has six electrons which occupy $1s^2$, $2s^2$, and $2p^2$ orbitals. CNTs are curved graphene sheets and graphene sheets are seamless cylindrical derived from a honeycomb lattice, representing a single atomic layer of crystalline graphite. They are nanometre in diameter and can be as large as several millimetres in length. In graphene, carbon atoms are densely organized in a regular sp^2 bonded atomic scale pattern, and this pattern is the basic structure for fullerenes and CNTs. The binding in carbon nanotubes is sp^2,

where each atom is joined with three other neighbours, like that in graphite. Under high pressure, nanotubes can merge together, interchanging some sp^2 to sp^3 bonds. The sp^3 bonds give the possibility of producing strong length wires through nanotube linking. Depending on how the graphene sheets are rolled, the chirality of CNTs can be determined. Different types of chiralities are; zig-zag, armchair and chiral. CNTs are characterized by two integer numbers (n, m), which describes the chiral vector between two equivalent points on a graphene sheet. Two important chiralities are armchair (n, n), where C-C bonds are perpendicular to the tube axis, and zigzag (n, 0) where C-C bonds are parallel to the tube axis. A nanotube with any other chirality (n, m) is called the chiral tube.

Intrinsic geometry of CNTs greatly influences their properties, particularly the electrical conductivity [107]. Depending upon their different structures, CNTs can exhibit metallic or semiconducting properties, which is related to their band structure. The band structure tells us the relationship between the valence band, the highest filled energy band, the conduction band and, the lowest unfilled available energy band. When electrons move into the conduction band, they are mobile and generally responsible for the conduction of a material. For example, in metals, the valence band overlaps the conduction band and electrons are readily available for conduction, making metals conductive. Conversely, for an insulator the band gap is large, hence it has low electrical conductivity. The armchair CNTs are always metallic as there are no band gaps in between. The conduction and valence band in an armchair CNTs tend to overlap since the Fermi level is in the conduction band, this gives armchair CNTs conductive properties. Zigzag nanotubes are either metallic or semiconducting in nature. Generally, a natural mix of a CNT will have 1/3 metallic and 2/3 semiconducting properties [107].

CNTs can be divided into three types based on the number of tubes present. Figure 3-1 (a) shows single-walled carbon nanotubes (SWNT). SWNTs are made of a single graphene sheet rolled upon itself with a diameter of 1-2nm. Length can vary depending on the preparation method used[108].

Figure 3-1 (c), shows multi-walled carbon nanotubes (MWNT). MWNTs consist of multiple layers of graphene rolled upon itself with diameters ranging from 2 to 50 nm depending on the number of graphene tubes[109]. The inner diameter of MWNTs ranges from 0.4 nm up to a few nanometres and the outer ranges from 2 nm to 30 nm. MWNTs can be formed in two structural models: Russian doll model and Parchment model. When a carbon nanotube contains another nanotube inside it and the outer nanotube has a greater diameter than thinner nanotube, it is called the Russian doll model. On the other hand, when a single graphene sheet is wrapped around itself continuously, it is called the Parchment model [110].

3.1.2 Method of CNT synthesis

CNTs can be prepared by various methods, such as the arc discharge method, chemical vapor deposition, and laser ablation, chemical vapor deposition, and the vapor phase growth method. In the arc discharge method, carbon is vaporized into plasma at high temperatures (≥ 3000ºC) generated by arcing of a DC current[111]. A voltage of 20−25V is applied to graphite rod electrodes that are separated by ~ 1 mm, typical arc current is ~ 100A. The chamber is kept at high sub-atmospheric pressure (~ 100−500 Torr) with He gas flow for cooling. The carbon vaporizes at the anode and deposits onto the cathode where CNTs form. This is the most efficient method for producing large quantities of SWCNTs by weight, with a yield of ~ 30% by weight [101].

In the laser ablation method, a target consisting of graphitic carbon and some transitional metal such as Co or Ni is vaporized using a laser pulse at high temperatures (1200ºC) inside a tube furnace. The vapor is then flushed, using inert Ar, towards the end of the tube which houses a water-cooled copper collector tip where CNTs are formed as the vapor condenses. It has been shown that this method mostly produces ropes (bundles) of long (~ 100μm) SWNTs with a narrow diameter distribution and has a relatively high conversion ratio of 70% − 90% by weight.

By varying the growth temperature, the catalyst composition, and other parameters the CNT diameter distribution can be varied [112][113].

In 1996, a chemical vapor deposition (CVD) method was discovered for nanotube synthesis. During this process, a mixture of hydrocarbon gases, acetylene, methane or ethylene, and nitrogen gas were introduced in the reaction chamber. During this reaction, nanotubes are formed on the substrate by the decomposition of the hydrocarbon. This technique has two major benefits, nanotubes can be obtained at much lower temperatures and the catalyst can be deposited over the substrate, which will allow the CNTs to adopt a well-organised structure [114][115].

A vapor-phase growth method is a modified form of CVD. Inside a reaction chamber, two furnaces are placed inside a reaction chamber. The catalyst used in this process is called ferrocene. Vaporization of catalytic carbon is maintained at a relatively low temperature in the first furnace. Catalytic particles are formed here and when they reach the second furnace, the decomposed carbons are absorbed in this catalyst by diffusion where they are converted into CNTs.

The flame synthesis method is another method of producing CNTs. In this method, hydrocarbon flames are used. Gases used in this method are CO, CH_4, C_2H_2, C_2H_4 and they are a rich source of carbon. The reaction is exothermic and chemical energy released in the form of heat in the flame sites for the deposition of solid black carbon. The various method of preparation may yield CNTs with structural characteristics that might influence their electrical and conductive properties. In the next section, the electrical and conductive properties have been discussed.

3.1.3 Electrical and conductive properties of CNTs

In this project CNT have been selected because of their extremely high conductivity properties, supported by literature and their potential to interact with MW.

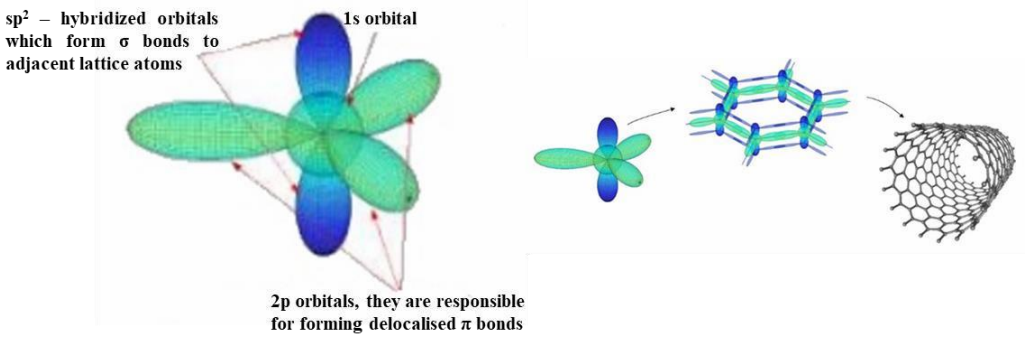

Figure 3-2: Schematic representation of a hybridized carbon atom forming a graphene layer followed by CNTs

Researchers have demonstrated that CNTs exhibit unique conductive properties. Geometric differences such as defects, chirality, different diameters and the degree of crystallinity of the tubular structure greatly influence the electronic properties [115][116]. Considering the bonding of the carbon atoms in CNTs arranged in a hexagonal lattice, where each carbon atom is covalently bonded to three neighbour carbons via sp^2 molecular orbitals. Thus, the fourth valence electron remains free in each unit, and these free electrons are delocalised over all atoms and contributes to the electrical nature of CNTs. Due to which, CNTs can be conducting or semi-conducting [117][118]. CNTs due to their electronic nature are used in transistors, as an emitter, sensors, and for X-ray generation.

Individual CNTs can be considered as electrically conducting wire. They are long but extremely narrow conductors with diameters in the range of several atomic distances and are hollow. Like quantum wires, CNTs show ballistic electron transport i.e. negligible electrical resistivity without any scattering [119][120]. Electrons in CNTs can travel over micrometre range distances without experiencing scattering at room temperature. Ballistic conduction allows substantial current flow with minimal heat generation, which allows the nanotubes to carry enormous amounts of current. Caron nanotubes can carry the highest current density, with conductivities measured as high as

109 A/cm^2, whereas copper has a current density of about 107 A/cm^2, so nanotubes can carry current densities about 100 times that of traditional metal conductors [121]. Advantage of ballistic conduction is that the charge carriers can move rapidly through nanotubes under the influence of an electric field[122].

Electronic transport properties of CNTs may be changed by disorders such as structural defects formed during synthesis processes or physical distortions, evoked by mechanical forces. Point defects such as vacancies, improper location of carbon atoms e.g. deformed structures, rearrangement of atoms in a new form, such as the Stone-Wales defect and the presence of doped foreign atoms are some of the defects involved with the structure of carbon nanotubes[123] [124][125][126].

These defects can be categorized into two main groups; i.e. topological defects occurring in the structure of the CNTs, compared with the ideal arrangement of atoms, as well as defects that arise due to the doping of foreign atoms to the structure of CNTs. These defects may have undesirable influence on the properties of CNTs, such as decrease of mechanical strength of the structure, or lowered electrical conductivity.

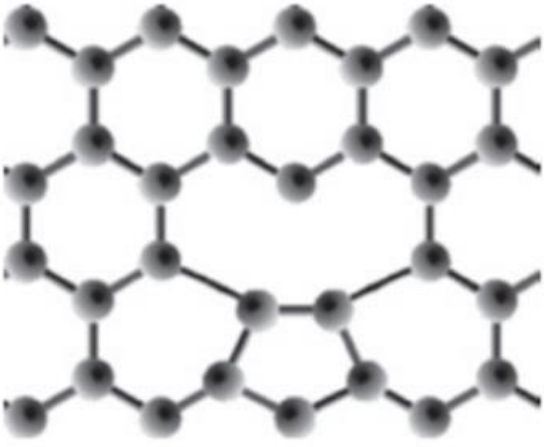

Figure 3-3: Schematic representation of reconstructed monovacancy 5-membered pentagonal ring [107].

A vacancy defect is a point defect that occurs naturally in the hexagonal lattice of CNTs, in which one or several atoms are missing from the structure. Vacancies, as shown in figure 3-3, may be formed during the solidification process, because of the vibration of atoms, or by heavy ion bombarding and irradiation of high energy beams [127]. Once the atom gets knocked out its lattice site, the dangling bonds in the vacant sites would rehybridize to create some new bonds. The three free bonds can bridge to form a strained 5- membered pentagonal ring (Fig. 3-3). Vacancies in CNT even after rehybridization are energetically unfavourable, hence in many cases, they can split into pentagon-heptagon defects as shown in Figure 3-4. This type of defect is also known as the Stones-wales defect.

The Stones-wales defect consists of four adjacent hexagons convert into two pairs of pentagon-heptagon configuration. As mentioned above, this defect is also known as the pentagon-heptagon defect, which occurs naturally after the initial formation of vacancies.

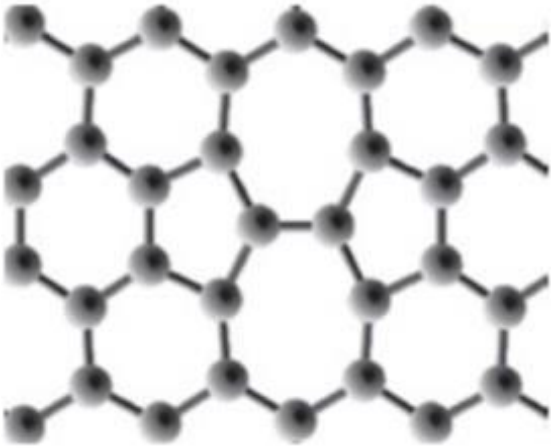

Figure 3-4: Schematic representation of Stones-wales defect. Figure adapted from [107]

This defect is created by rotation of C-C bonds by 90º, which results in two pentagons connected by a pair of the heptagon. This type of effect is expected to influence the electrical, optical, thermal and mechanical properties on CNTs [128].

Also, doping of foreign atoms can influence the electrical, mechanical and chemical properties of CNTs. During the functionalization reaction, many defects are created on the CNT sidewalls.

Carbon hybridization changes from sp^2 to sp^3. These effects result in damaging effects on the mechanical properties of CNTs. The π electron system gets disrupted, this is detrimental for the transport properties of CNTs because defect sites scatter electrons and phonons which are responsible for the electrical and thermal conductions of CNTs [129]. Due to the conductive nature of CNTs they have been previously tested for MWI purposes, hence it is viable to test them further for their use in MWI applications. Dielectric properties of CNTs in different mediums was tested.

3.1.4 Functionalisation of CNTs

For biomedical applications, the lack of solubility of carbon nanotubes in aqueous media has been a major technical barrier [130]. To overcome this problem, the modification of the surface of CNTs, such as functionalization is required without hampering its desired physical properties. The overall objective of functionalization is to is to increase their solubility or dispersion in biocompatible media. Functionalization is carried out by either adsorption, electrostatic interaction or covalent bonding of different molecules. Through this modification, the water solubility of CNTs can be improved and this could lead to better biocompatibility. Different methods are used to improve the dispersive properties of CNTs, such as non- covalent functionalization and covalent functionalization[131].

The end caps of nanotubes are composed of highly curved fullerene-like hemispheres which are highly reactive as compared with the side walls. Sidewalls themselves contain defects as mentioned above. Chemical functionalization is based on the covalent bond of functional groups onto carbon form of CNTs. It is generally performed at the end caps of nanotubes. Direct covalent sidewall functionalization is associated with a change of hybridization from sp^2 to sp^3 and a simultaneous loss of the p-conjugation system. Desired groups such as carboxylic, p-aminobenzoic acid, fluorine, are attached to the surface or at the ends of CNTs [132][133][134][135]. These functional groups are rich in chemistry and the CNTs can be used as precursors for further chemical

reactions. The advantage of chemical functionalization is that it can be attached covalently with polymeric materials and dispersed well in different solvents. The disadvantage of covalent functionalization is that the chemical modifications can cause defects within the CNTs. Functionalisation of CNTs has been shown to enhance the electrical properties of MWNTs [136]. The non-covalent functionalization is based on Van der Waal's forces. This type of interaction does not destroy the conjugated system of the CNTs sidewalls, and therefore it does not affect the final structural properties of CNTs. Some common examples of this type of functionalization are by the use of surfactants such as polyethylene glycol, sodium dodecyl sulfate, and, dodecyl-benzene sodium sulfonate is commonly used to reduce the aggregative tendency of CNTs [137].

3.1.5 Bio fate of CNTs and biomedical applications

The pharmacokinetics and biodistribution of CNTs rely to a considerable extent on their physiochemical characteristics such as size, shape, aggregation, chemical composition, surface functionalization and solubility [138][139]. SWNTs and MWNTs have already proven their potential to serve as effective alternatives to imaging and in drug delivery methods. They can pass through membranes, carrying therapeutic drugs, vaccines and nucleic acids deep into the cells [140]. Overall, CNTs have shown a very promising future in medicine. In a study carried out by Ou *et al.*, they functionalized SWNTs with phospholipids bearing PEG and with integrin αvβ3 to modulate the targeting system. Their results showed a successful entry of CNTs in the U87MG cells by integrin-mediated endocytosis and there was enough accumulation of CNTs for imaging and drug delivery purposes [141]. In a study by Gidcumb *et al.*, CNTs were used for the improvement of X-ray imaging. It was shown that utilizing the CNT array field emission x-ray source, could increase the spatial resolution and reduce the imaging time. In another study targeting properties of MWNTs were improved with functionalization by glucose amine. Covalent and non-covalent functionalization were performed. The potential was assessed both in vitro and

in vivo. The results indicated higher blood circulation time, late urinary clearance and higher accumulation in cancer cells by the non-covalently functionalized CNTs [142].

CNTs represent the most unique inventions in the field of nanotechnology. CNTs are electrically conductive in nature, hence we decided to explore their effect on the dielectric properties of the medium. The aim of this chapter is to understand the behaviour of several types of CNTs on the dielectric properties of different mediums for their potential use as contrast agents for MW imaging and sensing[143].

3.2 Study objectives

The aim of this chapter is to explore the dielectric properties of different CNTs in a high and low dielectric constant medium and in tissue-mimicking (TM) phantom. The high dielectric constant medium used was water; low dielectric constant medium was 60% glycerol and the TM phantom used can mimic tumour properties. Since previous findings have suggested that CNTs have the potential of enhancing the dielectric properties, we decided to study hydroxylated and non-hydroxylated CNTs with different lengths and diameters for their potential use as contrast agents. Described in this chapter is the structural characterization of CNTs via SEM and Raman spectroscopy. Dielectric characterization of CNTs has been carried out in water (high-dielectric constant medium), 60% glycerol (low – dielectric constant medium) and, tissue-mimicking (TM) phantom at a concentration of 2 mg/mL from 1-4 GHz.

3.2.1 Aims of the study

- To characterize the size and the structure of single-walled CNT (SWNT), hydroxylated single-walled CNT (SWNT-OH), multi-walled CNT (MWNT), hydroxylated multi-walled (MWNT-OH), short-single walled CNT (sSWNT), hydroxylated short-single walled CNT (sSWNT-OH) via scanning electron microscopy (SEM).

- To assess the electronic properties and sample imperfections (defects) of CNTs via Raman spectroscopy.
- To carry out the dielectric characterization of all the CNTs at a concentration of 2 mg/mL in RO water, 60% glycerol and tissue-mimicking phantom from 1-4 GHz using the coaxial-probe method.
- To study the effect of different concentrations: 2, 1, 0.5 and 0.25 mg/mL of SWNT on the dielectric properties of the medium.

3.3 Results

3.3.1 CNTs morphology and analysis

3.3.1.1 Nanoparticle characterisation using SEM

To understand how length, diameter, and functionalization of CNTs affect the dielectric properties of a medium, varied CNTs were studied. SWNTs have been previously studied for MWI purposes , however, different structures of CNTs had never been explored before[74]. Therefore, six different types of CNTs have been studied in this thesis. The morphology of CNTs was characterized using the SEM (Fig. 3-5). Samples were prepared at a concentration of 2 mg/mL for measurements and 100μL was pipetted on a glass microscopic slide which was dried using nitrogen gas. The glass slide was coated with an electrically conducting layer of gold and then SEM images were taken.

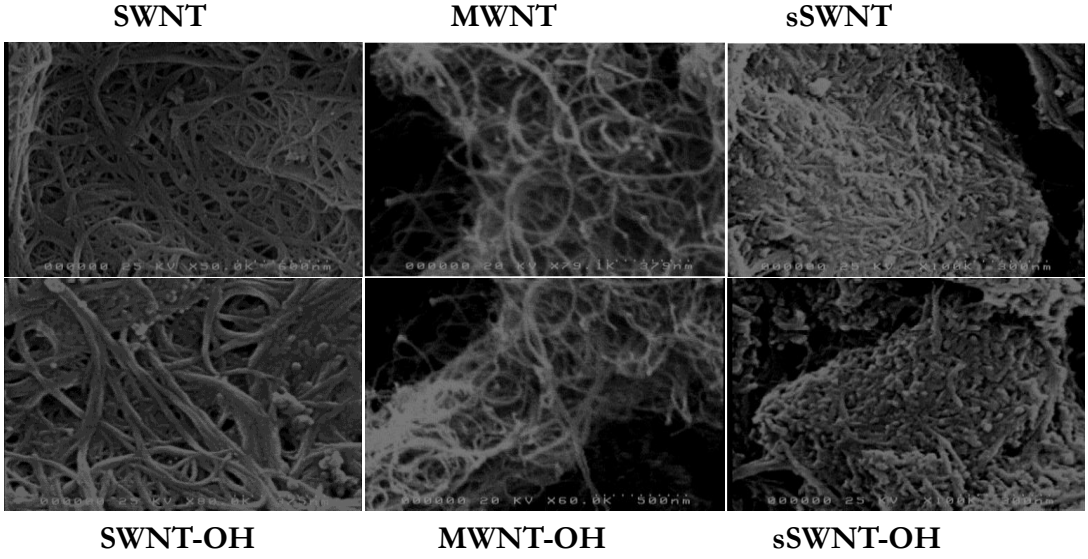

Figure 3-5: The morphology is observed from SEM. SEM images of SWNT (top left with a scale of 600nm), MWNT (top middle) and sSWNT (top right), SWNT-OH (bottom left with a scale of 375nm), MWNT-OH (bottom middle), and sSWNT-OH. Images were taken at room temperature. SEM images were taken in a vacuum by Hitachi scanning electron microscope (S4000 FEG SEM with Oxford Instruments INCA EDX).

Results suggested that all nanomaterials have a tube/rod-like structure in nature. The short nanotubes were confirmed, and aggregation of nanotubes was clearly seen at this concentration. In this experiment, no surfactant was used before preparing the dispersions for microscopy.

Analysis of SEM micrographs confirmed the average diameter tube size of 3.6nm, 3.4 nm, 27.5 nm, 21 nm, 1.7 nm and 1.2 nm for SWNT-OH, SWNT, MWNT-OH, MWNT, sSWNT-OH, and sSWNT respectively. The diameters obtained clearly show the difference between SWNT, MWNT, and sSWNT. It was difficult to measure the length of CNTs because they were aggregated, however, the diameter of the CNTs obtained agreed with what was stated by the manufacturer.

3.3.1.2 Characterization of CNTs by Raman spectroscopy

Figure 3-6. shows the Raman spectra of all different CNTs. The Raman spectra of CNTs, shows two individuals characteristics peaks.

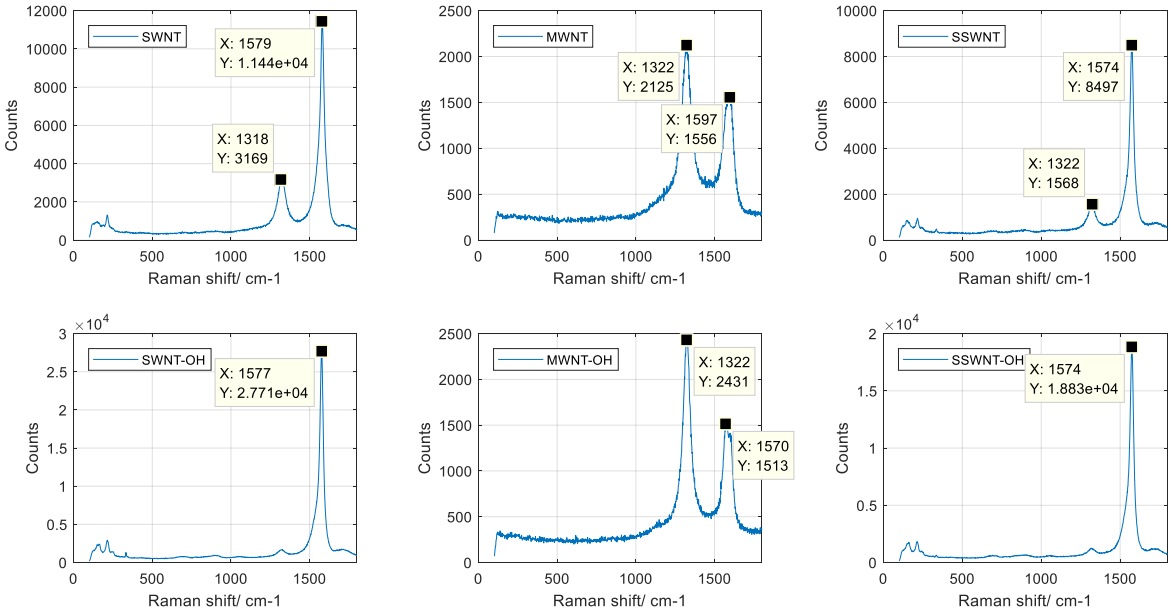

Figure 3-6: Raman spectra of SWNT-OH (top left), MWNT-OH (top middle), sSWNT-OH (top right), SWNT (bottom left), MWNT (bottom middle) and sSWNT-OH (bottom right).

One at the Raman shift of 1318cm^{-1}, 1324cm^{-1}, 1322cm^{-1}, 1322 cm^{-1}, 1322 cm^{-1} and 1322cm^{-1} for SWNT, SWNT-OH, MWNT, MWNT-OH, sSWNT-OH, sSWNT respectively. This shift is named as the D-band which is assigned to the disordered graphitic structure of CNTs [144]. The Raman shift at 1579 cm^{-1}, 1597 cm^{-1}, 1568 cm^{-1}, 1577cm^{-1}, 1570 cm^{-1} and 1574 cm^{-1} for SWNT, SWNT-OH, MWNT, MWNT-OH, sSWNT-OH, and sSWNT respectively is named as the G-band, which is assigned to the C-C bonds in the graphitic plane. The ID/IG ratio of SWNT,

SWNT-OH, MWNT, MWNT-OH, sSWNT-OH, sSWNT is 0.06, 0.3, 0.64, 0.75, 0.07 and 0.18 respectively. The lower the ID/IG ratio, the lower the defect concentration. ID/IG ratio, Functionalisation of CNTs have higher ID/IG ratio, suggesting that functionalisation has caused some level of defects within the structure [145]. The ID/IG ratio is defined as the intensity of defect and sp^2 clusters. These defects are likely to affect electron transfer and conductivity. On the other hand, functionalisation helps the dispersion in aqueous media. Good dispersion is a key requirement for accurate measurements of nanomaterials' dielectric properties.

3.4 Dielectric properties of CNT suspension at MW frequencies

3.4.1 Dielectric properties of CNT suspensions in RO water

CNTs were dispersed in water at 2 mg/mL. The dispersions were sonicated before measurement of their dielectric constant and conductivity at room temperature using our coaxial probe set up.

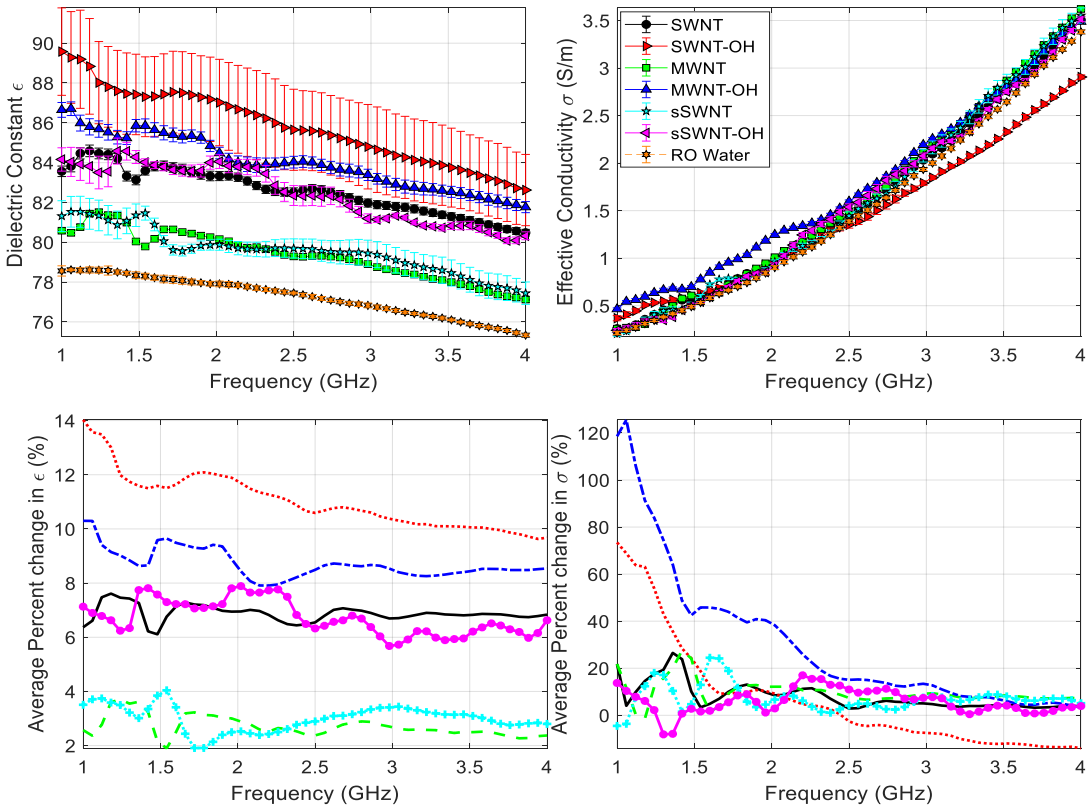

Figure 3-7: (a) dielectric constant, (b) effective conductivity (c) average change in epsilon, and (d) average change in sigma of different CNTs in water characterised between 1-4 GHz at a concentration of 2mg/mL in RO water. Each curve represents the average of three different samples (n=3+/-SD).

Figure 3-7 shows the measured dielectric properties of different types (length and functionalised CNTs) of carbon nanotubes at a concentration of 2 mg/mL dispersed in RO water over the frequency range of 1-4 GHz. The dielectric constant shows a dependency on the different CNT studied and it decreases as the frequency increases. Dielectric constant of SWNT-OH at 2 mg/mL (1 GHz) is 89.58 ± 2.19 with 14.04 % change to water compared with the dielectric constant of sSWNT, which has shown the lowest average change of dielectric constant of 3.54 % at a frequency of 1.78 GHz.

Table 3-1: Table showing the dielectric properties of SWNT in water at different concentrations between at 1, 2, 3 and, 4 GHz.

SWNT						
Frequency (GHz)	**2mg/mL**		**1mg/mL**		**0.5mg/mL**	
	Dielectric constant	**Effective conductivity**	**Dielectric constant**	**Effective conductivity**	**Dielectric constant**	**Effective conductivity**
1	84.16±0.58	0.26±0.001	83.48±0.42	0.22±0.003	82.74±0.42	0.21±0.01
2	83.32±0.23	0.97±0.016	81.42±0.36	0.90±0.04	80.79±0.23	0.78±0.11
3	81.97±0.20	2.09±0.02	79.46±0.11	1.98±0.012	77.64±0.45	1.91±0.03
4	80.48±0.17	3.51±0.01	78.21±0.12	3.01±0.19	76.11±0.18	2.98±0.12

The maximum average change in dielectric constant for other CNTs at 2 mg/mL is, 10.6%. (1GHz), 7.12% (1GHz), 7.61% (1.18GHz) and, 4.04% (1.54GHz) in MWNT-OH, sSWNT OH, SWNT and sSWNT respectively. Variability observed with SWNT-OH is possibly due to aggregation of the NPs in RO water, which led to sedimentation of the nanotubes. This was also observed visually.

Since SWNTs have been previously explored, it was important to examine the effect of different concentration of SWNTs on the dielectric properties of a medium. Three different concentrations

of SWNTs were prepared in water and dielectric properties were measured. Results tabulated in table 3-1, suggest that dielectric constant shows a dependency on the NP concentration.

Dielectric constant at 2 mg/mL at 1 GHz is 84.16±0.58 compared with 82.74±0.42 in similar conditions for 0.5 mg/mL. These results suggest that higher the concentration, higher are the dielectric properties.

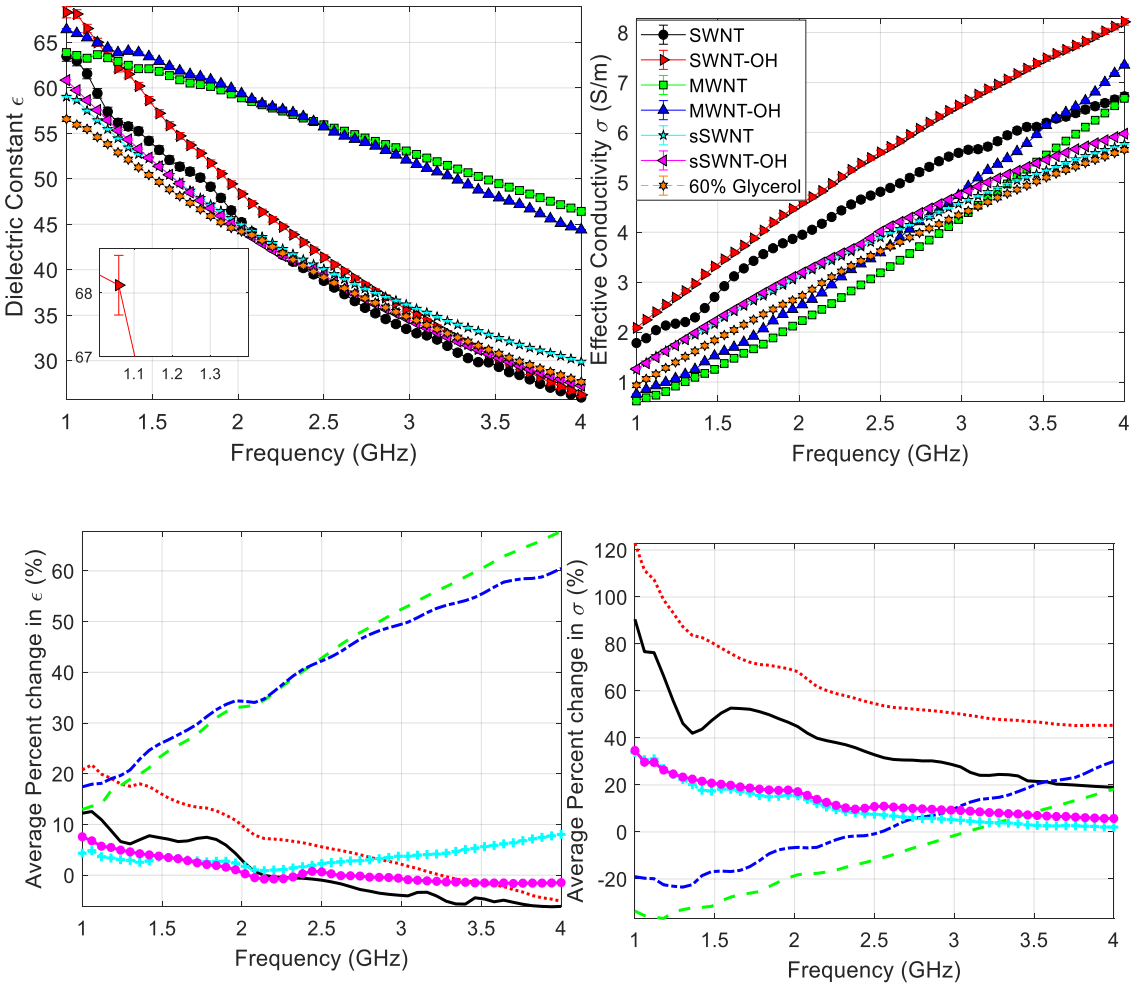

Figure 3-8: (a) dielectric constant, (b) effective conductivity (c) average change in epsilon, and (d) average change in sigma of different CNTs at a concentration of 2 mg/mL in 60% glycerol and RO water characterised between 1-4 GHz. Each curve represents the average of three different samples (n=3+/-SD).

Figure 3-8 displays the dielectric properties of different CNTs in 60% v/v glycerol in water mixture. Overall the dielectric properties are much higher than that of several types CNTs in water. The maximum average change in dielectric constant value for SWNT, SWNT-OH, MWNT, MWNT-OH, sSWNT and sSWNT-OH is 12.93% (1 GHz), 21.75% (1.06 GHz), 67.79% (4 GHz), 60.47% (4 GHz), 8.04% (4 GHz) and 7.57% (1 GHz) across the whole frequency range. MWNT-OH and MWNT shows the largest increase amongst all the other CNTs.

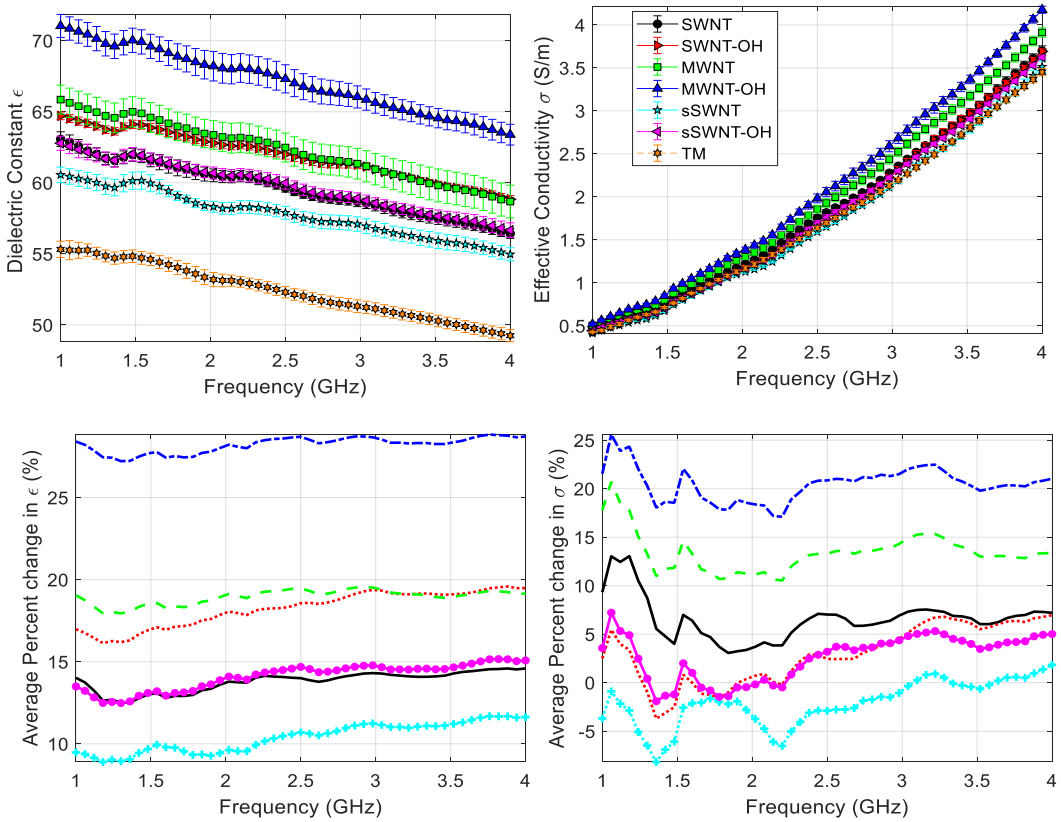

Figure 3-9: (a) dielectric constant, (b) effective conductivity (c) average change in epsilon, and (d) average change in sigma of different CNTs at a concentration of 2 mg/mL in TM phantom characterised between 1-4 GHz. Each curve represents the average of three different samples (n=3+/-SD).

It is important to mention, that the strange behaviour which is observed with the inclusion of the NPs in 60% glycerol could be because glycerol has glass forming properties[146]. 60% glycerol water mixtures have a larger H-bond network, which are disturbed by the inclusion of NPs. As seen in Fig. 3-8, with MWNT and MWNT-OH a different behaviour is observed compared with other nanomaterials. This can be attributed to the fact, that specific inclusion of these

nanomaterials disturbs the large intact H-bond network, which is more profound in MWNT and MWNT-OH.

Figure 3-9 displays the dielectric properties of different carbon nanotubes in tissue mimicking (TM) phantom. TM phantom containing 2 mg/mL of MWNT-OH showed the highest dielectric constant, whereas, sSWNT-OH dispersions were found to have the lowest compared with all other carbon nanotubes. However, the dielectric constant of all the carbon nanotubes is higher when compared with the control (i.e. tissue mimicking phantom). The dielectric constant of MWNT-OH, MWNT, SWNT-OH, SWNT, sSWNT, sSWNT-OH, is 70.95(±0.82). 66.04(±1.13), 64.64(±0.33), 63.01(±0.52), 62.85(±0.51) and 60.63(±0.56) respectively at 1GHz compared to 55.32 (±0.57) of tissue mimicking phantom at similar frequency. MWNT-OH shows the maximum average change of 28.26% and sSWNT shows the lowest average change of 9.61% at 1GHz.

3.5 Discussion

Pristine CNTs are conductive, therefore several types of CNTs were studied to explore their effect on the dielectric properties of different mediums. CNTs have been extensively studied previously due to their distinctive dielectric properties. Mashal *et al.* reported the effect of SWNTs in TM phantom where they reported that higher the concentration of SWNT, resulted in higher dielectric properties i.e. the dielectric constant at a concentration of 2 mg/mL (3 GHz) was 63.7 compared 73.0 at 3mg/mL (3 GHz) [74]. Similarly, Lie *et al.* measured the dielectric properties of PL-PEG (phospholipid-PEG) functionalised SWNTs at a concentration of 2mg/mL. Results showed a 10% increase in the dielectric constant and 90% increase in the conductivity compared with just PL-PEG in water. These studies and the conductive nature of CNTs motivated me to study the effect of CNTs on the dielectric properties of different mediums for MW imaging and sensing purposes. Dielectric properties of several types of CNTs were explored in three different mediums; water (medium with a high dielectric constant), 60% Glycerol (medium with a low dielectric constant)

and TM phantom (phantom prepared to mimic the properties of a tumour consisting of oil and gelatin) between a frequency range of 1-4GHz. This frequency range was selected as it is the relevant frequency range for microwave tomography studies.

3.5.1 CNT morphology analysis

As CNTs may come from commercial sources it was of high importance to characterise them before dispersing them in different mediums. Satisfactory agreement was observed between the sizes and shape of CNTs obtained via SEM and manufacturers stated size. Raman spectroscopy of SWNTs can provide us with information about the properties of carbon materials such as their phonon structure, their electronic structure and sample imperfections i.e. defects. The ID/IG ratio obtained for -OH functionalized CNTs compared with non-hydroxylated CNTs is much higher. This increase is because the functionalisation of CNTs destroyed their graphitic structure, i.e. leading to defects hence an increase in ID/IG ratio is observed. The results show a clear difference between hydroxylated and non-hydroxylated CNTs.

3.5.2 Dielectric analysis

Dielectric properties of different CNTs were measured to assess the contrast enhancing properties in high, low dielectric constant medium and in TM phantoms (phantoms with tumour mimicking

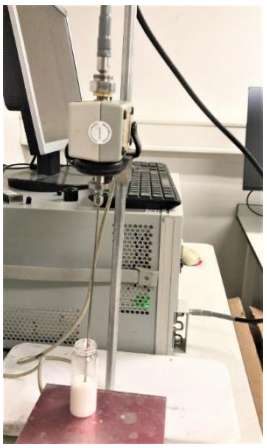

Figure 3-10: Schematic representation of coaxial probe inserted inside our in-house made TM phantom for dielectric measurements.

properties). It is important to mention that desired contrast should be visible in the real part of the dielectric constant compared with the imaginary part.

Increase in the conductivity would increase the dielectric loss, hence being unreliable for imaging purposes. Increase in dielectric loss would lead to excessive heating of a tissue due to the amount of power absorbed. Hence, the contrast should be visible in the real part of dielectric constant. From the dielectric analysis results obtained, it can be concluded that CNTs were better dispersed in 60% glycerol medium and in TM phantom (Fig. 3-8 & 3-9), compared to in RO water.

A TM phantom (Fig. 3-9) is a semi-solid phantom for microwave radar imaging have been produced using rubber matrix and varying concentrations of carbon black to increase the electrical properties[147] . These phantoms are mechanically strong and electrically stable over time but present several challenges[147][148]. First, the error between high water content dielectric tissues and their phantoms' dielectric constant is more significant than that of low water content tissue and its respective phantoms. Therefore, oil-in-gelatine phantoms were produced. They had been previously suggested by Lazebnik *et al.*, [149]. The advantages of these phantoms are that they mimic electrical properties of varying biological tissue at wideband frequency range between 0.5 GHz – 20 GHz and it is simple to alter the dielectric properties, which remain constant over a prolonged period (3 months). NPs will remain dispersed better in TM phantoms compared to water solutions. It is important to consider the effect of length of CNTs, different concentrations and the effect functionalization has on the dielectric properties in different mediums.

3.5.3 Effect of length on CNTs on the dielectric properties of mediums

In the above experiments we considered that all CNTs remain in dispersion while they are assessed for their electrical properties. To understand the effect aspect ratio of CNTs has on the dielectric properties, it is useful to describe the CNT bonding structure in terms of the electronic structure of graphene. The electronic structure within graphene can be described using hybridisation theory.

Of the four valence orbitals of the carbon atom (*2s*, *2px*, *2py* and *2pz* with the z-axis perpendicular to the atomic-plane), the *s*, *px* and *py* orbitals are combined into a planar sp^2 hybridisation scheme. These sp^2 orbitals are symmetric with respect to the planar symmetry and hybridise with equivalent orbitals on adjacent carbon atoms producing strong, covalent $\sigma/\sigma*$ bonds that are responsible for most of the binding energy and elastic properties of the graphene sheet. The remaining *pz* orbitals are out-of-plane and, for a flat graphene lattice, cannot couple with the $\sigma/\sigma*$ bonds due to symmetry. Interactions between neighbouring *pz* orbitals, however, are strong creating delocalised $\pi/\pi*$ orbitals which exist in the planes above and below the atomic sheet. The energy of the $\sigma/\sigma*$ bonds lie far from the fermi energy (fermi energy is the kinetic energy of the highest occupied state), and therefore contribute little towards conduction. The Fermi energy is located within the $\pi/\pi*$ bands making them the dominant contributor to conduction within the material [63]. The conduction band is the band of orbitals that electrons can jump into from the valence band (the outermost electron orbital of an atom that electrons occupy) when excited. When electrons are in the conduction band, they have enough energy to move freely in the material. This movement is responsible for creating an electric current.

It should be considered that electrons in graphene have a longer mean free path. Mean free path is the average length that an electron can travel freely before a potential collision [150]. It can be said that electrons in graphene act like photons in their mobility due to their lack of mass. These electrons can travel a distance without getting scattered, a phenomenon known as ballistic conduction. MWNTs are shown to be ballistic conductors at room temperatures, with mean free paths of the order of tens of microns [151]. MWNT-OH in 60% glycerol shows an average change in dielectric constant of 67.79% compared with 60.47%, 20%, 12.93%, 7.57% and 4.33% of MWNT-OH, SWNT, SWNT-OH, sSWNT and sSWNT-OH respectively. Longer and thicker CNTs would ensure a more effective conduction pathway along the nanotubes, hence it can be said that CNTs which are longer would be able to enhance the dielectric properties further. CNTs

with larger diameter favours more compact structures so that separation between individual tubes decreases. MWNTs have larger diameters and are longer compared with SWNTs and sSWNT hence provide a longer conduction pathway. This is what is observed with MWNTs in low dielectric constant medium (60% glycerol) and in TM phantom compared with other CNTs. However, a similar trend is not observed with RO water. This could be because sedimentation and flocculation of NPs is much higher in RO water compared with 60% glycerol and TM phantom, hence difference in the results is observed. Also, the study carried out to assess the effect different concentrations of SWNTs in water has on the dielectric properties and proves that higher the concentration higher are the dielectric properties of a medium, although linearity isn't visible. This may be attributed to the resolution of the probe.

3.5.4 Effect of functionalisation of CNTs on the dielectric properties of a medium

Results obtained in this study suggest that length and the diameter influence the dielectric properties of different nanotubes studied. As mentioned earlier, functionalisation of CNTs is carried out because agglomeration is a problem associated with CNTs due to weak intermolecular forces. The surface of CNTs is hydrophobic in nature, and the aggregation of the particles happens because of the hydrophobic nature and weak Van der Waals interactions [152]. Moreover, since the nanotubes are not rigid and have very long aspect ratios, entanglement is significant. Therefore, functionalisation of CNTs is crucial [153]. Functionalisation of CNTs has the ability of improving the dispersion of NPs in different mediums and solvents. Dielectric analysis results obtained in this study suggest that hydroxylated CNTs have higher dielectric properties compared with non-hydroxylated CNTs [154][155].

Functionalization allows the properties of CNTs to be characterised and studied. CNTs are often modified by covalent functionalisation to improve their dispersion in solvents. Covalent functionalisation involves that modifier molecules are attached to the outer sidewalls and ends of

the CNTs by covalent bonds. Direct covalent sidewall functionalisation is associated with a change from sp^2 to sp^3 hybridization and a simultaneous loss of π conjugation system on graphene layer.

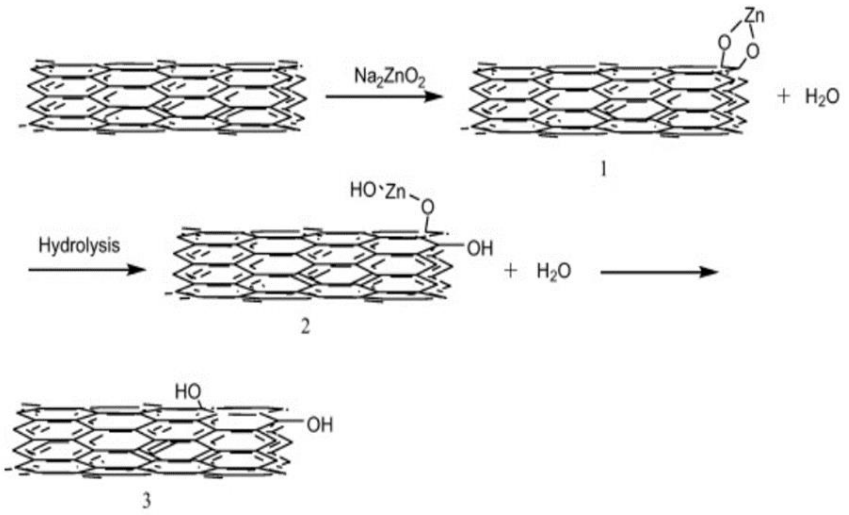

Figure 3-11: Reaction scheme for the modification of MWNTs with hydroxyl groups. Figure adapted from [76].

Tran *et al.* attached oxygen-containing functional groups (carboxy, carbonyl and hydroxyl groups) to the open ends and sidewalls of CNTs to make CNTs dispersible [156]. The functional groups on the CNTs, such as carboxyl, carbonyl, hydroxyl and amino group can not only improve the dispersion in solvents or polymers but can also act as reactive sites for further chemical modification. In recent years hydroxyl-functionalized CNTs have attracted a lot of attention. Chen *et al.* reported that hydroxyl-functionalised MWNTs were prepared by simple wet-mechanochemical reaction with potassium hydroxide at room temperature [157]. Kang *et al.* obtained MWNTs modified with hydroxyl group by using sodium zincate as an electrophile reagent (Fig. 3-11). Intermediate product 1 is prepared through the reaction between Na_2ZnO_2 and MWNTs. The intermediate product 1 was reacted with H_2O to produce MWNT-OH [158].

Ling *et al.* obtained MWNTs modified with hydroxyl group by using sodium aluminate (Fig. 3-12). Sodium aluminate reacts with MWNTs to produce the intermediate product 1. Intermediate products react with water and hydroxylated MWNTs are produced [159]. Hydroxyl groups are rich in chemistry and functionalization will change CNTs hydrophobic nature to being hydrophilic because of the attachment of polar groups [160].

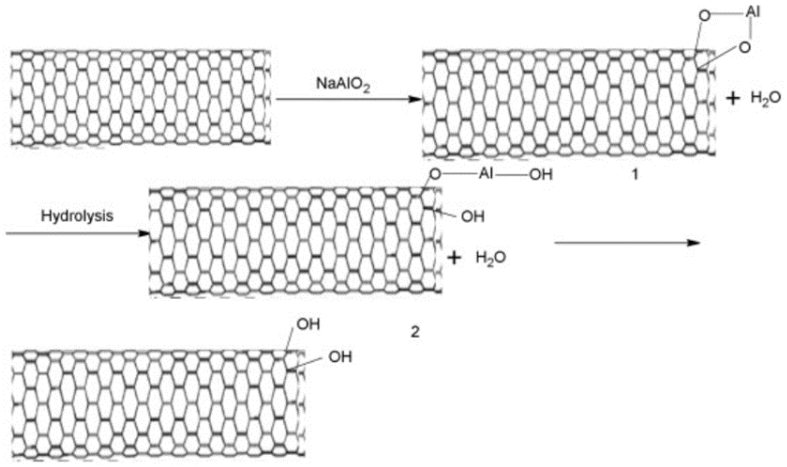

Figure 3-12: The mechanism scheme of the reaction between MWNTs and $NaAlO_2$. Figure adapted from [77].

The hydroxyl groups present on CNTs readily form a strong hydrogen bonds with water, allowing better dispersion of CNTs in water. Whereas, within the 60% glycerol medium, glycerol forms a bridging alkoxy bond through an alcohol group and participates in a lewis acid/base interaction between the oxygen atoms of carbon nanotubes, allowing better dispersion of CNTs in 60% glycerol compared with water.

The dispersion properties were found to be higher for hydroxylated CNTs compared with non-hydroxylated in their respective mediums. Dispersion properties of MWNT-OH, SWNT-OH and sSWNT-OH is higher than MWNT, SWNT, sSWNT in water, because hydroxyl groups are improving the dispersion properties of the CNTs by forming hydrogen bonds with water. This interaction leads to stabilization of the suspension, hence an increase in the dielectric properties is observed. So, it can be said that hydroxylation shows better dispersion and dielectric properties in

all the mediums. However, true dielectric nature of CNTs is seen in 60% glycerol and TM phantom because sedimentation and flocculation of the CNTs are greatly reduced compared with water.

3.6 Conclusion & Summary

In this chapter dielectric properties of different CNTs were characterized in three different mediums. This study showed that multi-walled CNTs have higher dielectric properties compared with single-walled CNTs and short-single-walled CNTs because of the longer mean free path and effective conduction pathway. Also, functionalization of CNTs improved the dispersion properties of CNTs which effectively improved the overall dielectric properties of all the mediums. Maximum change in the dielectric properties was observed with MWNT-OH in 60% glycerol and water compared with just water and TM phantom. This is because 60% glycerol is a viscous solution and can hold the particles dispersed for the duration of the measurement, hence the dispersion of the particles is better compared to water. This study shows that the concentration of the CNT also has a proportional effect on the resultant dielectric properties of the colloidal suspension. It can be concluded that a homogenous dispersion of the NPs is extremely important to conduct measurements and for dielectric characterization.

4 Zinc Oxide NPs as Contrast Enhancing Agents for Microwave Imaging and Sensing

4.1 Introduction

At present, a variety of nanoparticle systems are being investigated to explore their potential use in molecular imaging for treatment of cancer [161]. Nanoparticles have emerged as powerful tools because of their unique physiochemical properties, such as surface area to volume ratio. Iron oxide NPs have been applied as contrast agents for MRI and their contrast effects has been improved by varying size and composition of nanoparticles [162][163]. Semiconductor nanoparticles such as quantum dots (QDs) have been used as fluorescent probes in optical imaging due to their high quantum yields. Gold NPs, gold nanorods, and carbon nanotubes are being used in photoacoustic molecular imaging[164][165][166][167]. To date, nanomaterials such as liposomes, micelles have also been studied for molecular imaging purposes [168]. In this chapter we are proposing the use of zinc oxide (ZnO) NPs which have never been explored before for their potential use for MWI. ZnO NPs are semiconducting and exhibit size dependent electrical properties [169]. Sameera *et al*, carried out a study where multi-walled nanotubes (MWNT) were decorated with ZnO by wet chemical route to form MWNT/ZnO NPs hybrids to alter the electrical conductivity of the MWNT network. Zhang *et al.* carried out a study where MWNT- reduced graphene oxide (RGO) hybrid NPs were decorated with ZnO nanorods to improve the electrical and mechanical properties of poly(vinyl chloride) (PVC)/MWNT-RGO composites. Results showed that by introducing ZnO nanorods, the RGO-ZnO-MWNT hybrid particles increased 160% in capacitance compared with just MWNT-RGO [170]. These studies suggest that ZnO NPs possess high electrical conductivity and can be explored as potential contrast agents for MWI.

Zinc oxide (ZnO) NPs are versatile and have varied applications. ZnO NPs have been researched in several biomedical applications such as bio-sensing, anticancer medicine, treatment of skin conditions, antimicrobial and anti-bacterial potential [171]. Tu *et al.*, functionalised ZnO nanohybrids with a carboxylic group for sensitising the NPs for photo-electrochemical bio-sensing platform for the detection of bio-molecules such as cysteine[172]. Hwa and Subramani

implemented ZnO nanoparticles to be a component in graphene and SWNT nanocomposites for potential detection of glucose in the presence of oxygen; due to their non-toxicity, electrochemical activity and high electron transfer rate[173]. ZnO NPs have a wide range of applications in cancer therapy, biosensing, drug/gene delivery, nanomachines that can act as biological mimetic, biomaterials for tissue engineering [174]. They also showed inherent preferential cytotoxicity against cancer cells. ZnO NPs demonstrate their anticancer activity by inducing ROS generation and by inducing apoptosis [175]. Another useful characteristic of ZnO NPs that has been utilized for anticancer activity is their electrostatic properties. ZnO NPs exhibit a different type of surface charge behaviour, because of the neutral hydroxyl chemisorbed on their surface. The surface charge of ZnO particles is dependent on the pH of the aqueous medium, and lower pH, like physiological conditions, prompt positive surface charge which would therefore be more likely to interact with negatively charged phospholipids attached to the membrane of cancer cells [176]. ZnO NPs are suitable for opto-electronic applications. They are extensively used in cosmetics such as sun creams because they have excellent UV- absorbing properties, paints, and ceramics. ZnO is comparatively inexpensive, biocompatible and relatively less toxic compared with other metal oxide NPs which further supports it's applications [177]. In most cases, a highly stable dispersion is required. For this reason, a method of producing stable colloidal dispersion of ZnO NPs is crucial.

As we have seen an important parameter in all bioactive nanoparticles is the dispersion and lack of aggregation. In a colloidal suspension of nanoparticles; the interaction is dominated by short-range forces, such as Vaan der Waals attraction and surface charges. To prevent aggregation and sedimentation of these particles due to their high surface area, attractive forces between them need to be reduced and repulsive forces between them need to be increased to maintain a colloidal stability. The quality of dispersion of ZnO NPs were improved by capping with different types of surfactants such as non-ionic, cationic, and anionic. Triton X 100, polyethylene glycol (Mw –

6000), cetyltrimethylammonium bromide (cationic), and sodium dodecyl sulfate (anionic) have been studied. Study showed that ZnO dispersions stabilized with anionic surfactant sodium dodecyl sulfate showed better stability [178]. ZnO NPs have also been modified by polymethacrylic acid (PMAA) in aqueous system. The hydroxyl groups present on ZnO surface interact with the carboxyl groups of PMAA and form poly (zinc methacrylate) complex on the surface of ZnO. It was shown that PMAA enhanced dispersibility of ZnO NPs in water. Polymeric adsorption may serve as an effective way of modifying the surface of ZnO NPs and hence improving their stability of the suspension against aggregation or flocculation. Previously, adsorption of polymers such as poly (vinylpyrrolidone) (PVP), poly (ethylene glycol) (PEG), poly (vinyl alcohol) (PVA), poly (acryl amide) (PAM), poly (acrylic acid) (PAA) and poly (ethylene oxide) (PEO) on the surface of some metal oxide powders (CeO_2, TiO_2, Fe_3O_4 and Al_2O_3) in aqueous suspensions has been investigated [179][180][181]. The adsorption of polymeric additives onto the surface of the metal oxides is a combination of chemical and electrostatic interaction, hydrogen bonding and van der waals force. However, for non-ionic polymer, hydrogen bonding is the key mechanism [182].

4.1.1 Polyethylene glycol (PEG) as enhancer of colloidal stability

PEG is the common abbreviation for polyethylene glycol, which refers to a chemical compound of repeating ethylene glycol units. PEG is known to have different molecular weights. For example, 'PEG 600' typically denotes the preparation that includes a mixture of oligomers having an average M_W of 600 and 'PEG 10000' denotes a mixture of PEG molecules having an average M_W of 10,000 g/mol.

NPs come with a lot of advantages, however, there are some fundamental challenges which needs to be addressed. Some challenges include uptake of reticuloendothelial system (RES) in which NPs are rapidly shuttled out of circulation to the liver, spleen or bone marrow [183]. Concerns regarding NP toxicity often arise because of this RES accumulation. Aggregation of NPs can lead to NP

entrapment in the liver, lunch or elsewhere in the capillaries [183]. Capping of the NPs with hydrophilic groups such as polyethylene glycol (PEG) is a common approach to improve many functions, such as in vitro dispersion, in vivo circulation, stability, solubility, biocompatibility and to reduce toxicity.

For solid NPs, such as gold, thiol binding is a classic approach where sulfhydryl-capped PEG chain adheres to the gold surface [184]. A common used approach for noncovalent PEGylation is coating the hydrophobic NP surface with lipid-PEG conjugates. For example, PEGylated phospholipids with linear or branched PEG chain binds to the hydrophobic surface of single-walled carbon nanotubes in such a way that hydrophilic PEG groups are facing the aqueous exterior and provide nanotubes with hydrophilic PEG corona. For the liposomal preparations it is feasible to include PEGylated lipids into the lipid mixture or incubate non-PEGylated lipid Nano capsules with aqueous micellar solution of PEGylated lipids.

Various inorganic NPs have been previously explored for their potential use as contrast agents for molecular imaging. Semiconductor quantum dots (QDs), offer a broad range of emission spectra which covers both the visible and near-infrared wavelengths and have much higher photostability. Therefore, QDs have been studied as contrast agents for florescence imaging modalities and can be applied for photoacoustic imaging [185]. Superparamagnetic NPs are commercially used as contrast agents for MR imaging. Gold NPs can show extinction peaks in the visible regions. Such strong extinction peaks originate from the collective oscillations of their conduction electrons in the presence of an incident light. Gold NPs with large scattering cross sections are ideal for enhancing the contrast in optical imaging (OCT) [186]. They exhibit a photoluminescence capability suitable for multi-photon microscopy [187].

In this paper, we prepare ZnO NPs and ZnO NPs PEGylated with polyethylene glycol at M_W 8000 Da to observe stability and particle size when suspended in aqueous solution. All NPs are characterised by atomic force and scanning electron microscopy. The dielectric characterisation

was also recorded between 1-4 GHz, to observe if any contrast between the background medium and the introduced nanoparticle. Dielectric properties of ZnO and ZnO-PEG (M_w = 8000) have been measured at different concentrations to observe any change. CNT-OH has been used as a control for our study to compare the results obtained for SiO_2, ZnO and ZnO-PEG.

4.2 Study objectives

The aim of this chapter is to explore the effect of some metallic oxide NPs on the dielectric properties of a medium. In this chapter we show how the structure of NPs affects its dielectric properties and how improving the dispersion of nanomaterials can further enhance the dielectric properties of a medium.

4.2.1 Aims of the study

- To characterize the structural properties of Zinc oxide (ZnO) NPs, Silicon dioxide (SiO_2) NPs and ZnO-PEG NPs via SEM.
- To characterize the stability of the NPs via dynamic light scattering (DLS) and ultraviolet - visible spectroscopy (UV-Vis).
- To characterize the dielectric properties of ZnO NPs, ZnO-PEG NPs, CNT-OH (hydroxylated single walled nanotubes) and SiO_2 NPs at 2, 1, 0.5 and 0.25 mg/mL from 1-4 GHz in water (high dielectric constant medium).
- To characterize the dielectric properties of ZnO NPs and ZnO-PEG NPs at 2, 1, 0.5 and 0.25 mg/mL from 1-4 GHz in 60% glycerol (low dielectric constant medium) and tissue-mimicking (TM) phantom (phantom mimicking tumour properties)
- To understand the colloidal stability of ZnO and ZnO-PEG NPs in water over time, at t=0 and t=25.

4.3 Results

4.3.1 Morphology and Stability Analysis

We have characterized the surface morphology of SiO_2, ZnO, and ZnO-PEG by AFM and SEM (Fig. 4-1). For SEM analysis 2 mg/mL of each NP in water was prepared and 100 µl of each was pipetted on the glass microscopic slide. This was then dried using nitrogen gas and thereafter SEM analysis was carried out. For AFM analysis 1 mg/mL of the solution for each NP was prepared in water and 100 µl was pipetted on the glass microscopic slide which was dried using nitrogen gas and thereafter AFM analysis was carried out.

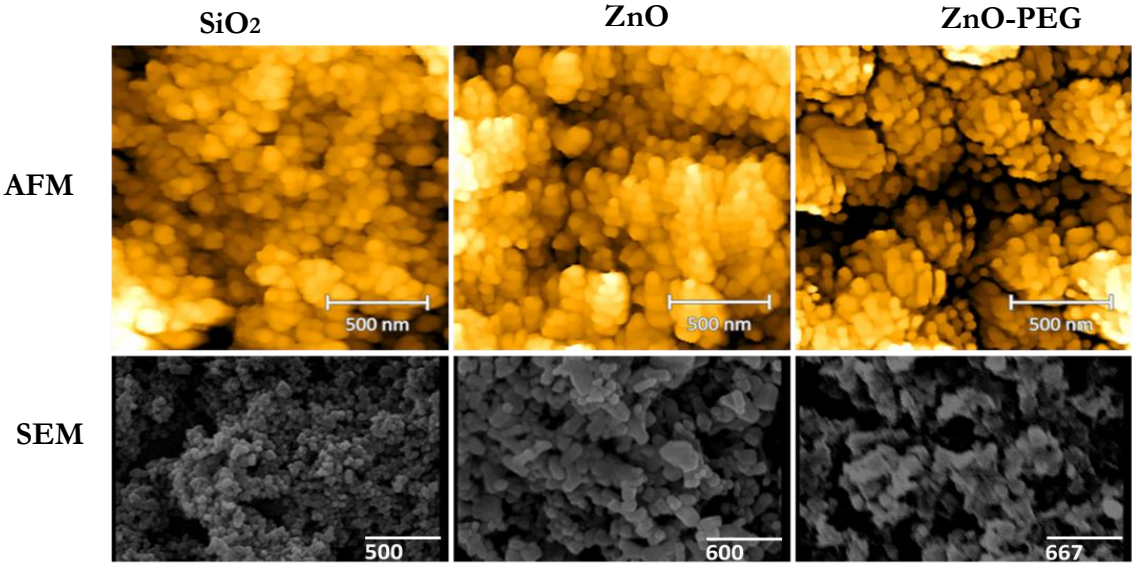

Figure 4-1: The surface morphology is observed from AFM and SEM. AFM images of SiO_2, ZnO and ZnO-PEG. SEM images of SiO_2, ZnO and ZnO-PEG. Images were taken at room temperature. SEM images were taken in a vacuum environment by Hitachi scanning electron microscope (S4000 FEG SEM with Oxford Instruments INCA EDX), while the AFM images were taken in open air conditions via Bruker icon dimension atomic force microscope.

Table 4-1: Nanoparticle sizes of SiO_2, ZnO, ZnO-PEG obtained by AFM and SEM

Nanomaterial	AFM (nm)	SEM (nm)
SiO_2	53.2 ±10.7	14.33 ±12.7
ZnO	51.58 ± 4.72	59.6 ±3.5
ZnO-PEG	65.65 ±6.02	91.1 ± 8.7

Sizes obtained by AFM and SEM have been tabulated in table 4-1. The shape of all the NPs are shown to be spherical in nature, although they are highly varied in sizes. Results obtained from both imaging techniques agree with each other and both modalities, SEM and AFM confirmed that ZnO-PEG are spherical nanoparticles.

TEM was another technique which could have been used and was a better technique to use, however, due to refurbishment issues it was not possible to conduct imaging with TEM. Therefore, size measurements were conducted via SEM, AFM and DLS.

Figure 4-2 (a) shows the Ultraviolet visible spectroscopy (UV-Vis) transmission spectra of ZnO and different molecular weight ZnO-PEG NP dispersions. In this experiment all NPs were dispersed in dd (double distilled) water.

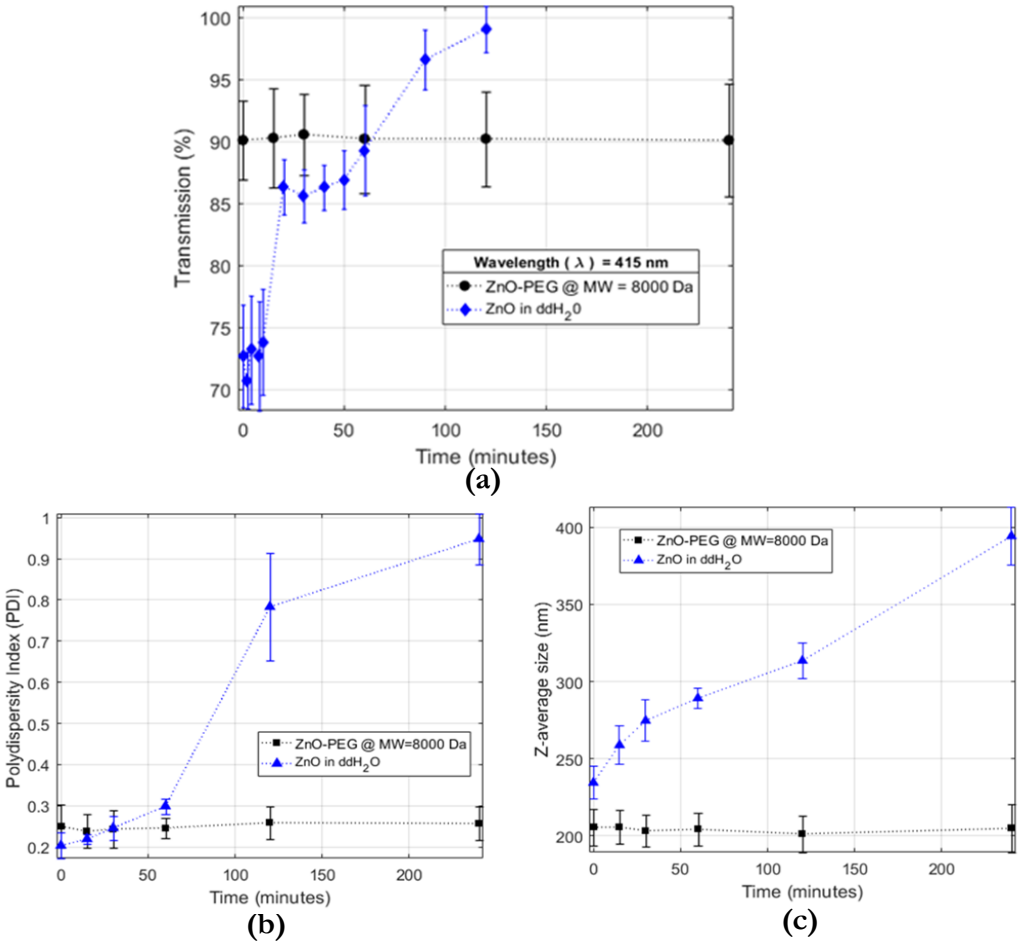

Figure 4-2: (a) Effect of PEG on colloidal stability of ZnO NP. Light transmission through ZnO NP and ZnO-PEG (M_W=8000) in ddH_2O, where λ=415nm. n=6 +/-SD, (b) Polydispersity index (PDI) and (c) Hydrodynamic size (nm) of ZnO and ZnO-PEG NPs in ddH_2O over a time of 240 minutes. n=6 +/-SD

Appropriate wavelength was chosen to be 415 nm because at this wavelength ZnO and ZnO-PEG NPs were found to be absorbing light hence transmission spectra were generated.

NPs were suspended in aqueous solution at a concentration of 1mg/mL and serially diluted to 20 μg/mL. This which was chosen as optimal, because lower concentrations would show increased baseline fluctuations and a higher intercept in the correlation function.

Measurements were taken at a wavelength of 415 nm. The measurements for different ZnO-PEG were taken at an interval of 15 minutes. Results suggest that the transmission of light through unmodified ZnO NP dispersion increases rapidly after 30 minutes and continues to increase to 100 % in most samples within 2 hours, suggesting sedimentation of the ZnO NPs. Also, this was observed visually due to the apparent precipitation of the NPs. The sedimentation of the NPs decreases with an increase in the size of PEG, suggesting higher the molecular weight of the PEG, less is the sedimentation of the NPs. ZnO-PEG showed an initial transmission of 75 %, and they were found to have a similar transmission over a 4-hour period; suggesting dispersion of ZnO NPs is better and stable after PEGylation (Fig. 4-2). UV-Vis measurements for SiO_2 were taken in similar conditions. Transmission of light increased rapidly after 30 minutes from 82% to 95% and remained at 95% till 240 min time point.

Dynamic light scattering measurements (DLS) (Fig. 4-2 (b) and (c)) of ZnO and ZnO-PEG in solution were carried out to characterise the intensity weighted Z-average size and polydispersity index (PDI). For DLS measurements, 20 μg/mL of ZnO and ZnO-PEG NP suspension was used. 20 μg/mL was chosen as the optimal concentration, because lower concentrations would show increased baseline fluctuations and a higher intercept in the correlation function For DLS measurements, the mean particle size is very specific to light scattering and to the presence of NP aggregates. Values of PDI ranges from 0 to 1; a PDI value smaller than 0.1 shows the sample is nearly monodisperse, while a PDI equal to 1 indicates the sample has a large variation in particle size. PDI of ZnO-PEG remains to be around 0.25 and stays constant throughout 4 hour.

However, the PDI for ZnO NPs increases from 0.2 to 0.95 within the measurement period. High PDI suggests a broad distribution of particle sizes and presence of large aggregates. The Z-average size of ZnO increases from 240 nm to 400 nm compared to ZnO-PEG which has a constant size of 210 nm throughout 240 minute. This suggests that aggregation of the ZnO NPs is reduced after the PEGylation process and the particles were stable.

4.4 Dielectric properties of nanoparticle suspensions in water

Figure 4-3 shows the measured dielectric properties of single-walled carbon nanotubes functionalised with hydroxyl group (SWNT-OH) dispersed in RO water. The dielectric constant shows a dependency on the concentration of NPs in the material under test (MUT). The variation of measurements at 2 mg/mL (max σstd = ±2.47) is considerably higher compared to lower concentrations, which may be due to the instability of the NPs at higher concentrations.

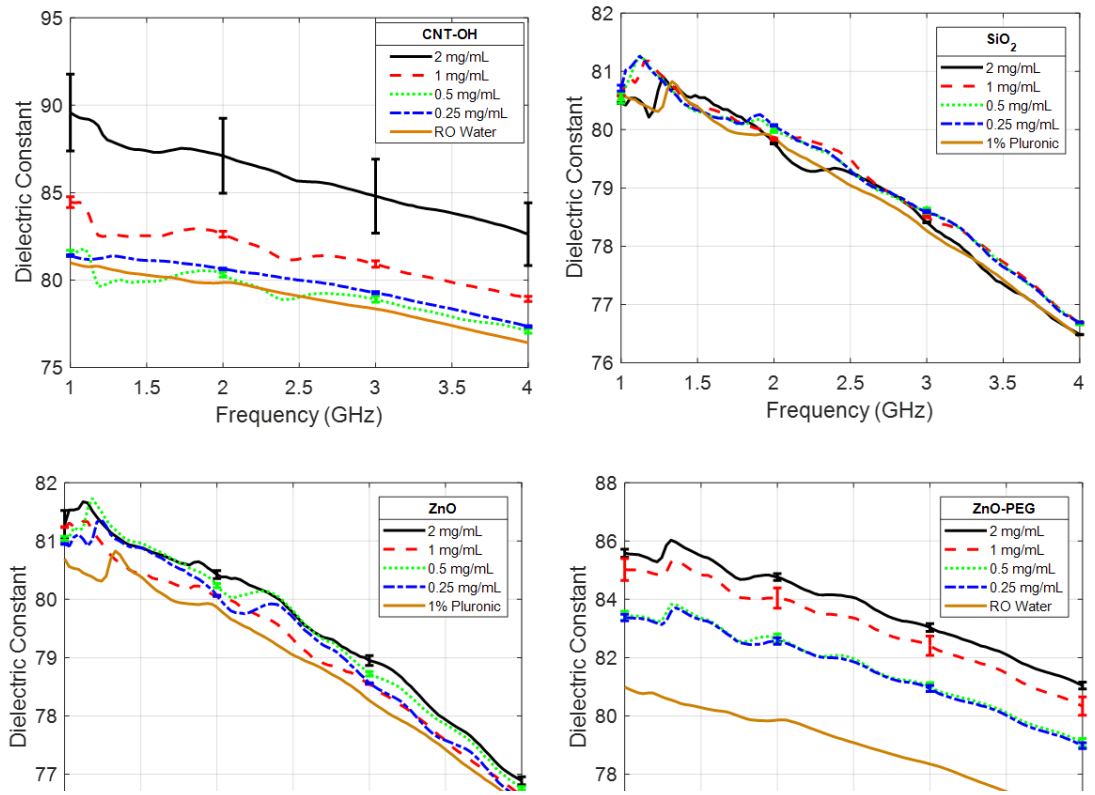

Figure 4-3: Averaged dielectric constant of colloidal dispersions of (a) CNT-OH in RO water, (b) SiO_2 with 1 % Pluronic, ZnO with 1 % Pluronic, and (d) ZnO-PEG in RO water characterised between 1-4 GHz. The control is the dispersant used for each NP. Each curve represents the average of three different samples (n=3+/-SD).

SWNT-OH has been used as a control in this study because it has been studied extensively previously for MWI purposes. Since the materials selected were being tested for the first time, it was important for us to compare our results with a material which has already been studied before. Since, CNTs have been studied previously, it gives us an indication of what we should be expecting with the contrast agents we are proposing for the first time in this study.

Figure 4-3 displays the dielectric constant of silicon dioxide dispersed in RO water with 1 % (v/v %) Pluronic surfactant at different concentrations. Pluronic-F127 is a non-ionic triblock copolymer composed of a central hydrophobic chain of polyoxypropylene with two hydrophilic chains of polyoxyethylene. Pluronic is known to have high solubility in water. The surfactant was used to improve the dispersion of NPs in water. The maximum dielectric constant value is 80.91 (f = 1.27 GHz), 81.18 (f = 1.12 GHz), 81.27 (f = 1.12 GHz), 81.26 (f = 1.12 GHz), in descending order of SiO_2 concentration. The maximum value of 1% Pluronic in water is 80.3 recorded at 1.33 GHz. The average change of dielectric constant with respect to the background is less than 1.5 % below 2 GHz.

Figures 4-3 & 4-4 show the dielectric constant and effective conductivity properties of zinc oxide NPs in frequency range of 1 to 4 GHz. Dielectric constant of ZnO at 2 mg/mL at 1 GHz is 81.28 ± 0.24 with 0.73 % change to water compared to 80.95 ± 0.01 with 0.32 % change of the 0.25 mg/mL concentration. Therefore, the concentration dependence of NPs is visible.

Figure 4-3 (d) shows the dielectric constant of ZnO-PEG NPs. It is evident that increase in the ZnO-PEG concentration is directly proportional to the increase in the dielectric constant over the whole frequency range. The maximum average change of dielectric constant of ZnO NPs at 2, 1, 0.5, and 0.25 mg/mL is 1.99 %, 1.58%, 2.11 % and 1.70 %, respectively.

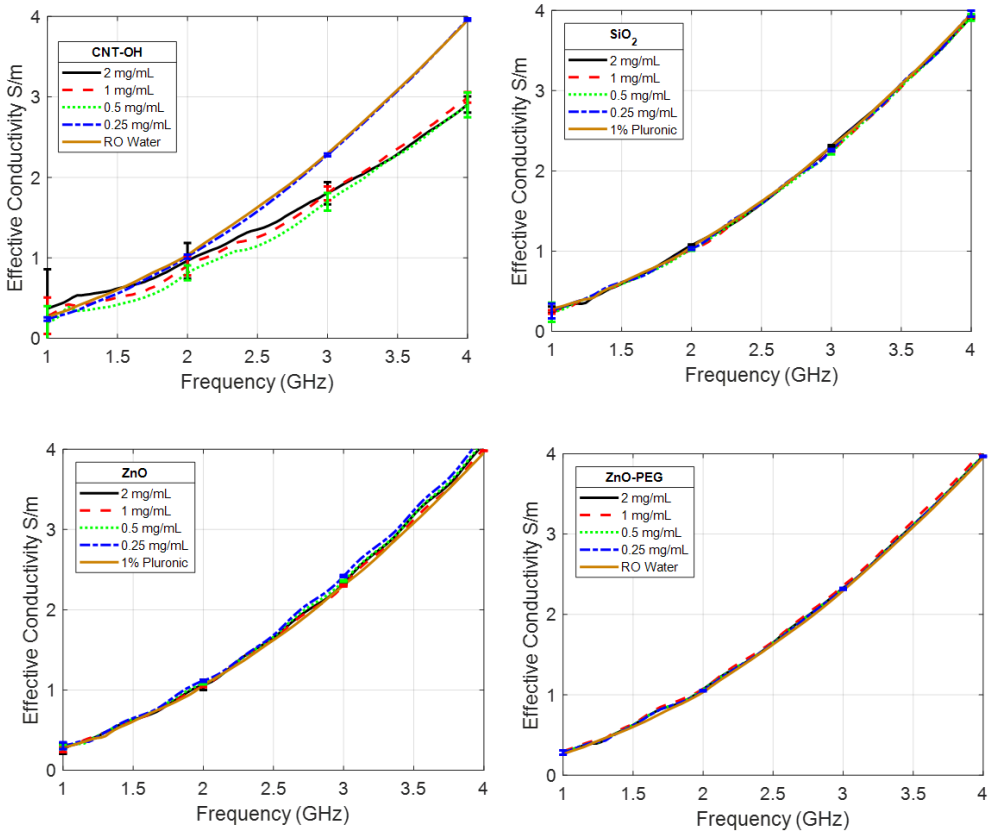

Figure 4-4: Averaged effective conductivity of colloidal dispersions of (a) CNT-OH in RO water, (b) SiO_2 with 1 % Pluronic, (c) ZnO with 1 % Pluronic, and (d) ZnO-PEG in RO water characterised between 1–GHz. The control is the dispersant used for each NP. Each curve represents the average of three different samples (n=3+/-SD).

The maximum average change of dielectric constant of PEGylated zinc oxide NPs (Fig. 4.5) at 2, 1, 0.5, and 0.25 mg/mL is 6.80 %, 6.03 %, 4.14 % and 4.00 % accordingly, over the whole frequency range.

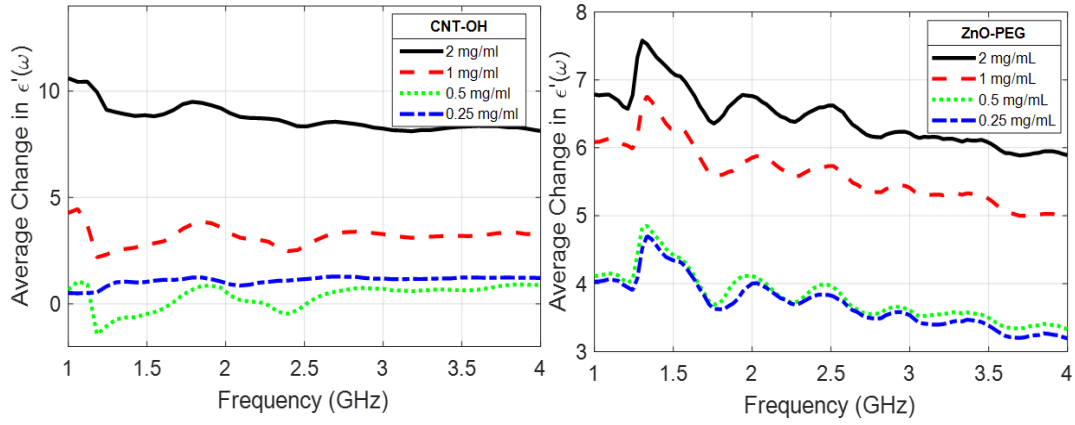

Figure 4-5: Average change of the dielectric constant of colloidal dispersions of (a) CNT-OH and b) ZnO-PEG in aqueous solution from 1–4 GHz. Each curve represents the average of three different samples (n=3+/-SD).

Figure 4-6 shows the average change in the effective conductivity of ZnO-PEG and CNT-OH in RO water from 1-4 GHz. At 2mg/mL CNT-OH shows the maximum average change of 42.63% at 1 GHz, whereas, ZnO-PEG shows the maximum average change of 15.44% at similar conditions.

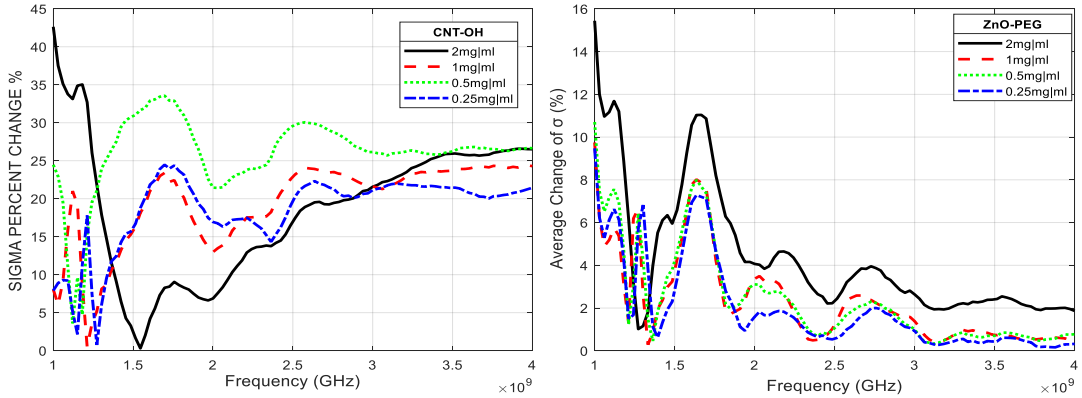

Figure 4-6: Average change of the effective conductivity of colloidal dispersions of (a) CNT-OH and b) ZnO-PEG in aqueous solution from 1–4 GHz. Each curve represents the average of three different samples (n=3+/-SD).

4.5 Dielectric properties of ZnO and ZnO PEG colloidal dispersions at different concentrations in 60% glycerol and in TM phantom

4.5.1 Dielectric properties of ZnO colloidal dispersion at different concentrations in 60% glycerol

Figure 4-7 shows the measured dielectric properties of ZnO NPs dispersed in 60% glycerol which is used as low dielectric constant medium. The dielectric constant shows a dependency on the concentration of NPs in the MUT.

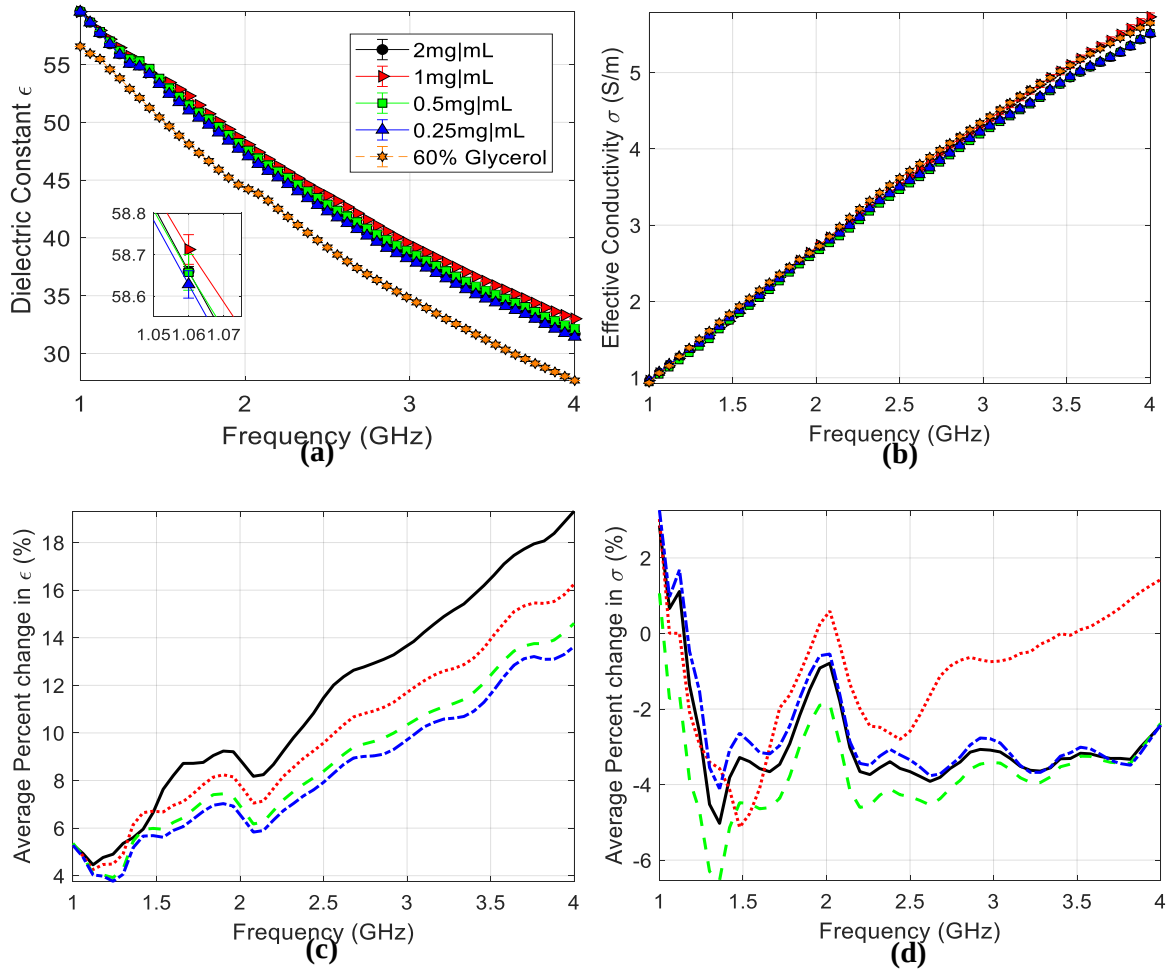

Figure 4-8: (a) dielectric constant, (b) effective conductivity, (c) average percent change in epsilon and d) average percent change in sigma of ZnO NP colloidal dispersion at different concentrations in 60% glycerol characterised between 1-4 GHz. Each curve represents the average of three different samples (n=3+/-SD).

The maximum dielectric constant value is 59.6, 59.57, 59.54 and 59.546 at 1 GHz, in descending order of ZnO concentration compared with 56.57±0.0047 of 60% glycerol (Fig 4.7 (a)). The

average change of dielectric constant is 5.36, 5.302, 5.28, and 5.279 for 2, 1, 0.5 and 0.25mg/mL at 1 GHz (Fig 4.7 (c)). The maximum average change of dielectric constant is 19.32, 16.26, 14.61 and, 13.63 at 4 GHz in descending order of ZnO concentration whereas the maximum average change effective conductivity was 4.5% at 1 GHz for 1 mg/mL of ZnO colloidal suspension.

A change in concentration does not seem to have a big effect on the dielectric properties as seen by the results above. This may be because a very small concentration is needed to observe a desired dielectric property change. Also, because the dispersion properties of nanomaterials are enhanced in 60% glycerol, therefore, a small amount of nanomaterial is enough to observe the desired results and a higher concentration may not be necessary.

4.5.2 Dielectric properties of ZnO-PEG colloidal dispersion at different concentrations in 60% glycerol

Figure 4.8 shows the dielectric properties of ZnO-PEG in 60% glycerol. The dielectric constant shows a dependency on the concentration and the dielectric constant is improved further in 60% glycerol after ZnO has been PEGylated.

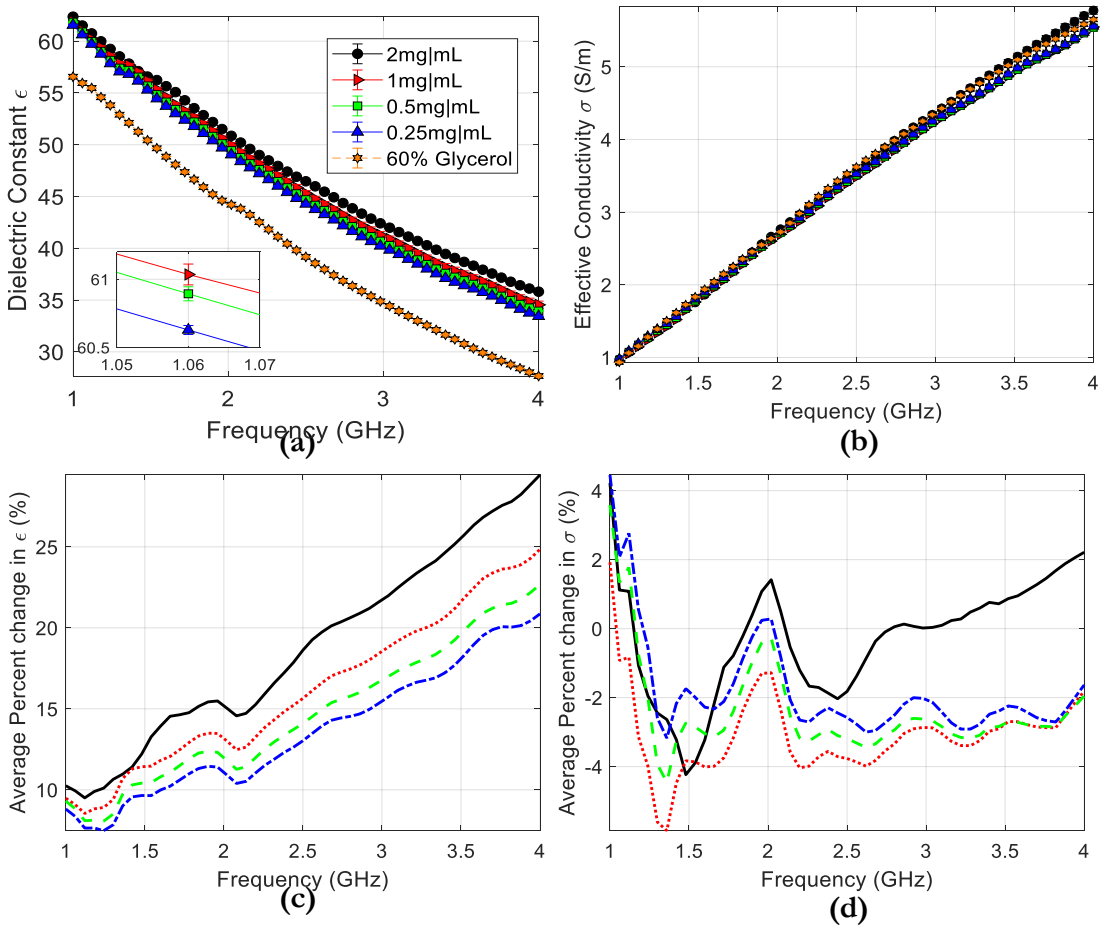

Figure 4-8: (a) dielectric constant, (b) effective conductivity, (c) average percent change in epsilon and d) average percent change in sigma of ZnO-PEG NP colloidal dispersion at different concentrations in 60% glycerol characterised between 1-4 GHz. Each curve represents the average of three different samples (n=3+/-SD).

The maximum average change in dielectric constant is 29.44, 24.85, 22.68 and, 20.86 at 2mg/mL, 1mg/mL, 0.5mg/mL and, 0.25mg/mL respectively at 4 GHz. The minimum average change observed for ZnO-PEG in 60% glycerol is higher than water. 10.25, 9.48, 8.83, and 8.81 is the minimum average change observed at 1 GHz in descending order of concentration.

4.5.3 Dielectric properties of ZnO and ZnO-PEG colloidal dispersions in TM phantom

The effect of 2 mg/mL of ZnO and ZnO-PEG in tissue mimicking (TM) phantom was studied, since 2 mg/mL showed the maximum change in dielectric properties for ZnO and ZnO-PEG colloidal suspensions in water and in 60% glycerol.

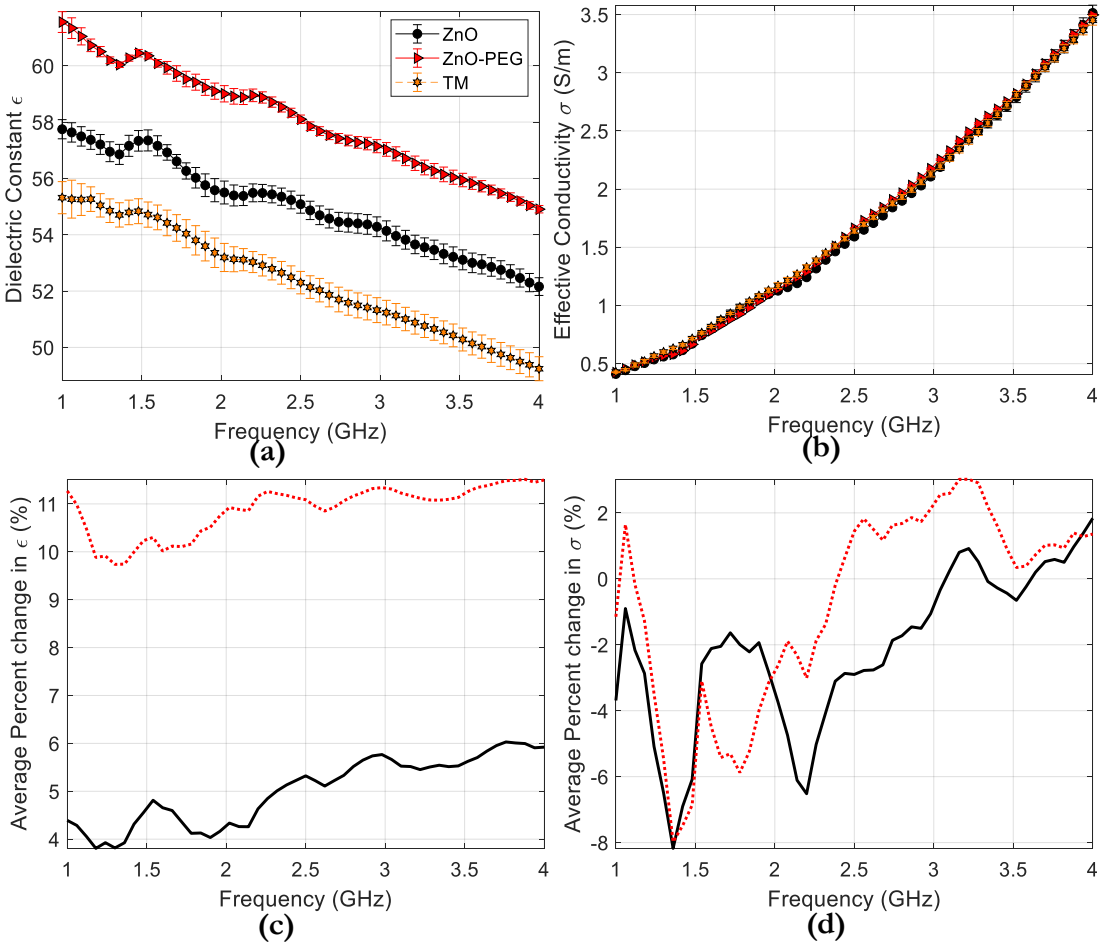

Figure 4-9: (a) dielectric constant, (b) effective conductivity, (c) average change in dielectric constant and d) average change in sigma of ZnO and ZnO-PEG colloidal dispersion at 2mg/mL in TM phantom characterised between 1-4 GHz. Each curve represents the average of three different samples (n=3+/-SD).

There was a clear increase in the dielectric properties between ZnO and ZnO-PEG. ZnO showed an average change in dielectric constant of 11.27% compared with 4.4% change of dielectric constant at 1 GHz. The maximum average change in dielectric constant across the whole frequency range was 11.27% (Fig. 4-9). There was ~ 7% increase in the average change dielectric constant (%) seen by ZnO-PEG compared with ZnO NPs at 1GHz.

4.6 Dielectric properties of nanomaterials in water at a higher frequency range

Table 4-2: Dielectric properties of ZnO (1% Pluronic), ZnO-PEG (RO H2O), SiO_2 (1% Pluronic), and CNT- OH (RO H_2O) between the frequency range of 5–10 GHz.

Frequency (GHz)	ZnO (1% pluronic)		ZnO-PEG (RO water)		SiO_2 (1% pluronic)		CNT-OH(RO water)	
5	74.44	0.54	78.90	6.56	74.41	0.50	80.85	9.20
6	72.04	0.17	76.06	5.76	70.89	-1.43	78.26	8.82
7	70.72	1.39	74.05	6.16	68.41	-1.92	76.10	9.10
10	63.06	2.31	65.86	6.88	60.86	-1.23	67.59	9.68

Dielectric properties of colloidal dispersions presented in this study at frequency range from 5-10 GHz (Table 4-2). The purpose for characterising the dielectric properties at high frequencies was to identify if the dielectric contrast observed at low frequencies, is observed at high frequencies, and to what effect. Also, microwave radar imaging methods rely on higher frequencies, therefore potentially opening another viable application. We observed that as the frequency increases, the dielectric constant decreases and the dielectric loss becomes much more dominant, as seen by our results above. Regarding ZnO colloidal suspension, we observe that across a wide frequency range, the average change remains to be ~2%, which is what we observed at lower frequency range, and SiO_2 remains to have similar dielectric properties to that of water with 1% Pluronic as observed at lower frequency range. With regards to ZnO-PEG the overall average change remains to be ~6% and has slightly changed depending on the frequency points. However, the results are like that of lower frequency range. Average change for CNT-OH across the large frequency range remains to be the highest amongst the different nanomaterials we measured.

4.7 Dielectric properties of ZnO and ZnO-PEG colloidal suspensions at different probe positions at different time intervals

To understand how the stability of the colloid's effects dielectric properties, measurements were taken at different positions in the sample (Fig. 4.10 – Fig 4.13).

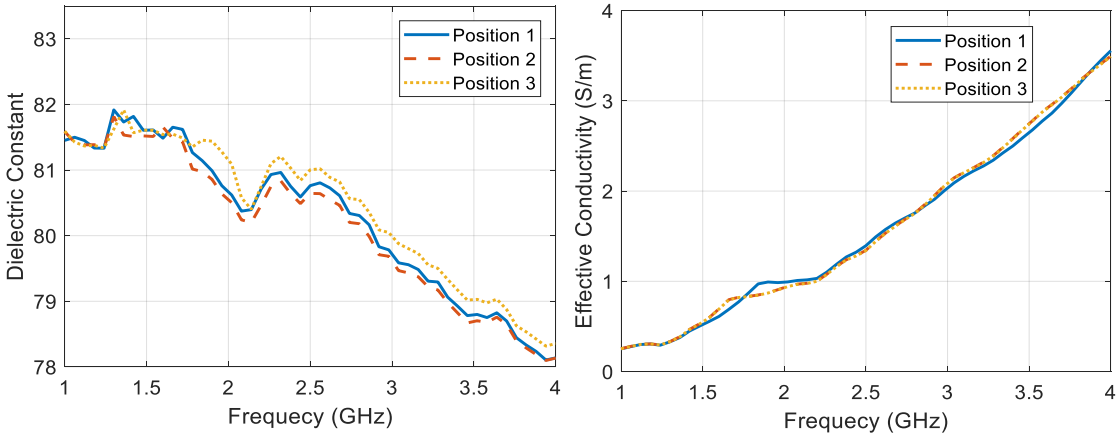

Figure 4-10: Dielectric properties of ZnO NPs at a concentration of 2 mg/mL in RO water with 1% Pluronic at three different probe positions from frequency range of 1-4 GHz at t = 0. Each curve represents the average of three different samples (n=3+/- SD).

We performed measurements immediately after preparation of samples to guarantee that the ZnO NPs and ZnO-PEG (Mw = 8000) NPs at a concentration of 2mg/mL are still dispersed in the aqueous medium for the duration of the measurement. Furthermore, we took a measurement after 25mins, to examine the effect of aggregation and sedimentation on the dielectric properties.

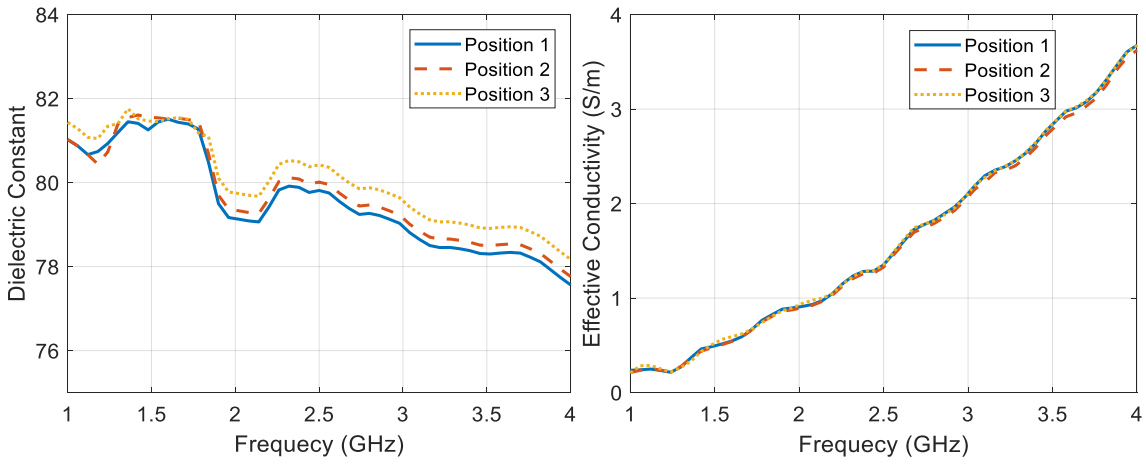

Figure 4-11: Dielectric properties of ZnO NPs at a concentration of 2 mg/mL in RO water with 1% Pluronic at three different probe positions from frequency range of 1-4GHz at t = 25mins. Each curve represents the average of three different samples (n=3+/-SD).

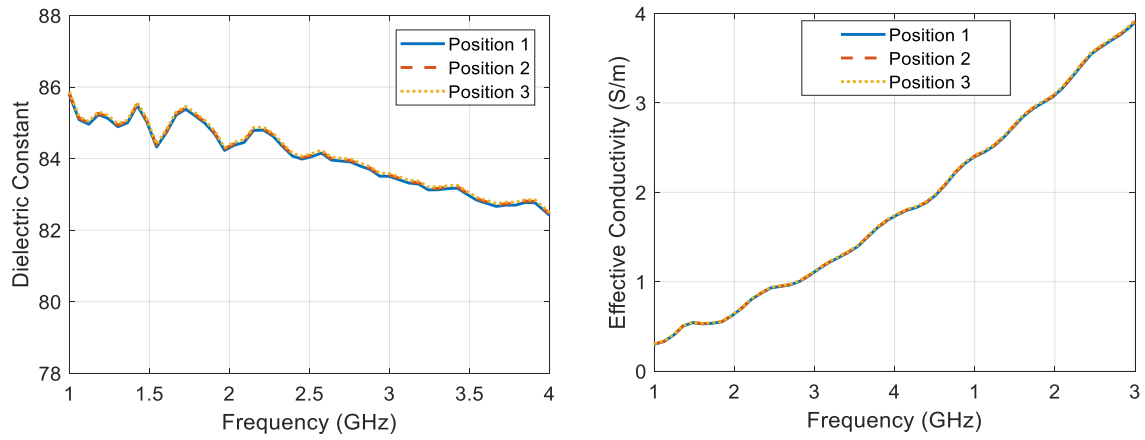

Figure 4-12: Dielectric properties of ZnO-PEG NPs at a concentration of 2 mg/mL in RO water at three different probe positions from frequency range of 1-4GHz at t = 0. Each curve represents the average of three different samples (n=3+/-SD).

The samples height is 20 mm, and the probe is lowered by 5.5 mm for different positions. We selected three axial positions to immerse the probe prior to taking the measurement. Probe position 1 is immersed 5 mm into the sample; probe position 2 was immersed 10.5 mm into the sample, and probe position 3 was immersed 16.5mm into the sample.

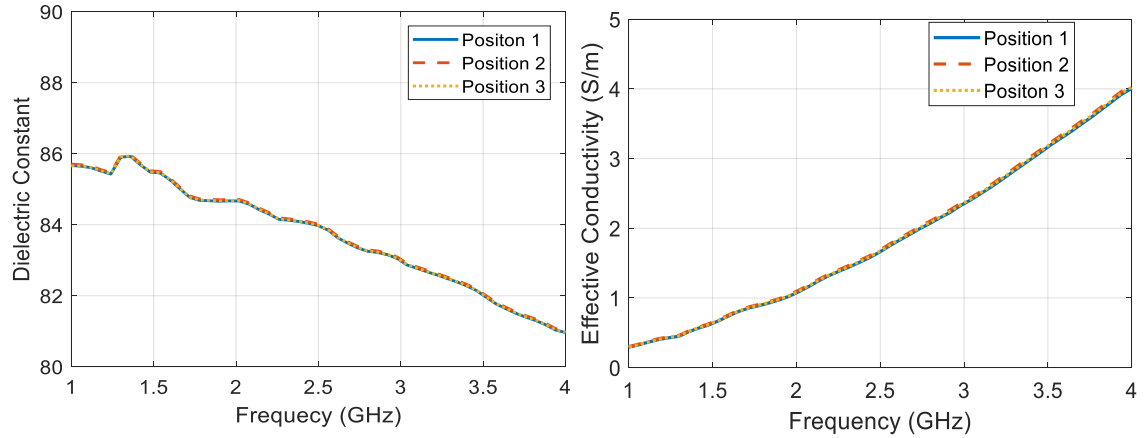

Figure 4-13: Dielectric properties of ZnO-PEG NPs at a concentration of 2 mg/mL in RO water at three different probe positions from frequency range of 1-4GHz at t = 25mins. Each curve represents the average of three different samples (n=3+/-SD).

The maximum average change of ZnO-PEG NPs at position 1, position 2 and position 3 at t=0 was 6.28%, 6.31% and 6.38% respectively. After 25 min, maximum average change was 6.44%,

6.49% and 6.45% at position 1, 2 and 3 respectively. The average change over time shows insignificant change for all probe positions. This highlights that the modified particles dispersed in RO water are stable over this period, as well as portraying similar contrast.

The maximum average change observed for ZnO NPs at t = 0 was 1.61%, 1.42% and 1.62% at position 1, 2 and 3 respectively. However, average change slightly dropped to 1.4%, 1.22% and 1.02% after 25 mins. Slight drop in the average change can be assigned to the fact that these particles have started to aggregate and hence have started to sediment.

4.8 Discussion

4.8.1 Morphology and stability analysis

Dispersion is a process by which agglomerated particles separate from each other by forming a new interface, between an inner surface of the liquid dispersion medium and the surface of the particles to be dispersed. Particles tend to behave differently when in their natural state compared to solutions [179].

Satisfactory agreement is shown between the size as well as the shape of AFM and SEM morphology characterisation for ZnO, SiO_2 and ZnO-PEG. ZnO-PEG has much larger size compared with ZnO, suggesting PEGylation has been effective. The shape of all the nanoparticles are represented as spherical in SEM and AFM.

Hydrodynamic size produced from the DLS differs greatly from the AFM and SEM particle size. By using this technique, we were able to measure the size of the NPs when dispersed in a solution. Hydrodynamic size is an intensity weighted mean particle diameter, which is relevant to scattering of light and is sensitive to large aggregates, due to its inherent intensity weighting and dependency on viscosity and temperature. It presents the size of a spherical particle that has equal diffusion as the particle in question. The diffusion of the particles in solution will also depend on the

conformation of the PEG attached. Large PEG chains, such as the ones used in this study may be described by the Flory radius equation (1), F is the Flory radius, α is the length of a single monomer repeat and n (n = (MW)/44) is the number of monomers on the PEG chain itself ; the Flory radius for PEG 8000 is 79.4 nm[188].

$$F = an^{3/5} \quad \text{(Equation 1)}$$

The distance between the NP surface and the PEG may induce a brush or mushroom conformation [189]. If F is smaller than the distance between the surface and the PEG chain, then a mushroom conformation occurs, however if F is larger than the surface density then it would lead to a brush conformation. The ionic concentration of the samples was minimal, therefore the electrical Debye length ($\varkappa$ ($^{-1}$)) around the particle would be extended, reducing the diffusion speed, hence a larger hydrodynamic size would be present.

4.8.2 Dielectric analysis

We have measured the dielectric properties of selected nanomaterials to assess contrast enhancing properties in high dielectric constant media. The desired contrast should be visible in the real part of the complex dielectric constant rather than the imaginary part. Microwave reflection measurements (S11) using the coaxial probe are susceptible to systematic errors, which causes the jitter in the frequency dispersion, especially at low frequencies. To minimize this error, repeated calibrations were performed and observation of the polar plot for each calibration standard was inspected as a confidence check. Moreover, the contrast observed must be larger than the stated 2 % error of the probe [87]. Dielectric properties were measured between 1-4 GHz. This range was chosen as it is the relevant frequency range for microwave tomography studies [190]. Generally, the complex dielectric constant may depend on temperature as well as frequency and increase in the temperature of water will increase the loss index and therefore decrease dielectric constant [191].

The measurements of the dielectric properties of colloidal dispersions could be influenced by aggregation and precipitation phenomena. The probe's stated sensing depth is 5 mm; however, the actual sensing volume is experimentally much smaller. 90 % of the overall dielectric property of a mixture is dependent on the initial 500 μm from the tip of the probe length [192]. The overall dielectric property of an MUT is considered as a ratio of the composition of that sample within the measurement region and doesn't behave such that the resultant dielectric value is an average of the whole volume. Also, the probe assumes the sample is isotropic and non-magnetic. Therefore, homogenous dispersion of contrast agents in the background medium is crucial for reliable electrical differences.

4.8.3 Evaluation of NP colloidal dispersions (I)

Previously CNTs have been extensively explored as potential contrast agents for MWI due to their distinctive electrical and conductive properties. The purpose of measuring CNTs was to use them as a control since they have been previously suggested as effective contrast agents for MWI [73][74]. Results obtained for CNT-OH correlate positively with previously reported data. It's important to note that OH functionalized CNTs showed an average change of 10.61 % increase in the real component at 2 mg/mL at 1 GHz, which is comparable with previously reported (CNTs stabilised with biocompatible PL-PEG) 10 % increase in the dielectric constant and 90 % increase in conductivity at similar conditions[193]. However, we only observed an increase of 42.63 % in the conductivity, like what was observed in [76].

Carbon atoms in a CNT structure are known to be arranged in a hexagonal lattice, where each carbon atom is covalently bonded to three neighbouring carbons via sp^2 molecular orbitals. The fourth valence electron remains empty and delocalized, hence making CNTs conductive in nature [194]. CNTs have been reported to have a high aspect ratio, which has been stated to increase the dielectric constant due to the presence of a large dipole moment [79]. When an alternating electric field is applied, the hydroxyl group in CNT would experience orientational polarisation, which

leads to a torque acting on the polar -OH bond. The torque prompts the nanotubes to orient along the electric field, hence an increase in the dielectric constant is observed [195][196]. However, biocompatibility of CNTs is in question, which further motivated us to study other nanomaterials for their potential as contrast agents for MWI. CNTs may have adverse effects on human health, especially in human pulmonary system [197]. It is understood that surface modifications are important to minimise CNT toxicity [198].

The suspension of silicon dioxide NPs in water shows a negligible change in the dielectric constant over the whole frequency range compared to zinc oxide NPs and CNT-OH. Silicon dioxide is not conductive and has no net dipole due to its crystalline structure. Silicon dioxide has a tetrahedral arrangement of four sp^3 hybrid orbitals. In a silicon-oxygen tetrahedra, each silicon atom is surrounded by four oxygen atoms. The individual Si-O bonds are very polar but there are four Si-O bond which cancels each other out, hence there is no net dipole effect.

One of the key features of ZnO NPs is their low toxicity and biodegradability. It is involved in various aspects of metabolism. Numerous studies have shown the biocompatibility and biosafety of ZnO nanostructures when applied in biological applications [199][200]. We propose the increase in the dielectric constant perceived with the presence of ZnO NPs is because they are known to have a wide band gap energy (3.4 eV), large exciton binding energies (60 meV), and they have a structure of alternating planes composed of tetrahedral coordinated O^{2-} and Zn^{2+} ions [201]. This results in non-central symmetric structure and consequently piezoelectric and pyro-electric behaviour [202][203]]. Zinc oxide has polar surfaces at the positive Zn-(0001) and the negative O-(0001) surfaces, resulting in a normal dipole moment [180][204]. The opposing charged ions produce a polar surface, which leads to the formation of a dipole moment and spontaneous polarisation when an electric field is applied, hence increase in the dielectric constant with ZnO NPs is seen at lower frequencies. However, at higher frequencies, dipoles tend to freeze with no effective change in the dielectric constant.

4.8.4 Impact of PEGylation on dielectric constant

Colloidal solutions tend to lower their stability because of particle size and free surface energy [205]. Nanoparticles stabilise themselves either by sorption of molecules from their surroundings or by lowering their surface area through coagulation and agglomeration [206].

Homogenous solution was obtained at lower concentrations; however, particles were still un-stable and higher concentrations caused sedimentation. Since, ZnO NPs showed a potential increase in the dielectric constant hence, they were PEGylated to further improve their stability in the solution and to confirm the effect dispersion has on the dielectric properties.

Polyethylene glycol (PEG) is a chemically inert molecule of varying lengths, making it a good dispersant in water[207]. PEGylation provides hydrophilicity to the nanoparticles by making them water dispersible. PEG macromolecules adsorb to the solid surface via the hydroxyl groups present on the ZnO NPs through hydrogen bonding. The total amount of adsorbed polymer is higher with higher molecular weight PEG because of greater loop and tail segments at the interface, which will increase the thickness of the adsorption layer.

PEG can be attached onto the surface of nanoparticles via adsorption; hydrophobic interactions, through the formation of covalent bonds or hydrogen bonding [208]. PEG is adsorbed onto the ZnO particle surface and then attains the adsorption plateau. The total amount of PEG adsorbed is larger for larger molecular weights due to greater participation of loop and tail segment at the surface. The type ($-ZnOH^{+2}$, -ZnOH, $-ZnO^{-}$) and number of surface groups on ZnO NPs may determine the extent of polymer adsorption [209]. The dispersion of ZnO NPs was improved after PEGylation as shown by the UV-Vis and by DLS. Dielectric properties of ZnO NPs was further improved after PEGylation, suggesting the importance of a homogenous and a stable solution. However, ZnO-PEG NPs in water show a nonlinear concentration-dependent change in the

dielectric constant. This might be because a minimum nanomaterial concentration is required to provide a significant contrast, below which dielectric probe measurements are not reliable.

PEG has been used to modify the surface properties of ceramic materials to improve the dielectric properties of the composites. Zhu *et al.* reported that the dielectric properties of PEG modified Fe_2O_3 composites have much higher dielectric constant [210]. PEG is also known as polyoxyethylene and is commonly expressed as $H-(O-CH_2-CH_2)\ n-OH$. Since, the dielectric properties of PEG-ZnO were higher than basic ZnO, this can be because of the contribution of oxyethylene chain towards the total dipole moment. Similar behaviour is observed with diethyl carbitol. Diethyl carbitol has no -OH groups present, but the high dielectric constant observed is because of the oxyethylene chain it possesses [211]. With PEG, high dielectric constant can be attributed to end -OH groups and flexible oxyethylene chain.

Our dielectric spectroscopy results in Figure. 3-4 and 3-5 do not suggest a linear dependence between the dielectric properties of NPs in liquid solutions with their concentrations in water. This may be due to following reasons: at low concentrations, the effect of NPs may be very low to be distinguishable within the error of the probe measurement. For example, the dielectric properties of CNT-OH dispersions for 0.25 and 0.5 mg/mL concentrations in Fig. 3-4(a) almost overlaps the control, suggesting a variability that is very difficult to measure accurately with the probe. On the other hand, plots for the same concentrations of ZnO-PEG in Fig. 3-4(d), are quite distinct from the control, but are still under 5% difference. The almost perfect overlap of these curves merits further investigation. At higher concentrations, dispersion of the NPs in the liquids may be less effective as their concentration increases, hence it is possible that a concentration increase from 0.5 to 1.0 mg/mL has a stronger impact on the dielectric properties of the liquid solution than an increase from 1.0 to 2.0 mg/mL, as seen in Figure.3-6.

4.8.5 Evaluation of NP colloidal dispersion (II)

Dielectric contrast measured for ZnO and ZnO-PEG colloidal suspensions in 60% glycerol were comparatively much higher than in RO water. Glycerol has a high ability to solubilize both organic and inorganic polar compounds. It also has high polarity, long relaxation time, high loss tangent value and high acoustic impedance which makes it appropriated to be used under microwave and ultrasound irradiation conditions [212]. ZnO NPs tend to agglomerate due to high surface energies, this presents an obstacle for the use of ZnO NPs in various applications. Studies have been carried out where ZnO NPs have been successfully synthesized in various polyol medias such as ethylene glycol or glycerol. The polyol media will serve both as a solvent and stabilizing agent for the NPs. This study showed that ZnO NPs synthesized without glycerol were much larger compared with NPs which were synthesized with glycerol stabilizer. When the concentration of zinc ions and OH- ions increases without a stabilizer, supersaturated ZnO nuclei would more easily aggregate, growing larger [213]. Glycerol has three hydroxyl groups present, with which the zinc ions could interact to form a zinc-glycerol complex, hence stabilizing the NPs and eventually improving the dispersion properties of the NPs [214][215].

Dielectric contrast of ZnO-PEG colloidal dispersions in 60% glycerol was much higher than in RO water. As we have already seen and discussed that PEG molecules can stabilize ZnO NPs. Dielectric properties are further enhanced for ZnO-PEG in 60% glycerol because of the hydrogen bonding interaction between hydroxyl groups present on the PEG molecule and three hydroxyl groups present within the glycerol. This interaction promotes stabilization of ZnO-PEG NPs in the medium hence an increase in dielectric properties is observed. Also, the -OH groups present on the glycerol, -OH groups of the PEG molecule, the flexible oxyethylene chain of PEG and the dipole present within ZnO could be going through dipolar polarisation.

ZnO NPs and ZnO-PEG NPs were further tested in oil-in-gelatin TM phantoms. TM phantom is a 10% oil-in-gelatin phantom and can mimic the dielectric properties of breast tumors. Results

indicated that the average change of dielectric constant for ZnO-PEG NPs was 11.27% compared with basic ZnO NPs which was 4.4%. The average change of dielectric constant of ZnO-PEG in TM phantom was similar to when the NPs were dispersed in 60% glycerol. These results suggest that attaining a homogenous solution is crucial. Particle stability is better in TM phantom compared with water due to the less Brownian motion of the NPs. Furthermore, the -OH groups of the PEG chain can be the contributing factor towards the dipole moment [216][217].

4.9 Conclusion & Summary

The dielectric properties of modified ZnO nanomaterials were assessed in a frequency range between 1–4 GHz. We have demonstrated that zinc oxide NPs have the potential of producing a difference within the dielectric properties when dispersed in high dielectric constant medium i.e. water. It is possible that this difference is observed with zinc oxide NPs because of the nanomaterial's polar surfaces. We could see an increase within the dielectric properties of ZnO in water after they had been PEGylated because of colloidal stability. The concentration of NPs effects the dielectric properties of the medium, however the linearity of concentration is dependent on the resolution of the measurement technique. We also showed that ZnO-PEG NPs showed a potential increase in the dielectric properties within a low dielectric constant medium and in TM phantom. These results suggest that ZnO NPs are promising candidates as contrast agents for microwave medical diagnostic applications.

5 Iron oxide and ferrite NPs as potential contrast agents for MWI

5.1 Introduction

Iron oxide NPs have attracted a lot of attention in nanomedicine due to their unique properties such as being superparamagnetic, tuneable surface-to-volume ratio, large surface area and easy preparation and separation methodology [218]. Iron and oxygen chemically combine to form iron oxides (compounds), and there are ~16 identified iron oxides [219]. Iron (III) oxide is found in the form of rust. The three most common forms of iron oxides in nature are magnetite (Fe_3O_4), maghemite (γ-Fe_2O_3), and hematite (α-Fe_2O_3). Hematite is also known as ferric oxide. Magnetite is also known as black iron oxide and exhibits the strongest magnetism. The magnetism in materials arises from the magnetic moment of electrons [220].

The iron oxide nanocrystal with controllable size and shape have attracted the interest of many researchers because of their microwave absorption properties. The large surface area of nanocrystals has several dangling bonds which increase the interfacial polarisation and multiple scattering to improve microwave absorption [221][222]. Liu *et al.*, showed that a large surface area and shape of polycrystalline Fe_3O_4 contributed significantly to enhance the microwave absorption properties.

Bucci *et al.* studied the potential use of magnetic NPs (MNPs)as contrast agents, and their work has been discussed in chapter 1. In these studies it was proposed that contrast enhanced MWI can be achieved by exploiting MNPs to induce a magnetic contrast localized in a tumour, due to non-magnetic behaviour of human body[84][223][81]. MNPs are already approved as a contrast agent for MRI and magnetic hyperthermia. There are three main types of hyperthermia: A) local hyperthermia, B) regional hyperthermia, and C) whole-body hyperthermia. In a whole-body hyperthermia, the entire body is heated up, but this can lead to major side effects given the fact that heating is not selective. Regional hyperthermia is used to deliver heat to advanced stage tumours. For regional hyperthermia, applicators such as microwave antenna are used for regional hyperthermia. Local hyperthermia is used to treat localised tumours. This is based on transmitters

emitting high energy microwaves, radio waves or ultrasound. Innovative technology where MNPs have been proposed to mediate heat, are called magnetic fluid hyperthermia (MFH)[224]. MFH consists of a colloidal suspension of MNPs, which is injected into a tumor. A Magnetic field is applied, which will cause the NPs to heat up and eventually kill cancer cells. MNPs in comparison with other metal oxides are superior in terms of biocompatibility and stability[225]. Due to many advantages MNPs possess, we decided to explore them further for their potential use as contrast agents for MWI.

Several methods like thermal decomposition, co-precipitation, sol-gel, microemulsion, hydro-thermal, sonochemical, microwave, electrochemical and biosynthesis were evolved to synthesize iron oxide NPs [226]. However, the relationship between size, shape, and magnetism in iron oxide NPs play a very important role in exhibiting their properties. Fe_2O_3 and Fe_3O_4 NPs display different ferrimagnetism at room temperature. Iron oxide NPs tend to lose their dispersion due to aggregation of particles and their magnetism gets diminished due to oxidation with air. Many approaches have been used to chemically stabilize these NPs, such as the use of a surfactant or chemical functionalization of MNPs to overcome physicochemical issues and promote biocompatibility and targeting.

5.1.1 Structure of iron oxide NPs used in biomedicine

The crystal structure of the three iron oxides can be described in terms of close-packed planes of oxygen anions with iron cations in octahedral or tetrahedral interstitial sites.

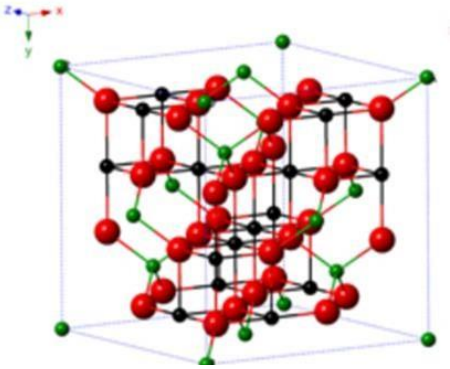

Figure 5-1: Crystal structure of magnetite [16]. The black spheres represent Fe^{2+}, the green spheres represents Fe^{3+} and, the red spheres represent O^{2-} [16].

Within the hematite, oxygen ions are in a hexagonal close-packed arrangement, with Fe(III) ions in the octahedral sites. In magnetite and maghemite, the oxygen ions are in a cubic close-packed arrangement. Magnetite is a mixed $Fe^{2+}$and Fe^{3+} oxide in a ratio of 1:2. It has an inverse spinel structure with Fe (III) ions distributed randomly between octahedral and tetrahedral sites, and Fe(II) ions in octahedral sites [227].

The crystal structure of the three iron oxides can be described in terms of close-packed planes of oxygen anions with iron cations in octahedral or tetrahedral interstitial sites. Within the hematite, oxygen ions are in a hexagonal close-packed arrangement, with Fe(III) ions in the octahedral sites. In magnetite and maghemite, the oxygen ions are in a cubic close-packed arrangement. Magnetite is a mixed $Fe^{2+}$and Fe^{3+} oxide in a ratio of 1:2. It has an inverse spinel structure with Fe(III) ions distributed randomly between octahedral and tetrahedral sites, and Fe(II) ions in octahedral sites [227].

Maghemite has a spinel structure which is like that of magnetite but with vacancies in the cation sublattice. Spinal ferrites possess the crystal structure of the natural spinel AB_2O_4, first determined by Bragg *et al.*,[228]. In the spinel structure of general formula AB_2O_4 there are twice as many octahedral (B) sites as tetrahedral (A) sites. If M^{2+} (metal ion) occupies only the A sites, the spinel is normal; and if it occupies only the B sites, the spinel is inverse[229]. A and B are tetrahedrally and octahedrally coordinated cations and O is the anion, respectively. Two-thirds of the sites are filled with Fe(III) ions arranged regularly, with two filled sites being followed by one vacant site [219].

Magnetite NPs (Fe_3O_4) has a face cantered cubic spinel structure on 32 O^{2-}ions and close-packed along the [111] direction. Fe_3O_4 differs from other iron oxides because it contains both divalent and trivalent iron. Fe_3O_4 has a cubic inverse spinel structure that consists of a cubic close-packed an array of oxide ions, where all the Fe^{2+}ions occupy half of the cathedral sites and the $Fe^{3+}$are split evenly across the remaining octahedral and tetrahedral sites [230]. As mentioned above,

magnetite crystallizes in an inverse spinel structure ($[Fe^{3+}]A[Fe^{2+}Fe^{3+}]BO_4$) where A is the tetrahedral site and B is the octahedral site. The valence band of O (2p) to the empty Fe (4s) is separated. Between these bands, crystal field-bands of the octahedral and tetrahedral sites appear. Therefore, because of an excitation (such as MW irradiation), electron transfer may appear from the O (2p) band to the empty Fe (4s) orbital [231]. This mechanism can be advantageous from a MWI point of view.

Metal spinel ferrites NPs have a general molecular formula MFe_2O_4 (e.g. M (metal) = Zn, Ni, Co, Mn or Mg), and they have a face-centered-cubic (fcc) close packing structure [232]. Among the spinel ferrites already known, zinc ferrites have been studied extensively and getting a lot of attention due to their applications in magnetic resonance imaging (MRI) as a contrast agent. due to their high electromagnetic performance, excellent chemical stability, making it a suitable candidate for being a low loss material which is useful for MWI purposes[232].

5.1.2 Superparamagnetic iron oxide (SPION) and ferrite NPs biomedical applications

SPIONs have been extensively studied for their remarkable diagnostic, practical and therapeutic applications in the biomedical field and their biocompatibility has already been proven [233]. SPIONs have attracted a lot of attention for protein immobilization, thermal therapy, drug delivery cancer treatment, tissue repair, cell labelling and magnetic cell sorting [234]. One of the most intriguing applications of SPIONs as mentioned above is as an MRI contrast agent for cancer diagnosis [235]. SPIONs also act as probes in positron emission tomography (PET), near-infrared fluorescence (NIRF) imaging, and in biosensors for detection of biomolecules like glucose, proteins, urea, and uric acid. They can also be used as nano-carriers, for enhancing the drug activity in combination therapy or as hyperthermia agents [236]. In 1957, Gilchrist et al., showed that lymph nodes could be heated to kill lymphatic metastases after the administration of MNPs. In the mid-1990s, the idea of using NP hyperthermia was revisited. This method involved the

injection of MNP directly into the tumors and exciting these NPs with alternating magnetic fields to produce heat. Further progress has been made in directing NPs to tumors with targeting agents such as antibodies [237].

SPIONs provide significant advantages over traditional contrast agents, including high magnetic signal strength, relatively low cytotoxicity, longer lasting contrast enhancement, improved delineation of tumor margins and low sensitivity to the number of water molecules around them [238]. Studies have also shown that the iron released from degrading SPIONs are metabolized by the body, reducing the potential for long-term cytotoxicity and small iron oxide particles have been applied in vitro diagnostics for nearly 40 years [239]. SPIONs have had practical applications such as in magnetic cell targeting, ferrofluids and catalysis [240][241]. In addition to therapeutic applications in drug delivery and hyperthermia [242][243]. They are unique in that they exhibit paramagnetism. In definition, this means that the individual atomic magnetic moments of the particles are randomly aligned with each other producing a zero-net magnetic moment. On exposure to an external magnetic field, some of these moments align and constitute a net magnetic moment. Once functionalized, they are known to be tolerated well by the human body and constitute a favourable biocompatibility profile [244]. Due to many qualities that MNPs possess, we decided to study the effect of these particles on the dielectric properties at MW frequencies.

5.2 Study objectives

In this study, we perform experiments to understand the potential of iron oxide and ferrite NPs as dielectric contrast enhancers. The aim of this chapter is to investigate the effect on dielectric properties of a medium of a) commercially available iron oxide NP b) in-house synthesized zinc ferrites with varying concentrations of zinc and coated with a polymer.

5.2.1 Aims of the study

1. To synthesize SPION functionalized with Polymaleic Anhydride-alt-1-octadecane. [Fe_3O_4]-PMAO and Zinc ferrites-PMAO – 1) [($Zn_{0.18}Fe_{0.82}$) Fe_2O_4]-PMAO and 2) [($Zn_{0.39}Fe_{0.61}$)Fe_2O_4]-PMAO.

2. To characterize the amount of zinc (Zn) and iron (Fe) present within different compositions of zinc ferrites via TXRF (total reflection X-ray fluorescence)

3. To characterize the size and structure of iron oxide NPs from Sigma Aldrich (SA), Sienna$^+$, Liquid Research (Water based ferrofluid; FF), SPION functionalised with poly(maleic anhydride-alt-1-octadecene); [Fe_3O_4]-PMAO and Zinc ferrites- PMAO 1) [($Zn_{0.18}Fe_{0.82}$)Fe_2O_4]-PMAO and 2) [($Zn_{0.39}Fe_{0.61}$)Fe_2O_4]-PMAO via SEM.

4. To characterize the colloidal stability of NPs via UV-Vis and DLS

5. To characterise the dielectric properties of Sigma Aldrich (SA), Sienna+, Liquid Research (Ferrofluid; FF) and, SPION functionalized with poly(maleic anhydride-alt-1-octadecene); [Fe_3O_4]-PMAO, and Zinc ferrites-PMAO; 1) [($Zn_{0.18}Fe_{0.82}$)Fe_2O_4]-PMAO and 2) [($Zn_{0.39}Fe_{0.61}$)Fe_2O_4]-PMAO ; in A) water and B) 60% glycerol from 1-4 GHz.

6. To characterize the dielectric properties of SPION functionalized with poly(maleic anhydride-alt-1-octadecene); [Fe_3O_4]-PMAO and Zinc ferrites-PMAO; 1) [($Zn_{0.18}Fe_{0.82}$)Fe_2O_4]-PMAO and 2) [($Zn_{0.39}Fe_{0.61}$)Fe_2O_4]-PMAO in TM (tissue mimicking) phantom from 1-4 GHz.

5.3 Description of commercial iron oxide NPs studied

5.3.1 Commercially available or clinically tested Sienna$^+$ from Endomagnetics

Superparamagnetic iron oxide nanoparticles (SPION) were obtained from Endomagnetics Ltd. and are being used for the detection of infiltrated lymph nodes using

magnetometry. Sienna$^+$ is a black-brown solution containing dextran (a water-soluble polysaccharide) coated SPION particles. The carboxydextran coating prevents the particles from agglomerating and allows particles to have biocompatible properties. Stated manufacturer size of SPION particles is known to be of size 60 nm with 5 nm dextran coating. These particles were supplied at a stock concentration of 28 mg/mL [245][246].

Clinically Sienna$^+$ are injected into the breast, they drain through the lymphatics and accumulate in the sentinel node (SN). Sentinel lymph node biopsy is used to evaluate axillary staging for clinically node-negative breast cancer. Since the solution is dark brown, and the nodes are often coloured, which helps the surgeon to identify the SN visually. A handheld probe, SentiMag is used to identify the Sentinel nodes [247].

5.3.2 FF obtained from Liquid Research UK

Water-based ferrofluids (FF) were obtained from Liquid Research Ltd. Ferrofluids are stable colloidal dispersions of magnetic (Fe_3O_4) particles. Particles are held in water suspension by a dispersing agent (anionic surfactant with a carboxylate group end). Stated manufacturer size of these particles is 10 nm[248].

5.3.3 Iron oxide – SA

Iron (II, III) oxide were obtained from Sigma Aldrich (SA). Stated manufacturer size was between 50-100 nm confirmed by SEM. These are just basic NPs without any surface modifications.

5.4 Results (I) – Commercial iron oxides

5.4.1 Morphology and colloidal stability analysis using DLS, UV-Vis and SEM

5.4.1.1 UV-Vis analysis of the colloidal stability commercial iron oxide NPs

To understand the aggregation properties over time UV-VIS light transmission was employed.

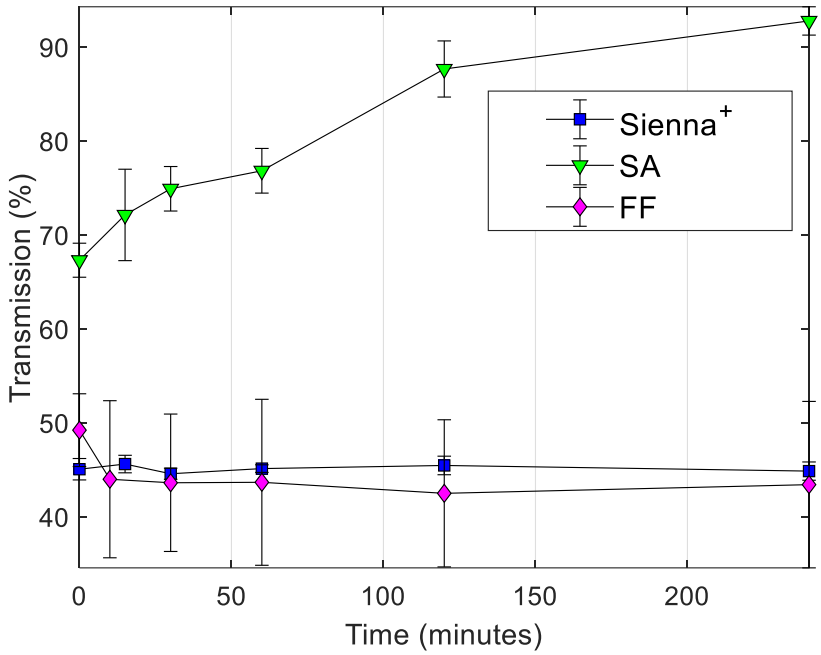

Figure 5-2: UV-Vis analysis of iron oxide Sienna+, FF and SA, at a wavelength (λ) of 415nm. The measurements were taken over a 4-hour period n=6 +/-SD.

A vertical cuvette was used, and light transmittance was measured over time. If NPs aggregate and precipitate the solution becomes clear and light transmittance increases.

Commercial iron oxide NPs were dispersed in water at a concentration of 1 mg/mL and serially diluted to 10 μg/ml and after brief sonication light transmission was measured at different time points. Increase in the transmission indicates aggregation of NP suspensions. Transmission of light (Fig. 5-2) through SA NPs increases to almost 100% over a period of 4 hours, suggesting aggregation and precipitation of iron oxide NPs in water. However, FF and Sienna$^+$ had a transmission of light between 40-50%. Transmission for both ferrofluid and Sienna$^+$ remained similar throughout 4 hours suggesting these particles are much more stable in water compared to

SA. Ferrofluid NPs have a presence of anionic surfactant (not disclosed) within their dispersion and Sienna$^+$ NPs have carboxy-dextran coating around them, hence increasing the stabilization of the NPs compared with iron oxide (sigma) NPs.

5.4.1.2 DLS assessment of nanoparticle size over time

Values of PDI (Fig. 5.3) ranges from 0 to 1; a PDI value smaller than 0.1 shows the sample is nearly monodisperse, while a PDI equal to 1 indicates the sample has a large variation in particle size. The PDI values for both FF and Sienna$^+$ are between 0.25-0.45. However, PDI for SA (Fig. 5.4) is 1 suggesting very large aggregates forming over time. Results of DLS obtained for FF, Sienna$^+$ and, SA have been further tabulated in Table 1.

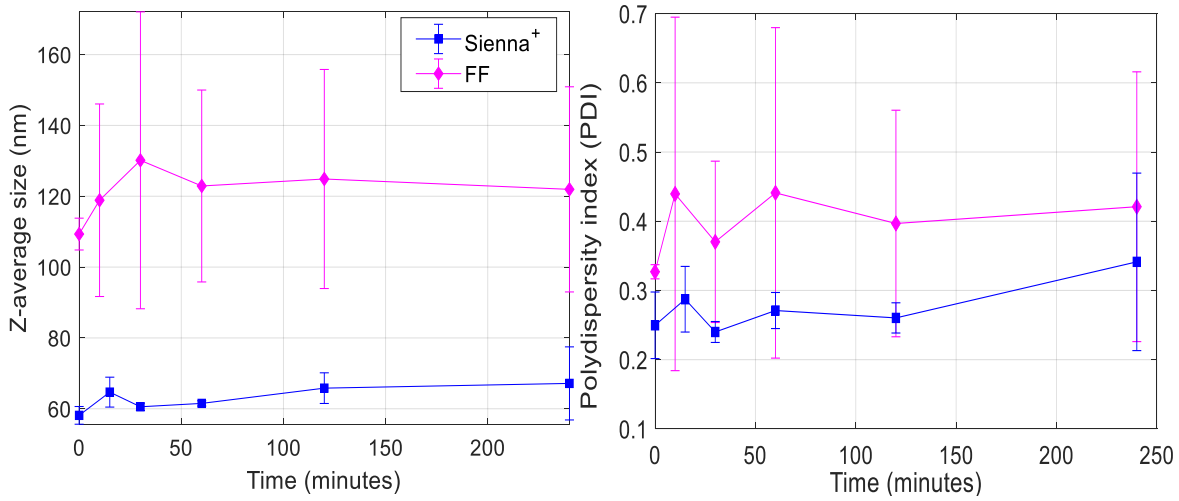

Figure 5-3: Z- average size and PDI of Sienna$^+$ and FF over a period of 4 hours n=6+/-SD

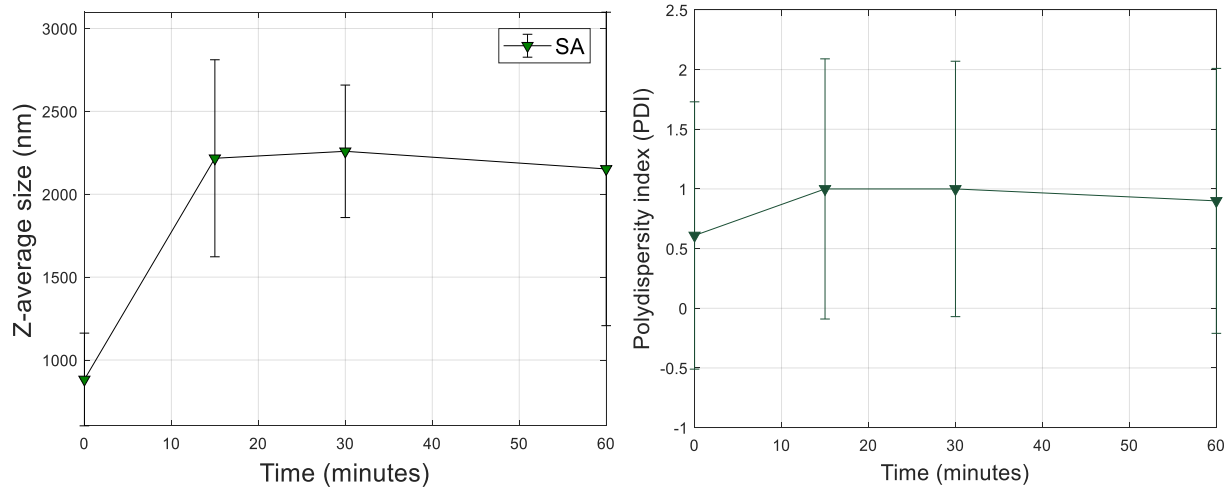

Figure 5-4: Z- average size and PDI of SA over a time of 4 hours with a sample n=6+/-SD

Results in Table 5-1 confirm that SA NPs showed poor compatibility in water. The polydispersity index (PDI) at t_0 showed that the particles instantly aggregate causing large variation of particle size, while after t_{60} most of the particles have sedimented. Sienna$^+$ and FF showed better colloidal stability. This can be explained by the presence of an anionic surfactant with FF and the presence of carboxydextran coating with Sienna$^+$.

Table 5-1: Size (nm) and PDI obtained at t_0 and t_{60} for commercial magnetite's via DLS

Magnetite	Size (nm)	PDI (t_0)	PDI (t_{60})
SA	-	0.95±0.11	-
Sienna$^+$	64.74±3.22	0.25±0.02	0.24±0.05
FF	118.88±27.18	0.33±0.08	0.71±0.12

5.4.1.3 SEM analysis

Further analysis of all iron oxide NPs was characterized for their size chemical stability morphology using scanning electron microscopy (SEM). For SEM analysis, 1 mg/mL for each NP suspension was prepared. This was an optimal concentration to be used for SEM imaging purposes. Results in Figure 5-5 show the surface morphology of Sienna$^+$, FF, and SA. The SEM images show that samples exhibit a compact arrangement of homogeneous NPs and are spherical in shape. The average particle size of SA, FF, and Sienna$^+$ is 47.52±7.61, 73.93±6.20, and 61.46±9,02, respectively.

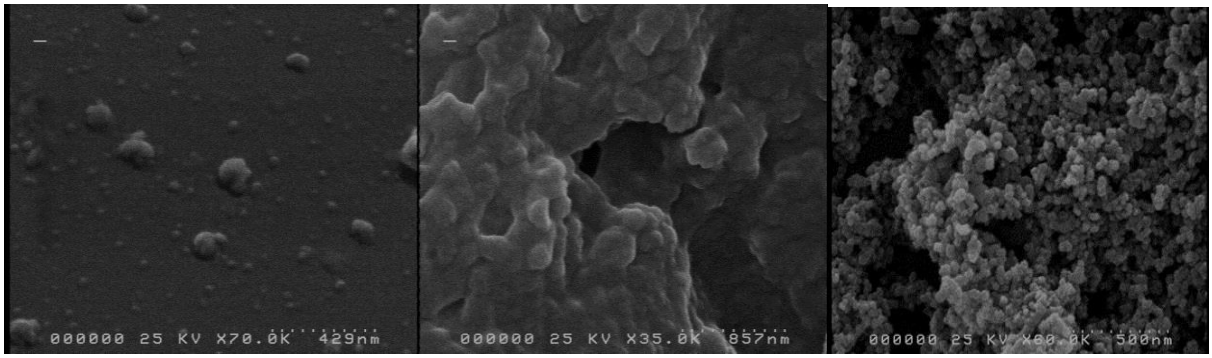

Figure 5-5: The surface morphology is observed from SEM. SEM images of Sienna$^+$ (left), FF (middle) and SA (right). Images were taken at room temperature and in a vacuum environment with a Hitachi scanning electron microscope (S4000 FEG SEM with Oxford Instruments INCA EDX).

5.5 Dielectric properties of commercial iron oxide nanoparticle suspension at different concentrations in water

5.5.1 Dielectric properties of SA at different concentrations in water

Dielectric constant of SA at 2, 1, 0.5 and 0.25 mg/mL is 79.99±0.09, 80.19±0.02, 80.71±0.02 and 80.34±0.04 at 1.18GHz compared with water which has a dielectric constant of 78.61±0.16 at 1.18GHz. The maximum average change in epsilon was -0.85% at 2 mg/mL (f=1.12GHz), 2.095 at 1 mg/mL (f=1.12GHz), 2.68% at 0.5 mg/mL; f=1.18GHz) and 2.27 at 0.25% mg/mL (f=1GHz).

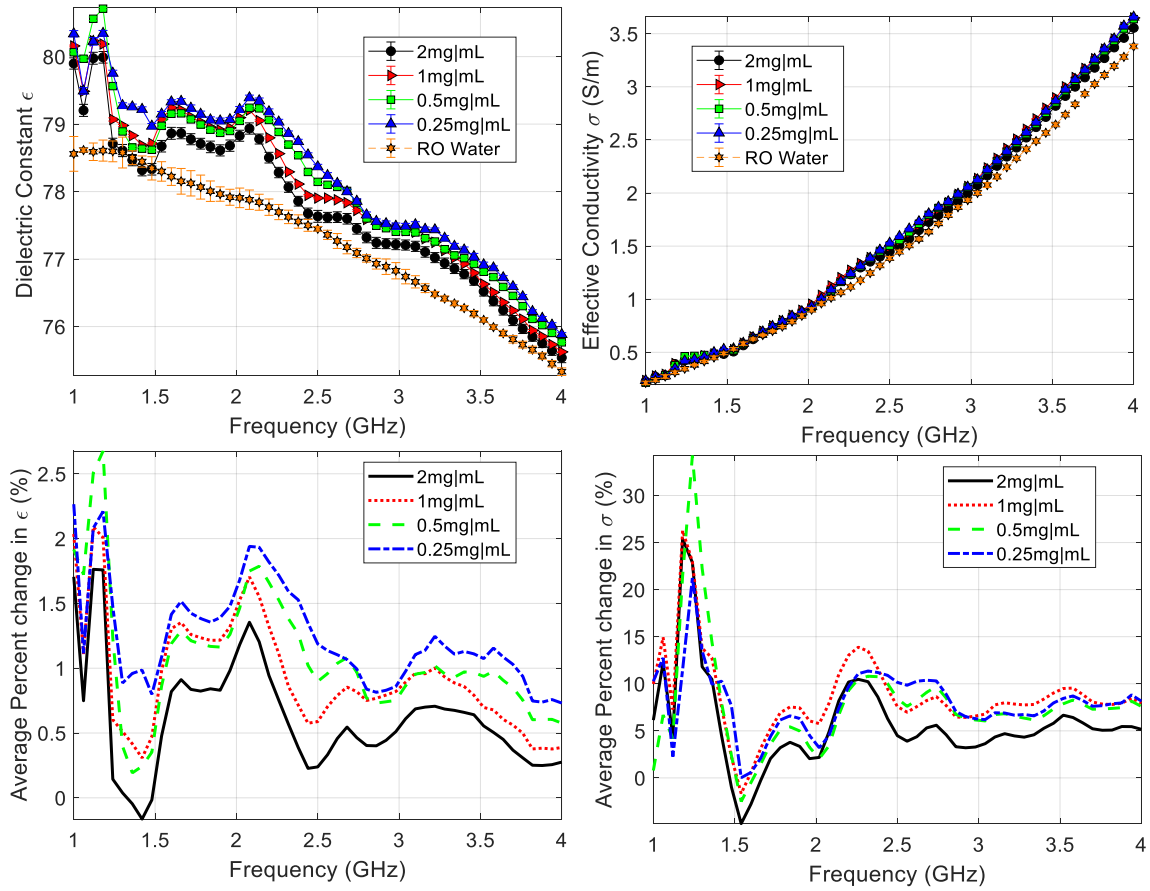

Figure 5-6: (a) dielectric constant, (b) effective conductivity, (c) average change in epsilon and (d) average change in sigma of colloidal dispersion of SA at different concentrations in RO water characterised between 1- 4 GHz. Each curve represents the average of three different samples (n=3+/- SD)

Results tabulated in table 5-2 show that the average change in dielectric constant of SA at 0.25 mg/mL was the highest across the frequency range compared with other concentrations. The highest average change in sigma of 34.23% was observed for SA at 0.25 mg/mL.

Table 5-2: Average percent change in epsilon of SA at concentrations of 2, 1, 0.5,0.25 mg/mL at frequency range between 1-4GHz

Frequency (GHz)	2mg/mL	1mg/mL	0.5mg/mL	0.25mg/mL
1	1.92	2.04	1.93	2.27
2	1.46	1.53	1.47	1.69
3	0.86	0.82	0.76	0.87
4	0.58	0.39	0.58	0.74

From the results obtained it can be concluded that lower the concentration of SA, higher is the average change in epsilon, suggesting aggregation and flocculation of NPs at higher concentrations is more dominant, hence in this situation a lower concentration of the nanomaterial might be useful to observe the desired change.

SA samples were necessary to study to make a comparison between particles which are not stable in suspension and particles which are stable ins suspension, such as Sienna^{+} and FF. But, these SA particles have no translational potency and due to their bad stability cannot be used for clinical applications.

5.5.2 Dielectric properties of Sienna$^+$ at different concentrations in water

On the other hand, microwave properties of iron oxide (Sienna$^+$) in water from the frequency range of 1-4 GHz show a different dielectric behaviour (Fig. 5.8 and table 5.3). Overall, it can be said that the average change epsilon observed for iron oxide obtained from Sienna$^+$ is much higher than that of SA. This can be because of the higher stability of Sienna$^+$ NPs due to the carboxydextran coating.

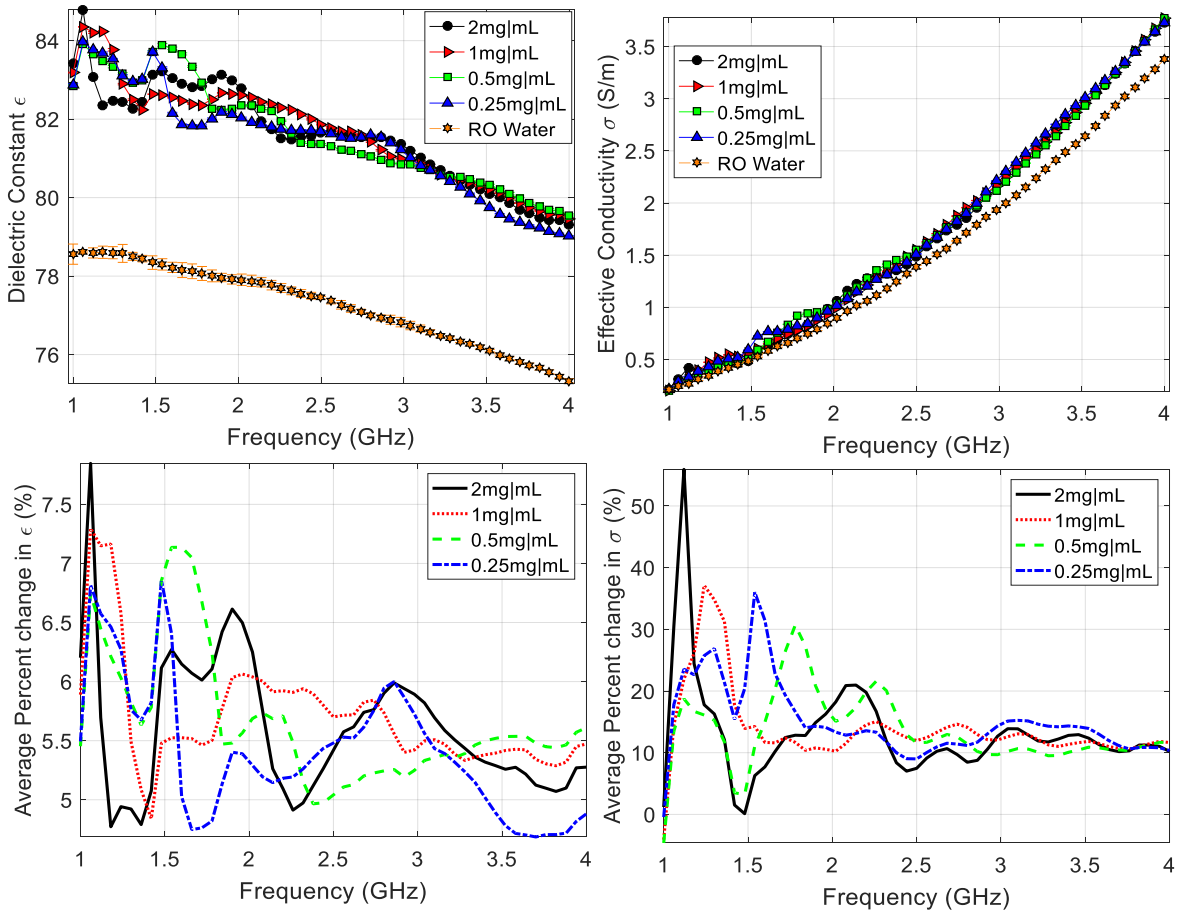

Figure 5-8: (a) dielectric constant, (b) effective conductivity, (c) average change in epsilon and (d) average change in sigma of colloidal dispersion of Sienna$^+$ at different concentrations in RO water characterised between 1- 4 GHz. Each curve represents the average of three different samples (n=3+/-SD).

The carboxydextran coating does two things; 1) Carboxydextran coating can be contributing to the overall polarisation of the NPs, hence increase in the dielectric properties observed and 2) coating of the NP allows better dispersion of the NPs in water hence sedimentation of the NPs is prevented therefore an increase in the dielectric properties is observed. The maximum average

change in epsilon of Sienna^{+} showed a change of 7.96% at 2 mg/mL(f=1.18GHz), 7.42% at 1 mg/mL(f=1.18GHz), 7.21% at 0.5 mg/mL(f=1.6GHz) and 6.91% at 0.25 mg/mL (f=1.5 GHz).

Table 5-3: average change in epsilon of Sienna+ at concentrations of 2, 1, 0.5, 0.25mg/mL at frequency range between 1-4 GHz

Frequency (GHz)	2mg/mL	1mg/mL	0.5mg/mL	0.25mg/mL
1	6.24	5.8	5.5	5.51
2	6.35	6.09	5.56	5.45
3	5.91	5.5	5.47	5.57
4	5.22	5.49	5.52	4.8

5.5.3 Dielectric properties of FF at different concentrations in water

Figure 5-9 & table 5-4 shows the microwave properties of ferrofluid (FF) in water at concentrations of 2, 1, 0.5 and 0.25 mg/mL from the frequency range of 1-4 GHz. The highest dielectric constant of FF at 2, 1, 0.5 and 0.25 mg/mL is 80.68±0.02 (f=1.18 GHz), 82.31±0.04 (f=1.12 GHz), 82±0.02 (f=1.18 GHz) and 82.39±0.03 (f=1.18 GHz) compared with water which has a dielectric constant of 78.61±0.16 at 1.18GHz. The maximum average change in epsilon was 2.63% at 2 mg/mL (f=1.18GHz), 4.49% at 1 mg/mL(f=1.12GHz), 4.32% at 0.5 mg/mL (f=1.18GHz) and 4.81% at 0.25 mg/mL(f=1.18GHz).

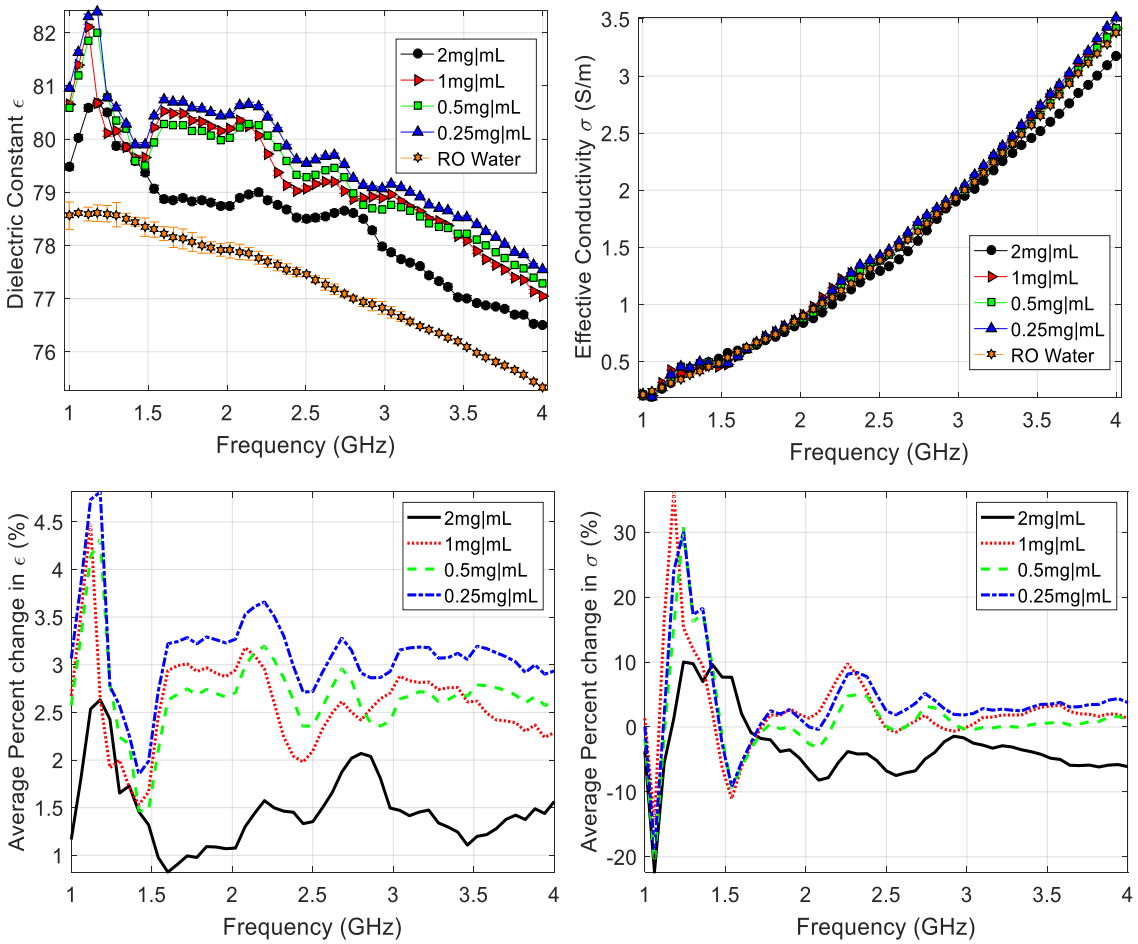

Figure 5-9: (a) dielectric constant, (b) effective conductivity, (c) average change in epsilon and (d) average change in sigma of colloidal dispersion of FF at different concentrations in RO water characterised between 1- 4 GHz. Each curve represents the average of three different samples (n=3+/-SD).

Results tabulated in table 5-4, suggest that the average change epsilon was highest at lower concentrations as seen with SA. The maximum average change in sigma of 36.19 was observed for 1 mg/mL of FF at 1.18 GHz, whereas the lowest average change in sigma of 1.32 was observed for 2 mg/mL of FF at a similar frequency.

Table 5-4: average change in epsilon of FF at concentrations of 2, 1, 0.5, 0.25mg/mL at frequency range between 1-4 GHz

Frequency (GHz)	2mg/mL	1mg/mL	0.5mg/mL	0.25mg/mL
1	1.16	2.67	2.57	3.07
2	1.08	2.95	2.71	3.27
3	1.47	2.88	2.64	3.15
4	1.57	2.29	2.59	2.93

The dielectric constants of all commercial products show irregular patterns of undulation, approximately between 1-2 GHz. This is a characteristic for VNA measurements in water or mediums with high dielectric constant. This behaviour disappears with a low dielectric constant medium such as 60% glycerol or even in TM phantom. These undulations in water become more prominent in the presence of NPs. This is because the coaxial probe assumes that NPs under test are homogenous, which is not generally achieved with water, hence errors are more pronounced in the case where NP's are not dispersed homogenously.

5.6 Dielectric properties of commercial iron oxide nanoparticle suspension in 60% Glycerol

5.6.1 Dielectric properties of iron oxide (sigma), iron oxide (Sienna$^+$) and Ferrofluid at different concentrations in 60% glycerol

Not many studies have been carried out where the dielectric properties of NP inclusion in 60% glycerol have been measured. However, Semenov et al., carried out a study where ferroelectric such $BaTiO_3$ and $CaTiO_3$ in glycerol for potential contrast enhancement for microwave tomography purposes were tested.

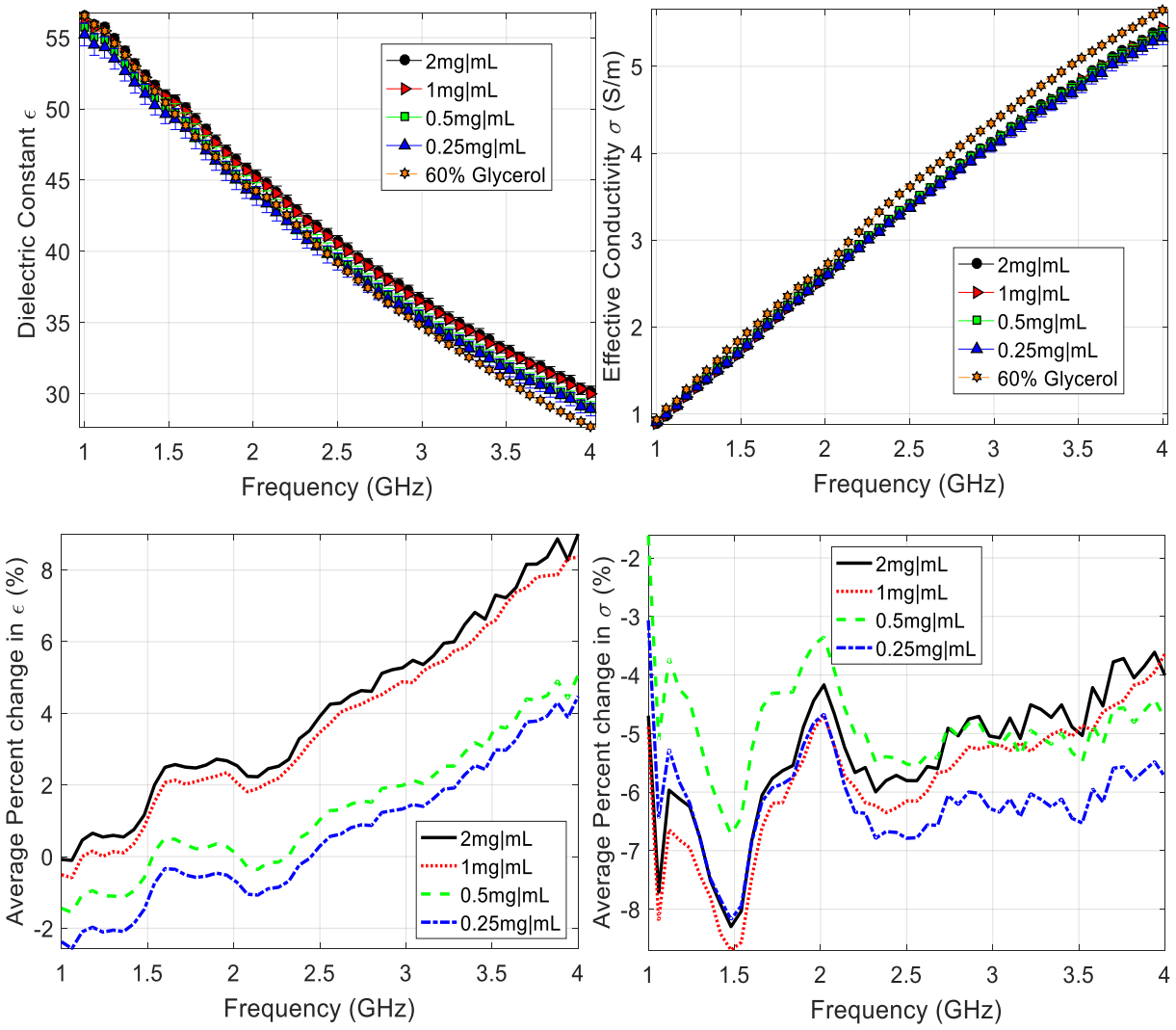

Figure 5-10: : (a) dielectric constant, (b) effective conductivity, (c) average change in epsilon and (d) average change in sigma of colloidal dispersion of SA at different concentrations in 60% glycerol characterised between 1- 4 GHz. Each curve represents the average of three different samples

The concentration of materials used was not disclosed. Dielectric properties of both ferroelectrics were measured in glycerol at 1 and 2.45 GHz and an increase in the dielectric properties after the inclusion of NPs was observed [249]. 60% glycerol was studied, because it approximately mimics the properties of a tumor, and it was important to understand the behaviour of NPs in a low dielectric constant medium.

Table 5-5: Average change in epsilon of SA at concentrations of 2, 1, 0.5, 0.25mg/mL at frequency range between 1-4 GHz in 60% glycerol.

Frequency (GHz)	2mg/mL	1mg/mL	0.5mg/mL	0.25mg/mL
1	-0.08	-0.51	-1.44	-2.38
2	2.54	2.05	0.07	-0.73
3	5.48	4.85	2.13	1.45
4	9.01	8.36	5.08	4.48

Overall, it was observed that the average change of epsilon was much higher in 60% glycerol than in water for all the nanomaterials. Dielectric properties result obtained for nanomaterial in 60% glycerol shows a linear dependency with concentrations, i.e. higher the concentration of NPs higher are the dielectric properties compared with dielectric properties in water. The maximum average change of dielectric constant observed with SA with 60% glycerol (Fig. 5.10) was 9.01% (2 mg/mL), 8.36% (1 mg/mL), 5.08% (0.5 mg/mL) and 4.48% (0.25 mg/mL) at 4 GHz (Table 5-5).

Figure 5.11 shows the dielectric properties of Sienna^{+} in 60% glycerol. Maximum dielectric constant of 58.56±0.02, 56.89±0.02 and 56.57±0.01 was observed at 1, 0.5 and 0.25 mg/mL.

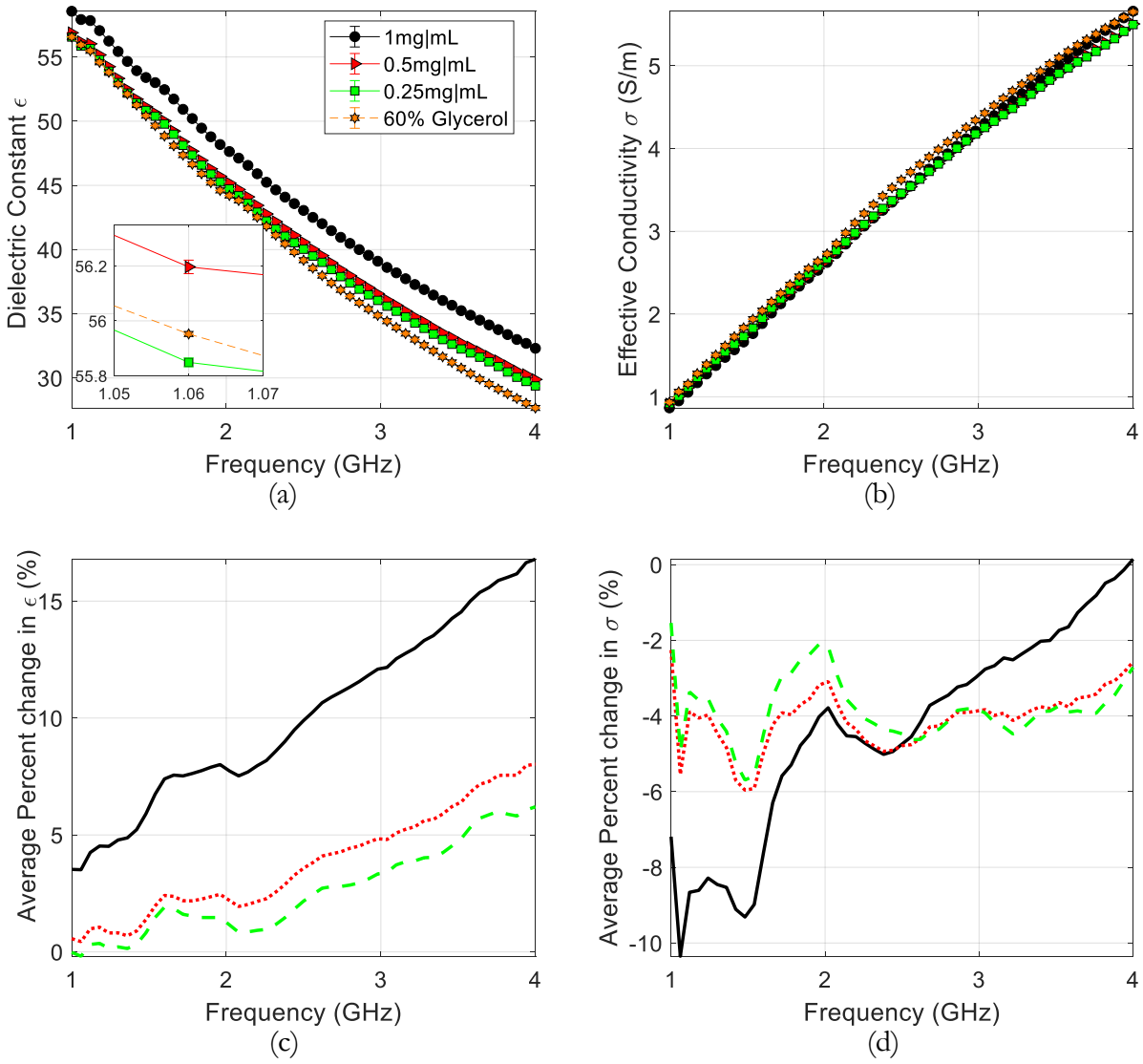

Figure 5-11: (a) dielectric constant, (b) effective conductivity, (c) average change in epsilon and (d) average change in sigma of colloidal dispersion of Sienna$^+$ at different concentrations in 60% glycerol characterised between 1- 4 GHz. Each curve represents the average of three different samples (n=3+/-SD).

The maximum average change in dielectric constant of 16.79% (1 mg/mL), 8.03% (0.5 mg/mL), 6.20% (0.25 mg/mL) was observed at 4 GHz for Sienna$^+$ in 60% glycerol.

FF have been studied previously by Bucci *et al.*, where they were dispersed in PBS (phosphate buffer saline). Dielectric properties in that study were measured at a concentration of 25 mg/mL from 0.1-8 GHz to observe potential dielectric and magnetic contrast [83]. Since these particles had already been studied before, dielectric properties of FF were further characterized in 60% glycerol.

Table 5-6: Average change in epsilon of sienna+ at concentrations of 2, 1, 0.5, 0.25mg/mL at frequency range between 1-4 GHz in 60% glycerol

Frequency (GHz)	1mg/mL	0.5mg/mL	0.25mg/mL
1	3.52	0.57	-0.02
2	7.74	2.20	1.16
3	12.17	4.80	3.40
4	16.79	8.03	6.20

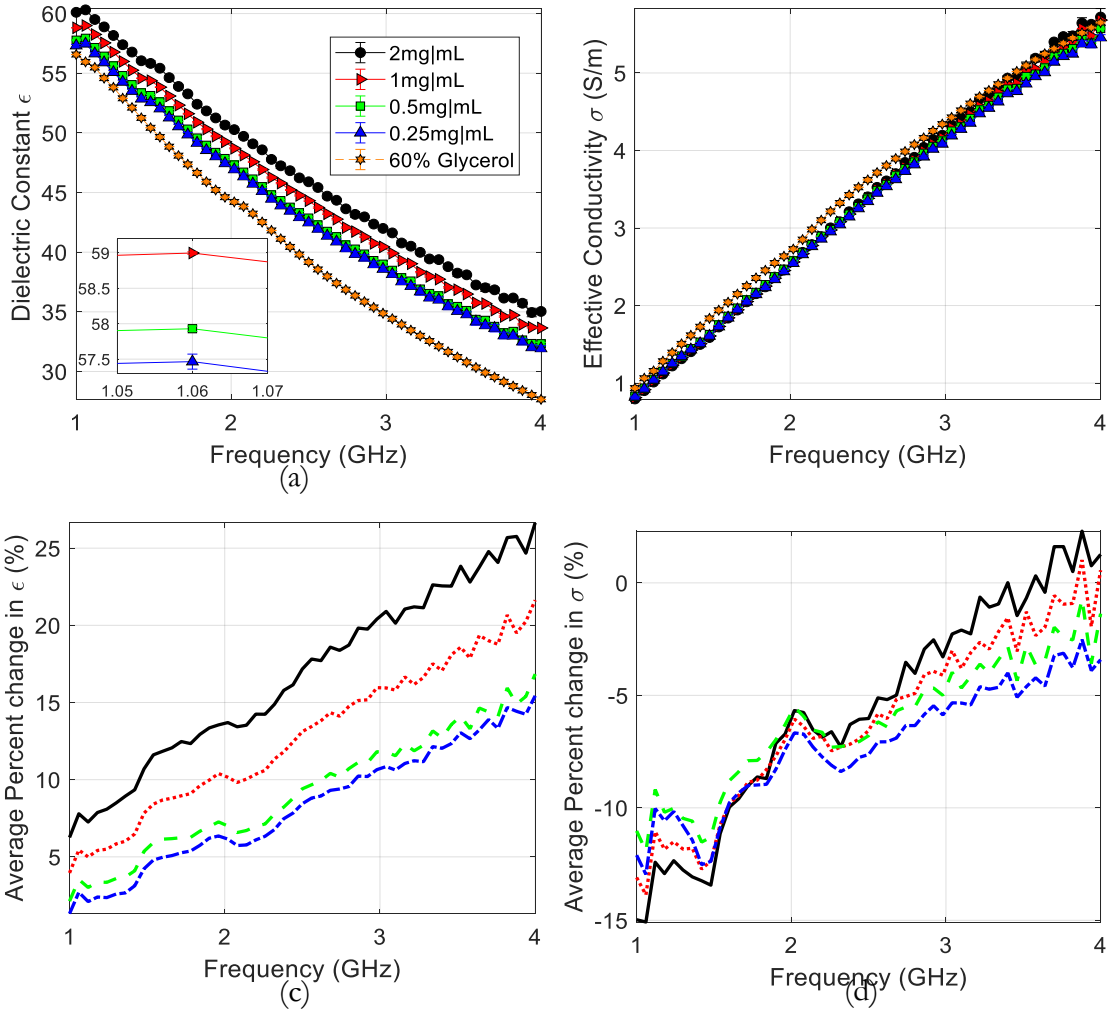

Figure 5-13: (a) dielectric constant, (b) effective conductivity, (c) average change in epsilon and (d) average change in sigma of colloidal dispersion of FF at different concentrations in 60% glycerol characterised between 1- 4 GHz. Each curve represents the average of three different samples (n=3+/-SD).

FF showed the maximum average change in dielectric constant compared with SA and Sienna^{+} at higher frequencies (Fig. 5.12). A maximum dielectric constant of 60.11±0.10, 58.81±0.01, 57.77±0.04 and 57.31±0.09 was observed for 2, 1, 0.5 and 0.25 mg/mL respectively at 1 GHz compared with the dielectric constant of 56.57±0.01 for 60% glycerol at similar frequency. Maximum average change in dielectric constant observed with FF was 26.64% (2 mg/mL), 21.635 (1 mg/mL), 16.84% (0.5 mg/mL) and 14.34% (0.25 mg/mL) at 4 GHz (Table 5.7).

Table 5-7: Average change in epsilon of FF at concentrations of 2, 1, 0.5, 0.25mg/mL at frequency range between 1-4GHz in 60% glycerol

Frequency (GHz)	2mg/mL	1mg/mL	0.5mg/mL	0.25mg/mL
1	6.25	3.96	2.13	1.32
2	13.70	10.16	7.00	6.15
3	20.90	15.94	11.79	10.84
4	26.64	21.63	16.84	15.43

5.7 Result (II)- Zinc ferrites with PMAO polymer

One type of SPION and two types of zinc ferrites (Table 5-8) was synthesized by the thermal decomposition method. Both SPION and Zn Ferrites were coated with PMAO. Addition of PMAO improved aqueous dispersion of ferrous nanoparticles.

Table 5-8: Different zinc ferrites prepared for this study. (AcAc stands for Acetal Acetate and PMAO stands for Poly (maleic anhydride-alt-1-octadecene)

Sample compositions	**$FeCl_2$**	**$Fe(AcAac)_3$**	**$ZnCl_2$**
Fe_3O_4 - PMAO	-	0.353g	-
$[(Zn_{0.18}Fe_{0.82})\ Fe_2O_4]$- PMAO	0.06g	0.353g	0.01g
$[(Zn_{0.39}Fe_{0.61})\ Fe_2O_4]$ - PMAO	0.04g	0.353g	0.03g

This section will be discussing the structural and dielectric characterization of different zinc ferrites in water, 60% glycerol and, tumor mimicking (TM) phantom. TM phantom study has been carried out only with zinc ferrites because other commercial iron oxide NPs, mentioned in the above section has been used for comparison and have been tested in two mediums. Our in-house synthesized SPIONs and zinc ferrites have the potential of being novel, biocompatible NPs for acting as potential contrast agents for MWI, hence it was important to measure the dielectric properties in TM phantoms as well. For the synthesis and functionalization of ferrites we used the methodology kindly provided by Prof N. Long and his team in Imperial College London. Based on their methodology, ferrites were synthesized and functionalised by me at King's College London.

5.7.1 Morphology and colloidal stability analysis of zinc ferrites via DLS, UV-Vis and SEM

5.7.1.1 UV-Vis analysis

To measure the stability of our synthesized NP, UV-Vis analysis was carried to measure their measure the stability over a period of 4 hours (Fig. 4-12).

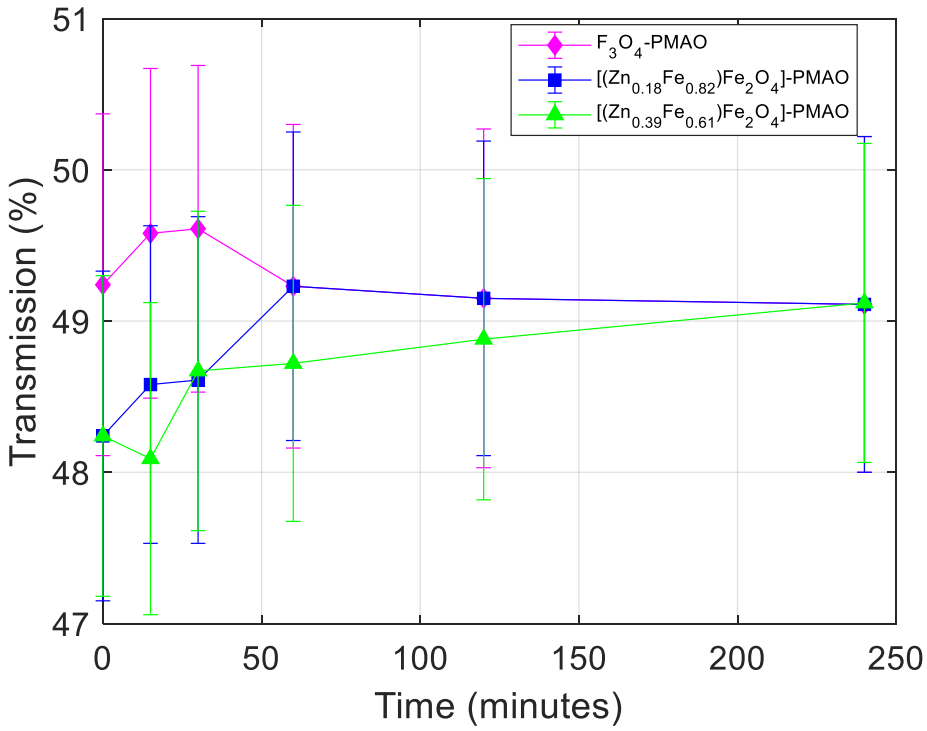

Figure 5-16: UV-Vis analysis of Fe_3O_4 – PMAO, [$(Zn_{0.18}Fe_{0.82})$ Fe_2O_4]- PMAO and, [$(Zn_{0.39}Fe_{0.61})$ Fe_2O_4] - PMAO at a wavelength (λ) of 415nm. The measurements were taken over a 4-hour period n=6 +/-SD.

2 mg/mL of each ferrite suspension was serially diluted to 20 μg/mL for UV-Vis measurement purposes. These particles seemed to be stable over a period of 4 hours and light transmission was similar to Sienna$^+$ NPs (Fig. 5-13). Transmission of light from Fe_3O_4 – PMAO, [$(Zn_{0.18}Fe_{0.82})$ Fe_2O_4]- PMAO and [$(Zn_{0.39}Fe_{0.61})$ Fe_2O4] – PMAO starts of at 49.24%, 48.24% and, 48.24% respectively. Fe3O4 – PMAO showed an increase in light transmission from 49.24% to 49.58% at 15 minutes. All three ferrites were found to have a light transmission of 49.12 at 4-hour time point. After 60 minutes there was stabilization in light transmission for all ferrites till 4-hour time point, suggesting stability of NPs in water.

5.7.1.2 DLS assessment of NPs in water over time

Figure 5-14 shows the DLS analysis of ferrites. For DLS analysis, similar concentration as UV-Vis was used. The PDI values range from 0 to 1. The PDI values of all ferrites are between 0.27 - 0.36. PDI value of Fe_3O_4 – PMAO is 0.35 at t_0 and increases to only 0.36 at 4- hour time point. [$(Zn_{0.18}Fe_{0.82})$ Fe_2O_4]- PMAO and [$(Zn_{0.39}Fe_{0.61})$ Fe_2O_4] – PMAO has a PDI of 0.34 at 4-hour time point. Overall, the PDI values of all the ferrites are stable of particles over a period of 4 hours

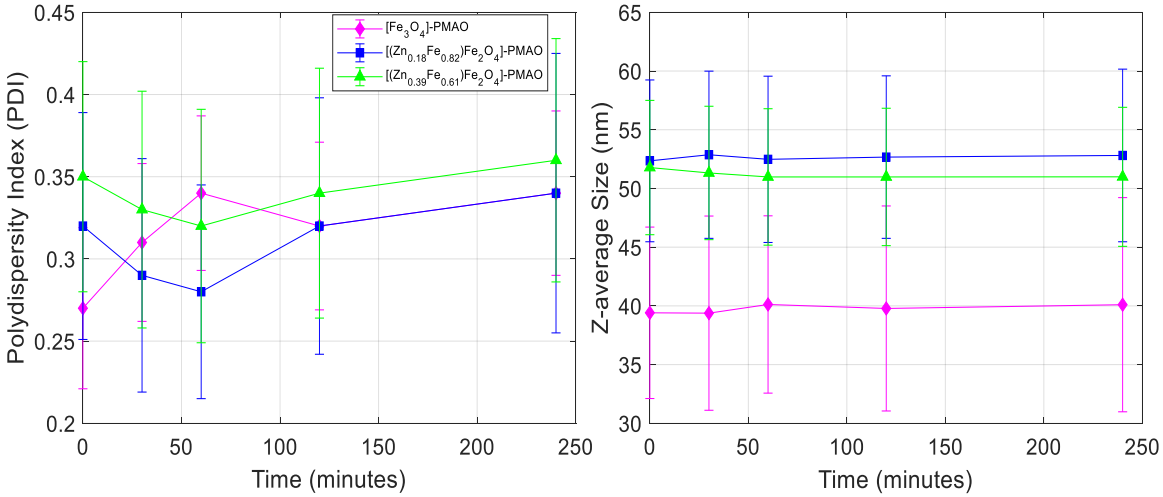

Figure 5-19: Z- average size and PDI of [Fe_3O_4]-PMAO, [$(Zn_{0.18}Fe_{0.82})Fe_2O_4$]-PMAO and [$(Zn_{0.39}Fe_{0.61})Fe_2O_4$]-PMAO over a period of 4 hours n=6+/-SD

5.7.1.3 SEM analysis

To characterize the surface morphology and the size of our in-house synthesized zinc ferrites, SEM was carried out (Fig. 5-15). For SEM analysis 2 mg/mL of each of the sample was used for characterization.

Most of the particles, from the image, seem to be aggregated, however, the average particle size of 35±3.6 nm, 45±6.5 nm, and 47±3.5 nm were obtained for [Fe_3O_4]-PMAO, [$(ZnO_{0.18}Fe_{0.82})$ Fe_2O_4]-PMAO and [$(Zn_{0.39}$ $Fe_{0.61})Fe_2O_4$]-PMAO respectively. From our DLS measurements the sizes observed were 39.41±7.3, 51.78± 5.7 and 52.35± 6.9 for [Fe_3O_4]-PMAO, [$(Zn_{0.18}Fe_{0.82})Fe_2O_4$]-PMAO and [$(Zn_{0.39}Fe_{0.61})Fe_2O_4$]-PMAO respectively. The slight increase in size observed with DLS compared with SEM could be because for SEM, samples are in a dry state.

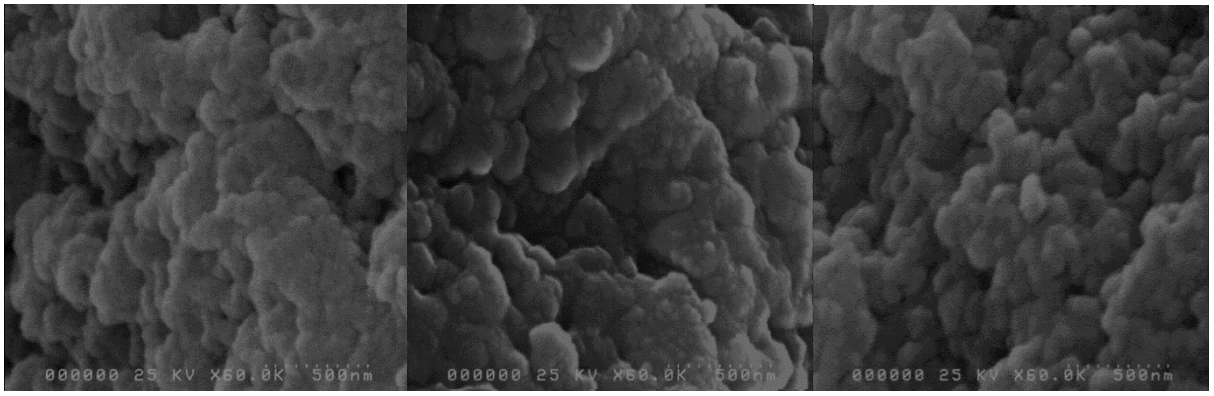

Figure 5-20: The surface morphology is measured via SEM. Fe_3O_4-PMAO (left), $[Zn_{0.18}Fe_{0.82}]Fe_2O_4$-PMAO (middle) and $[Zn_{0.39}\ Fe_{0.61}]Fe_2O_4$-PMAO (right). Images were taken at room temperature and in a vacuum environment

Whereas for DLS, samples are in a solvent (i.e. water) where there are solvent molecules associated with our NPs, hence a slight increase in our size is observed. Samples were prepared for TXRF analysis of metals and results were correlated with doping metal levels. For TXRF analysis, on prepared siliconized quartz discs, our samples were diluted with the standard gallium to achieve a concentration and pipetted the final solution on to those discs (detail methodology provided in chapter 6; material & methods). TXRF measurements were carried out by Bruker S2 Picofox. ICP-MS (Inductively coupled plasma mass spectrometry) is another technique which is used to detect the concentrations of metals. However, we decided to use TXRF because ICP-MS required high sample volume. Since high volume of sample was needed for ICP-MS, TXRF was chosen instead. Also, sample preparation for TXRF is easier than ICP-MS. TXRF was carried out to establish different concentrations in mM for Zn and Fe in each composition prepared. $[(Zn_{0.39}Fe_{0.61})Fe_2O_4]$-PMAO was prepared to have a higher concentration of Zn which was confirmed by TXRF analysis.

In the next section, dielectric properties of our in-house synthesized zinc ferrites in water, 60% glycerol and in TM phantom is discussed. Concentration dependency was not measured in this case, because it was important to understand the effect different amounts of zinc and iron within the composition have on the dielectric properties of mediums.

5.7.2 Dielectric properties of zinc ferrites in water, 60% glycerol and tissue-mimicking phantom

5.7.2.1 Dielectric properties of zinc ferrite suspensions in water

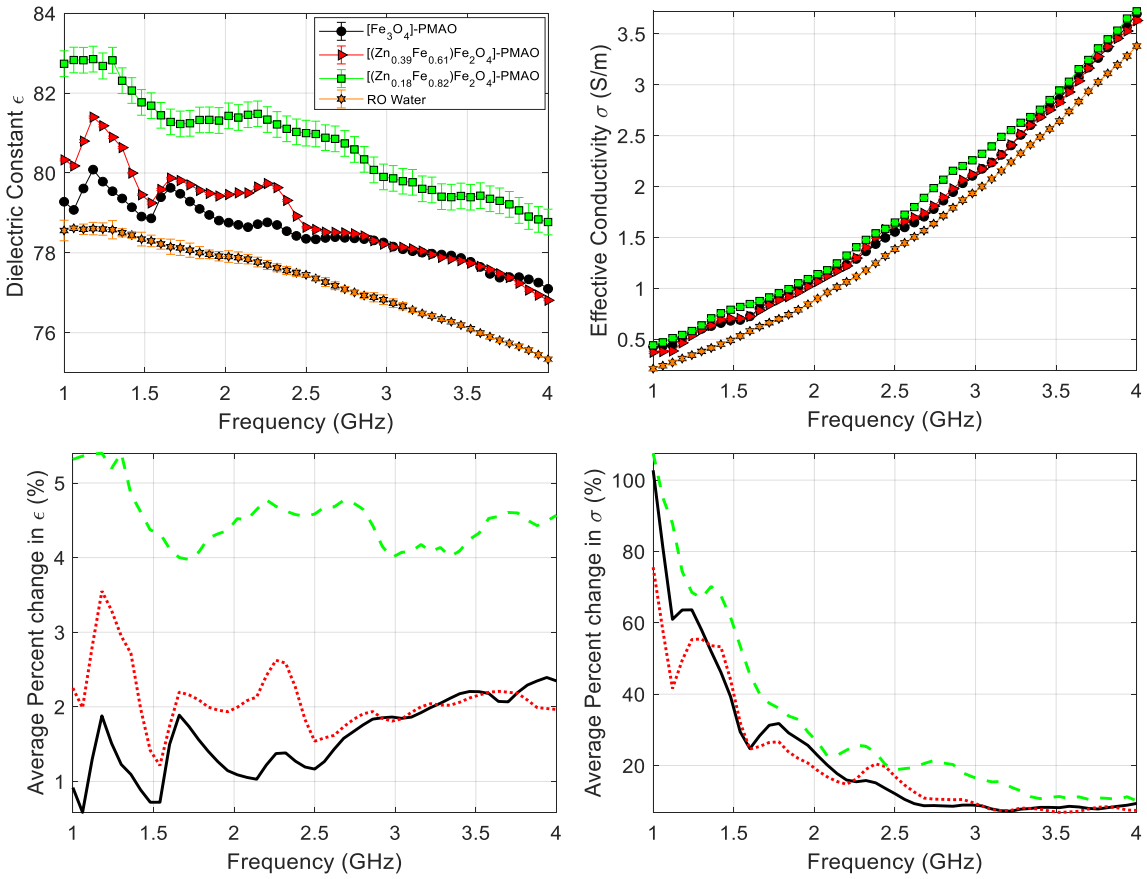

Figure 5-23: (a) dielectric constant, (b) effective conductivity, (c) average change in epsilon and (d) average change in sigma of Fe_3O_4-PMAO, $[Zn_{0.18}Fe_{0.82}]Fe_2O_4$-PMAO and $[Zn_{0.39}Fe_{0.61}]Fe_2O_4$-PMAO in water characterised at a concentration of 2mg/mL between 1-4 GHz. Each curve represents the average of three different samples, n=3+/-SD

Dielectric properties of "in-house" synthesized zinc ferrites at a concentration of 2 mg/mL was characterized between 1-4 GHz (Fig. 5-16). Iron oxide obtained commercially were used as our controls to compare the dielectric properties with our synthesized zinc ferrites coated with PMAO polymer. The maximum average change in the dielectric constant was 5.4%, 3.6% and 1.87% at 1 GHz for $[(Zn_{0.18}Fe_{0.82})Fe_2O_4]$-PMAO, $[(Zn_{0.39}Fe_{0.61})Fe_2O_4]$-PMAO and $[Fe_3O_4]$-PMAO respectively. Lowest average change was 4.57%, 1.96% and 2.35% at 4 GHz for $[(Zn_{0.18}Fe_{0.82})Fe_2O_4]$-PMAO, $[(Zn_{0.39}Fe_{0.61})Fe_2O_4]$-PMAO and $[Fe_3O_4]$-PMAO respectively. Maximum

dielectric constant was 80.08±0.02(1.18 GHz), 81.4±0.03 (1.18 GHz) and 82.82±0.32 (1.3 GHz) for Fe_3O_4-PMAO, [$(Zn_{0.39}Fe_{0.61})Fe_2O_4$]-PMAO and [$(Zn_{0.18}Fe_{0.82})Fe_2O_4$]-PMAO respectively. The maximum average change of epsilon (%) of [$(Zn_{0.18}Fe_{0.82})Fe_2O_4$]- PMAO at 1 GHz was 5.4%, which was higher than SA and FF NPs at similar conditions, but lower than Sienna$^+$. The maximum average change in effective conductivity of [$(Zn_{0.18}Fe_{0.82})Fe_2O_4$]-PMAO was 107.60% which is significantly higher than commercial iron oxides. The higher conductivity of the zinc ferrites is attributed to the Verwey's electron hopping mechanism. Furthermore, polymers such as PMAO are conductive because electrons within them have the ability to jump from one chain to another, hence causing an increase within and between the chains of the polymer, hence increasing the conductivity of the medium.

5.7.2.2 Dielectric properties of zinc ferrites in 60% glycerol

Dielectric properties of our synthesized zinc ferrites were measured in 60% glycerol (Fig. 5-17) and were comparable with our commercial iron oxide NPs. The overall average change in epsilon was higher in 60% glycerol compared with water. Maximum average change in epsilon was 20.81%, 15.57% and, 7.85% for [$(Zn_{0.18}Fe_{0.82})Fe_2O_4$]-PMAO, [$(Zn_{0.39}Fe_{0.61})Fe_2O_4$]PMAO, and [$Fe_3O_4$]PMAO respectively at 4 GHz. The maximum average change in sigma was 3.54%, 5.41% and, 5.31% for[$(Zn_{0.18}Fe_{0.82})Fe_2O_4$]-PMAO, [$(Zn_{0.39}Fe_{0.61})Fe_2O_4$]PMAO, and [$Fe_3O_4$]PMAO respectively. Overall, it can be said that the average change epsilon was much higher in 60% glycerol compared with in the water.

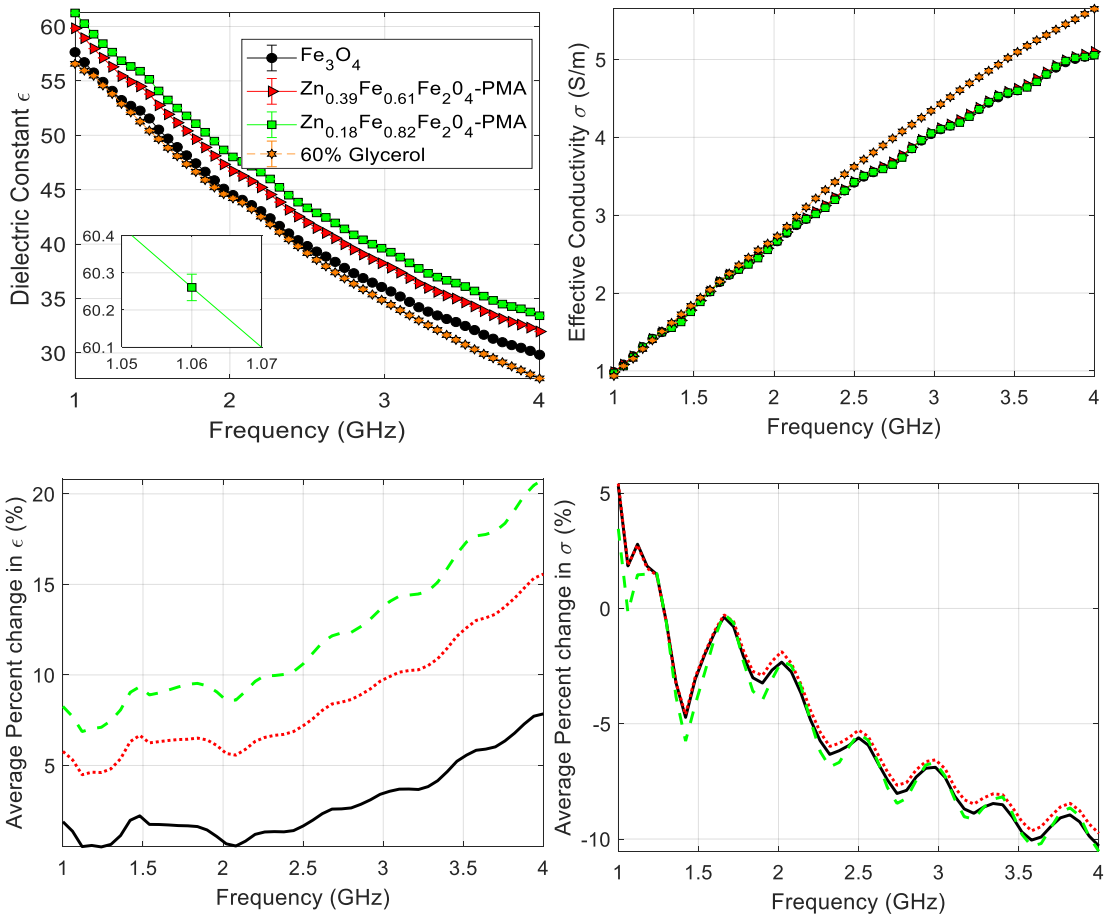

Figure 5-26: (a) dielectric constant, (b) effective conductivity, (c) average change in epsilon and (d) average change in sigma of [Fe_3O_4]-PMAO, [($Zn_{0.18}Fe_{0.82}$) Fe_2O_4]-PMAO and [($Zn_{0.39}Fe_{0.61}$)Fe_2O_4]-PMAO in 60% glycerol at a concentration of 2mg/mL characterised between 1-4 GHz. Each curve represents the average of three different samples, n=3+/-SD.

5.7.2.3 Dielectric properties of zinc ferrites in TM phantom

Figure 5-18 shows the dielectric properties of ferrites in oil-in-gelatin TM phantom between 1-4 GHz at 2 mg/mL. As these ferrites are biocompatible and have the potential of becoming potential contrast agent, we decided to further study their properties in TM phantom. The maximum dielectric constant was 57.02±0.17, 58.79±0.41 and, 59.5±0.19 at 1 GHz for [Fe_3O_4]-PMAO, [($Zn_{0.39}Fe_{0.61}$)Fe_2O_4]-PMAO and, [($Zn_{0.18}Fe_{0.82}$)Fe_2O_4]- PMAO respectively compared with 55.32±0.57 of the TM phantom at a similar frequency. [($Zn_{0.18}Fe_{0.82}$) Fe_2O_4-]PMAO composition showed the maximum average change of epsilon (%) of 7.56 with [Fe_3O_4]-PMAO showing the lowest average change of epsilon of 3.08 at 1 GHz.

PMAO is a hydrophilic polymer which could be contributing towards an increase in the dielectric properties of the material. However, a further increase in the dielectric properties is observed with inclusion of zinc within the composition. Therefore, these results clearly suggest that addition of zinc within the composition influences the dielectric properties of the material and this change is independent of the polymer coating. This has been further explained in the discussion section.

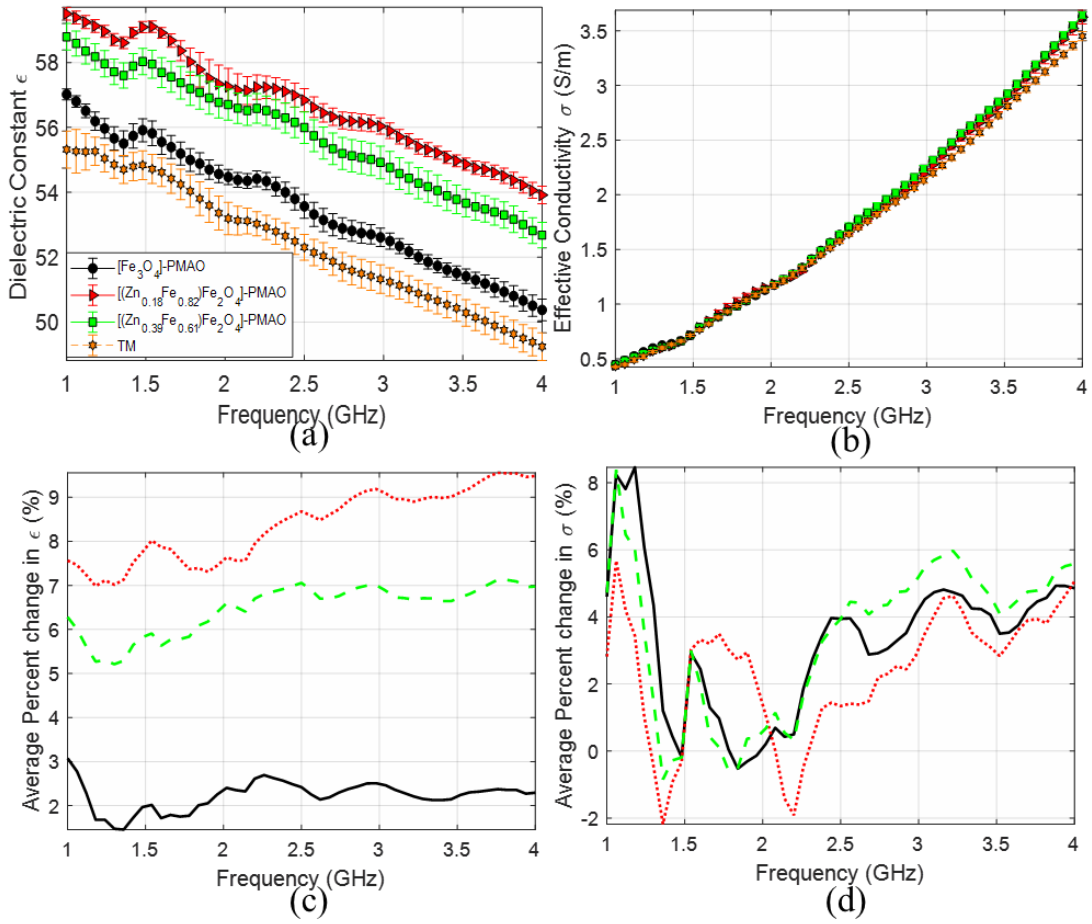

Figure 5-29: (a) dielectric constant, (b) effective conductivity, (c) average change in epsilon and (d) average change in sigma of Fe_3O_4-PMAO, $[(Zn_{0.18}Fe_{0.82})Fe_2O_4]$-PMAO and $[(Zn_{0.39}Fe_{0.61})Fe_2O_4]$PMAO in TM phantom characterised between 1-4 GHz at a concentration of 2 mg/mL. Each curve represents the average of three different samples, n=3+/-SD

5.8 Discussion

MNPs have previously shown a potential of being used as contrast agents for MWI applications. They are already used clinically for MRI purpose, hence in this study different types of iron oxide,

NPs were explored for their potential use. In this study, we investigated the colloidal stability and dielectric properties of commercial iron oxide from SA, Sienna+, and FF in water and in 60% glycerol. These NPs were used as controls against our synthesized zinc ferrites coated with PMAO polymer. It has been suggested previously, that stability of the particles will be better in a viscous medium and if they are coated which improves their dispersion properties. Dielectric properties of all nanomaterials tested showed higher contrast and better dispersion in 60% glycerol compared with water.

5.8.1 Stability and dielectric properties of commercial iron oxides

The colloidal stability of each nanomaterial was tested using UV-Vis and DLS. NPs with the presence of anionic surfactant i.e. FF and Sienna^{+} which had a carboxydextran coating around them showed higher stability compared to basic NPs without any surfactant or coating. SA NPs showed higher PDI compared with other iron oxides NPs. This is because iron oxides NPs with bare surfaces tend to agglomerate due to strong magnetic attraction among particles, Van der Waals forces, and high surface energy. These particles agglomerate and form large clusters due to hydrophobic interactions between the particles, resulting in increased particle size. Mutual magnetization also takes place due to adherence of remnant magnetic particles which results in the increased aggregation properties [205][250][251]. Hence, the stability of the NPs is limited.

Iron oxide NPs have a polar covalent bond between iron and oxygen, though the crystalline structure is in an octahedral form, therefore they are non-polar in nature. We propose that they do not go through dipolar polarization and therefore no increase is observed within the dielectric properties, such as the case with SA NPs.

The high stability of FF compared with SA NPs can be explained due to the presence of an anionic surfactant. The surface of iron oxide NPs is covered by iron atoms that act as Lewis acids, which coordinate with molecules that donate lone pair electrons. When iron oxide NPs are placed in an

aqueous medium, water dissociates, and the iron oxide surface becomes hydroxyl functionalized. These hydroxyl groups are amphoteric. The surface of iron oxide may be positive or negative, depending upon the pH of the solution. The isoelectric point of magnetite is 6.8; the surface charge density is too small, and the particles are no longer stable in water and they tend to flocculate. To obtain stable iron oxide NPs electrostatic and steric stabilization needs to be maintained [252][253]. This can be achieved by either surfactants or polymers which can be chemically anchored or physically adsorbed on the surface, which will create a balance between the magnetic and the Vaan der Waals attractive forces, hence making the NPs stable in suspension [254][255][256].

Surfactants attach to the surface of iron oxide NPs via their end functional groups through covalent and/or electrostatic interactions. They behave as protective agents and can constitute a layer of thickness varying between 1-5 nm [257]. Examples of anionic surfactant functional groups include sulfate, sulfonate, carboxylates, and phosphates. Surfactants can be adsorbed onto the surface via 1) electrostatic interaction between the ionic headgroup of the surfactant and charged surface sites, 2) hydrophobic interaction between the surfactant hydrophobic tails or 3) through covalent bonding between the surfactant and the surface of the NPs.

Presence of anionic surfactant seems to be increasing the dielectric properties of iron oxide, as seen with FF. Vadivel *et al.*, carried out a study where they showed that SDS (sodium dodecyl sulfate), an anionic surfactant, added to $CoFe_2O_4$ showed higher dielectric properties compared with bare $CoFe_2O_4$ [258][259].

The general trend seen with our results is that the dielectric constant decreases with an increase in frequency and the dielectric loss increase with an increase in frequency. At low frequency, surface charge polarization contributes towards the dielectric constant due to the accumulation of charge carriers beneath the applied electric field. As the frequency increases electric field changes rapidly and makes it difficult for the electrons to keep up, hence they lag the applied field. This lagging behind of electrons spreads over the whole domain and reaches to the grain boundaries, which

leads to a decrease of dielectric constant with frequency. The value of polarization tends to decrease with an increase in frequency hence dielectric constant follows in that trend. The high dielectric constant value at low frequencies is due to the better response of polarization mechanisms. The dielectric loss decreases as the frequency increases which is due to the reduction in the absorption current. However, at high frequency, the conversion of charge movement to lattice vibration i.e. phonon causes loss factor [260].

$$\varepsilon'' = \varepsilon''_{d} + \varepsilon''_{\sigma} \qquad \text{(Equation 1)}$$

Another factor which needs to be considered is that the imaginary part of the permittivity ε" contains two contributions, ε''_{d} which represents the dielectric loss and ε''_{σ}, which represents the loss due to the drift of ions [261]. Since the possibility of mobile ions is higher due to the presence of a surfactant, possibility of higher drift of ions is likely which increases the conductivity. As iron oxide NPs are non-polar in nature, the polar carboxy dextran, used to improve the dispersion of Sienna^{+} NPs goes through dipolar polarisation mechanism. The hydroxyl groups present on carboxy dextran, go through dipolar polarisation hence an increase in the dielectric constant is observed between iron oxide NPs obtained from Sienna^{+} compared with FF and SA. This was

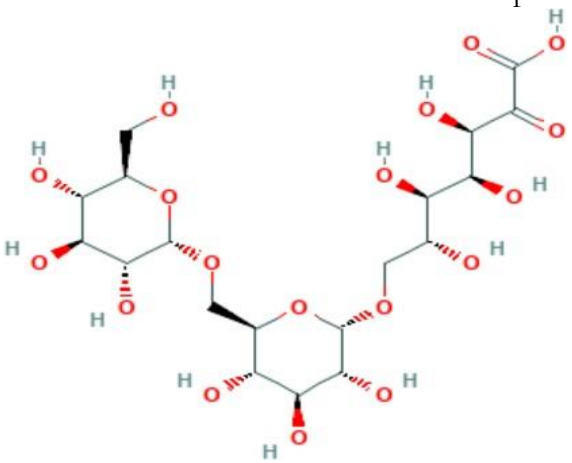

Figure 5-32

also stated by Ogunlade *et al.*, [78][262].

Dielectric relaxation is the momentary delay in the dielectric constant of a material. This is caused by the delay in molecular polarization with respect to the change of the electric field. The relaxation

behaviour of glycerol is affected when mixed with water, which can in turn, affect the dielectric properties of a suspension [263]. Glycerol is a three-carbon hydrocarbon with one hydroxyl group attached to each carbon atom and is highly soluble in water. Glycerol serves also for electrostatic stabilization of NPs, due to its supramolecular network [264]. For the binary mixtures of glycerol and water, we assume three types of active environments simultaneously co-existing: CD_W which contains only water, CD_G which contains only glycerol, and CD_{W-G} which includes both water and glycerol, respectively. The dielectric behaviour of these mixtures depends considerably on the bulk fraction of the CD_{W-G} which in turn is directly related to the mixture ratio of the two liquids. CD is a way of describing the relationship of the mixture constituents. This effectively shows how glycerol molecules align with water molecules to produce a single, composite dielectric relaxation time.

It is observed that dielectric constant decreases and effective conductivity increases with an increase in glycerol concentration. The slope of the curve of dielectric constant steepens within 1-2 GHz range and conductivity are concave upwards. This is because of the distinct shifting of relaxation frequency. With the results observed for 60% glycerol, there is a monotonic decrease in the dielectric constant with an increase in frequency and a monotonic increase in conductivity is observed. This behaviour is related to the distinct shifting of relaxation frequency [263]. It is possible that 60% glycerol provides electrostatic stability of the NPs, which has been highlighted in previous chapters as well, it can be concluded that stability of the NPs improves in 60% glycerol compared with water, hence the increase in dielectric properties is observed with 60% glycerol.

5.8.2 Stability and dielectric properties of PMAO coated zinc ferrites

Polymers make excellent ligand for nanoparticles as they surround NPs with substantial physical barrier [264]. There are many suitable polymeric ligands to provide water solubility. In this study, we coated our synthesized NPs with PMAO polymer. PMAO is a commercially available amphiphilic polymer; it is composed of hydrophobic alkyl chains which interact via hydrophobic

interactions of the NP surfaces, and a hydrophilic anhydride ring backbone that provides water solubility through charged groups such as COO^- [265]. The particles, therefore, become encapsulated in a polymer shell in which the outer surface is hydrophilic allowing excellent dispersion properties in water. PMAO has previously been reported to stabilize the particles in four main ways. Firstly, as the surface of the polymer becomes negatively charged, particles are stabilized by electrostatic repulsion. Second, through the entropic effect: the alkyl chains of the adsorbed polymer suffer from steric hindrance upon interacting with alkyl chains on another particle. This loss of conformational freedom causes a loss of entropy, which increases the free energy leading to repulsion between particles. The osmotic effect occurs when polymer chains on individual particles overlap and increase in concentration regions. Repulsion arises due to the osmotic pressure which occurs as the solvent attempts to dilute these regions. Lastly, on close approach, water molecules on the adsorbed surfaces are released causing repulsion. Polymerization is therefore useful as it provides water solubilization of the hydrophobic NPs.

The dielectric constant observed for [$(Zn_{0.18}Fe_{0.82})$ Fe_2O_4]-PMAO at 2 mg/mL was close to clinically used commercial Sienna$^+$. Verwey's hoping mechanism can explain the variation in conductivity. Ferrites structurally form a cubic close-packed oxygen lattices with cations at the octahedral site and the tetrahedral sites. The distance between two metal ions at an octahedral site is smaller than the distance between a metal ion at an octahedral site and another metal ion at a tetrahedral site. The electron hopping between octahedral and tetrahedral sites under normal conditions, therefore, has a very small probability compared with that for octahedral-octahedral hopping. Hopping between tetrahedral and tetrahedral sites does not exist because there are only Fe^{3+} ions at the tetrahedral site and Fe^{2+} ions formed prefer to occupy octahedral sites only. Zn^{2+} ions prefer to occupy tetrahedral sites, so when Zn^{2+} ions increases at the tetrahedral sites, then some of the Fe-ions from octahedral sites will migrate towards the tetrahedral site and as a result there will be fewer Fe^{3+} and Fe^{2+}ions at the octahedral site which are responsible for electrical

conduction, hence there is a decrease in electrical conductivity with an increase in Zn^{2+} ion concentration within the composition[266]. Polarization in ferrites is contributed by space charge polarization. Increase in the Zn^{2+} ion reduces the number of Fe^{3+} ions on the octahedral site which is mainly responsible for both space charge polarization and hopping exchange. $-COO^-$ groups at the end of the polymer, can be going through dipolar polarisation as well, hence it adds to the total polarisation of the composition [267]. This explains why we see an increase in the dielectric constant with a decrease in the amount of zinc. Average change in epsilon of [$(Zn_{0.18}Fe_{0.82})$ Fe_2O_4]-PMAO is higher in 60% glycerol compared with water. This is potential because further electrostatic stabilization of the NPs is provided in 60% glycerol compared with water, also, the hydroxyl groups present in a glycerol molecule can be contributing towards the total dipolar polarisation, hence a further increase is observed.

[$(Zn_{0.18}Fe_{0.82})Fe_2O_4$]-PMAO composition has the highest dielectric constant in TM phantom at 1 GHz. Many materials have been proposed to be used as potential TM phantoms such as polyacrylamide gels (PAG), oil-in-gelatin, and carbon-based synthetic. PAG has typically comprised of acrylamide polymerized in a liquid solvent and is used to stimulate the behaviour of biological tissues. They have high elasticity but short usage of life with only several hours. Compared with the above materials, oil-in-gelatin are popular because of simple preparation, stable mechanical properties for a long time. They are used to imitate the dielectric properties of biological tissue and the properties can be tuned by varying the amount of oil [149].

The increase in the dielectric constant can be because of the hydrophilic groups present on the PMAO polymer, which contribute towards the dipolar polarization. These results strongly suggest that [$(Zn_{0.18}Fe_{0.82})Fe_2O_4$]-PMAO composition has the potential of showing dielectric property changes in a tumor. In the experiments presented here we chose to assess the effect of iron oxide and ferrite nanoparticles on the dielectric properties of water, 60% glycerol and TM phantom. Our dielectric values of water agree well with the values reported in previous literature [191]. Data that

we have achieved of TM phantoms with an incorporation of NPs can be trusted because our dielectric data of oil-in-gelatin TM phantom agrees well with the literature [60]. There has been no study where just 60% glycerol has been measured or with an incorporation of NPs in it, however, Paul M. Meaney, carried out a study where the dielectric characterization of different glycerol: water mixtures were measured. Exactly 60% glycerol was not measured, but 55% and 70% in that study were measured. It can be concluded that dielectric values of our 60% glycerol agree well with values reported. This suggests, that the changes we see after the incorporation of NPs in respective controls, can be trusted and is reliable data.

5.9 Conclusion & Summary

In this study, we have measured the dielectric properties of commercially available iron oxide SA, sienna$^+$, and FF. These were used as a control to compare the dielectric properties we achieved from our synthesized zinc ferrites, with varying amounts of zinc and iron. Results obtained suggested that the stability of the commercial MNPs improved with the presence of an anionic surfactant, and due to the presence of carboxy dextran coating. Presence of surfactant and carboxy dextran coating was found to improve the dielectric properties of the suspension compared with iron oxide with a bare surface and no coating. The stability of our synthesized zinc ferrites was very similar to clinically available Sienna$^+$. From the three compositions that we prepared $[Zn_{0.18}Fe_{0.82}]Fe_2O_4$-PMAO showed to have the highest dielectric constant and we suggest that they have the potential of being used as potential contrast agents for MWI applications.

6 Summary & Future perspective

The studies throughout this thesis have focused on identifying potential contrast agents for MWI applications. In this project we studied NPs to explore if they have the potential of showing a contrast at MW frequencies.

During the duration of this project several nanomaterials were tested to identify their potential of changing water's dielectric constant not presented as results in this thesis. Nanomaterials tested at 1-4 GHz but provided no difference were: calcium phosphate NPs in RO water at 2 mg/mL, Gold NPs (40 nm) coated with CTAB (cetyl trimethylammonium bromide) at a concentration range of 2, 1, 0.5 and 0.25 mg/mL. Barium titanate (obtained from Effective conductivity Aldrich; < 100nm) and strontium titanate (obtained from Sigma Aldrich; were measured in RO water and 60% glycerol at concentrations of 2, 1, 0.5 and 0.25 mg/mL.

Due to small aspect ratio of Gold NPs they did not show a change within the dielectric properties. The Ca/P molar ratios affect the dielectric properties of the material. Synthesizing particles with an appropriate molar ratio might give an enhancement within the dielectric properties.

In this thesis I have conducted experiments with the following standard conditions:

Dielectric properties were assessed in water, 60% Glycerol and TM (tissue mimicking) phantom because it was important to understand the behaviour of different nanomaterials in high dielectric constant medium such as water, in low dielectric constant medium, such as 60% glycerol and in TM phantom because these phantoms have dielectric properties similar to that of a tumour, hence it was important to understand the dielectric properties in each medium.

Throughout our studies temperature has been maintained at 20ºC (room temperature). Coaxial probe system is used to perform dielectric measurements in this study. Coaxial probe system is a well-established system for performing measurements and has the ability to measure liquids and semi-solids.

Certain concentration range has been selected for nanomaterials tested in this study. 2-0.25 mg/mL is an appropriate range for measurements because any concentration above 2 mg/mL will cause aggregation of particles, which would eventually lead to an inhomogeneous solution which will not give accurate measurements. Concentration lower than 0.25 mg/mL would not be enough to show a contrast. Therefore, the range from 2-0.25 mg/mL was chosen as the optimal range for performing measurements.

I have selected CNTs as some types had been previously tested for MWI purposes and had shown potential increase in dielectric properties in RO water, 60% Glycerol and in TM (tissue-mimicking) phantom[2][3]. In this study we studied the effect of different lengths and functionalisation and type Single Wall vs Multi Wall of CNTs on the dielectric properties of different mediums. The results obtained suggested that length and functionalization have an effect on the dielectric properties. MWNT-OH showed the highest average change of dielectric constant of dielectric constant compared with MWNT, SWNT-OH, SWNT, sSWNT, and sSWNT-OH. Longer tubes allowed a longer mean free path and a better conduction pathway and functionalization of CNTs improved their dispersion hence an increase in the dielectric properties was observed against the non-hydroxylated. The properties were higher in low dielectric constant medium and in TM phantom compared with RO water because of dispersion properties of the nanomaterials in the medium.

ZnO NPs were measured in this study, because they possess a dipolar structure which we proposed. The dipoles will go through dipolar polarisation and show an increase in the dielectric properties in RO water, 60% glycerol and TM phantom between 1-4 GHz. The results were compared against our control, SiO_2, which had no dielectric contrast. Results suggested that 2 mg/mL of ZnO NP showed a maximum average change of dielectric constant of 2%, this was further improved to 6.80% after ZnO-PEG had been PEGylated. This suggested that improved dispersion of NPs was influencing the medium dielectric properties and improving their colloidal

stability further increased them. The ethylene oxide units present within a PEG molecule could also be going through dipolar polarisation, hence adding on to the effect of dielectric properties of the material. Though, more studies may be required to prove this effect. The introduction of biocompatible ferroelectric polymers as layers and dispersion enhancers should be investigated further.

We measured different commercial iron oxide NPs from Effective conductivity Aldrich, ferrofluid from Liquid Research and Sienna$^+$ from Endomagnetics. Ferrofluid form liquid research had been previously measured in PBS at 25 mg/mL, in this study we measured it in RO water and in 60% glycerol at lower concentrations. Sienna$^+$ and liquid research from ferrofluid showed better dispersive and electrical properties in water and in 60% glycerol compared with iron oxide from Effective conductivity Aldrich. The presence of anionic surfactant and the carboxy dextran coating is improving the dispersive properties of iron oxide and is also contributing towards the dielectric properties. Dispersion is key, and results are in agreement with results in chapter 2. Zinc ferrites were also studied in this study and their results were compared with commercial iron oxides. Ferrites were coated with PMAO polymer to improve their dispersibility. It was found that as the amount of zinc decreases within the composition, dielectric properties increased in water, 60% glycerol and TM phantom.

It could be that if CNTs are made biocompatible in such a way which the dielectric properties are not affected, they can be used as potential contrast agents. Also, ZnO-PEG can be used as a contrast enhancement agent for MWI application. Since, iron oxide and ferrites are promising nanomaterials that should merit additional studies as contrast enhancement for MWI. However, for future work, various NPs which show a dielectric change within different mediums need to be made and tested widely at different conditions and different laboratories.

Since we have performed measurements of nanomaterials in TM phantom, which mimics the tumor properties, this is closest to a real scenario. Due to the sensitivity of the coaxial probe,

contrast around 2% is considered as error. Hence anything above 2% will be considered as a contrast change. Contrast agents that we have identified in this study such as zinc ferrites, ZnO-PEG showed an increase of higher that 5% in TM phantom, hence show a potential of using as a contrast agents for MWI. The error is minimised when different MWI systems are used.

Feridex I.V.®(ferumoxides injectable solution) is a sterile aqueous colloid of superparamagnetic iron oxide associated with dextran for intravenous (I.V.) administration as a magnetic resonance imaging contrast media. Each millilitre of Feridex I.V. contains 11.2 milligrams of iron and 61.3 milligrams of mannitol. The recommended dosage of Feridex IV (ferumoxides injectable solution) is 0.56 milligrams of iron (0.05 mL Feridex IV) per kilogram of body weight[4]. Feridex is prepared as a dilution in 100 ml of 5% dextrose.

From previous literature we understand that on average 0.7% of injected dose of nanomaterials reach the tumour Based on these guidelines and estimates[5], if the contrast agents proposed in this study were to be used intravenously, we would expect a 0.5mg/mL tumour as concentration of nanomaterials . This concentration can achieve significant dielectric contrast. However, using higher concentrations such as 2 mg/mL and 1 mg/mL tumour would be challenging to administer.

Other suitable candidates for MWI purposes can be ferroelectric nanoparticles such as barium titanate, strontium titanate, calcium copper titanate which could be tested in different mediums for their potential use as contrast agents for MWI. These materials can have spontaneous polarization[6], hence they can be studied further for microwave applications.

My thesis highlights important parameters such as the need of having a homogenous dispersion of the nanomaterial and the material also having a dipolar structure is crucial. These conditions should be considered in developing potential NPs as contrast agents for MWI have been proposed and future ideas to take this work forward have been suggested.

7 References

[1] "Diagnostic imaging.". http://www.who.int/diagnostic_imaging/imaging_modalities/en/.

[2] L. Fass, "Imaging and cancer: A review," *Molecular Oncology*., pp. 115-152, 2008.

[3] M. J. Horner *et al.*, "Seer Cancer Statistics Review, 1975-2006," 2009.

[4] M. Malvezzi *et al.*, "European cancer mortality predictions for the year 2018 with focus on colorectal cancer," *Ann. Oncol.*, 1016-1022, 2018.

[5] R. L. Siegel, K. D. Miller, and A. Jemal, "Cancer statistics, 2015," *CA. Cancer J. Clin.*, vol. 65, no. 1, pp. 5–29, 2015.

[6] A. Modiri, S. Goudreau, A. Rahimi, and K. Kiasaleh, "Review of breast screening: Toward clinical realization of microwave imaging: Toward clinical realization of microwave imaging," *Medical Physics*., pp. 446-458, 2017.

[7] G. Bindu and K. T. Mathew, "Characterization of benign and malignant breast tissues using 2-D microwave tomographic imaging," *Microw. Opt. Technol. Lett.*, pp. 2341-2345, 2007.

[8] S. Caorsi, G. L. Gragnani, S. Medicina, M. Pastorino, and G. Zunino, "Microwave imaging based on a Markov random field model," *IEEE Trans. Antennas Propag.*, pp. 293-303, 1994.

[9] A. Redman, S. Lowes, and A. Leaver, "Imaging techniques in breast cancer," *Surg. (United Kingdom)*, vol. 34, no. 1, pp. 8–18, 2016.

[10] T. M. Kolb, J. Lichy, and J. H. Newhouse, "Occult cancer in women with dense breasts: detection with screening US--diagnostic yield and tumor characteristics.," *Radiology*, vol.

207, no. 1, pp. 191–199, 1998.

[11] H. Ding, M. J. Klopfer, J. L. Ducote, F. Masaki, and S. Molloi, "Breast Tissue Characterization with Photon-counting Spectral CT Imaging: A Postmortem Breast Study," *Radiology*, vol. 272, no. 3, pp. 731–738, 2014.

[12] K. M. Kelly, J. Dean, W. S. Comulada, and S. J. Lee, "Breast cancer detection using automated whole breast ultrasound and mammography in radiographically dense breasts," *Eur. Radiol.*, vol. 20, no. 3, pp. 734–742, 2010.

[13] R. F. Brem *et al.*, "Assessing Improvement in Detection of Breast Cancer with Three-dimensional Automated Breast US in Women with Dense Breast Tissue: The SomoInsight Study," *Radiology*, vol. 274, no. 3, pp. 663–673, 2015.

[14] E. A. Morris, "Breast cancer imaging with MRI," *Radiologic Clinics of North America*, vol. 40, no. 3. pp. 443–466, 2002.

[15] A. M. L.Mazzanti, "Molecular Magnetic Resonance Contrast Agents for the Detection of Cancer: Past and Present," *Mol. imaging Oncol.*, vol. 38, no. 1, pp. 42–54, 2011.

[16] M. Kristoffersen Wiberg, P. Aspelin, L. Perbeck, and B. Boné, "Value of MR imaging in clinical evaluation of breast lesions.," *Acta Radiol.*, vol. 43, no. 3, pp. 275–81, 2002.

[17] D. M. Schuster, "Clinical Utility of PET Scanning in Breast Cancer Management," *Am. J. Hematol. Oncol.*, pp. 20-25, 2015.

[18] N. Avril *et al.*, "Breast imaging with positron emission tomography and fluorine-18 fluorodeoxyglucose: Use and limitations," *J. Clin. Oncol.*, vol. 18, no. 20, pp. 3495–3502, 2000.

[19] F. L. Flanagan, F. Dehdashti, and B. A. Siegel, "PET in breast cancer," *Seminars in Nuclear Medicine*, vol. 28, no. 4. pp. 290–302, 1998.

[20] S. M. Friedewald *et al.*, "Breast Cancer Screening Using Tomosynthesis in Combination With Digital Mammography," *JAMA*, vol. 311, no. 24, pp. 2499, 2014.

[21] N. K. Nikolova, "Microwave imaging for breast cancer," *IEEE Microw. Mag.*, vol. 12, no. 7, pp. 78–94, 2011.

[22] S. Kwon and S. Lee, "Recent Advances in Microwave Imaging for Breast Cancer Detection," vol. 2016, pp. 1-26, 2016.

[23] H. E. Davies, C. G. Wathen, and F. V. Gleeson, "The risks of radiation exposure related to diagnostic imaging and how to minimise them.," *BMJ (Clinical research ed.)*, vol. 342. pp. 589-593, 2011.

[24] S. Semenov, "Microwave tomography: review of the progress towards clinical applications," *Philos. Trans. R. Soc. A Math. Phys. Eng. Sci.*, vol. 367, no. 1900, pp. 3021–3042, 2009.

[25] Y. Kuwahara, "Microwave Imaging for Early Breast Cancer Detection," in *Breast Imaging*, pp 48-50, 2017.

[26] A. Technologies, "Agilent, Basics of Measuring the Dielectric Properties of Materials, Application Note."

[27] G. G. Raju, "Polarization and Static dielectric constant," in *Dielectrics in electric fields*, pp. 29–48, 2003.

[28] "Dielectric polarization," 2010. [Online]. Available: https://eng.libretexts.org/Textbook_Maps/Chemical_Engineering/Supplemental_Modules_(Materials_Science)/Optical_Properties/Dielectric_Polarization.

[29] Y. Wang, D. Chen, X. Yin, P. Xu, F. Wu, and M. He, "Hybrid of MoS_2 and Reduced Graphene Oxide: A Lightweight and Broadband Electromagnetic Wave Absorber," *ACS Appl. Mater. Interfaces*, pp. 2626-2633, 2015.

[30] N. Wu, X. Liu, and S. W. Or, "Core/shell-structured nickel/nitrogen-doped onion-like carbon nanocapsules with improved electromagnetic wave absorption properties," *AIP Adv.*, pp. 0-56206-5, 2016.

[31] M. Kuriakose, S. Longuemart, M. Depriester, S. Delenclos, and A. H. Sahraoui, "Maxwell-Wagner-Sillars effects on the thermal-transport properties of polymer-dispersed liquid crystals," *Phys. Rev. E - Stat. Nonlinear, Soft Matter Phys.*, pp. 022551-5, 2014.

[32] G. J. Bin Quan, Xiaohui Liang, Y. Z. , Yan Cheng, Wei Liu, Jianna Ma, and G. X. Daoran Li, "Dielectric polarization in electromagnetic wave absorption: Review and perspective," *J. Alloys Compd.*, pp. 1065-1075, 2017.

[33] Q.-Q. L. Zhi-Min Dang, Lan Wang, Yi Yin, Qing Zhang, "Giant Dielectric Permittivities in Functionalized Carbon-Nanotube/Electroactive-Polymer Nanocomposites," *Adv. Mater.*, vol. 19, pp. 852–857, 2007.

[34] T. Xia, C. Zhang, N. A. Oyler, and X. Chen, "Hydrogenated TiO_2 Nanocrystals: A novel microwave absorbing material," *Adv. Mater.*, pp.6905-6910, 2013.

[35] S. Gabriel, R. W. Lau, and C. Gabriel, "The dielectric properties of biological tissues: III. Parametric models for the dielectric spectrum of tissues," *Phys. Med. Biol.*, vol. 41, no. 11, pp. 2271–2293, 1996.

[36] L. Sha, E. R. Ward, and B. Stroy, "A review of dielectric properties of normal and malignant breast tissue," *Proc. IEEE SoutheastCon 2002*, pp. 457-462, 2002.

[37] R. Pethig, "Dielectric properties of biological materials: Biophysical and medical applications," *IEEE Trans. Electr. Insul.*, pp. 453-474, 1984.

[38] C. Gabriel, "Compilation of the Dielectric Properties of Body Tissues at RF and Microwave Frequencies.," *Environ. Heal.*, vol. Report No., p. 21, 1996.

[39] C. Gabriel, S. Gabriel, and E. Corthout, "The dielectric properties of biological tissues: I. Literature survey," *Phys. Med. Biol.*, vol. 41, no. 11, pp. 2231–2249, 1996.

[40] S. Gabriel, R. Lau, C. Gabriel, Gabriel S., Lau R.W., and Gabriel C., "The dielectric properties of biological tissues: II. Measurements in the frequency range 10 Hz to 20 GHz," *Phys. Med. Bioil.*, vol. 41, pp. 2251–2269, 1996.

[41] S. Chaudary, R. Mishra, A. Swarup, and J. M. Thomas, "Dielectric properties of normal and malignant human breast tissues at radiowave and microwave frequencies," *Indian J. Biochem. Biophys.*, vol. 21, no. 1, p. 76, 1984.

[42] A. J. Surowiec, S. S. Stuchly, J. R. Barr, and A. Swarup, "Dielectric Properties of Breast Carcinoma and the Surrounding Tissues," *IEEE Trans. Biomed. Eng.*, vol. 35, no. 4, pp. 257–263, 1988.

[43] A. M. Campbell and D. V. Land, "Dielectric properties of female human breast tissue measured in vitro at 3.2 GHz," *Phys. Med. Biol.*, pp. 193-210, 1992.

[44] W. T. Joines, Y. Zhang, C. Li, and R. L. Jirtle, "The measured electrical properties of normal and malignant human tissues from 50 to 900 MHz," *Med. Phys.*, vol. 21, no. 4, pp. 547–550, 1994.

[45] P. M. Meaney, A. P. Gregory, N. R. Epstein, and K. D. Paulsen, "Microwave open-ended coaxial dielectric probe: interpretation of the sensing volume re-visited.," *BMC Med. Phys.*, vol. 14, no. 1, p. 3, 2014.

[46] W. C. Ji *et al.*, "Microwave detection of metastasized breast cancer cells in the lymph node; potential application for sentinel lymphadenectomy," *Breast Cancer Res. Treat.*, vol. 86, no. 2, pp. 107–115, 2004.

[47] M. Lazebnik *et al.*, "A large-scale study of the ultrawideband microwave dielectric properties

of normal, benign and malignant breast tissues obtained from cancer surgeries," *Phys. Med. Biol.*, vol. 52, no. 20, pp. 6093–6115, 2007.

[48] M. Lazebnik *et al.*, "A large-scale study of the ultrawideband microwave dielectric properties of normal breast tissue obtained from reduction surgeries," *Phys. Med. Biol.*, vol. 52, no. 10,pp. 2637 - 2656, 2007.

[49] "Applying Error Correction to Network Analyzer Measurements, Application Note, literature number 5965-7709E."

[50] "Free Space Materials Measurment Seminar, Agilent Technologies," 2005.

[51] A. La Gioia *et al.*, "Open-Ended Coaxial Probe Technique for Dielectric Measurement of Biological Tissues: Challenges and Common Practices," *Diagnostics*, 2018.

[52] M. Klemm, J. A. Leendertz, D. Gibbins, I. J. Craddock, A. Preece, and R. Benjamin, "Microwave radar-based breast cancer detection: Imaging in inhomogeneous breast phantoms," *IEEE Antennas Wirel. Propag. Lett.*, vol. 8, pp. 1349–1352, 2009.

[53] A. H. Golnabi, P. M. Meaney, S. Geimer, and K. D. Paulsen, "Microwave imaging for breast cancer detection and therapy monitoring," *2011 IEEE Top. Conf. Biomed. Wirel. Technol. Networks, Sens. Syst.*, pp. 59–62, 2011.

[54] K. A. Kabita Purkait, Subijit Mondal, Subhra Narayan Bose, Rounak Roy, Shuvankar Halder, "An approach to study the range of perturbations in Exact Algorithm on microwave tomography of biological targets with different beam width," pp. 1–6, 2015.

[55] D. W. Winters, J. D. Shea, P. Kosmas, B. D. Van Veen, and S. C. Hagness, "Three-dimensional microwave breast imaging: Dispersive dielectric properties estimation using patient-specific basis functions," *IEEE Trans. Med. Imaging*, vol. 28, no. 7, pp. 969–981, 2009.

[56] P. M. Meaney, M. W. Fanning, D. Li, S. P. Poplack, and K. D. Paulsen, "A clinical prototype for active microwave imaging of the breast," *IEEE Trans. Microw. Theory Tech.*, pp. 1841-1853, 2000.

[57] T. M. Grzegorczyk, P. M. Meaney, P. A. Kaufman, R. M. Diflorio-Alexander, and K. D. Paulsen, "Fast 3-D tomographic microwave imaging for breast cancer detection," *IEEE Trans. Med. Imaging*, pp. 1584 - 1592, 2012.

[58] A. E. Souvorov, A. E. Bulyshev, S. Y. Semenov, R. H. Svenson, and G. P. Tatsis, "Two-dimensional computer analysis of a microwave flat antenna array for breast cancer tomography," *IEEE Trans. Microw. Theory Tech.*, pp. 1413-1415, 2000.

[59] N. R. Epstein, P. M. Meaney, and K. D. Paulsen, "3D parallel-detection microwave tomography for clinical breast imaging," *Rev. Sci. Instrum.*, vol. 85, no. 12, pp. 124704-12, 2014.

[60] Q. Q. F. P. M. Meaney, M. W. Fanning, T. Raynolds, C. J. Fox and and K. D. P. C. A. Kogel, S. P. Poplack, "Initial clinical experience with microwave breast imaging in women with normal mammography," *Acad. Radiol.*, vol. 14, pp. 207–218, 2007.

[61] P. K. Poplack SP, Tosteson TD, Wells WA, Pogue BW, Meaney PM, Hartov A, Kogel CA, Soho SK, Gibson JJ, "Electromagnetic breast imaging: results of a pilot study in women with abnormal mammograms," *Radiology*, vol. 243, pp. 350-359, 2007.

[62] C. Gilmore *et al.*, "Microwave Imaging of Human Forearms: Pilot Study and Image Enhancement," *Int. J. Biomed. Imaging*, vol. 2013, pp. 1-18, 2013.

[63] S. C. Hagness, A. Taflove, and J. E. Bridges, "Two-dimensional FDTD analysis of a pulsed microwave confocal system for breast cancer detection: Fixed-focus and antenna-array sensors," *IEEE Trans. Biomed. Eng.*, vol. 45, pp. 1470-1479, 1998.

[64] A. W. Preece, I. Craddock, M. Shere, L. Jones, and H. L. Winton, "MARIA M4: clinical evaluation of a prototype ultrawideband radar scanner for breast cancer detection," *J. Med. Imaging*, vol. 3, no. 3, 033502-7, 2016.

[65] Micrima, "http://www.micrima.com/." .

[66] J. Bourqui, J. M. Sill, and E. C. Fear, "A prototype system for measuring microwave frequency reflections from the breast," *Int. J. Biomed. Imaging*, pp. 1-12, 2012.

[67] C. Rancoule *et al.*, "Nanoparticles in radiation oncology: From bench-side to bedside," *Cancer Letters*, vol. 375, no. 2. pp. 256–262, 2016.

[68] H. Maeda, "Macromolecular therapeutics in cancer treatment: The EPR effect and beyond," *Journal of Controlled Release*, vol. 164, no. 2. pp. 138–144, 2012.

[69] M. Thanou and W. Gedroyc, "MRI-Guided Focused Ultrasound as a New Method of Drug Delivery," *J. Drug Deliv.*, vol. 2013, pp. 1–12, 2013.

[70] K. Greish, "Enhanced permeability and retention (EPR) effect for anticancer nanomedicine drug targeting.," *Methods Mol. Biol.*, vol. 624, pp. 25–37, 2010.

[71] H. Yin, L. Liao, and J. Fang, "Enhanced Permeability and Retention (EPR) Effect Based Tumor Targeting: The Concept, Application and Prospect," *JSM Clin. Oncol. Res.*, pp. 25-37, 2014.

[72] A. D. C. and C. H. Maryam Malekigorji, "The Use of Iron Oxide Nanoparticles for Pancreatic Cancer Therapy," *Nanomedicine reserach*, vol. 1, no. 1, pp. 1-12, 2014.

[73] A. Mashal, J. H. Booske, and S. C. Hagness, "Toward contrast-enhanced microwave-induced thermoacoustic imaging of breast cancer: An experimental study of the effects of microbubbles on simple thermoacoustic targets," *Phys. Med. Biol.*, vol. 54, no. 3, pp. 641–650, 2009.

[74] A. Mashal *et al.*, "Toward carbon-nanotube-based theranostic agents for microwave detection and treatment of breast cancer: Enhanced dielectric and heating response of tissue-mimicking materials," *IEEE Trans. Biomed. Eng.*, vol. 57, no. 8, pp. 1831–1834, 2010.

[75] S. X. Xie, F. Gao, S. C. Patel, J. H. Booske, S. C. Hagness, and B. Sitharaman, "Clinically relevant CNT dispersions with exceptionally high dielectric properties for microwave theranostic applications," *IEEE Trans. Biomed. Eng.*, vol. 61, no. 11, pp. 2718–2723, 2014.

[76] S. X. Xie, F. Gao, S. C. Patel, J. H. Booske, S. C. Hagness, and B. Sitharaman, "Effect of synthesis and acid purification methods on the microwave dielectric properties of single-walled carbon nanotube aqueous dispersions," *Appl. Phys. Lett.*, vol. 103, no. 13, pp. 1–6, 2013.

[77] P. I. X. Li, C. A. V Sahakian, C. S. C. Hagness, and C. J. H, "Award Number : TITLE : Nanoparticle Contrast Agents for Enhanced Microwave Imaging and Thermal Treatment of Breast Cancer Principal Investigator : Northwestern University REPORT DATE : October 2010 TYPE OF REPORT : Final PREPARED FOR : U . S . Army Medica," pp. 1-19, 2010.

[78] O. Ogunlade and P. Beard, "Exogenous contrast agents for thermoacoustic imaging: An investigation into the underlying sources of contrast," *Med. Phys.*, vol. 42, no. 1, pp. 170–181, 2014.

[79] H. Tang, Z. Zhou, and H. A. Sodano, "Relationship between BaTiO3 nanowire aspect ratio and the dielectric permittivity of nanocomposites," *ACS Appl. Mater. Interfaces*, vol. 6, no. 8, pp. 5450–5455, 2014.

[80] G. Bellizzi, O. M. Bucci, I. Catapano, L. Crocco, and R. Scapaticci, "Magnetic nanoparticles enhanced microwave imaging: A feasibility assessment," in *Proceedings of 6th European Conference on Antennas and Propagation, EuCAP 2012*, pp. 696-698, 2012.

[81] G. Bellizzi, O. M. Bucci, and I. Catapano, "Microwave cancer imaging exploiting magnetic nanoparticles as contrast agent," *IEEE Trans. Biomed. Eng.*, vol. 58, no. 9, pp. 2528–2536, 2011.

[82] O. M. Bucci, G. Bellizzi, S. Costanzo, L. Crocco, G. Di Massa, and R. Scapaticci, "Assessing detection limits in magnetic nanoparticle enhanced microwave imaging," *IEEE Access*, pp. 43192 - 43202, 2018.

[83] O. M. Bucci, G. Bellizzi, and G. G. Bellizzi, "Microwave Broadband Characterization of a Diluted Water-Based Ferrofluid in Presence of a Polarizing Magnetic Field," *IEEE Trans. Magn.*, vol. 53, no. 3, pp. 5300108, 2017.

[84] O. M. Bucci, L. Crocco, and R. Scapaticci, "On the optimal measurement configuration for magnetic nanoparticles-enhanced breast cancer microwave imaging," *IEEE Trans. Biomed. Eng.*, vol. 62, no. 2, pp. 407–414, 2015.

[85] O. M. Bucci *et al.*, "Experimental framework for magnetic nanoparticles enhanced breast cancer microwave imaging," *IEEE Access*, pp. 16332 - 16340, 2017.

[86] M. A. Tshabalala, B. F. Dejene, and H. C. Swart, "Synthesis and characterization of ZnO nanoparticles using polyethylene glycol (PEG)," *Phys. B Condens. Matter*, vol. 407, no. 10, pp. 1668–1671, 2012.

[87] "Keysight 85070E Dielectric Probe Kit 200 MHz to 50 GHz.," USA, 2014.

[88] Z. Miao and P. Kosmas, "Multiple-Frequency DBIM-TwIST Algorithm for Microwave Breast Imaging," *IEEE Trans. Antennas Propag.*, vol. 65, no. 5, pp. 2507–2516, 2017.

[89] S. R. Kroto HW, Heath JR, O'Brien SC, Curl RF, "C60: buckminsterfullerene," *Nature*, vol. 318, pp. 162-163, 1985.

[90] C. Zhao, A. Zhang, Y. Zheng, and J. Luan, "Electromagnetic and microwave-absorbing

properties of magnetite decorated multiwalled carbon nanotubes prepared with poly(N-vinyl-2-pyrrolidone)," *Mater. Res. Bull.*, vol. 47, pp. 217-221, 2012.

[91] Y. Deng, L. Zhao, B. Shen, L. Liu, and W. Hu, "Microwave characterization of submicrometer-sized nickel hollow sphere composites," *J. Appl. Phys.*, pp. 014304-5, 2006.

[92] M. V. F. Nanni, P. Travaglia, "Effect of carbon nanofibres dispersion on the microwave absorbing properties of CNF/epoxy composites," *Compos Sci Technol*, vol. 69, pp. 485-490, 2009.

[93] J. M. J. X. Lv, S.L. Yang, J.H. Jin, L. Zhang, G. Li, "Microwave absorbing characteristics of epoxy composites containing carbon black and carbon fibers (in Korean)," *Polymer-Korea*, pp. 207-211, 2009.

[94] Y. Wang *et al.*, "Development for silicon carbide fibers with trilobal cross section," *J. Mater. Sci. Lett.*, pp. 350, 2002.

[95] R. M. M. V. Panwar, "Analysis of electrical, dielectric and electromagnetic interference shielding behavior of graphite filled high density polyethylene composites," *Polym Eng Sci*, vol. 48, pp. 2178-2187, 2008.

[96] J. Qiu and T. Qiu, "Fabrication and microwave absorption properties of magnetite nanoparticle-carbon nanotube-hollow carbon fiber composites," *Carbon N. Y.*, vol. 81, pp. 20-28, 2015.

[97] L. Qing-QingNi ToshiakiNatsuki YaqinFu, "Carbon nanotubes/magnetite hybrids prepared by a facile synthesis process and their magnetic properties," *Appl. Surf. Sci.*, pp. vol. 255, 8676-8681, 2009.

[98] A. Lekawa-Raus, J. Patmore, L. Kurzepa, J. Bulmer, and K. Koziol, "Electrical properties of carbon nanotube based fibers and their future use in electrical wiring," *Adv. Funct. Mater.*,

vol. 81, pp. 3661-3682, 2014.

[99] M. R. McDevitt *et al.*, "Tumor Targeting with Antibody-Functionalized, Radiolabeled Carbon Nanotubes," *J. Nucl. Med.*, vol. 48, pp. 1180-1189, 2007.

[100] B. Sitharaman and L. J. Wilson, "Gadofullerenes and gadonanotubes: A new paradigm for high-performance magnetic resonance imaging contrast agent probes," *Journal of Biomedical Nanotechnology.*, pp. 342-352, 2007.

[101] S. Iijima, "Helical microtubules of graphitic carbon," *Nature*, pp. 56-58, 1991.

[102] L. Radushkevich, "O strukture ugleroda, obrazujucegosja pri termiceskom razlozenii okisi ugleroda na zeleznom kontakte," *Zhurnal Fizicheskoi Khimii*, vol. 26. pp. 88–95, 1952.

[103] S. B. D. Akiladevi, "Carbon Nanotubes (CNTs) Production, Characterisation and Its Applications," *Int. J. Adv. Pharm. Sci.*, vol. 1, pp. 187–195, 2010.

[104] A. Oberlin, M. Endo, and T. Koyama, "Filamentous growth of carbon through benzene decomposition," *J. Cryst. Growth*, vol. 32, no. 3, pp. 335–349, 1976.

[105] J. Abrahamson, P. G. Wiles, and B. L. Rhoades, "Structure of carbon fibres found on carbon arc anodes," *Carbon N. Y.*, vol. 37, no. 11, pp. 1873–1874, 1999.

[106] M. Monthioux and V. L. Kuznetsov, "Who should be given the credit for the discovery of carbon nanotubes?," *Carbon*, vol. 44, no. 9, pp. 1621–1623, 2006.

[107] M. Brcic, M. Canadija, and and J. Brnic, "Influence of imperfections on carbon nanotube properties," in *8 nd International Conference on Physical and Numerical Simulation of Materials Processing, ICPNS'16*, pp. 1-6, 2016.

[108] S. Iijima and T. Ichihashi, "Single-shell carbon nanotubes of 1-nm diameter," *Nature*, vol. 363, no. 6430, pp. 603–605, 1993.

[109] K. S. Ibrahim, "Carbon nanotubes–properties and applications: a review," *Carbon Lett.*, vol. 14, no. 3, pp. 131–144, 2013.

[110] M. S. Dresselhaus *et al.*, "Nanowires and nanotubes," *Mater. Sci. Eng. C*, vol. 23, no. 1–2, pp. 129–140, 2003.

[111] D. S. Bethune *et al.*, "Cobalt-catalysed growth of carbon nanotubes with single-atomic-layer walls," *Nature*, vol. 363, no. 6430, pp. 605–607, 1993.

[112] M. S. Dresselhaus, *Physical Properties of Carbon Nanotubes.*, pp. 87-89, 2005.

[113] A. Thess *et al.*, "Crystalline ropes of metallic carbon nanotubes," *Science*, pp. 483-487, 1996.

[114] W. Li *et al.*, "Large-Scale Synthesis of Aligned Carbon Nanotubes," *Science*, vol. 274, no. 5293, pp. 1701–3, 1996.

[115] B. Chandra *et al.*, "Molecular-scale quantum dots from carbon nanotube heterojunctions," *Nano Lett.*, vol. 9, no. 4, pp. 1544–1548, 2009.

[116] H. Dai, E. W. Wong, and C. M. Lieber, "Probing Electrical Transport in Nanomaterials: Conductivity of Individual Carbon Nanotubes," *Science (80-.).*, vol. 272, no. 5261, pp. 523–526, 1996.

[117] P. R. Bandaru, "Electrical Properties and Applications of Carbon Nanotube Structures," *J. Nanosci. Nanotechnol.*, pp.1-29, 2007.

[118] C. N. R. Rao, A. Govindaraj, G. Gundiah, and S. R. C. Vivekchand, "Nanotubes and nanowires," in *Chemical Engineering Science*, pp. 136, 2004.

[119] C. T. White and T. N. Todorov, "Carbon nanotubes as long ballistic conductors," *Nature*, vol. 393, pp. 240-242, 1998.

[120] A. Javey, J. Guo, Q. Wang, M. Lundstrom, and H. Dai, "Ballistic carbon nanotube field-

effect transistors," *Nature*, pp. 654-657, 2003.

[121] B. Q. Wei, R. Vajtai, and P. M. Ajayan, "Reliability and current carrying capacity of carbon nanotubes," *Appl. Phys. Lett.*, pp. 1172-1174, 2001.

[122] M. S. Dresselhaus, G. Dresselhaus, J. C. Charlier, and E. Hernández, "Electronic, thermal and mechanical properties of carbon nanotubes," *Philosophical Transactions of the Royal Society A: Mathematical, Physical and Engineering Sciences*. pp. 2065-2098, 2004.

[123] M. Sammalkorpi, A. Krasheninnikov, A. Kuronen, K. Nordlund, and K. Kaski, "Mechanical properties of carbon nanotubes with vacancies and related defects," *Phys. Rev. B - Condens. Matter Mater. Phys.*, pp. 4013-4021, 2004.

[124] A. Pullen, G. L. Zhao, D. Bagayoko, and L. Yang, "Structural, elastic, and electronic properties of deformed carbon nanotubes under uniaxial strain," *Phys. Rev. B - Condens. Matter Mater. Phys.*, 2005.

[125] C. Pozrikidis, "Effect of the Stone-Wales defect on the structure and mechanical properties of single-wall carbon nanotubes in axial stretch and twist," *Arch. Appl. Mech.*, pp. 113-123, 2009.

[126] A. Rahmandoust, M., Öchsner, "Influence of structural imperfections and doping on the mechanical properties of single-walled carbon nanotubes," *J. Nano Res.*, pp. 185–196, 2009.

[127] P. G. Collins, *Defects and disorder in carbon nanotubes.*, pp. 8-11, 2017.

[128] S. Azadi, R. Moradian, and A. M. Shafaee, "The effect of Stone-Wales defect orientations on the electronic properties of single-walled carbon nanotubes," *Comput. Mater. Sci.*, pp. 699-703, 2010.

[129] R. Czerw *et al.*, "Identification of Electron Donor States in N-Doped Carbon Nanotubes," *Nano Lett.*, pp. 457-460, 2001.

[130] S. Vardharajula *et al.*, "Functionalized carbon nanotubes: Biomedical applications," *International Journal of Nanomedicine*. pp. 5361-5374, 2012.

[131] K. Milowska, M. Birowska, and J. A. Majewski, "Mechanical and electrical properties of carbon nanotubes and graphene layers functionalized with amines," *Diam. Relat. Mater.*, pp. 167-171, 2012.

[132] B.-G. M. Jung-Hwan Kim, "Functionalization of Multi-walled Carbon Nanotube by Treatment with Dry Ozone Gas for the Enhanced Dispersion and Adhesion in Polymeric Composites," *Carbon Lett.*, pp. 298–303, 2010.

[133] K. Saeed, "Review on Properties, Dispersion and Toxicology of Carbon Nanotubes," *J. Chem. Soc. Pakistan*, vol. 32, no. 4, pp. 559–564, 2010.

[134] H.-C. Wu, X. Chang, L. Liu, F. Zhao, and Y. Zhao, "Chemistry of carbon nanotubes in biomedical applications," *J. Mater. Chem.*, vol. 20, p. 1036, 2010.

[135] M. C. Hersam, "Progress towards monodisperse single-walled carbon nanotubes," *Nature Nanotechnology*, vol. 3, no. 7. pp. 387–394, 2008.

[136] C. H. Lau *et al.*, "The effect of functionalization on structure and electrical conductivity of multi-walled carbon nanotubes," *J. Nanoparticle Res.*, pp. 77-88, 2008.

[137] V. N. Popov, "Carbon nanotubes: Properties and application," *Materials Science and Engineering R: Reports*, vol. 43, no. 3. pp. 61–102, 2004.

[138] K. Kostarelos, "Rational design and engineering of delivery systems for therapeutics: Biomedical exercises in colloid and surface science," *Adv. Colloid Interface Sci.*, vol. 106, no. 1–3, pp. 147–168, 2003.

[139] A. Nel, T. Xia, L. Mädler, and N. Li, "Toxic potential of materials at the nanolevel," *Science*, vol. 311, no. 5761. pp. 622–627, 2006.

[140] R. Hirlekar, M. Yamagar, H. Garse, V. Mohit, and V. Kadam, "Carbon nanotubes and its applications: A review," *Asian Journal of Pharmaceutical and Clinical Research*. pp. 288-293, 2009.

[141] Z. Ou, B. Wu, and D. Xing, "A novel cancer-targeting transporter with integrin $\alpha_v\beta_3$ monoclonal antibody functionalized single-walled carbon nanotubes," in *Proceedings of SPIE - The International Society for Optical Engineering*, vol. 7519, 751904-8, 2009.

[142] M. Sheikhpour, A. Golbabaie, and A. Kasaeian, "Carbon nanotubes: A review of novel strategies for cancer diagnosis and treatment," *Materials Science and Engineering C*. pp. 1289-1304, 2017.

[143] M. Miao, "Electrical conductivity of pure carbon nanotube yarns," *Carbon N. Y.*, pp. 3755-3761, 2011.

[144] H. Chen, M. R. Golder, F. Wang, R. Jasti, and A. K. Swan, "Raman spectroscopy of carbon nanohoops," *Carbon N. Y.*, pp. 203-213, 2014.

[145] H. Murphy, P. Papakonstantinou, and T. I. T. Okpalugo, "Raman study of multiwalled carbon nanotubes functionalized with oxygen groups," *J. Vac. Sci. Technol. B Microelectron. Nanom. Struct.*, pp. 715-720, 2006.

[146] A. Puzenko *et al.*, "Relaxation dynamics in glycerol-water mixtures: I. Glycerol-rich mixtures," *J. Phys. Chem. B*, pp. 6031-6035, 2005.

[147] J. Garrett and E. Fear, "A New Breast Phantom With a Durable Skin Layer for Microwave Breast Imaging," *IEEE Trans. Antennas Propag.*, pp. 1693-1700, 2015.

[148] J. Garrett and E. Fear, "Stable and flexible materials to mimic the dielectric properties of human soft tissues," *IEEE Antennas Wirel. Propag. Lett.*, pp. 599-602, 2014.

[149] M. Lazebnik, E. L. Madsen, G. R. Frank, and S. C. Hagness, "Tissue-mimicking phantom materials for narrowband and ultrawideband microwave applications," *Phys. Med. Biol.*, vol.

50, no. 18, pp. 4245–4258, 2005.

[150] L. Banszerus *et al.*, "Ballistic Transport Exceeding 28 μm in CVD Grown Graphene," *Nano Lett.*, pp. 1387-1391, 2016.

[151] P. Poncharal, C. Berger, Y. Yi, Z. L. Wang, and W. A. De Heer, "Room temperature ballistic conduction in carbon nanotubes," *J. Phys. Chem. B*, pp. 12104-12118, 2002.

[152] N. Saifuddin, A. Z. Raziah, and A. R. Junizah, "Carbon nanotubes: A review on structure and their interaction with proteins," *J. Chem.*, vol. 2013, pp 1-18, 2013.

[153] C. M. Sayes *et al.*, "Functionalization density dependence of single-walled carbon nanotubes cytotoxicity in vitro," *Toxicol. Lett.*, vol. 161, no. 2, pp. 135–142, 2006.

[154] F. V. Ferreira *et al.*, "Dodecylamine functionalization of carbon nanotubes to improve dispersion, thermal and mechanical properties of polyethylene based nanocomposites," *Appl. Surf. Sci.*, pp. 267-277, 2017.

[155] C.-X. Liu and J.-W. Choi, "Improved Dispersion of Carbon Nanotubes in Polymers at High Concentrations," *Nanomaterials*, pp. 329-347, 2012.

[156] M. Q. Tran, C. Tridech, A. Alfrey, A. Bismarck, and M. S. P. Shaffer, "Thermal oxidative cutting of multi-walled carbon nanotubes," *Carbon N. Y.*, pp. 2341-2350, 2007.

[157] L. Chen, H. Xie, Y. Li, and W. Yu, "Carbon nanotubes with hydrophilic surfaces produced by a wet-mechanochemical reaction with potassium hydroxide using ethanol as solvent," *Mater. Lett.*, pp. 45-47, 2009.

[158] S. Z. Kang, D. er Yin, X. Li, and J. Mu, "A facile preparation of multiwalled carbon nanotubes modified with hydroxyl groups and their high dispersibility in ethanol," *Colloids Surfaces A Physicochem. Eng. Asp.*, pp. 363-367, 2011.

[159] X.-L. L. Yi-Zhe Wei, Li-Ming Zou Su Xu, "Preparation and characterization of hydroxylated multi-walled carbon nanotubes," *Colloids Surfaces A Physicochem. Eng. Asp.*, vol. 421, pp. 9–15, 2013.

[160] X. Wang, Q. Jiang, W. Xu, W. Cai, Y. Inoue, and Y. Zhu, "Effect of carbon nanotube length on thermal, electrical and mechanical properties of CNT/bismaleimide composites," *Carbon N. Y.*, vol. 53, pp. 145–152, 2013.

[161] P. Padmanabhan, A. Kumar, S. Kumar, R. K. Chaudhary, and B. Gulyás, "Nanoparticles in practice for molecular-imaging applications: An overview," *Acta Biomaterialia*, pp. 1-16, 2016.

[162] J. Kim *et al.*, "Multifunctional uniform nanoparticles composed of a magnetite nanocrystal core and a mesoporous silica shell for magnetic resonance and fluorescence imaging and for drug delivery," *Angew. Chemie - Int. Ed.*, pp. 8438-8441, 2008.

[163] S. K. Yen, P. Padmanabhan, and S. T. Selvan, "Multifunctional iron oxide nanoparticles for diagnostics, therapy and macromolecule delivery," *Theranostics.*, pp. 986-1003, 2013.

[164] W. Jiang, S. Mardyani, H. Fischer, and W. C. W. Chan, "Design and characterization of lysine cross-linked mercapto-acid biocompatible quantum dots," *Chem. Mater.*, pp. 872- 878, 2006.

[165] S. Mallidi, S.; Larson, T.; Tam, J.; Joshi, P.P.; Karpiouk, A; Sokolov, K.; Emelianov, "multiwavelength photoacoustic imaging and plasmon resonance coupling of gold nanoparticles for selective detection of cancer," *Nano Lett.*,pp. 2825-2831, 2009.

[166] J. V. Jokerst, A. J. Cole, D. Van De Sompel, and S. S. Gambhir, "Gold nanorods for ovarian cancer detection with photoacoustic imaging and resection guidance via Raman imaging in living mice," *ACS Nano*, pp. 10366-10377, 2012.

[167] A. De La Zerda *et al.*, "Carbon nanotubes as photoacoustic molecular imaging agents in living mice," *Nat. Nanotechnol.*, pp. 5575-562, 2008.

[168] J. Kim, N. Lee, and T. Hyeon, "Recent development of nanoparticles for molecular imaging," *Philosophical Transactions of the Royal Society A: Mathematical, Physical and Engineering Sciences*. pp. 1-17, 2017.

[169] R. B. V.Prasad, I.Sameera, "Preparation, characterization and electrical conductivity studies of MWCNT/ZnO nanoparticles hybrid," *Phys. B Condens. Matter*, vol. 405, no. 7, pp. 1709–1714, 2010.

[170] M. H. and G. Z. Feng Qiu, Guangjian He *, "Enhancing the Mechanical and Electrical Properties of Poly(Vinyl Chloride)-Based Conductive Nanocomposites by Zinc Oxide Nanorods," *Materials (Basel).*, vol. 11, no. 11, pp 1-15, 2018.

[171] H. Mirzaei and M. Darroudi, "Zinc oxide nanoparticles: Biological synthesis and biomedical applications," *Ceram. Int.*, vol. 43, no. 1, pp. 907-914, 2017.

[172] W. Tu, J. Lei, P. Wang, and H. Ju, "Photoelectrochemistry of free-base-porphyrin-functionalized zinc oxide nanoparticles and their applications in biosensing," *Chem. - A Eur. J.*, vol. 17, no. 34, pp. 9440–9447, 2011.

[173] K.-Y. Hwa and B. Subramani, "Synthesis of zinc oxide nanoparticles on graphene–carbon nanotube hybrid for glucose biosensor applications," *Biosens. Bioelectron.*, vol. 62, pp. 127–133, 2014.

[174] G. Bisht and S. Rayamajhi, "ZnO Nanoparticles: A Promising Anticancer Agent," *Nanobiomedicine*, pp. 1-11, 2016.

[175] P. K. Mishra, H. Mishra, A. Ekielski, S. Talegaonkar, and B. Vaidya, "Zinc oxide nanoparticles: a promising nanomaterial for biomedical applications," *Drug Discovery Today*.

pp. 1825-1834, 2017.

[176] J. W. Rasmussen, E. Martinez, P. Louka, and D. G. Wingett, "Zinc oxide nanoparticles for selective destruction of tumor cells and potential for drug delivery applications," *Expert Opin. Drug Deliv.*, vol. 7, no. 9, pp. 1063–1077, 2010.

[177] S. Sruthi, N. Millot, and P. V. Mohanan, "Zinc oxide nanoparticles mediated cytotoxicity, mitochondrial membrane potential and level of antioxidants in presence of melatonin," *Int. J. Biol. Macromol.*, pp. 808-818, 2017.

[178] K. Anand and S. Varghese, "Role of surfactants on the stability of nano-zinc oxide dispersions," *Part. Sci. Technol.*, pp. 67-70, 2017.

[179] S. Lakhwani and M. N. Rahaman, "Adsorption of polyvinylpyrrolidone (PVP) and its effect on the consolidation of suspensions of nanocrystalline CeO_2 particles," *J. Mater. Sci.*, pp. 3909-3912, 1999.

[180] O. Dulub, U. Diebold, and G. Kresse, "Novel Stabilization Mechanism on Polar Surfaces: ZnO(0001)-Zn," *Phys. Rev. Lett.*, vol. 90, no. 1, pp. 016102-0161024, 2003.

[181] S. Chibowski, M. Paszkiewicz, and M. Krupa, "Investigation of the influence of the polyvinyl alcohol adsorption on the electrical properties of Al_2O_3-solution interface, thickness of the adsorption layers of PVA," *Powder Technol.*, pp. 251-255, 2000.

[182] Y. W. Zhang, M. Tang, X. Jin, C. S. Liao, and C. H. Yan, "Polymeric adsorption behavior of nanoparticulate yttria stabilized zirconia and the deposition of as-formed suspensions on dense α-Al_2O_3substrates," *Solid State Sci.*, pp. 435-440, 2003.

[183] K. Knop, R. Hoogenboom, D. Fischer, and U. S. Schubert, "Poly(ethylene glycol) in drug delivery: Pros and cons as well as potential alternatives," *Angewandte Chemie - International Edition*. pp. 6288-6308, 2010.

[184] D. M. Collard and M. A. Fox, "Use of Electroactive Thiols to Study the Formation and Exchange of Alkanethiol Monolayers on Gold," *Langmuir*, pp. 1192-1197, 1991.

[185] E. V. Shashkov, M. Everts, E. I. Galanzha, and V. P. Zharov, "Quantum dots as multimodal photoacoustic and photothermal contrast agents," *Nano Lett.*, pp. 3953-3958, 2008.

[186] J. Chen *et al.*, "Gold nanocages: Bioconjugation and their potential use as optical imaging contrast agents," *Nano Lett.*, pp. 473-477, 2005.

[187] E. C. Cho, C. Glaus, J. Chen, M. J. Welch, and Y. Xia, "Inorganic nanoparticle-based contrast agents for molecular imaging," *Trends in Molecular Medicine.*, pp. 561-573, 2010.

[188] J. V Jokerst, T. Lobovkina, R. N. Zare, and S. S. Gambhir, "Nanoparticle PEGylation for imaging and therapy," *Nanomedicine*, vol. 6, no. 4, pp. 715–728, 2011.

[189] H. Lee, A. H. De Vries, S. J. Marrink, and R. W. Pastor, "A coarse-grained model for polyethylene oxide and polyethylene glycol: Conformation and hydrodynamics," *J. Phys. Chem. B*, vol. 113, no. 40, pp. 13186–13194, 2009.

[190] Z. M. and P. Kosmas, "Multiple-Frequency DBIM-TwIST Algorithm for Microwave Breast Imaging," *IEEE Trans. Antennas Propag.*, vol. 65, no. 5, pp. 2507–2516, 2017.

[191] U. Kaatze, "Complex Permittivity of Water as a Function of Frequency and Temperature," *J. Chem. Eng. Data*, vol. 34, no. 4, pp. 371–374, 1989.

[192] P. M. Meaney, A. P. Gregory, N. R. Epstein, and K. D. Paulsen, "Microwave open-ended coaxial dielectric probe: Interpretation of the sensing volume re-visited," *BMC Med. Phys.*, vol. 14, no. 1, pp. 1-11, 2014.

[193] B. J. Li X, Sahakian AV, Hagness, SC, "Nanoparticle contrast agents for enhanced microwave imaging and thermal treatment of breast cancer, Tech. Rep.," pp. 1-19, 2010.

[194] Valentin N Popov, "Carbon nanotubes: properties and applications," *Mater. Sci. Eng. R Reports*, vol. 43, pp. 61-102, 2004.

[195] A. K. Das, S. Sinha, A. Mukherjee, and A. K. Meikap, "Enhanced dielectric properties in polyvinyl alcohol - Multiwall carbon nanotube composites," *Mater. Chem. Phys.*, vol. 167, pp. 286-294, 2015.

[196] Y. Bao *et al.*, "Influence of surface polarity of carbon nanotubes on electric field induced aligned conductive network formation in a polymer melt," *RSC Adv.*, 2013.

[197] C. W. Lam, J. T. James, R. McCluskey, S. Arepalli, and R. L. Hunter, "A review of carbon nanotube toxicity and assessment of potential occupational and environmental health risks," *Critical Reviews in Toxicology*, pp. 189-217, 2006.

[198] J. Muller *et al.*, "Structural defects play a major role in the acute lung toxicity of multiwall carbon nanotubes: Toxicological aspects," *Chem. Res. Toxicol.*, vol. 21, no. 9, pp. 1698–1705, 2008.

[199] C. Hanley *et al.*, "Preferential killing of cancer cells and activated human T cells using ZnO nanoparticles," *Nanotechnology*, pp. 1-20, 2008.

[200] and Z. L. W. Zhou Li, Rusen Yang, Min Yu, Fan Bai, Cheng Li, "Cellular Level Biocompatibility and Biosafety of ZnO Nanowires," *J. Phys. Chem. C*, pp. 20114–20117 2008.

[201] A. Iglesias-Juez, F. Viñes, O. Lamiel-García, M. Fernández-García, and F. Illas, "Morphology effects in photoactive ZnO nanostructures: photooxidative activity of polar surfaces," *J. Mater. Chem. A*, vol. 3, no. 16, pp. 8782–8792, 2015.

[202] Z. L. Wang, "Zinc oxide nanostructures: Growth, properties and applications," *J. Phys. Condens. Matter*, vol. 16, no. 25, pp. R829–R858 2004.

[203] C. C. Vidyasagar and Y. Arthoba Naik, "Surfactant (PEG 400) effects on crystallinity of ZnO nanoparticles," *Arab. J. Chem.*, vol. 9, no. 4, pp. 507–510, 2016.

[204] O. Dulub, L. A. Boatner, and U. Diebold, "STM study of the geometric and electronic structure of ZnO(0001)-Zn, (000-1)-O, (10-10), and (11-20) surfaces," *Surf. Sci.*, vol. 519, no. 3, pp. 201–217, 2002.

[205] A. Ali *et al.*, "Synthesis, characterization, applications, and challenges of iron oxide nanoparticles," *Nanotechnology, Science and Applications*, vol. 9. pp. 49–67, 2016.

[206] J. Polte, "Fundamental growth principles of colloidal metal nanoparticles - a new perspective," *CrystEngComm*, vol. 36, pp. 6809-6830, 2015.

[207] J. ChenCurrent address: Key Lab. of Ra, S. K. Spear, J. G. Huddleston, and R. D. Rogers, "Polyethylene glycol and solutions of polyethylene glycol as green reaction media," *Green Chem.*, vol. 7, no. 2, pp. 64, 2005.

[208] S. Liufu, H. Xiao, and Y. Li, "Investigation of PEG adsorption on the surface of zinc oxide nanoparticles," *Powder Technol.*, vol. 145, no. 1, pp. 20–24, 2004.

[209] G. Nabiyouni, A. Barati, and M. Saadat, "Surface Adsorption of Polyethylene Glycol and Polyvinyl Alcohol with Variable Molecular Weights on Zinc Oxide Nanoparticles," *Iran. J. Chem.* …, vol. 8, no. 1, pp. 20–30, 2011.

[210] Srikanta MoharanaMukesh K. MishraBanarji BeheraR. N. Mahaling, "Enhanced dielectric properties of polyethylene glycol (PEG) modified $BaTiO_3$ (BT)-poly(vinylidene fluoride) (PVDF) composites," *Polym. Sci. Ser. A*, vol. 59, no. 3, pp. 405-415, 2017.

[211] T. Koizumi, Naokazu; Hanai, "Dielectric Properties of Polyethylene Glycols : Dielectric Relaxation in Solid State (Special Issue on Polymer Chemistry, I)," *Dep. Bull. Pap.*, pp. 115-127, 1964.

[212] I. Favier, D. Pla, and M. Gómez, "Metal-based nanoparticles dispersed in glycerol: An efficient approach for catalysis," *Catal. Today*, pp. 98-106, 2018.

[213] B. Faure *et al.*, "Dispersion and surface functionalization of oxide nanoparticles for transparent photocatalytic and UV-protecting coatings and sunscreens," *Science and Technology of Advanced Materials*. pp. 1-23, 2013.

[214] P. T. Charles, V. R. Stubbs, C. M. Soto, B. D. Martin, B. J. White, and C. R. Taitt, "Reduction of non-specific protein adsorption using poly(ethylene) glycol (PEG) modified polyacrylate hydrogels in immunoassays for staphylococcal enterotoxin B detection," *Sensors*, pp. 645-655, 2009.

[215] and M. C. S. S. K. Sudharsan Reddy, M. N. Prabhakar, P. Kumara Babu, G. Venkatesulu, U. Sajan Kumarji Rao, K. Chowdoji Rao, "Miscibility Studies of Hydroxypropyl Cellulose/Poly(EthyleneGlycol) in Dilute Solutions and Solid State," *Int. J. Carbohydr. Chem.*, pp. 1-9, 2012.

[216] Na. KOlZUMI, "Dielectric Properties of Polyethylene Glycols at Microwave Frequencies," *J. Chem. Phys.*, vol. 27, no. 3, pp.625-630, 1957.

[217] R. J. Sengwa, K. Kaur, and R. Chaudhary, "Dielectric properties of low molecular weight poly(ethylene glycol)s," *Polym. Int.*, pp. 599-608, 2000.

[218] N. V. S. Vallabani and S. Singh, "Recent advances and future prospects of iron oxide nanoparticles in biomedicine and diagnostics," *3 Biotech*, pp. 1-23, 2018.

[219] A. S. Teja and P. Y. Koh, "Synthesis, properties, and applications of magnetic iron oxide nanoparticles," *Progress in Crystal Growth and Characterization of Materials*,pp. 22-45, 2009.

[220] N. T. Thanh, *Magnetic nanoparticles: from fabrication to clinical applications*., pp 1-20, 2012.

[221] S. H. Hosseini, P. Zamani, and S. Y. Mousavi, "Thermal infrared and microwave absorbing

properties of $SrTiO_3$, $SrFe_{12}O_{19}$/polyaniline nanocomposites," *J. Alloys Compd.*, pp. 423-429, 2015.

[222] M. J. Molaei and M. R. Rahimipour, "Microwave reflection loss of magnetic/dielectric nanocomposites of $BaFe_{12}O_{19}/TiO_2$," *Mater. Chem. Phys.*, pp. 145-151, 2015.

[223] G. Bellizzi, O. Bucci, and I. Catapano, "Magnetic nanoparticle as contrast agent for microwave breast cancer imaging," in *Antennas and Propagation (EuCAP), 2010 Proceedings of the Fourth European Conference on*, pp. 1-5, 2010.

[224] A. Hervault and N. T. K. Thanh, "Magnetic nanoparticle-based therapeutic agents for thermo-chemotherapy treatment of cancer," *Nanoscale*, pp. 11553–11573, 2014.

[225] V. I. Shubayev, T. R. Pisanic, and S. Jin, "Magnetic nanoparticles for theragnostics," *Advanced Drug Delivery Reviews*, pp. 467-477, 2009.

[226] D. L. Huber, "Synthesis, properties, and applications of iron nanoparticles.," *Small , Wiley Verlag GmbH Co, Weinheim*, pp. 482-501, 2005.

[227] S. Klotz, G. Steinle-Neumann, T. Strässle, J. Philippe, T. Hansen, and M. J. Wenzel, "Magnetism and the Verwey transition in Fe_3O_4 under pressure," *Phys. Rev. B*, pp. 58-61, 2008.

[228] R. Valenzuela, "Novel applications of ferrites," *Physics Research International*, pp. 1-9, 2012.

[229] G. Thirupathi and R. Singh, "Magnetic properties of zinc ferrite nanoparticles," *IEEE Trans. Magn.*, pp. 3630 - 3633, 2012.

[230] W. Wu, Z. Wu, T. Yu, C. Jiang, and W. S. Kim, "Recent progress on magnetic iron oxide nanoparticles: Synthesis, surface functional strategies and biomedical applications," *Science and Technology of Advanced Materials*. pp. 1-43, 2015.

[231] A. Radoń, A. Drygała, Ł. Hawełek, and D. Łukowiec, "Structure and optical properties of Fe_3O_4 nanoparticles synthesized by co-precipitation method with different organic modifiers," *Mater. Charact.*, pp. 148-156, 2017.

[232] M. G. Naseri, E. B. Saion, M. Hashim, A. H. Shaari, and H. A. Ahangar, "Synthesis and characterization of zinc ferrite nanoparticles by a thermal treatment method," *Solid State Commun.*, pp. 1031-1035, 2011.

[233] L. Mohammed, H. G. Gomaa, D. Ragab, and J. Zhu, "Magnetic nanoparticles for environmental and biomedical applications: A review," *Particuology*, pp. 1-14, 2017.

[234] S. F. Hasany and A. R. , I. Ahmed, Rajan J, "Systematic Review of the Preparation Techniques of Iron Oxide Magnetic Nanoparticles," *Nanosci. Nanotechnol.*, vol. 2, no. 6, pp. 148–158, 2012.

[235] C. Cunningham and T. Arai, "Positive contrast magnetic resonance imaging of cells labeled with magnetic nanoparticles," *Magn. Reson. Med.*, vol. 53, no. 5, pp. 999–1005, 2005.

[236] Y. Ren *et al.*, "Multifunctional magnetic Fe_3O_4 nanoparticles combined with chemotherapy and hyperthermia to overcome multidrug resistance," *Int. J. Nanomedicine*, pp. 2261–2269, 2012.

[237] A. J. GIUSTINI, A. A. PETRYK, S. M. CASSIM, J. A. TATE, I. BAKER, and P. J. HOOPES, "MAGNETIC NANOPARTICLE HYPERTHERMIA IN CANCER TREATMENT," *Nano Life*, pp. 1-23, 2010.

[238] A. K. Gupta and M. Gupta, "Synthesis and surface engineering of iron oxide nanoparticles for biomedical applications," *Biomaterials*. pp. 3995-4021, 2005.

[239] J. E. Rosen, L. Chan, D. Bin Shieh, and F. X. Gu, "Iron oxide nanoparticles for targeted cancer imaging and diagnostics," *Nanomedicine: Nanotechnology, Biology, and Medicine*, pp. 275-

290, 2012.

[240] A. Yanai *et al.*, "Focused Magnetic Stem Cell Targeting to the Retina Using Superparamagnetic Iron Oxide Nanoparticles," *Cell Transplant.*, vol. 21, no. 6, pp. 1137–1148, 2012.

[241] A. S. C. Brown, J. S. J. Hargreaves, and B. Rijniersce, "A study of the structural and catalytic effects of sulfation on iron oxide catalysts prepared from goethite and ferrihydrite precursors for methane oxidation," *Catal. Letters*, vol. 53, no. 1, pp. 7-13–13, 1998.

[242] M. K. Yu *et al.*, "Drug-loaded superparamagnetic iron oxide nanoparticles for combined cancer imaging and therapy in vivo," *Angew. Chemie - Int. Ed.*, vol. 47, no. 29, pp. 5362-5365, 2008.

[243] D. K. Chatterjee, P. Diagaradjane, and S. Krishnan, "Nanoparticle-mediated hyperthermia in cancer therapy," *Ther. Deliv.*, vol. 2, no. 8, pp. 1001–1014, 2011.

[244] A. Orlando *et al.*, "Iron oxide nanoparticles surface coating and cell uptake affect biocompatibility and inflammatory responses of endothelial cells and macrophages," *J. Nanoparticle Res.*, vol. 17, no. 9, pp. 1-13, 2015.

[245] "Endomag.": http://www.endomag.com/sentimag.

[246] "Quentin Pankhurst.": http://www.rigb.org/our-history/people/p/quentin-pankhurst.

[247] A. Karakatsanis *et al.*, "The Nordic SentiMag trial: a comparison of super paramagnetic iron oxide (SPIO) nanoparticles versus Tc(99) and patent blue in the detection of sentinel node (SN) in patients with breast cancer and a meta-analysis of earlier studies," *Breast Cancer Res. Treat.*, pp. 281-294, 2016.

[248] "Ferrofluids." http://www.liquidsresearch.com/en-GB/ferrofluids-50.aspx

[249] S. Semenov, N. Pham, and S. Egot-Lemaire, "Ferroelectric nanoparticles for contrast enhancement microwave tomography: Feasibility assessment for detection of lung cancer," in *IFMBE Proceedings*, pp. 311-313, 2009.

[250] L. M. Bronstein *et al.*, "Hydrophilization of magnetic nanoparticles with modified alternating copolymers. Part 1: The influence of the grafting," *J. Phys. Chem. C*, pp. 21900–21907, 2010.

[251] T. Tepper *et al.*, "Magneto-optical properties of iron oxide films," in *Journal of Applied Physics*, pp. 6948-6950, 2003.

[252] S. Laurent *et al.*, "Erratum: Magnetic iron oxide nanoparticles: Synthesis, stabilization, vectorization, physicochemical characterizations, and biological applications (Chemical Reviews (2008) 108 (2064))," *Chemical Reviews*. pp. 2064–2110, 2010.

[253] R. Qiao, C. Yang, and M. Gao, "Superparamagnetic iron oxide nanoparticles: from preparations to in vivo MRI applications," *J. Mater. Chem.*, pp. 6274-6293 2009.

[254] A. H. Lu, E. L. Salabas, and F. Schüth, "Magnetic nanoparticles: Synthesis, protection, functionalization, and application," *Angewandte Chemie - International Edition*. 6, pp. 1222 – 1244, 2007.

[255] S. Dutz and R. Hergt, "Magnetic particle hyperthermia - A promising tumour therapy?," *Nanotechnology*, pp.1-28, 2014.

[256] P. I. P. Soares *et al.*, "Thermal and magnetic properties of iron oxide colloids: Influence of surfactants," *Nanotechnology*, pp. 1-11, 2015.

[257] G. Kandasamy and D. Maity, "Recent advances in superparamagnetic iron oxide nanoparticles (SPIONs) for in vitro and in vivo cancer nanotheranostics," *International Journal of Pharmaceutics*, pp. 191-218, 2015.

[258] G. K. Sidhu and R. Kumar, "Role of anionic and cationic surfactants on the structural and dielectric properties of ZrO_2 nanoparticles," *Appl. Surf. Sci.*, pp. 598-607, 2017.

[259] A. Radoń, D. Łukowiec, M. Kremzer, J. Mikuła, and P. Włodarczyk, "Electrical conduction mechanism and dielectric properties of spherical shaped Fe_3O_4 nanoparticles synthesized by co-precipitation method," *Materials (Basel).*, pp. 1-12, 2018.

[260] Q. Huo *et al.*, "Organization of Organic Molecules with Inorganic Molecular Species into Nanocomposite Biphase Arrays," *Chem. Mater.*, pp. 1176-1191, 1994.

[261] K. Nörtemann, J. Hilland, and U. Kaatze, "Dielectric Properties of Aqueous NaCl Solutions at Microwave Frequencies," *J. Phys. Chem. A*, pp. 6864–6869, 1997.

[262] P. B. Olumide Ogunlade, "Electric and magnetic properties of contrast agents for thermoacoustic imaging," in *Photons Plus Ultrasound: Imaging and Sensing*, pp. 1-6, 2014.

[263] P. M. Meaney, C. J. Fox, S. D. Geimer, and K. D. Paulsen, "Electrical Characterization of Glycerin: Water Mixtures: Implications for Use as a Coupling Medium in Microwave Tomography," *IEEE Trans. Microw. Theory Tech.*, pp. 1471 - 1478 2017.

[264] N. T. K. Thanh and L. A. W. Green, "Functionalisation of nanoparticles for biomedical applications," *Nano Today*. pp. 213-230, 2010.

[265] T. Pellegrino *et al.*, "Hydrophobic nanocrystals coated with an amphiphilic polymer shell: A general route to water soluble nanocrystals," *Nano Lett.*, pp. 703-707, 2004.

[266] A. S. Fawzi, A. D. Sheikh, and V. L. Mathe, "Structural, dielectric properties and AC conductivity of $Ni_{(1-x)}Zn_xFe_2O_4$ spinel ferrites," *J. Alloys Compd.*, pp. 231-237, 2010.

[267] R. Rani, G. Kumar, K. M. Batoo, and M. Singh, "Electric and Dielectric Study of Zinc Substituted Cobalt Nanoferrites Prepared by Solution Combustion Method," *Am. J. Nanomater.*, pp. 9-12, 2013.